The Study and Development of Distributed Devices for Concurrent Vibration Attenuation and Energy Harvesting

Ryan L. Harne

Dissertation submitted to the faculty of the
Virginia Polytechnic Institute and State University
in partial fulfillment of the requirements for the degree of

Doctor of Philosophy
in
Mechanical Engineering

Ricardo A. Burdisso, Chair
Daniel J. Inman
Rakesh K. Kapania
Alexander Leonessa
Cory M. Papenfuss

January 18, 2012
Blacksburg, Virginia

KEYWORDS: *vibration suppression, energy harvesting, structural dynamics, piezoelectricity, electromagnetism*

The Study and Development of Distributed Devices for Concurrent Vibration Attenuation and Energy Harvesting

Ryan L. Harne

(ABSTRACT)

This work focuses on the broadband attenuation of structural vibration and, in the process, employs a new perspective of vibrational energy harvesting devices. The first part of the research studies and develops a continuously distributed vibration control device which combines the benefits of point mass-spring-dampers at low frequencies as well as the resistive or dissipative influence of constraining treatments at high frequencies. This embodiment provides broadband passive vibration attenuation for a minimal cost in added mass, spanning the present divide between the ability to attenuate a single low frequency and the need to attenuate all frequencies. The second part adopts a vibration control perspective to energy harvesting analysis and considers the harvesting devices to be electromechanically stiffened and/or damped vibration absorbers. Rigorous analysis and experiments are carried out which show that vibration control and energy harvesting appear to be mutually beneficial given that maximum harvested energy from structural vibrations is achieved when the harvesters exert a finite dynamic influence on the host system. This suggests that vibration control concerns presently alleviated using tuned-mass-dampers are ideal energy harvesting applications.

A generalized analytical model is derived which is applicable to both portions of the work. Continuously distributed vibration control devices are studied in depth and a superposition method is presented which allows for convenient implementation of a realistic device design into the numerical model. Tests carried out with the distributed device validate the model as well as show the device's competitive benefits compared with traditional, and much heavier, vibration control treatments. The in-

clusion of electromechanical coupling effects into the modeling is straightforward and numerous analyses are carried out to observe how electromagnetic and piezoelectric energy harvesting devices affect the dynamics of the host vibrating structure while the harvesters themselves convert the "absorbed" energy into electrical power. Altering the device created in the first portion of the research to use a piezoelectric material as the distributed spring yields one such embodiment capable of both surface vibration control and energy harvesting. Tests carried out with the device additionally serve as model validation but also indicate that, for a given harvester, the attenuation of and energy harvesting from structural vibrations are nearly simultaneously maximized as modeling predicted.

to my Parents and Grandparents

Acknowledgements

This dissertation is presented in a unique format. As such, I deem it appropriate to include a unique section of acknowledgements to those whose contributions or involvement in my graduate research and studies have made profound impacts in my life in the areas of leadership, mentorship and friendship. My selections in this manner are not intended to appear as rigid declarations of the individuals' impact in my life but rather in what area those persons lent the most substantial influence. Those multiply-listed are deservedly so.

Leadership: • Dr. Ken Ball • Dr. Romesh Batra • Dr. Ricardo Burdisso • Dr. Marty Johnson • Dr. Alexander Leonessa • Dr. Paul Torgersen

Mentorship: • Dr. Ken Ball • Dr. Ricardo Burdisso • Ms. Gail Coe • Dr. Karen DePauw • Dr. Dan Inman • Dr. Rakesh Kapania • Dr. Alexander Leonessa • Dr. Cory Papenfuss • Dr. Mike Roan

Friendship: • Ms. Gail Coe • Dr. Brian Goode • Dr. Cory Papenfuss • Dr. Marcel Remillieux

To those above, with all genuine sincerity and humility: Thank You.

I must express a considerable recognition and gratitude to Kevin Smith at Newport News Shipbuilding for continued financial support throughout my time at Virginia Tech. I also thank the NASA–VSGC (Virginia Space Grant Consortium) for honoring me with a Graduate Research Fellowship in my final year of research and study. Finally, I would like to thank the North Carolina Chapter of the Acoustical Society of America (ASA) for honoring me with the 2011 ASA Royster Award; it will be my career-long charge to uphold the aims of research and development in noise control, hearing conservation and acoustics for which the honor was established.

It is likely that those doing absurd experiments
will be the ones to make discoveries.

J.W. Lane [1]

Contents

List of Figures

List of Tables

CHAPTER 1

Introduction

This research focuses on two related fields of study: passive vibration control of structures and vibrational energy harvesting. This work considers energy harvesting devices to be analogous to electromechanical vibration absorbers which are capable of substantial mechanical dynamic influence on the host structure while converting absorbed energy into electrical power. Analysis is first directed towards the dynamic influence of continuously distributed vibration control devices. Then, the two fields are unified in the theory and applications in energy harvesting are considered in tandem with structural vibration control. Experimental results are provided throughout for model validations and as additional supporting examples of the research potential.

To concentrate the results of the research, the dissertation is presented in three chapters. A brief introduction to the fields is hereafter given, including specified research objectives and explanation of the dissertation organization. Then, a comprehensive summary of the research is provided in one chapter, helping to consolidate the development and results of several publications which are provided as appendices. Finally, concluding remarks and synthesis of the work is provided in a third chapter with additional suggestions for future research.

1.1 Literature review

1.1.1 Passive vibration suppression

Structural vibration may be a concern for numerous reasons: shaking of sensitive attached components; radiated noise as the structural vibrations couple with the local acoustic field; fatigue of the structure leading to weakening and/or failure; to name a few. Passively attenuating such vibration by employing devices or treatments has long been pursued, one of the first patented efforts being the one-dimensional

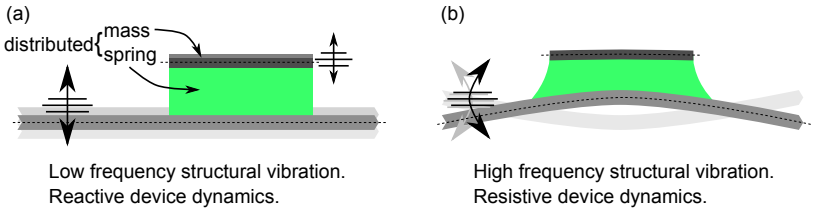

Figure 1.1: (a) Reactive and (b) resistive dynamic illustrations of a device in attenuating structural vibration.

vibration absorber by Frahm [2]. At a designed frequency this mass-spring-damper device reactively works against the excited system by supplying an equal and opposite force to suppress the structural vibration.

An alternative class of treatments are characterized by resistive effects. Within this class falls constraining layer treatments, originally considered by Oberst and Frankenfeld [3] and Liénard [4]. These treatments are deformed extensionally as the host structure vibrates in bending while a constraining layer applied to the exposed material surface amplifies the shear stress exerted against the host structure [5]. Use of damping materials either solely or as a sandwiched layer allows for energy dissipation. The dynamic influence of these two treatment classes are illustrated in Figure 1.1.

Reactive and resistive treatments, here designated as such due to mechanical impedance notation, are best suited for certain applications. Reactive devices are generally applied for localized, low frequency vibration problems; resistive treatments are most useful for mid to high frequency vibration. To achieve broadband surface vibration attenuation using reactive devices would entail employing a vast number of oscillators distributed over the surface each tuned to a different natural frequency. To enhance the low frequency attenuation capability of resistive treatments is possible only by adding further mass.

For aircraft, ships or land vehicles, added mass to control unwanted vibration comes at the cost of increased propulsive power. However, it is often the case that low frequency vibration of structural panels is the greatest nuisance. From a practical perspective, solution to this is neither satisfactory by employing numerous tuned

mass-spring systems nor with heavy constraining treatments. This concern has stimulated research interest in highly damped composite materials, *i.e.* carbon fiber reinforced polymers or plastics (CFRP), which promise substantial stiffness-to-weight in addition to damping by means of their lay-up and design [6–8]. These composite panels thereafter replace the lightly-damped metallic structural panels, providing an equivalent level of strength but greater dissipation of structural vibration. However, the cost of such materials for large-scale production remains prohibitive and the development of cost-effective, lightweight and broadband passive vibration control solutions is preferred.

Most present embodiments achieve a subset of these goals. Arrays of point oscillators have been considered on numerous occasions [9–12] but this is neither cost-effective, easy to apply nor significantly beneficial at high frequencies. One-dimensional, continuously distributed treatments have been considered for the suppression of vibrating beams [13, 14]. These were designed like especially thick constrained-layer damping (CLD) and were found to be very useful around a targeted natural frequency, similar to a series of single degree-of-freedom (SDOF) oscillators.

Some plate-like or two-dimensionally distributed oscillators appear in the literature but were considered to have discrete, linear spring attachment to the vibrating structure [15–17]. Apart from an architecturally focused study of a continuously distributed spring–mass [18], it appears that only Fuller and Cambou [19] and Marcotte et al. [20] have addressed distributed vibration absorbers which employ continuous spring and mass layers. However, in both cases, modeling was carried out neglecting the in-plane dynamic coupling between the spring layer and the host structure. Thus, it was assumed the devices operate like distributed mass layers resting atop a bed of linear transverse springs.

To achieve broadband passive vibration control of surfaces for a minimum of added mass, it is necessary to combine reactive and resistive dynamics for targeted effects at a low natural frequency but also substantial stiffness in the cross-planar directions

such that the device extensionally resists the surface vibration at higher frequencies. This appears to be an area left unaddressed by research study due to the focus on advanced material development. Until availability of these materials is more affordable, a more cost efficient passive vibration control solution embodying the reactive and resistive dynamics described is an appropriate remedy.

1.1.2 Vibrational energy harvesting

The rapid increase in deployment and interest in structural health monitoring following the I-35W Mississippi River bridge collapse in 2007 [21] has uncovered some concerns of electrically powering the systems. It is often desired to implement wireless transponders coincident with each structural sensor so as to relay all information back to a central monitoring station [22, 23]. Harnessing the vibrational energy of the structure promises a viable solution to regular battery replacement of the wireless sensor nodes, which require a power supply on the order of 0.01–10 mW [24, 25].

Converting this vibrational energy into useful electric power is achieved by the design and employment of electromechanically coupled devices—energy harvesters—frequently in the form of mass-spring systems. Electromechanical coupling is often achieved by inclusion of a piezoelectric spring or magnetic mass, Figure 1.2. The piezoelectric device is regularly embodied as a cantilevered piezoelectric beam with a tip mass [26–30]. Alternatively, magnetic masses which oscillate through the axis of a coil are suspended either by a spring-damper or perhaps by magnetic levitation [31–34]. Either the piezo electrodes or the ends of the coil are attached to external energy harvesting circuitry, modeled as a simple resistive load [35–41]. The harvester is designed such that it exhibits a natural frequency equal to that of the host vibrating structure. When excited by the structure, the harvester resonates and, via its electromechanical coupling mechanism, converts the vibrational energy into an electrical signal which is thereafter converted to DC for immediate use or as a charging supply.

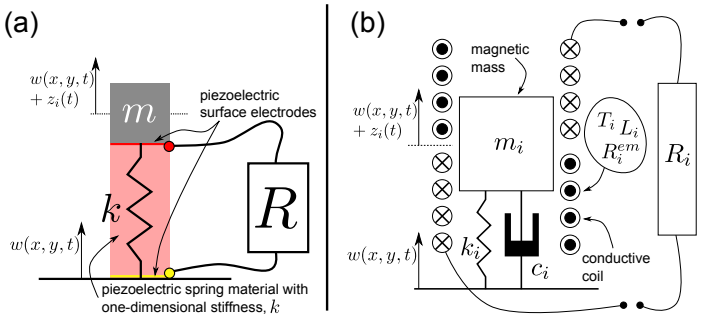

Figure 1.2: Example forms of one-dimensional energy harvester devices using (a) piezoelectric spring material or (b) magnetic mass oscillating through a coil.

1.1.3 Simultaneous achievement of surface vibration attenuation and power harvesting

To date, many studies in vibrational energy harvesting assume that the electromechanical mass-spring systems have no dynamic effect upon the structure to which they are attached. This is evidenced in the mathematical models by the use of base vibration as the source of excitation to the harvester [26, 28, 30, 36, 38, 39, 42]. This assumption may be valid if the inertial influence of the device is negligible compared to that of the host structure (*e.g.* harvesters on a bridge) and has become a mainstay in energy harvesting analysis.

The effect of shunted and resonant shunted piezoelectric materials applied directly to vibrating structures has been exploited as a passive dissipation mechanism for several decades [43–48]. The passive shunt damping effect is observed as a natural byproduct of piezoelectric harvesting energy from vibrating structures, whether in regards to the damping of the harvester dynamics itself or of the host structure in the event of directly applied piezoelectric materials [35–37, 40, 43, 44, 49–51]. One such piezoelectric energy harvesting application directly exploited the shunt damping effect in attenuating the induced flutter of an aircraft wing [52]. By selection of an optimum load resistance for the external harvesting circuit, the magnitude of the wing flutter was reduced by half of the maximum displacement, *e.g.* 6 dB of attenuation. Damping effects induced by electromagnetic energy harvesting have also been documented and

long-been employed as a useful means for shock isolation and damping [36, 38, 53–55].

1.2 Objectives of the dissertation

With the successful demonstration of energy harvesting devices following the first major thrust of research has come an interest to harness electrical power from nearly any source of vibration. In addition, combining vibration control and energy harvesting applications is a novel way to achieve two objectives simultaneously. However, as compared with conventional tuned-mass-dampers which exert a significant mechanical influence on the host structure, the energy harvesting devices to date are limited by shunt damping dissipation due to their design and implementation. By embedding or applying piezoelectric materials to vibrating surfaces, there is relatively little mechanical authority that the harvesters exert on the host structure as compared with purely passive tuned-mass-dampers. Furthermore, though electromagnetic energy harvesting devices are oftentimes constructed in a form identical to mass-spring-dampers, they have yet to be employed for the dual-purpose aim of vibration control and energy harvesting.

Adopting a new perspective of energy harvesters as electromechanical vibration absorbers transforms nearly any vibration control concern into an energy harvesting opportunity. This must be met not simply with numerical modeling for predictive capabilities but also with comparable devices for experiment: energy harvesting devices designed to operate in a mechanically identical fashion to tuned-mass-dampers. These devices would supply substantial mechanical authority in attenuating the host structure's vibrations while converting the "absorbed" energy into electrical power.

The objectives of this dissertation are three-fold:

1. Develop analytical models to study the fully coupled electro-elastic response of an arbitrarily bounded and excited vibrating structure to which a number of electromechanical, distributed vibration control devices are attached.

2. Utilize one such model, eliminating electromechanical effects, to evaluate the

best design methods for continuously distributed passive vibration control devices to achieve broadband structural vibration attenuation and damping. Following analysis, a practical embodiment of this device is to be developed, tested and compared with a conventional damping treatment.

3. Employ the full electro-elastic model to evaluate the coupled dynamics of energy harvesting devices on vibrating structures and how numerous design parameters affect the achievement of structural vibration attenuation and energy harvesting. Carry out experiments to validate the predictions and best design practices stemming from modeling analysis.

The modeling formulation here utilized is referred to as "semi-analytical". Though this approach is not as computationally efficient as closed form solutions, it is significantly faster to compute than finite element (FE) modeling. Researchers and industrial experts who presently rely on FE analysis may notably benefit by employing the proposed analytical models of reduced computational requirements. As energy harvesting considers a broader range of structural vibration sources, it is intended that these fully coupled models may be utilized with assurance of their accuracy and validity.

The use of the model, neglecting electromechanical coupling, is anticipated to lead to a broader understanding of the potential of continuously distributed passive vibration control devices. Since present research in passive and lightweight vibration control treatments has tapered to a minimum, it is hoped to develop a device which is genuinely useful in suppressing the broadband vibrations of transport vehicle components like aircraft panels or ship hulls. Parametric evaluation of the model is expected to shed light on other possible solutions which could be practically constructed. In addition, while the numerical modeling is composed so as to evaluate the vibration attenuation capability of arrays of electromagnetic oscillators, it is not within the scope of this work to consider the passive vibration benefits of simple, discrete mass-spring systems on a vibrating structure as this has been rigorously considered in past

literature [9–12, 56–59].

Using the design of the continuously distributed device as a foundation, an electromechanically coupled version is to be produced, namely by employing piezoelectric elements as the distributed spring layer. This embodiment therefore meets development goals of a device which is suitable for concurrent attenuation of and energy harvesting from surface vibrations. The fully coupled electro-elastic model is utilized to consider how the devices, and similar manifestations, interact with the host structure and to what degree vibration suppression and energy harvesting are simultaneously achievable by changing design parameters.

Taking a perspective of energy harvesting as on equal footing with vibration control shows the clear similarities between the two fields of research. As opposed to anticipating that small energy harvesting devices will exert negligible dynamic influence on the host structure, this dissertation seeks to exploit the mass-spring resonant dynamics of such devices in order to harvest electrical power while solving a vibration control problem with the very same device. Proper design of energy harvesting vibration absorbers may lead to greater achievement of both goals than attempting to solve either problem individually.

1.3 Organization of the dissertation

This dissertation is organized for succinctness. The body of the text—a single chapter—is a consolidation of the results of several submitted, accepted and/or published peer-reviewed journal articles. Each article is thereafter included as an appendix. Within the appendices, additional supporting analysis, model validations and/or experimental results are included than was provided in the respective article.

By thus concentrating the research results, it is intended to provide clarity to the analysis and experiments performed and to the conclusions reached. Following this introductory chapter, the comprehensive research summary chapter is included. Thereafter is provided a chapter of concluding remarks and a presentation of potential

future research that this research brings to light.

Appendix A presents the model formulation, the generalized Hamilton's principle, used throughout most of the dissertation. The studied system is an arbitrarily shaped, bounded and excited structural body containing piezoelectric elements. A Ritz method form of approximate solution is utilized for the mechanical and electrical system responses and the governing equations of motion are provided. Appendix B presents results specific to thin plates partially composed of piezoelectric materials, which is repeatedly used elsewhere in this work. Expressions for quantities of interest are included, *e.g.* the plate flexural vibration response. Appendices A and B are not published articles but are included to provide the reader a depth of background into the present modeling formulation as opposed to merely suggesting textbooks for detailed reference.

Appendix C presents a numerical analysis of passive, continuously distributed vibration control devices when applied to excited structural panels. Certain design parameters affecting the distributed spring and mass layer elastic properties are considered which are unique to continuously distributed treatments. Parametric studies are performed to observe how these features affect passive vibration attenuation performance of the attached devices.

The analysis of Appendix C indicates that continuously distributed spring layers which are stiff in bending and shearing but are transversely compressible would be prime for passive vibration attenuation using both resonant and constraining-type dynamics. Appendix D describes a specific modeling technique to characterize one such spring layer using a corrugated material bounded by thin facing sheets. In conjunction with a distributed mass layer, this spring layer design is anticipated to exhibit a SDOF resonance at low frequencies as well as a capability to constrain higher frequency structural vibration due to exhibiting high bending stiffness. Numerous model validations are carried out using both 3D FE and experimental results for verification.

Appendix E details the development, final design and employment of a passive, continuously distributed vibration control device in a realistic testing environment on a ship hull. The design of the device was derived from the earlier analysis and model validations of Appendices C and D. The objectives of this practical application are to achieve equal or improved vibration suppression of a typical, vibrating ship hull panel as compared with an existing damping treatment while adding less total mass to the structure. The experimental test is thoroughly described and the measurements are presented in detail.

Expanding the research focus to include energy harvesting as well as passive vibration attenuation, Appendix F presents a fundamental model and analysis of point, electromagnetic oscillators attached to an excited simply supported structural panel. Since the harvester devices act on the host structure at a given point attachment, the modeling most closely resembles the manner by which present energy harvester prototypes dynamically influence their respective host structures. Parametric analysis of certain design features show conclusively that the suppression of and energy harvesting from surface vibrations are not contradictory ends and optimum harvester design parameters for both goals are nearly identical.

Returning the focus to the continuously distributed vibration control devices, Appendix G introduces the electromechanical coupling of the general modeling formulation when the spring layer is fully or partially composed of a piezoelectric material. As the spring layer deforms at the device SDOF resonance, the piezoelectric material is strained and external circuit connections are made to the piezoelectric surface electrodes to evaluate the potential for the device to harness electrical power. The model predictions are validated against 3D FE analysis and an initial application example is presented which considers the possibility of continuously distributed piezoelectric devices to simultaneously suppress structural vibrations while converting the absorbed energy into electrical power.

Appendix H employs the general model formulation to determine the combined

energy harvesting and vibration suppression capability of a piezoelectric distributed vibration control device developed using the design of Appendix D as a foundation. The model is validated by experimental measurements on a shaker platform. Thereafter, the numerical model is utilized to assess numerous design features of interest for such continuously distributed devices. A realistic test is described using a vibrating simply supported panel to which the piezoelectric device is attached. The experimental results show the potential for lightweight, continuously distributed energy harvesting devices in simultaneously suppressing the vibration of surfaces while converting the absorbed energy into electrical power.

CHAPTER 2

Comprehensive Research Summary

This chapter presents a concise review of the work in two sections. Focus is first directed to the study of continuously distributed devices for the passive attenuation of surface vibration. Then, consideration is directed towards energy harvesting when coupled structural dynamics between the harvesters and the greater host structure are introduced. Each of the sections is divided into portions tailored to modeling, analysis and experiments. Descriptions of the modeling are kept to a minimum; governing equations are therefore presented directly since complete detail of derivations are provided in the appendices. Validations of the models, both experimental and numerical (finite element comparison), are provided in the experimental portions of the sections for consistency. Analysis provided in the chapter serves to condense a greater volume of work into the principal outcomes of the numerous studies. Experimental results are hoped to provide valuable evidence of the potential of continuously distributed devices for vibration attenuation and the new opportunities posed by unifying vibration control and energy harvesting objectives.

2.1 Continuously distributed, passive vibration control devices

Structural vibrations are oftentimes dominated by the lowest order modes of the system. Attenuation of the vibration is a difficult problem in practice, namely due to the trade-offs between the common treatments: resonant mass-spring systems and constraining-type treatments. The prior are ideal for low frequency vibration control due to their ability to target a specific frequency of vibration, but applying them over large surfaces is impractical. Constraining-type treatments are easy to apply over surfaces, and often cost-efficient to manufacture, but supply insufficient low frequency vibration reduction, a shortcoming remedied only by the significant addition of mass.

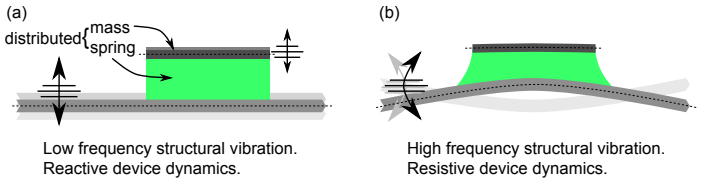

Figure 2.1: (a) Reactive and (b) resistive dynamic illustrations of a device in attenuating structural vibration.

The ease of application to large surfaces make continuously distributed treatments preferable. However, such devices would also need to exhibit a low SDOF natural frequency, such that the distributed mass layer oscillates transversely compressing the distributed spring layer beneath, Figure 2.1 (a). To study the potential of such a device, a model is derived using Hamilton's principle to determine the coupled dynamics of an arbitrarily bounded and excited structural panel and continuously distributed vibration control devices. Various parametric analyses are then carried out to determine designs of distributed devices which promise the greatest potential for the passive vibration suppression. Finally, experiments are performed to validate the analytical predictions and to verify the versatility of one such design.

2.1.1 Modeling

2.1.1.1 Model formulation and performance metrics

Consider an arbitrarily bounded, rectangular panel excited by a number of point forces to which one or more distributed vibration control devices are attached, Figure 2.2. The applied devices may be point mass-spring-dampers or continuously distributed treatments. The base panel and the continuously distributed top mass layers are assumed to be thin plates. The continuously distributed spring layers are assumed to be equivalent, orthotropic thick plates having known or otherwise approximated elastic stiffness characteristics. Continuity of displacement and transverse stress between the spring layer and bounding plates allows the response of the spring layer to be expressed in terms of the top and base plates.

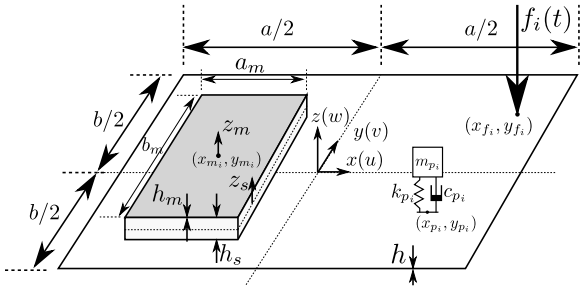

Figure 2.2: Thin plate with attached distributed absorbers and mass-spring-dampers.

Employing the Ritz method [60, 61] to approximate the coupled mechanical displacements of the system when the panel is excited by a point force, yields a system of equations in the form:

$$\begin{bmatrix} \mathbf{M}+\mathbf{M}_s^{base}+\mathbf{M}_p^{base} & \tilde{\mathbf{M}}_s & \tilde{\mathbf{M}}_p \\ \left(\tilde{\mathbf{M}}_s\right)^t & \mathbf{M}_m+\mathbf{M}_s^{top} & \mathbf{0} \\ \left(\tilde{\mathbf{M}}_p\right)^t & \mathbf{0} & \mathbf{M}_p \end{bmatrix} \begin{bmatrix} \ddot{\mathbf{r}}(t) \\ \ddot{\mathbf{d}}(t) \\ \ddot{\mathbf{z}}(t) \end{bmatrix} + \begin{bmatrix} \mathbf{C}+\mathbf{C}_s^{base} & \tilde{\mathbf{C}}_s & \mathbf{0} \\ \left(\tilde{\mathbf{C}}_s\right)^t & \mathbf{C}_m+\mathbf{C}_s^{top} & \mathbf{0} \\ \mathbf{0} & \mathbf{0} & \mathbf{C}_p \end{bmatrix} \begin{bmatrix} \dot{\mathbf{r}}(t) \\ \dot{\mathbf{d}}(t) \\ \dot{\mathbf{z}}(t) \end{bmatrix} + \begin{bmatrix} \mathbf{K}+\mathbf{K}_s^{base} & \tilde{\mathbf{K}}_s & \mathbf{0} \\ \left(\tilde{\mathbf{K}}_s\right)^t & \mathbf{K}_m+\mathbf{K}_s^{top} & \mathbf{0} \\ \mathbf{0} & \mathbf{0} & \mathbf{K}_p \end{bmatrix} \begin{bmatrix} \mathbf{r}(t) \\ \mathbf{d}(t) \\ \mathbf{z}(t) \end{bmatrix} = \begin{bmatrix} \mathbf{Q}(t) \\ \mathbf{0} \\ \mathbf{0} \end{bmatrix} \tag{2.1}$$

Eq. 2.1 contains the direct and coupled mass, $\mathbf{M}$, dampening, $\mathbf{C}$, and stiffness, $\mathbf{K}$, matrices; and the generalized co-ordinates of the base plate, top masses and relative oscillator displacements: $\mathbf{r}$, $\mathbf{d}$ and $\mathbf{z}$, respectively. Matrices with subscripts s, m and p represent components related to the spring layers, distributed mass layers and oscillators, respectively; those without subscripts represent the base plate contributions. Matrices with superscript *base* and *top* indicate the components described in terms of the base and top layers co-ordinates, respectively. Matrices with an over ($\tilde{}$) indicate coupling expressions and $(\ )^t$ indicates the matrix transpose operator. Since the

mass-spring-damper displacements are relative and not absolute, a contribution from the oscillators inertial influence appears directly in the sub-matrix for the mass of the host panel, $\mathbf{M}_p^{base}$, along with corresponding coupling, $\tilde{\mathbf{M}}_p$.

The generalized forces, $\mathbf{Q}$, are computed by the evaluation of the base plate trial functions at the location of the applied force locations, Equation C.9. Dampening in the plate layers is included by means of terms proportional to the mass and stiffness matrices, Equation C.10. Note that matrices $\mathbf{M}_p$, $\mathbf{C}_p$ and $\mathbf{K}_p$ are diagonal with elements containing the mass, damper coefficient and spring constant of each oscillator, respectively. Eq. 2.1 is solved assuming harmonic time dependence of the form $\exp(j\omega t)$ over a range of frequencies, ω.

The out-of-plane mean-square velocity of the panel is useful in evaluating the vibration attenuation capability of applied treatments. If the components of the base panel trial functions and generalized co-ordinates related to out-of-plane displacements, $w(x, y, t)$, are denoted $\Phi^w(x, y)$ and $\mathbf{r}^w(t)$, respectively, then the mean-square velocity is found by

$$\langle \dot{w}(\omega) \rangle^2 = \frac{\omega^2}{2ab} \sum_{m=1}^{M^w} \sum_{n=1}^{M^w} r_m^w(\omega)^* r_n^w(\omega) \int_{-a/2}^{a/2} \int_{-b/2}^{b/2} (\Phi_m^w)^t \, \Phi_n^w \mathrm{d}y\mathrm{d}x \tag{2.2}$$

where there are M^w generalized co-ordinates and trial functions for the out-of-plane panel displacement and $()^*$ indicates the complex conjugate.

The accelerance is the transfer function between the panel acceleration and the input force. In experiments, the spatial average of the panel acceleration is computed as the square root of the ensemble average of the sum of the squares of the individual acceleration measurements. The accelerance is thereafter the ratio of this value to the driving force. In modeling, the accelerance is integrated over the panel surface:

$$\frac{\ddot{w}(\omega)}{\mathbf{Q}(\omega)} = \left[\frac{\omega^4}{2ab\mathbf{Q}(\omega)} \sum_{m=1}^{M^w} \sum_{n=1}^{M^w} r_m^w(\omega)^* r_n^w(\omega) \int \int (\Phi_m^w)^t \, \Phi_n^w \mathrm{d}y\mathrm{d}x \right]^{1/2} \tag{2.3}$$

The mean-square velocity in a frequency bandwidth is computed by the mean of

values over the bandwidth, BW, assuming 1 Hz resolution:

$$\langle \underline{\dot{w}} \rangle^2 = \frac{1}{BW} \sum_{j=1}^{BW} \langle \dot{w}\left(\omega_j\right) \rangle^2 \tag{2.4}$$

Finally, the attenuation of the panel vibration from the untreated levels is expressed as the difference

$$\Delta \langle \underline{\dot{w}} \rangle^2 = \langle \underline{\dot{w}} \rangle^2_{with\ treatments} - \langle \underline{\dot{w}} \rangle^2_{untreated} \tag{2.5}$$

2.1.1.2 Computation of equivalent stiffnesses for corrugated spring layer

The elastic parameters constituting the spring layer stiffness, or compliance, matrix are assumed to be known or otherwise computed using an approximate method. For some distributed spring layers, this is a straightforward task: *e.g.* with a poroelastic foam layer, like melamine, the bending moduli are all roughly equal to the Young's modulus as quoted from manufacturer's specifications. Thereafter, the shear moduli may be approximated by the relation $G = E/2(1+\nu)$ providing all needed components for the spring layer stiffness matrix.

However, for non-continuous spring layers exhibiting highly orthotropic characteristics it is desirable to equate the non-continuous material to be an equivalent continuous material like a thick, orthotropic plate, such that the volumetric integrals in the Hamilton's formulation are more tractable. To perform this equivalency, two techniques are frequently employed: asymptotic homogenization or small deflection plates theories [62–64]. The present work employs the latter method.

A distributed spring layer is considered, constructed of a periodically corrugated cross-section bounded by two facing sheets, Figure 2.3. The layer exhibits high stiffness in bending, twisting and shearing but is transversely compressible. Combined with a distributed mass on top of the spring layer, the full device exhibits a transverse SDOF resonance tunable based on material and geometric characteristics of the corrugated spring and mass selection.

A technique is employed to equate the periodically corrugated spring layer to be the superposition of an incompressible sandwich panel and a layer of vertical springs

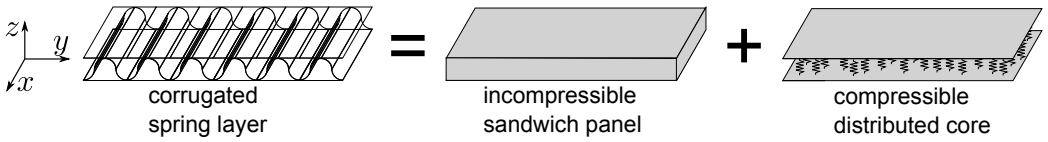

Figure 2.3: Approximation of compressible spring layer as the superposition of an incompressible core with a layer of transversely compressible springs.

such that the layers are coincident [65], Figure 2.3. Since the method employs superposition, linearity of the elastic deformation of the spring layer is assumed and thus only small transverse displacements are considered. To date, this superposition technique has been utilized for sandwich panel constructions of truly continuous materials, *e.g.* foams sandwiched between facing sheets [66, 67]. Thus, the present work aims to take advantage of the concept in modeling the circularly corrugated spring layer of interest which does not yield a continuous volume of material. Using FE analysis, the equivalent sandwich panel elasticity parameters may be computed from a small deflection theory of sandwich plates and the transverse stiffness may be approximated using textbook, one-dimensional elasticity theory, Sections D.2.1 and D.2.2. This yields a stiffness matrix indicating the decoupled in-plane and transverse dynamics:

$$\mathbf{c}_s = \begin{bmatrix} \frac{E_x}{1-\nu_{xy}\nu_{yx}} & \frac{\nu_{yx}E_x}{1-\nu_{xy}\nu_{yx}} & 0 & 0 & 0 & 0 \\ \frac{\nu_{xy}E_y}{1-\nu_{xy}\nu_{yx}} & \frac{E_y}{1-\nu_{xy}\nu_{yx}} & 0 & 0 & 0 & 0 \\ 0 & 0 & E_z & 0 & 0 & 0 \\ 0 & 0 & 0 & G_{yz} & 0 & 0 \\ 0 & 0 & 0 & 0 & G_{xz} & 0 \\ 0 & 0 & 0 & 0 & 0 & G_{xy} \end{bmatrix} \tag{2.6}$$

2.1.1.3 Variable stiffness spring layer formulation

In contrast to point mass-spring systems, continuously distributed vibration control devices may employ a spring layer which changes in properties along the length of the device. This of course may also be the case with the mass layer, but only spring layer variation is here considered; mass layer variation would follow a similar formulation

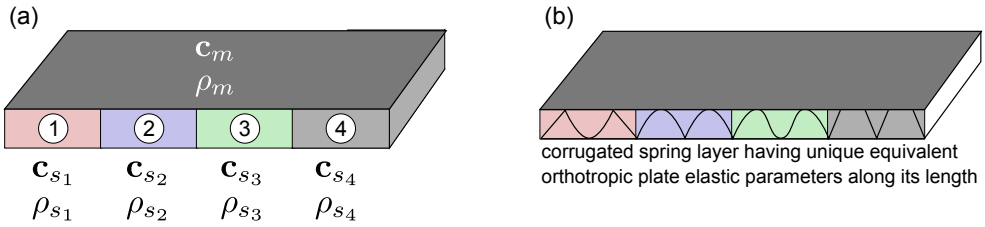

Figure 2.4: (a) Continuous vibration absorber having unique stiffnesses along the length, (b) one embodiment of the concept using a corrugated spring layer.

as hereafter provided.

Within the framework of the Hamilton's principle formulation of the present system, a spring layer exhibiting varying stiffness characteristics and densities along one dimension is approximated to be composed of discrete segments having unique stiffness matrices and densities, Figure 2.4. Thus, the sum of the kinetic and potential energies constituting the full distributed spring layer in the model formulation are given by

$$T_{spring} = \frac{1}{2}\sum_{i=1}^{N_s}\rho_i \int_{V_{s_i}} \left(\dot{\mathbf{u}}_{s_i}\right)^t \dot{\mathbf{u}}_{s_i} \mathrm{d}V_{s_i} \tag{2.7}$$

$$U_{spring} = \frac{1}{2}\sum_{i=1}^{N_s} \int_{V_{s_i}} \left(\epsilon_{s_i}\right)^t \mathbf{c}_{s_i}\epsilon_{s_i} \mathrm{d}V_{s_i} \tag{2.8}$$

where N_s are the number of segments along the layer. The remaining variables in Eqs. 2.7 and 2.8 are detailed in Appendix A. Note that in the event $N_s \to \infty$, one realizes a truly continuously varying spring layer. However, implementation is practically limited to computational capability, since the volumetric integrals must be numerically computed for each segment, and to the specific comparison being made, *i.e.* a test sample having just 3 unique segments along the length.

2.1.2 Analysis

2.1.2.1 Continuity of devices

The low frequency vibration attenuation benefit of constraining layer damping (CLD) materials is known to be improved by segmenting the treatment into smaller samples

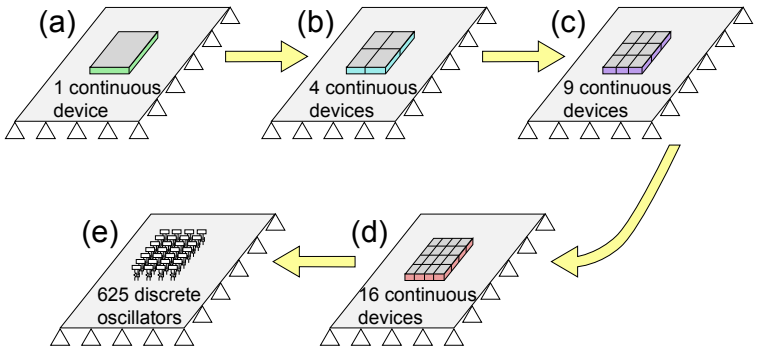

Figure 2.5: Segmentation of continuous device on the SS panel, from (a) one single piece to (b,c,d) several continuous pieces to (e) a distribution of point oscillators. Not to scale.

when applied to large surfaces [68–70]. Since no similar study has been performed in regards to continuously distributed devices which exhibit a transverse SDOF resonance, it is desirable to determine the influence of segmentation for such distributed treatments in achieving tuned and broadband vibration attenuation.

Consider a simply-supported (SS) panel excited by a harmonic point force. A distributed vibration control device is designed to exhibit a SDOF natural frequency of 260.9 Hz, very close to the panel (3,1) resonance of 261.1 Hz. The device is considered to have an isotropic spring layer which, for the present geometric and mechanical parameters used in the study, may be satisfied by using a spring layer composed of poroelastic foam.

When positioned at the center of the panel, the device increases the total system mass by 2.43%, *i.e.* the device represents a mass ratio of $\mu = 0.0243$. The structural panel is excited by a point force and the panel mean-square velocity is computed without any treatment present and when the centrally-positioned device is segmented into 1, 4, 9, 16 pieces constituting the original size, Figure 2.5. Finally, over the same area covered by the treatment is considered a 25×25 grid of mass-spring-dampers having the same total mass as the continuously distributed device and also each tuned to 260.9 Hz; the panel vibration levels are computed when the oscillator array is attached.

Table 2.1: Cumulative mean-square velocity reduction (dB), segmentation dependence

# of devices	tuned frequency range	broadband
1	-3.19	-1.36
4	-4.27	-3.40
9	-2.15	-2.89
16	-1.73	-2.21
625	-1.42	-1.88

Table 2.1 presents the reduction in panel mean-square velocity over the tuning frequency bandwidth, 200-400 Hz, and for a broadband range of frequencies, 10-600 Hz. Like conventional constraining treatments, it is found that continuously distributed devices exhibiting a SDOF natural frequency provide greater vibration attenuation when segmented over the applied surface. Not only is broadband attenuation increased but the attenuation around the tuned frequency range is improved when the distributed devices are segmented. Table 2.1 shows that maximum benefit occurs when the area coverage is broken into 4 equal pieces, but that further segmentation becomes a disadvantage. This is most pronounced in considering the array of oscillators which yield some of the smallest levels of vibration attenuation.

Depending on the selection of materials and frequency range of interest, there are optimum segmentation parameters for conventional CLD [5]. Likewise, it is observed that segmentation of distributed vibration control treatments which exhibit resonant dynamics is also a benefit for both broadband and tuned vibration suppression.

2.1.2.2 Constraining effects

The distributed spring layer in the prior section was isotropic and, given the low transverse stiffness needed to yield a SDOF resonance in a low frequency range, would be mostly decoupled from the extensional vibrations of the host structure. However, high in-plane stiffness in the spring layer would improve broadband vibration attenuation by resisting the flexural vibration of the structure. Continuous spring layers which are stiff in bending and shearing but transversely compressible could offer the best of both worlds: a resonant dynamic at a low tuned frequency as well as resis-

tance to higher frequency structural vibration, Fig. 1.1. This could be met in practice by employing a spring layer constructed like a corrugated sandwich panel using thin materials; in bending and shearing, sandwich panels are notably strong but the thin core material would provide for transverse flexure and therefore a low SDOF natural frequency, Fig. 2.3.

Two dimensionless parameters are defined to evaluate the design possibilities for such continuously distributed devices:

$$\text{Orthotropy ratio}: \quad \Lambda = \frac{E_t}{E_z}; \qquad \text{Modulus ratio}: \quad \Gamma = \frac{E_m}{E} \tag{2.9}$$

where the spring layer is considered to be transversely isotropic such that $E_x = E_y = E_t$; the transverse stiffness, related to the SDOF natural frequency, is E_z; the Young's modulus of the top mass is E_m; and the Young's modulus of the base plate is E. The remaining stiffness matrix components for the spring layer are calculated in the manner given in Section C.4.

High ratios of orthotropy, $\Lambda \gg 1$, represent elastic characteristics of the corrugated sandwich panel construction described above. Smaller values, $\Lambda < 1$, may be physically realizable by using a honeycomb core with the axis of extrusion in the transverse direction, which is intuitively a poor design to yield a SDOF natural frequency in a low frequency range. The modulus ratio, Γ, is known to be a useful design parameter to modify for constraining treatments to improve vibration attenuation, selection of which is dependent, like segmenting samples, on material properties and the frequency range of interest [5].

As in the previous section, a vibrating SS panel is considered to which a continuously distributed vibration control device is attached, centered on the panel, as in the manner of Fig. 2.5 (a). The device exhibits a SDOF natural frequency of 172 Hz, close to the (3,1) mode of the host panel, 175 Hz, and constituted a mass ratio $\mu = 0.0388$. The spring layer is very lightly damped, $\eta = 0.005$, and therefore dissipates little energy. The overall reduction in the panel mean-square velocity from untreated levels, Eq. 2.5, is computed over a range of Γ and Λ from 10–600 Hz. Changes in Λ reflect,

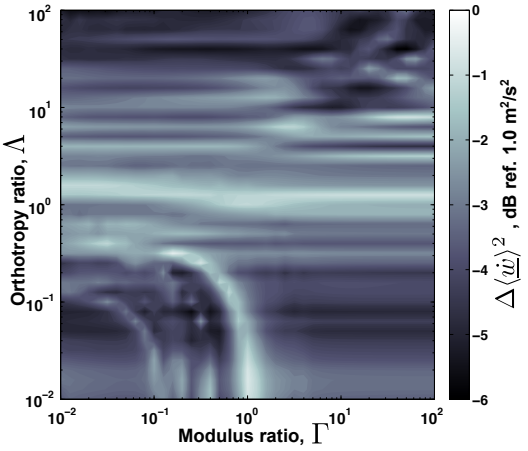

Figure 2.6: Reduction in cumulative panel mean-square velocity from applied absorber, orthotropic and modulus ratios dependence

for example, different corrugated spring layer cross-sections or material thicknesses, while maintaining the same transverse SDOF natural frequency; changes in Γ simply reflect stiffer or softer top mass layers.

Figure 2.6 plots the results of the simulation. No clear region of converged optimum values for Λ or Γ is observed. However, it is noted that change in Γ is less influential than modification of Λ. Modification of the orthotropy ratio shows that very stiff spring layers, $\Lambda \gg 1$, improve the vibration attenuation capability of the device. This may be explained due to the fact that greater Λ indicate the spring layer will resist the structural vibration while the device still exhibits its reactive effect at the tuned natural frequency.

To consider the effects of modifying Γ and Λ, Figure 2.7 plots the panel mean-square velocity for the untreated case, when the added device has $\Lambda = \Gamma = 1$ and when $\Lambda = 39.8$ and $\Gamma = 50.1$. Cumulative vibration levels are shown as dashed lines. The reactive effects of the device around the tuned natural frequency of 175 Hz are evident for the device of $\Lambda = \Gamma = 1$ showing the panel (3,1) resonance to be nearly completely suppressed.

When the orthotropy and modulus ratios are modified, $\Lambda = 39.8$ and $\Gamma = 50.1$,

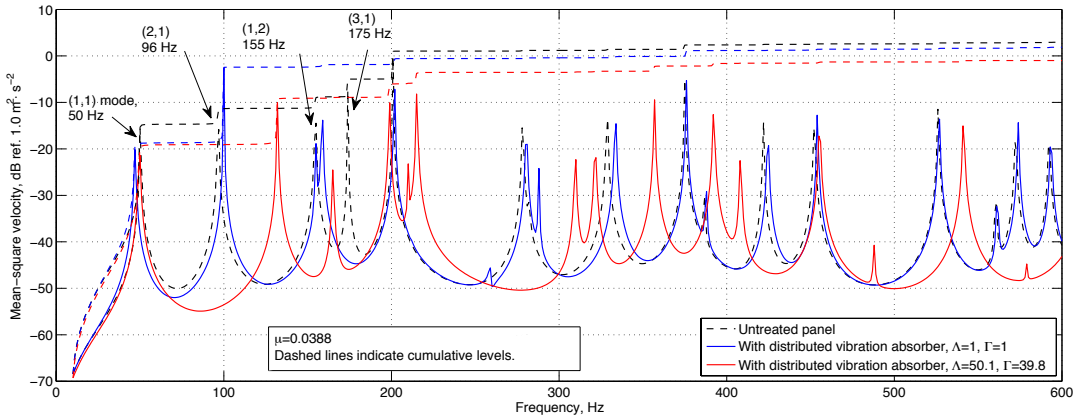

Figure 2.7: Panel mean-square velocity, (black) untreated, (blue) with absorber $\Lambda = \Gamma = 1$, (red) with absorber $\Lambda = 39.8$, $\Gamma = 50.1$

the device substantially stiffens the panel locally due to its extensional displacement coupling. By being centrally located on the panel, the spring layer resists all of the asymmetric panel modes, increasing the frequency of these modes, *i.e.* the (2,1) mode shifts from 96.6 Hz to 132 Hz. Such stiffening of the modes is one explanation for the lack of convergent maxima or minima in Figure 2.6. Changes in Λ are found to shift some resonances outside of the bandwidth of computation, >600 Hz. This explains the lack of convergence in Fig. 2.6 since some of the vibrational energy is increased beyond the spectrum of calculation.

However, what is clear from Figure 2.7 is that spring layers exhibiting greater ratios of orthotropy are capable of substantial localized stiffening of the structure. While the results of this section have only considered lightly damped spring layers, the results suggest that the prominent structural influence of the highly orthotropic spring layer could be a prime match for the inclusion of a damping mechanism for energy dissipation.

2.1.2.3 Spring layers of high in-plane stiffness and damping

In light of this discovery that spring layers of high bending and shear stiffness exert a substantial dynamic influence on the host structure, consideration of damping effects

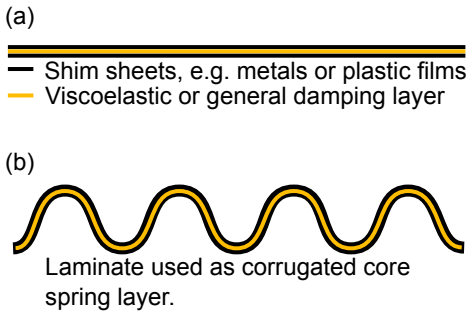

Figure 2.8: Laminated core design to increase net dissipative effects. (a) Component lay-up. (b) Corrugation of net laminate material to yield a distributed spring layer.

should be made as the ratio of orthotropy, Λ, is modified. In practice, this could be achieved by a laminate design for a sandwich panel construction, a core cross-section of which is shown in Figure 2.8. Such a laminated and corrugated spring layer construction maintains high bending and shearing stiffnesses, would yield transverse compressibility for a low SDOF natural frequency and would also be highly damped.

The simulation was repeated now modifying the ratio of orthotropy, Λ, and the spring layer loss factor, η. Figure 2.9 plots the results of simulation, showing a clear benefit in vibration attenuation as damping of the spring layer is increased in tandem with the in-plane stiffnesses of the spring layer. Thus, novel design of the spring layer construction is needed to yield practical embodiments of the present theoretical results.

Summarizing the previous two sections of results, spring layers exhibiting nearly uniform in-plane stiffnesses as the transverse stiffness, $\Lambda = 1$, could be realized using a foam material. With a distributed mass layer, such a vibration control device is practically only useful at the tuned natural frequency (see Fig. 2.7 blue plot). However, by employing a spring layer of high bending and shearing stiffness relative to the transverse stiffness, $\Lambda \gg 1$, and by adding a damping mechanism into the layer, the resulting vibration control device is much more useful in suppressing broadband vibrations. Continuing with the circularly corrugated spring layer of this work which is stiff in bending and shear but relatively soft in compression, the added damping

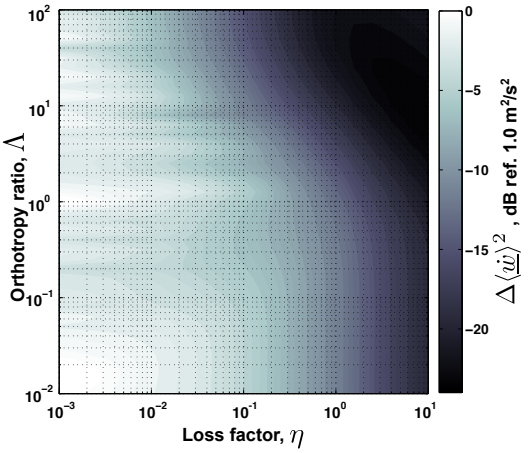

Figure 2.9: Reduction in cumulative panel mean-square velocity from applied absorber, orthotropic ratio and loss factor dependency.

mechanism could be a laminated damping film as in Figure 2.8.

2.1.2.4 Device modal dynamics

In contrast to point mass-spring systems, continuously distributed vibration control devices provide for the possibility that the top mass layer may oscillate not just in translation but also modally. Arpaci and Savci [71] observed that beam vibration absorbers were more useful when designed such that the beam oscillated in the half-wavelength modal dynamic (the mode shape being equivalent in form to the first mode of a simply-supported beam). Thus, extending this possibility to the present distributed device, it is important to consider the possibility of "tuning" the distributed device such that the mass oscillates in the freely suspended plate pumping mode, compared with the translational dynamic in Figure 2.10 when the device is attached to an excited SS host panel.

The model was utilized to compare the translational and modal dynamics of the top mass layer. A device was considered to be centrally located on a SS panel. The device represented a mass ratio of $\mu = 0.0539$ and exhibited a SDOF resonance of 229 Hz, equal to the (1,1) mode of the structural panel. Evaluation of the reduction in panel mean-square velocity was computed for this case. Next, the top mass of the

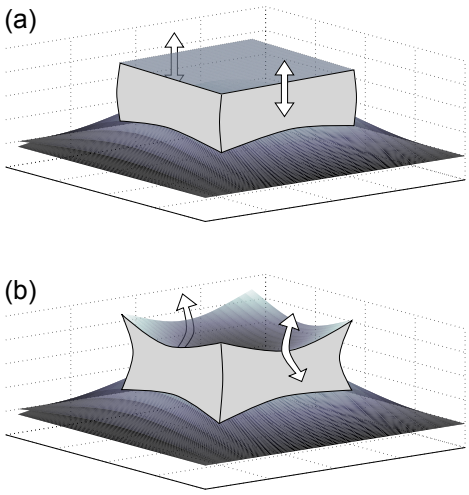

Figure 2.10: (a) Translational (SDOF) dynamic of absorber; (b) Modal dynamic of absorber on a SS panel vibrating in (1,1) mode.

Table 2.2: Cumulative mean-square velocity reduction (dB), dynamics dependence

Mass layer dynamic	tuned frequency range	broadband
Translational	-5.72	-1.35
Modal	-7.20	-1.69

applied device was considered to have a reduced Young's modulus such that at 229 Hz the top mass would exhibit the freely suspended modal dynamic, Fig. 2.10 (b), while still covering the same panel surface area and retaining the same mass ratio. The reduction in panel mean-square velocity was again computed.

Table 2.2 presents the reduction in panel mean-square velocity for two bandwidths, that around the (1,1) host panel resonance and the broadband computation. The absorber designed for modal response of the top mass outperforms the translationally absorber design both around the targeted panel resonance and broadband. This exactly corroborates with the findings in [71] for beam absorbers, although in this case the distributed spring layer is completely coupled to the host structural motion rather than by discrete springs as in the prior study.

Note that designing a continuously distributed device in this fashion requires modification of both the spring layer characteristics and the top mass mechanical and/or

geometric parameters. In other words, first the device must be designed such that it would exhibit a SDOF translational resonance at the target frequency, Fig. 2.10 (a). Next, the properties of the mass layer would need to be modified such that the mass would exhibit the pumping mode shape at the same frequency to which the device was translationally tuned. In practice, since the mass layer moduli are not easily manipulated, the thickness and span of the mass layer would need to be simultaneously considered to yield a sample which exhibited a SDOF translational resonance as well as the mass layer modal dynamic.

2.1.2.5 Variable stiffness spring

Arrays of mass-spring-dampers may include individual oscillators each tuned to a unique natural frequency, but in attenuating the vibrations of large surfaces this approach is costly to design, manufacture and employ. Instead, a variably stiffened and continuously distributed device is preferred, such that it exhibits a range of SDOF natural frequencies and far fewer devices need be applied over the vibrating surface.

A variable stiffness ratio is defined: $\Xi = (\max[(E_z)_i] - \min[(E_z)_i])/\text{mean}[(E_z)_i]$, where $(E_z)_i$ is the transverse stiffness of the i^{th} section of the spring layer, extracted from the stiffness matrix of that region of the spring layer (see Fig. 2.4). The stiffness ratio is defined along one length of the device, such that the transverse stiffness of each spring layer component either increase or decrease along that length. Thus, large Ξ indicate a substantial variation in transverse stiffness between the left side of the device and the right side of the device; $\Xi = 0$ indicates a uniform transverse stiffness along the length of the device.

The model was therefore employed to simulate the effects of a centrally-positioned device having 5 distinct regions of transverse stiffness, with a mean tuning frequency of 175 Hz, which corresponded to the structural panel (3,1) mode. Further details of the model implementation are given in Section C.7. Simulations were then carried out to compute the cumulative reduction in panel mean-square velocity over a broad range of frequencies as compared to untreated panel vibration excited by a point

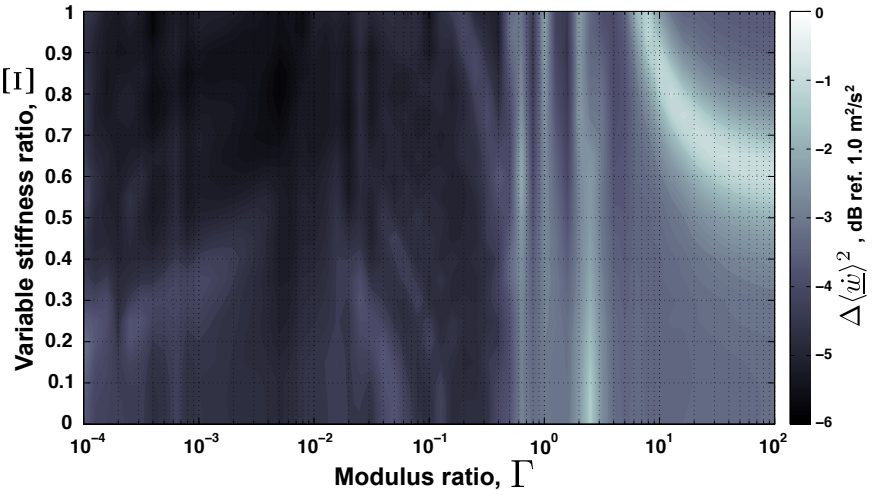

Figure 2.11: Reduction in cumulative panel mean-square velocity from applied absorber, variable stiffness and modulus ratios dependence.

force.

Figure 2.11 plots the result of modifying Ξ and the modulus ratio Γ for the applied device in terms of the broadband reduction in panel mean-square velocity. A region of optimum Ξ and Γ is apparent around $\Xi \approx 1$ and $\Gamma \approx 0.01$. Designing the device in this fashion is predicted to yield approximately a 6 dB reduction in the broadband panel vibration as compared with $\Xi = 0$ and $\Gamma = 1$, *i.e.* the "normal" device and spring layer design.

An explanation for this improved vibration suppression may be presented for the combination of increased Ξ and reduced Γ. Should the stiffness ratio increase but the top mass modulus remain the same, the top mass of the device is likely to rock from side-to-side since the ends of the spring layer exhibit significantly different transverse stiffnesses. This would likely yield a device which primarily exhibits only the highest tuning frequency and lowest tuning frequency represented by the end segment transverse stiffnesses. However, as Ξ is increased and Γ is decreased, the "softer" top mass material reduces the amount of side-to-side rocking the mass would exhibit and therefore allows the whole device to exhibit a full continuum of natural frequencies from the lowest to highest.

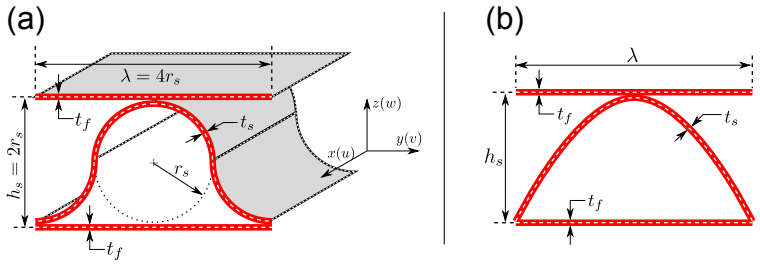

Figure 2.12: Corrugated spring layer period having (a) circular and (b) half sine cross-section.

2.1.3 Experiments

2.1.3.1 Model validation: superposition approach for corrugated spring layers

Two distributed spring layers using a periodically corrugated cross-section are considered: circular and half sine corrugations. These two forms are studied namely to determine the extensibility of the superposition approach to calculating equivalent elasticity parameters for sandwich panels having a continuous core material (the circular cross-section) and a non-continuous material (the half sine). The two cross-sections and related geometric parameters are depicted in Figure 2.12. When combined with a distributed mass layer, these devices may then exhibit both reactive and resistive dynamics.

For a constant mass layer selection, an eigenfrequency analysis is carried out using the model of Section 2.1.1 compared against results computed using a 3D FE software package solution. The base of the vibration control device is fixed such that the computed eigenvectors represent the natural vibration modes of the full device. The wavelength, or period, of the cross-section is maintained at $\lambda = 12.7$ mm but the thickness of the core material is varied. Each run of the proposed model with the superposition method requires computation of the necessary equivalent elasticity parameters, given in Table D.2.

Table 2.3 compares the 3D FE model results against the solutions predicted using the equivalent 2D analysis. The first four modes of the continuously distributed

Table 2.3: Natural frequencies [Hz] as computed by 3D FE analysis and 2D model (percent difference)

Core shape (t_s μm)	Model	Mode 1	Mode 2	Mode 3	Mode 4
Circular (50.8)	3D FE	362.8	536.8	538.5	540.4
	2D	360.0 (-0.7%)	529.6 (-1.3%)	530.3 (-1.5%)	536.3 (-0.7%)
Circular (76.2)	3D FE	652.7	957.7	960.4	964.1
	2D	644.7 (-1.2%)	937.9 (-2.1%)	939.7 (-2.1%)	957.5 (-0.6%)
Half sine (50.8)	3D FE	611.7	683.2	686.3	688.3
	2D	608.1 (-0.5%)	643.8 (-5.7%)	648.3 (-5.5%)	649.2 (-5.6%)
Half sine (76.2)	3D FE	1103	1243	1249	1253
	2D	1087 (-1.4%)	1115 (-10.2%)	1125 (-9.9%)	1127 (-10.0%)

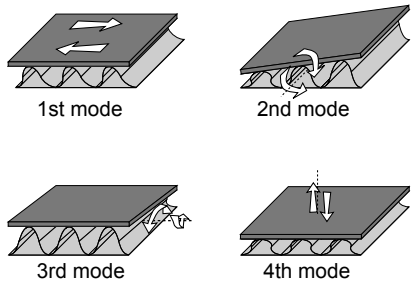

Figure 2.13: First four mode shapes of device having a fixed based.

device are accurately predicted by the 2D analysis. An illustration of these modes is provided in Figure 2.13. The non-continuous half sine corrugation is found to be more susceptible to error than the circular cross-section when employing the equivalent stiffnesses of the 2D model. This is likely due to the generation of stress concentrations at each of the discontinuities along the periodic cross-section which the 3D FE model can predict while the 2D model neglects this geometric resolution. For the circular corrugated spring layer of greatest interest in this work, however, the superposition method provides an accurate approximation of the elasticity characteristics of the layer.

Experimental samples were produced, with the spring layer made from thin sheet steel material and a specially crafted spot welding tool. A photograph is shown in Figure 2.14 of a sample circularly corrugated spring layer using these materials and manufacturing techniques, with the core material thickness of $t_s = 25$ μm and period of $\lambda = 12.7$ mm.

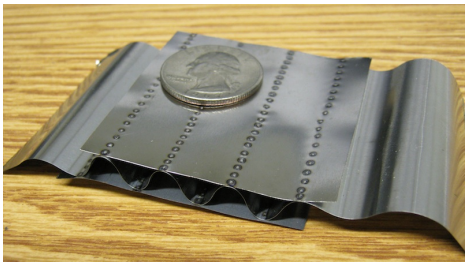

Figure 2.14: Welded steel corrugated core sample having consistent circular core shape and minimal, adverse welding effects.

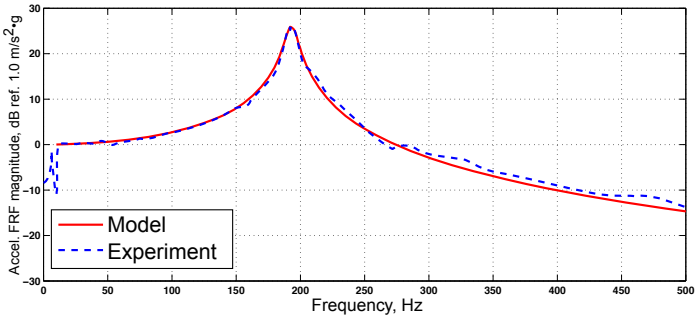

Figure 2.15: Comparison of modeled and measured FRF for device employing a standard circularly corrugated spring layer design.

A full sample was produced using $t_s = 50$ μm and $\lambda = 25.4$ mm with a mass layer composed of perforated steel. This sample was then attached to a shaker table for testing. The acceleration frequency response function (FRF) was measured as the ratio between the shaker table acceleration and that as measured at the center of the top mass of the device. Figure 2.15 compares the experimental results against the model predictions finding a very close agreement for both the location of resonance and the magnitude of the response. Since the SDOF resonant dynamic is that which lends the distributed device its reactive effect when working against the host structure, it is necessary that the model accurately predict this response.

2.1.3.2 Model validation: device on an excited panel

With the transverse dynamics replicated accurately by the model, a more comprehensive assessment of the superposition approach should be carried out to consider

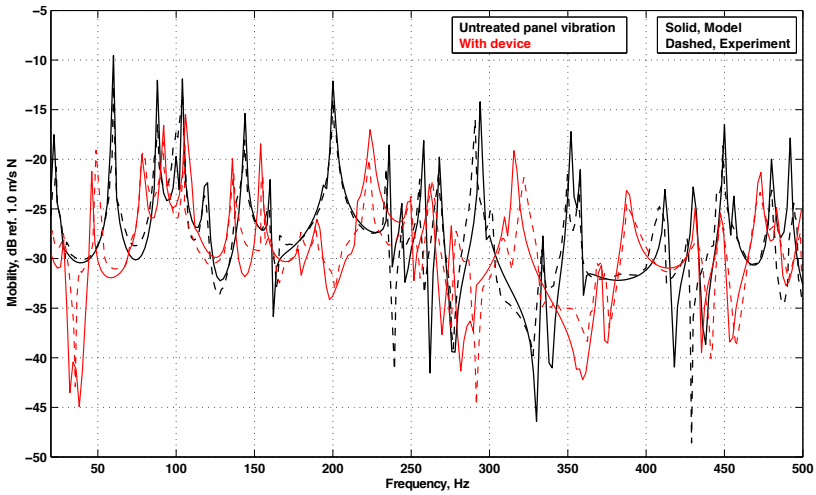

Figure 2.16: Mobility of vibrating panel when untreated (black curves) and with the distributed device (red curves). Solid lines are model predictions, dashed plots are experimental results.

the full range of dynamic coupling the distributed device would induce on a host vibrating structure. A steel panel was freely suspended in the laboratory and attached to a shaker through a force transducer at one corner, Figure D.13. A laser vibrometer measured the untreated panel mobility transfer function (TF) at (0,102) mm from the plate center, following which a continuously distributed device was attached as shown in Figure D.13. Approximate elasticity parameters of the circularly corrugated spring layer of the device and mass layer characteristics are provided in Tables D.4 and D.5. The device represented a mass ratio of $\mu = 0.0912$ and was predicted to have a transverse natural frequency of 193 Hz. The device was positioned at an anti-node of the (2,3) mode of the suspended panel which was predicted to occur at approximately 200 Hz. Thus, the device was best located so as to suppress the panel vibration for the frequency to which it was tuned.

Figure 2.16 compares the untreated panel mobility (black plots) with that as measured and predicted once the distributed device was attached (red plots). The solid curves represent numerical predictions while the dashed lines are the measurements. The model fairly accurately predicts the panel vibration when untreated, as is to be

expected. The (2,3) mode is observed at 200 Hz, which was the targeted mode the added device was anticipated to significantly suppress.

With the device attached to the panel, the (2,3) mode is greatly attenuated. But the constraining effects observed in earlier analysis are found to affect the panel vibration over the whole frequency range. Most notably are the increases in panel resonances above 200 Hz after application of the device: *e.g.* the resonance at 293 Hz is stiffened up to 320 Hz and slightly attenuated. Prior work has shown that continuously distributed vibration control devices using spring layers like poroelastic foam primarily affect structural vibration around the tuned natural frequency of the device since such a spring layer is much less resistant to bending and shear [72]. However, the present corrugated spring layer is highly resistive to both bending and shear and, as a result, influences panel vibration to a greater degree. The model is found to fairly accurately represent the effects of the added device, generally maintaining a close prediction of both the location and magnitude of the shifted panel resonances. This serves as a validation of the superposition approach to simplify the intricate corrugated spring layer composition into an analytical equivalent for easier implementation in 2D continuum models.

2.1.3.3 Application: devices for large surface vibration attenuation

The traditional solution that some industries elect to suppress low frequency vibration of surfaces is to apply heavy mass damping layers. Therefore, it was desired to design an appropriate continuously distributed vibration control device that would yield similar or improved broadband vibration attenuation for a reduced cost in added weight to the structure. The design recommendations stemming from the analysis of Section 2.1.2 were employed. Namely, it was determined to construct the spring layer from a circularly corrugated laminate material (Fig. 2.8), varying the wavelength of the corrugations from one end of the device to another, depicted in Figure E.6. Thus, the device was anticipated to be: stiff in bending and shear but transversely compressible; highly damped such that it may dissipate substantial in SDOF oscillation

as well as when strained extensionally; and had a varying transverse stiffness to yield a bandwidth of SDOF natural frequencies.

The vibrating structure was a realistic ship hull surface exhibiting the greatest vibrational amplitudes below 600 Hz, primarily due to the four lowest resonances of 100, 138, 144 and 189 Hz. It was desired to design just one distributed vibration control device, similar to the mass damping layer then employed, and to apply the devices in a predetermined layout, Fig. E.5. Thus, the variable stiffness approach would be most useful in constructing a single device which may attenuate the full range of vibrational frequencies. It was predicted the final devices should exhibit a range of SDOF natural frequencies from 90 to 220 Hz.

Following design and laboratory evaluation, the devices were manufactured by the author using the spot welding apparatus with great care to minimize over-heating of the spring material which could induce warping of the steel spring laminates and damage the damping material within the layup. The ship hull was excited by a centrally-positioned shaker and force transducer attachment and an accelerometer array measured the accelerance over the surface of the panel. Afterwards, the constructed devices were applied and the hull vibration was measured. Lastly, the devices were removed and a traditional, heavy mass damping layer was attached over the same surface as the devices. The distributed devices represented a mass ratio of $\mu = 0.16$ while the damping material represented a mass ratio of $\mu = 0.20$.

Figure 2.17 plots the accelerance for the three cases while Figure 2.18 plots the attenuation of the panel accelerance in one-third octave bands. The distributed devices are found to be less effective at the low end of the tuning frequency range, 90–220 Hz, but substantially more beneficial in attenuating the panel vibration at the higher end of this bandwidth. Despite great care in manufacturing the spring layers for the devices, it was known from extensive experience that the present welding method oftentimes over-stiffened the laminated spring layer. This may explain the reduced attenuation capability of the devices at the 100 Hz panel resonance but the

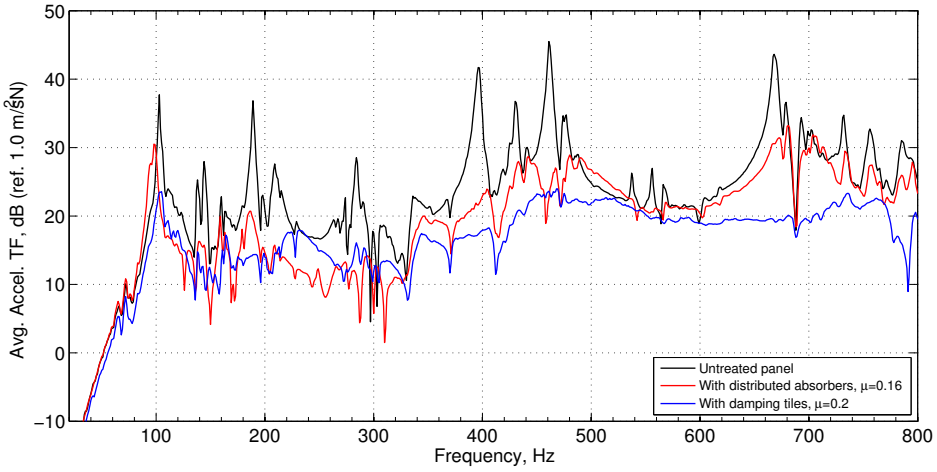

Figure 2.17: Comparison of panel vibration (black) untreated; (red) with distributed absorbers; and (blue) with damping tiles.

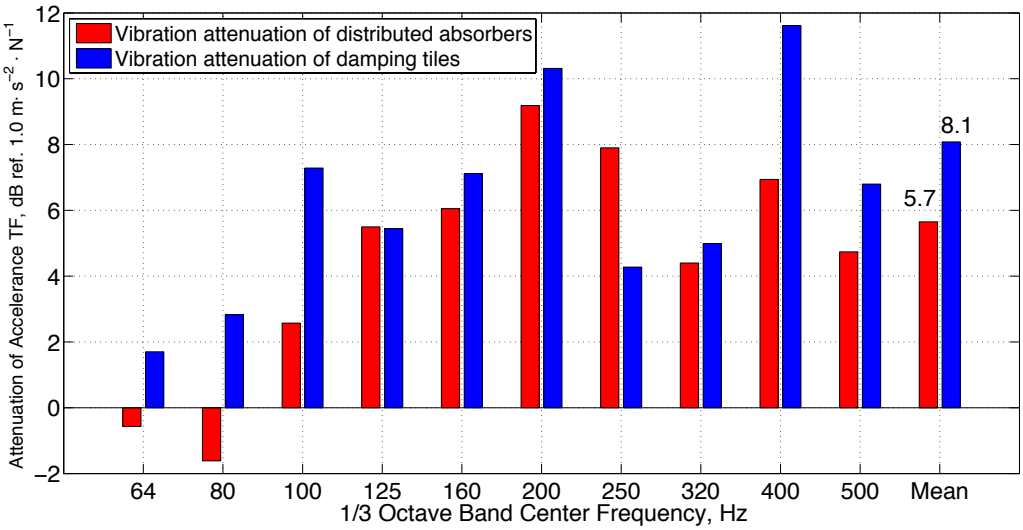

Figure 2.18: One-third octave band attenuation of panel vibration.

more prominent attenuation observed for the higher bandwidth of the tuning range. Indeed, as Figure 2.18 shows, there is a 1 dB or less difference in performance between the distributed absorbers and the damping tiles from 125–320 Hz, with the exception of the 250 Hz one-third octave band where the absorbers are seen to provide 3.7 dB more attenuation.

The distributed devices are found to provide significant attenuation from approximately 250–500 Hz, despite having negligible reactive effects in this bandwidth. This suggests the highly damped spring layer is capable of dissipating energy as it is extensionally deformed off-resonance. This corroborates with the modeling predictions of Section 2.1.2.3 that indicated orthotropic and highly damped spring layers provide significantly greater broadband vibration attenuation capability than orthotropic but undamped springs which would stiffen the structure locally but not dissipate considerable energy.

The damping tiles, weighing 20% more than the absorbers, are seen to provide improved attenuation below and above the absorbers tuning frequency range. This is markedly clear in Figure 2.17 above 600 Hz, in an excitation range much suited to the damping mechanism of the tiles. However, a plot of the panel vibration autospectrum in Figure E.13 (as opposed to the accelerance) shows that the panel is much less easily excited above 500 Hz; thus, as the project sponsor of the test confirmed, the important bandwidth of vibration to consider was <500 Hz. The difference of the mean levels of vibration attenuation in one-third octave bands in this range is just 1.7 dB, in favor of the damping tiles of 20% greater mass.

2.1.4 Concluding remarks

In summary, the original goal in the development of the continuously distributed vibration control devices was to supply targeted low frequency attenuation capability due to reactive effects while also resisting higher frequency structural vibration and dissipating such energy through damping mechanisms akin to CLD. In tandem with

this goal was the desire to yield a product of reduced weight to conventional mass damping layers. Modeling and analysis of the devices showed that well-damped spring layers exhibiting high in-plane and shearing stiffnesses with low transverse stiffness would improve broadband vibration attenuation performance of the distributed devices. By varying the spring layer transverse stiffness along the length of the device, the reactive effects were predicted to be useful over a range of frequencies, as compared with a single frequency like a point mass-spring-damper. Analysis also predicted that, like CLD, the distributed devices would perform better both at their tuning frequency and broadband when they were broken into a finite number of devices, as opposed to being one very large distributed device. These features were incorporated into the final design of the distributed devices which were tested on the realistic ship hull.

As is evident in Figure 2.18, the tuned frequency benefit of the distributed devices is more apparent at the higher end of the tuning range but can be more prominent than the attenuation of the heavier damping tiles, *e.g.* at the 250 Hz one-third octave band. However, over the range of excitation <500 Hz which mattered most in this application, there was <2 dB difference in the mean attenuation capability between the treatments. Depending on the bandwidth of excitation frequencies of interest, the advantage of the distributed devices in providing a lightweight alternative to the damping tiles could become more apparent.

Thus, as the bandwidth of troublesome frequencies becomes narrower, it is anticipated that the distributed devices would be of greater benefit per added mass given their reactive effects like classical vibration absorbers. In the event of true broadband vibration attenuation, it appears that damping layers still yield the best performance, though at the cost of increased mass. The developed distributed devices thus span this divide between interest in attenuating a single frequency and the need to attenuate all frequencies by supplying reactive effects over a certain tuned bandwidth of low frequencies and dissipative capabilities at higher frequencies.

2.2 Energy harvesting from structural vibrations

Conversion of ambient vibrational energy from structures into electrical power has been the focus of research for over a decade with the greatest thrust occurring in the last few years [38, 73–76]. Though the piezoelectric stiffening, shunt damping and/or electromagnetic damping effects induced upon harvester devices are well known, only one study specifically exploited the effect this had on the host structure [52]. An aircraft wing, partially composed of a flow-induced vibrational energy harvester, was found to reduce wing flutter while simultaneously generating electrical power. In contrast to the prior example, most studies in energy harvesting focus solely on the harvester design itself which generally encourages highest power output as opposed to a simultaneous aim for vibration control. Therefore, the modeling of many harvesting studies neglect the dynamic coupling between harvester and structure, justifying the existing assumption that the devices are excited by base vibration.

Though this assumption may be valid for certain applications, it is of limited scope particularly given that many harvesting devices are designed to resonate in an identical fashion as do classical tuned-mass-dampers. Tuned-mass-dampers exert substantial dynamic influence to work against a host structure's vibrations and frequently dissipate significant mechanical energy per cycle but this feature has yet to be exploited in an energy harvesting context. Therefore, this section considers the results of retaining complete structural dynamic coupling in conventional power harvesting analyses and evaluates the potential of distributed devices to concurrently attenuate and harvest energy from the structural vibrations. With this perspective, energy harvesting devices are analogous to electromechanical vibration absorbers. The modeling is briefly presented, which is a simple extension of the modeling of Section 2.1 to include select electromechanical effects. Analyses are provided for a variety of scenarios which represent reasonable energy harvesting applications and shed light on the potential of uniting the two research objectives. Finally, numerical and experimental validations are provided along with further testing results.

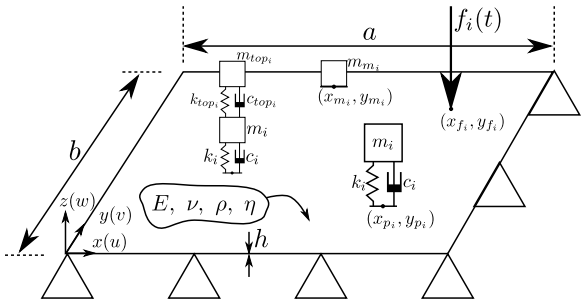

Figure 2.19: Simply-supported panel with attached electromagnetic oscillators or point masses.

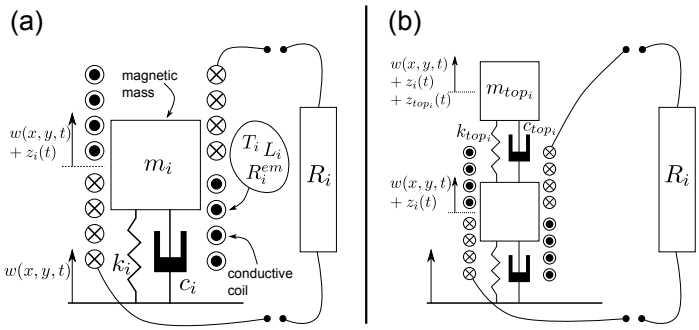

Figure 2.20: Schematics of (a) SDOF E–M oscillators and (b) 2DOF oscillators, here showing electromagnetic coupling for the bottom oscillator sub-system.

2.2.1 Modeling

2.2.1.1 Model formulation: electromagnetic oscillators

Consider an excited, simply-supported, rectangular panel to which a number of SDOF or 2DOF oscillators and/or point masses are attached, Figure 2.19. The oscillators are composed of magnetic masses resting on spring-dampers, and the masses are displaced through the axis of a wound coil, Figure 2.20. The coil ends are connected to an external energy harvesting circuit modeled as a load resistance, R_i.

Employing Lagrange's equations yields the governing equations of motion of the

coupled electromechanical system:

$$\begin{aligned}
&\left[-\omega^2\left(M_{mn}+H_{mn}+G_{mn}+P_{mn}\right)+j\omega C_{mn}+K_{mn}\right]a_m(\omega)\\
&-\omega^2\left[\sum_{i=1}^{N_p} m_i\Psi_m(x_{p_i},y_{p_i})z_i(\omega)+\sum_{i=1}^{N_p} m_{top_i}\Psi_m(x_{p_i},y_{p_i})z_{top_i}(\omega)\right]=F_m(\omega)\\
&\qquad\qquad m=1,2,\ldots,N;\ n=1,2,\ldots,N
\end{aligned}\tag{2.10}$$

$$\begin{aligned}
&-\omega^2 m_i\sum_{m=1}^{N}\Psi_m(x_{p_i},y_{p_i})a_m(\omega)+\left[-\omega^2 m_i+j\omega c_i+k_i\right]z_i(\omega)\\
&\qquad -\omega^2 m_{top_i}z_{top_i}(\omega)-j\omega T_i q_i(\omega)=0\\
&\qquad\qquad i=1,2,\ldots,N_p
\end{aligned}\tag{2.11}$$

$$\begin{aligned}
&-\omega^2 m_{top_i}\sum_{m=1}^{N}\Psi_m(x_{p_i},y_{p_i})a_m(\omega)-\omega^2 m_i z_i(\omega)\\
&\quad+\left[-\omega^2 m_{top_i}+j\omega c_{top_i}+k_{top_i}\right]z_{top_i}(\omega)=0\\
&\qquad\qquad i=1,2,\ldots,N_p
\end{aligned}\tag{2.12}$$

$$\begin{aligned}
&j\omega T_i z_i(\omega)+\left[-\omega^2 L_i+j\omega\left(R_i+R_i^{em}\right)\right]q_i(\omega)=0\\
&\qquad\qquad i=1,2,\ldots,N_p
\end{aligned}\tag{2.13}$$

with components detailed in Section F.2. Eq. 2.10 describes the dynamics of the structural panel; Eq. 2.11 describes the dynamics of the bottom oscillator mass, assuming it to be electromagnetically (E–M) coupled; Eq. 2.12 describes the dynamics of the top oscillator mass; and Eq. 2.13 determines the external harvester circuit dynamics. In the event that the top oscillator mass is E–M coupled, the relation to the charge, q_i, would be inserted into Eq. 2.12 and removed from Eq. 2.11. In the event the device is a SDOF E–M oscillator, all terms z_{top_i} are set to zero.

Notes on Eqs. 2.10–2.13:

- The influence of the external circuit charge, q_i, on the structural panel vibration, a_m, is through a varying magnitude of electrically-induced damping, $j\omega T_i$ where $T_i = B\ell$, dependent on the magnetic flux through the coil, B, and length of the coil, ℓ.

- The inductance of the coil, L_i, indirectly affects the mechanical system response.
- No change in oscillator stiffness is induced via electromagnetic coupling effects.

For N_p oscillators, the mass ratio is defined as

$$\mu = \frac{\sum_{i=1}^{N_p} [m_i + m_{top_i}]}{abh\rho} \tag{2.14}$$

The average mean-square panel velocity is computed as

$$\langle \dot{w}(\omega) \rangle^2 = \frac{\omega^2}{2ab} \sum_m^N \sum_n^N a_m^*(\omega) a_n(\omega) \int_0^a \int_0^b \Psi_m^t(x,y) \Psi_n(x,y) \mathrm{d}x \mathrm{d}y$$
$$m = 1, 2, \ldots, N; \; n = 1, 2, \ldots, N \tag{2.15}$$

with overall values representing the sum over a computed bandwidth of frequencies. Average electrical power over the harvester circuit load resistance is found by $P_i(\omega) = |v_i(\omega)|^2 / 2R_i$, where $v_i(\omega) = i_i(\omega) R_i$ and $i_i(\omega) = \dot{q}_i(\omega)$. The electrical power transfer function is the ratio of the power to the point force excitation.

2.2.1.2 Model formulation: distributed piezoelectric devices

As in Section 2.1.1.1, an excited and arbitrarily bounded plate is considered to which a number of continuously distributed vibration control devices are attached, Figure 2.21. Now, however, the distributed spring layers exhibit piezoelectric characteristics due to either having embedded inclusions of piezoelectric material or due to being fully composed of piezoelectric material. When deformed, the piezoelectric spring layers convert the elastic strain into an electrical potential which is measured by means of connecting the piezoelectric electrodes to an external harvester circuit, modeled as a resistive load R_1. The distributed spring layer is considered to be a thick, transversely deformable, orthotropic plate. Elastic properties of the spring layer, described by the stiffness matrix $\mathbf{c}_s^E$ evaluated at constant electric field, are assumed to either be known or are able to be computed approximately.

Depending on the specific embodiment of piezoelectric spring layer under study, one must appropriately select how to include electromechanical coupling effects in the

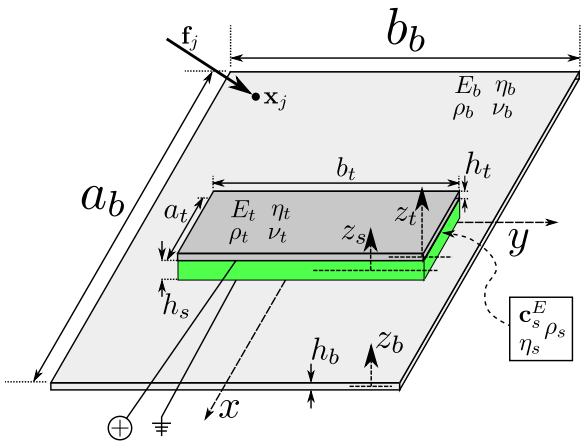

Figure 2.21: Geometry and material properties of base plate structure with attached piezoelectric vibration control devices.

analysis. Chapter G considers one manifestation referred to in literature as "smart foam" which is traditionally used as an acoustic actuator [77–79]. However, the focus here will be on a spring layer composed of a circularly corrugated piezoelectric material, a cross-section of which is shown in Figure 2.22 (a). As may be anticipated, at the SDOF natural frequency of the device, the mass transversely deforms the corrugated piezoelectric material generating tensile and compressive bending strains along the corrugated length of the film, Fig. 2.22 (b). Thus, etching of the electrodes is necessary so as to appropriately combine the equal-and-opposite voltage potentials to maximize the output (see Fig. H.4) [80, 81].

Similar to Section 2.1.1.2, the mechanical response of the circularly corrugated spring layer is assumed to be the superposition of responses from an equivalent incompressible panel and a layer of transverse springs. Consequent of this method is the assumption of linearity in the transverse deformation of the spring layer and only small variations from the undeformed configuration are considered. Continuity of displacement and transverse stress between the spring layer and bounding plates is applied to express spring layer displacements in terms of the top and base plate displacements. Using the generalized Hamilton's principle to determine the forced

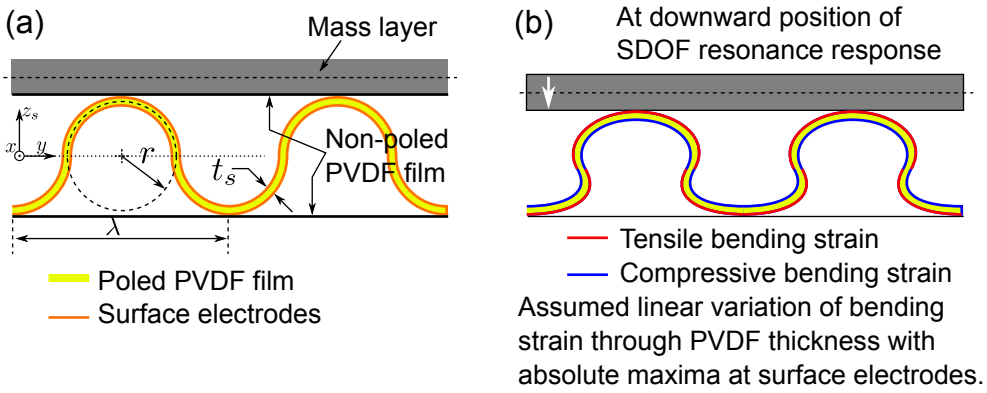

Figure 2.22: (a) Undeformed cross-sectional geometry of circularly corrugated piezoelectric spring layer with exaggerated electrode thickness and arbitrary top mass layer. (b) Illustrated cross-sectional response when top mass layer is displaced downward during SDOF resonant vibration. Bending strain is assumed to vary linearly through the thickness of the PVDF film.

mechanical and electrical response of the coupled system of Figure 2.21, yields a system of electromechanical equations of the form:

$$\left\{ \begin{bmatrix} \frac{1}{R_1} & \mathbf{0} & \mathbf{0} \\ -\Theta_{s,t} & \mathbf{K}_t + \mathbf{K}_{s,t} & \tilde{\mathbf{K}}_{s,b} \\ -\Theta_{s,b} & \tilde{\mathbf{K}}_{s,t} & \mathbf{K}_b + \mathbf{K}_{s,b} \end{bmatrix} + j\omega \begin{bmatrix} C_p & \Theta_{s,t}^T & \Theta_{s,b}^T \\ \mathbf{0} & \mathbf{C}_t + \mathbf{C}_{s,t} & \tilde{\mathbf{C}}_{s,b} \\ \mathbf{0} & \tilde{\mathbf{C}}_{s,t} & \mathbf{C}_b + \mathbf{C}_{s,b} \end{bmatrix} \right. \\ \left. -\omega^2 \begin{bmatrix} 0 & \mathbf{0} & \mathbf{0} \\ \mathbf{0} & \mathbf{M}_t + \mathbf{M}_{s,t} & \tilde{\mathbf{M}}_{s,b} \\ \mathbf{0} & \tilde{\mathbf{M}}_{s,t} & \mathbf{M}_b + \mathbf{M}_{s,b} \end{bmatrix} \right\} \begin{bmatrix} v_p(\omega) \\ \mathbf{m}_t(\omega) \\ \mathbf{m}_b(\omega) \end{bmatrix} = \begin{bmatrix} 0 \\ \mathbf{0} \\ \mathbf{F}(\omega) \end{bmatrix} \tag{2.16}$$

where matrices $\mathbf{K}$, $\mathbf{C}$, $\mathbf{M}$ and Θ are the stiffness, damping, mass and electromechanical coupling terms, respectively; C_p is the capacitance of the piezoelectric film; $\mathbf{m}_t$ and $\mathbf{m}_b$ are the top and base plate generalized co-ordinates, respectively; v_p is the voltage output as measured across the load resistance R_1; and matrices having subscript (s,i) with $i = b, t$ indicate components ascribed to the spring layer written in terms of the base plate, b, or the top plate, t, displacements. Note that electromechanical coupling is due to the spring layer; yet, because the spring layer mechanical displacements are written in terms of the base and top plate responses, the coupling is seen to directly affect the host structural vibration as well as the response of the top mass layer of

the vibration control and energy harvesting device.

To evaluate the electromechanical coupling, Θ in Equation 2.16, it is assumed that the piezoelectric effects are coupled only to the transverse motion of the spring layer. Since transverse dynamics of the continuously distributed spring are decoupled elastically from bending and shearing response by employing the superposition approach (see Section 2.1.1.2), the piezoelectric effects are an equivalent one-dimensional problem in electrical and mechanical co-ordinates. Applying these elastic and electrical assumptions would ordinarily yield

$$\Theta_s = \frac{d_{33} E_z^s}{h_s} \int_x \int_y \left[\Psi_{w_{to}} - \Psi_{w_{bo}}\right] \mathrm{d}y \mathrm{d}x \tag{2.17}$$

where $\Psi_{w_{to}}$ and $\Psi_{w_{bo}}$ are the trial functions of the top and base plate transverse displacements, respectively; h_s is the equivalent thickness of the spring layer; d_{33} is the through-thickness piezoelectric constant; and E_z^s is the equivalent transverse stiffness of the spring layer. However, following extensive experimental observation and by considering the spring layer dynamics in a more intuitive light, this formulation has been modified as follows:

$$\Theta_s = N_c\left(h_s\right) \frac{2h_s}{\pi t_s} \frac{d_{31} E_z^s}{h_s} \int_x \int_y \left[\Psi_{w_{to}} - \Psi_{w_{bo}}\right] \mathrm{d}y \mathrm{d}x \tag{2.18}$$

Eq. 2.18 has been tailored to reflect a more intuitive representation of the linear transverse strain induced in the corrugated piezoelectric film. Though the spring layer is deformed transversely, the piezoelectric coefficient d_{31} related to bending is employed, as opposed to d_{33} which is related to through-thickness deformation. Secondly, a weighting term is applied, $N_c \frac{2h_s}{\pi t_s}$, which is the product of the number of corrugations, N_c (a function of h_s), and the ratio of the equivalent continuous area to the actual corrugated cross-sectional area of the spring layer. These modifications have been made following empirical observation of the devices' electrical response in the laboratory but in fact reflect an intuitive connection to the bending strain of the corrugated spring as it is transversely deformed.

Notes on Eq. 2.16:

- Expressing the equivalent, continuous spring layer displacements in terms of the top and base plate displacements results in the electromechanical coupling effects, Θ, to be expressed in terms of the top and base plates.
- Changes in the harvester load resistance will vary the stiffness of the piezoelectric spring layer, which in turn modify the top and base plate dynamics.
- Piezoelectric damping effects are frequency dependent and are determined by the capacitance of the piezoelectric spring layer, C_p, which is a function of the electrode area-to-thickness ratio; *e.g.* for the same film thickness, t_s, increasing the electrode area by using a larger span of the spring layer will increase C_p and yield greater shunt damping effects.

Performance metrics of interest are the acceleration FRF, Eq. 2.19; voltage FRF, Eq. 2.20; average mean-square velocity of the host panel, Eq. 2.21; accelerance of the host panel, Eq. 2.22; and average electrical power TF over the harvester load resistance, Eq. 2.23. Complete detail on the variational formulation is provided in Chapters A, B and H.

$$\left|\mathrm{FRF}_{accel}\left(\omega\right)\right| = \left|\frac{-\omega^2 w_{to}(x_1, y_1, \omega)}{-\omega^2 w_{bo}(x_2, y_2, \omega)}\right| = \left|\frac{\Psi_{w_{to}}(x_1, y_1)\mathbf{m}_{w_{to}}(\omega)}{\Psi_{w_{bo}}(x_2, y_2)\mathbf{m}_{w_{bo}}(\omega)}\right| \tag{2.19}$$

$$\left|\mathrm{FRF}_{volt}\left(\omega\right)\right| = \left|\frac{v_p(\omega)}{-\omega^2 \Psi_{w_{bo}}(x_2, y_2)\mathbf{m}_{w_{bo}}(\omega)}\right| \tag{2.20}$$

$$\left\langle \dot{w}_{bo}\left(\omega\right)\right\rangle^2 = \frac{\omega^2}{2a_b b_b}\int\int \left(\Psi_{w_{bo}}(x, y)\mathbf{m}_{w_{bo}}(\omega)\right)^* \left(\Psi_{w_{bo}}(x, y)\mathbf{m}_{w_{bo}}(\omega)\right) \mathrm{d}x\mathrm{d}y \tag{2.21}$$

$$\frac{\ddot{w}_{bo}(\omega)}{\mathbf{F}(\omega)} = \left[\frac{\omega^4}{2a_b b_b \mathbf{F}(\omega)}\int\int \left(\Psi_{w_{bo}}(x, y)\mathbf{m}_{w_{bo}}(\omega)\right)^* \left(\Psi_{w_{bo}}(x, y)\mathbf{m}_{w_{bo}}(\omega)\right) \mathrm{d}x\mathrm{d}y\right]^{1/2} \tag{2.22}$$

$$\frac{P(\omega)}{\mathbf{F}(\omega)} = \frac{\left|v_p(\omega)\right|^2}{2R_1}\frac{1}{\mathbf{F}(\omega)} \tag{2.23}$$

2.2.2 Analysis

2.2.2.1 E–M oscillators: μ and R_i dependence, broadband considerations

The model of Section 2.2.1.1 is employed to consider the effect of E–M oscillators attached to an excited vibrating panel. For brevity, results for 2DOF oscillators are here neglected since analysis in Section F.3 shows such devices to be uniformly less beneficial for both vibration suppression and energy harvesting purposes than SDOF oscillators. Consider an E–M oscillator to be centrally positioned on a SS panel excited by an harmonic point force. The oscillator is tuned to exhibit a natural frequency of 50 Hz, the same as the panel (1,1) mode. As the panel is excited, the oscillator also vibrates which induces a flow of current into the external circuit which induces a damping effect on the oscillator mass vibration which thereafter influences the panel vibration.

Predictions of the reduction in overall panel mean-square velocity from untreated levels and the overall average electrical power are made from 1–300 Hz. This bandwidth encompasses the first 7 modes of the panel vibration. The mass ratio of the added oscillator, μ, is then adjusted and the natural frequency of the device kept the same by appropriately modifying the stiffness such that $f_n = \sqrt{k_i/m_i}/2\pi = 50$ Hz for each simulation. The load resistance of the harvester circuit, R_1, is also modified over a selected range. Geometric and electromechanical properties for the simulation are provided in Section F.3 with constant electromagnetic characteristics used throughout simulation which correspond to reasonable values elsewhere employed in the literature [36]. Note that the oscillator is lightly damped mechanically, $\zeta_i = c_i/2\sqrt{m_i k_i} = 0.01$.

Figure 2.23 (a) plots the reduction in overall panel vibration from 1–300 Hz. Not surprisingly, heavier devices yield greater attenuation of the panel vibration, with an observed maximum attenuation occurring for $\mu \approx 0.1$. The optimum load resistance to attenuate the panel vibration corresponds to $R_1 = R^{em}$ where R^{em} is the resistance of the wound coil. Thus, impedance-matching the harvester resistance to the coil

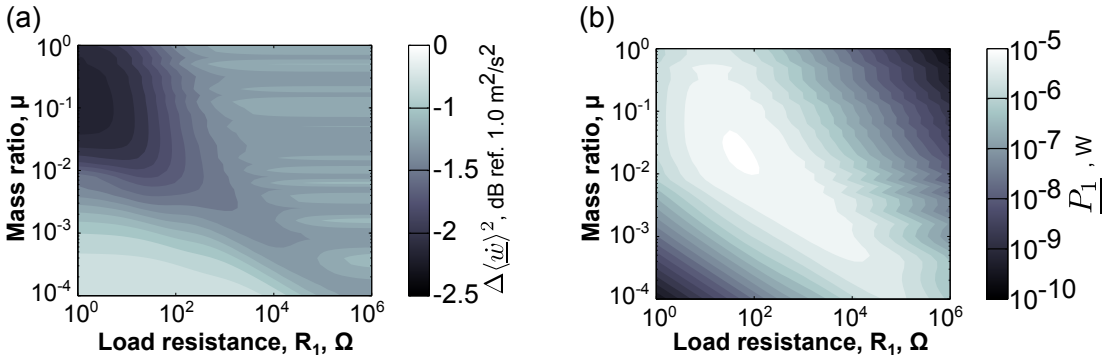

Figure 2.23: (a) Reduction in panel mean-square velocity and (b) cumulative average electrical power for one, central SDOF E–M oscillator. Cumulative results 1–300 Hz.

resistance maximizes the flow through the external circuit and maximizes induced damping effects.

Figure 2.23 (b) plots the overall electrical power. An optimum oscillator mass ratio and load resistance are observed: $\mu \approx 0.01$ to 0.02 and $R_1 \approx 40\ \Omega$. These optimized parameters are not substantially different than those which best suit vibration attenuation objectives. The important connections to make with these results are *(i)* that an optimum mass ratio is observed for energy harvesting purposes which is not $\mu \to 0$ which is assumed in conventional harvesting analyses; and *(ii)* the optimized mass ratio and harvester resistance for energy harvesting falls very close to that which maximizes the passive vibration attenuation of the host structure.

Figure 2.24 (a) and (b) plot the panel vibration and electrical power TF, respectively, for when the optimum μ and R_1 are selected to maximize the individual objectives. From Fig. 2.24 (a) it is clear that the oscillator is positioned at the panel center since it has no influence on the asymmetric panel modes, *i.e.* the (2,1) mode at 96 Hz. The electrically-induced damping is apparent around the (1,1) panel mode of 50 Hz. Classical one-dimensional vibration absorber design aims at suppressing the split resonances around the tuned natural frequency to an equal degree by modifying the damping of the device [82]. It is interesting to observe this is almost exactly met for the optimum energy harvesting case. What is perhaps more interesting is the

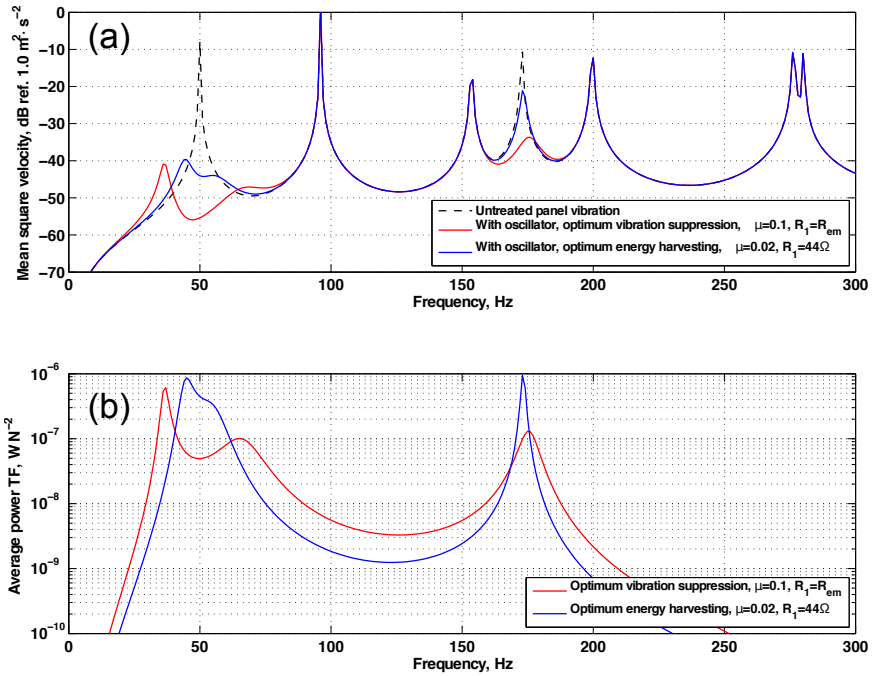

Figure 2.24: The results of optimized conditions for vibration attenuation (red) and energy harvesting (blue): (a) Panel mean-square velocity and (b) electrical power TF.

negligible difference in attenuation achieved for the optimum vibration suppression case, particularly in light of the fact that this scenario requires 5× the mass as for optimum energy harvesting.

Considering Figure 2.24 (b), the induced damping is also apparent in the electric power TF. It is important to recall how this plot differs from traditional energy harvesting analyses. In the absence of structural dynamic coupling, harvesters will vibrate most at their natural frequency, having an amplitude limited by the combination of electrical and mechanical damping. In Figure 2.24 (b) it is found that the oscillator is no longer vibrating at its tuned frequency of 50 Hz, but exhibits a maximum electrical power TF at 46 Hz, one of the split resonances resulting from the dynamic coupling between SS panel and the oscillator. In the limit that $\mu \to 0$, the device has no dynamic effect on the host structure, the oscillator is excited at its tuned natural frequency and conventional energy harvesting analyses hold. However,

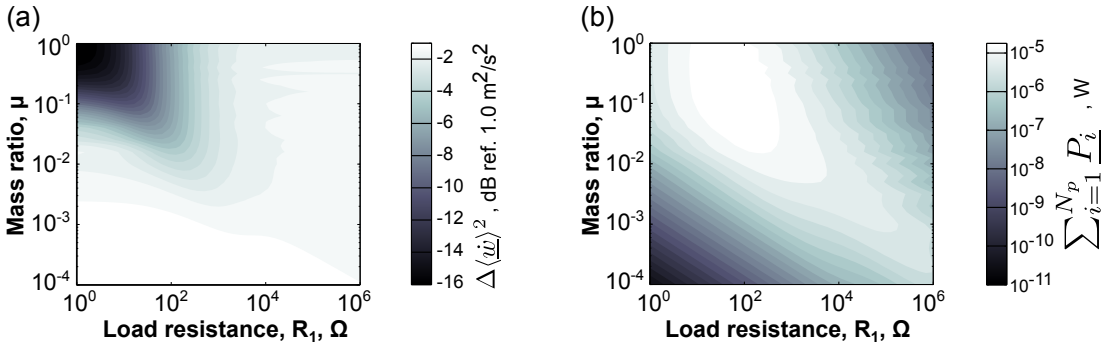

Figure 2.25: (a) Reduction in panel mean-square velocity and (b) cumulative average electrical power for 15 SDOF E–M oscillators. Cumulative results 1–300 Hz.

discovering that structural vibration attenuation and energy harvesting objectives are both optimized for nearly identical design conditions poses a unique opportunity to simultaneously meet both ends.

Next, consider an application of 15 oscillators, each tuned to 50 Hz, positioned on the vibrating panel in the configuration of Figure F.5. Each oscillator was considered to have the same external load resistance and electromechanical characteristics. Due to the arbitrary placement of the devices, they are more capable of broadband vibration attenuation than an individual, centrally-located device. The model was employed once more to evaluate the influence of changing R_1 and μ where the mass ratio is now split evenly over the 15 devices.

Figure 2.25 plots the results for the 15 oscillators attached to the excited panel in terms of (a) vibration attenuation and (b) net electrical power over the 1–300 Hz bandwidth. Optimum load resistances are predicted to be the same selections as when employing one E–M oscillator. Thus, when the oscillators are themselves mechanically undamped, the maximum damping achievable occurs when the external circuit is impedance-matched to the coil resistance. However, the optimized mass ratio is now skewed towards heavier total treatments of devices. The magnitude of broadband vibration attenuation is much greater for the 15 oscillators which represents the ability of the distributed devices to attenuate both symmetric and asymmetric panel

modes. However, it is noted that the magnitude of net electrical power is not also significantly increased; in other words, there is no 15× improvement in the electrical power output as may be anticipated. This drawback to applying numerous energy harvesting devices to a single vibrating structure is explored further in Section 2.2.2.4.

2.2.2.2 E–M oscillators: μ and R_i dependence, narrowband considerations

In Figure 2.24 (a), it is observed that there is substantial reduction in the panel vibration levels around the (1,1) mode but that the greater amplitude of vibration over the 1–300 Hz bandwidth is observed for the (2,1) mode at 96 Hz. This explains the relatively small reduction in overall mean-square velocity computed in Fig. 2.23 (a), approximately 2 dB total attenuation of panel vibrational energy though one observes substantial suppression of the (1,1) mode in Fig. 2.24 (a).

Then, simulation is again evaluated for one centrally-located E–M oscillator but now considering overall levels up to 75 Hz, *i.e.* the vibrational energy contribution of the first panel mode. Figure 2.26 (a) and (b) present the overall reduction in panel vibration and overall electrical power only up to 75 Hz. This represents a more plausible excitation characteristic for larger structures given the greater difficulty in exciting higher order modes. For example, energy harvesting literature has shown that the first mode of a bridge is the dominant vibrational dynamic under typical excitation mechanisms [42]. Thus, Figure 2.26 presents overall values of vibration attenuation and generated electrical power in a more important bandwidth of excitation frequencies.

Optimized vibration attenuation of the first mode shows similar trends as for broadband attenuation with the exception that very heavy treatments are uniformly the best solution. Though this is an unreasonable solution in practice, the finding is intuitive given that mass-loading a structure to an extreme is ultimately the best manner by which to attenuate the vibration. One also notes the significant vibration reduction around $R_1 \approx 10\ \Omega$ and $\mu \approx 0.1$ which corresponded to best broadband

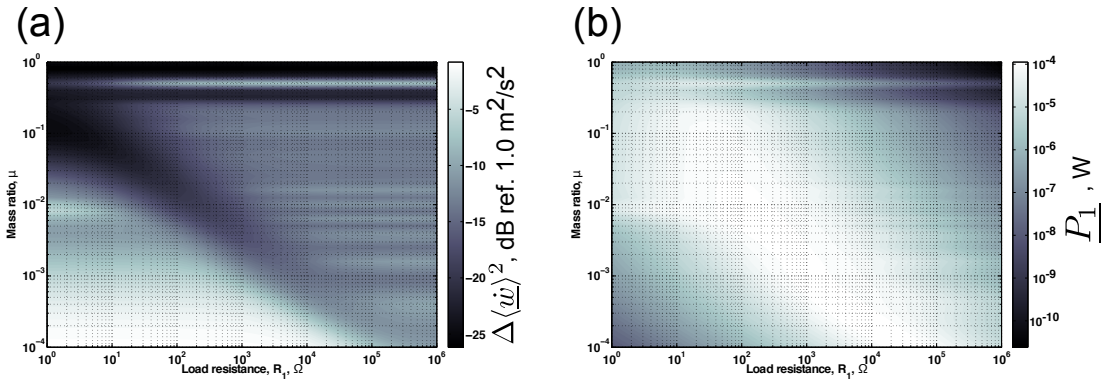

Figure 2.26: (a) Reduction in panel mean-square velocity and (b) cumulative average electrical power for one, central SDOF E–M oscillator. Cumulative results 1–75 Hz.

attenuation parameters: roughly a 20 dB reduction in the 50 Hz panel (1,1) mode. This magnitude of attenuation is consistent with what was observed in Figure 2.24 (a) around the lowest panel resonance, 50 Hz, to which the oscillator was tuned.

The optimum selection of parameters for energy harvesting objectives now show a broadened region of best μ and R_1 when the oscillator is excited only by one structural mode. The optimum design parameters are found to occur for $\mu \approx 0.0002$ and $R_1 \approx 9$ kΩ, which yields approximately a 18% increase in output electrical power over the broadband optimum parameters $\mu \approx 0.01$ to 0.02 and $R_1 \approx 40$ Ω. In contrast to broadband considerations, as the mass ratio decreases the reduction in electrical power does not precipitously decrease if R_1 is correspondingly increased. Thus, a larger window of design parameters exist for narrowband excitation by which to maximize the generated electrical power. However, like broadband attenuation, it is observed that the (1,1) panel mode may be dramatically suppressed and maximum electrical power produced for nearly the same selection of μ and R_1, thus simultaneously achieving both vibration control and energy harvesting objectives.

2.2.2.3 E–M oscillators: mechanical damping

An initial hypothesis regarding the concurrent attenuation of and energy harvesting from surface vibrations is that mechanically damped devices may serve the prior

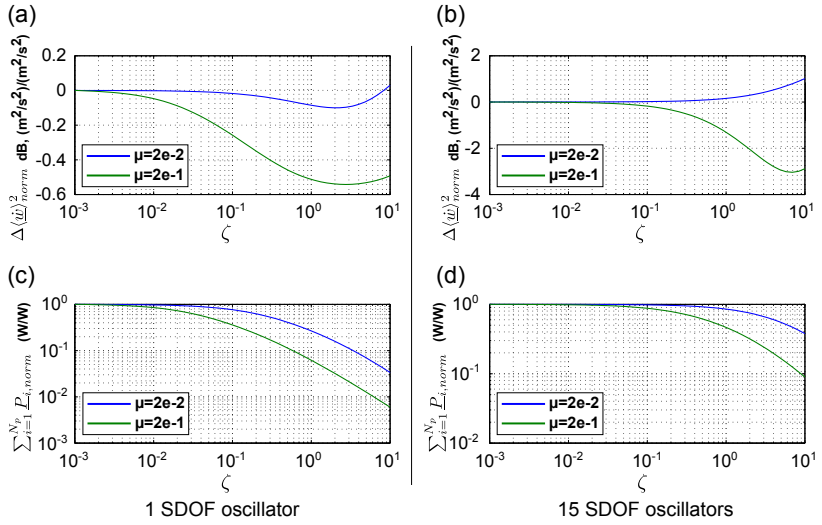

Figure 2.27: Vibration suppression for case of the panel having (a) 1 SDOF oscillator, (b) 15 SDOF oscillators. Energy harvesting for panel having (c) 1 SDOF oscillator, (d) 15 SDOF oscillators. Variation of ζ with results normalized to undamped data.

while inhibiting the latter. This hypothesis can be tested using the present model by selecting a specific μ and R_1 for a number of E–M oscillators and varying the damping ratio, ζ, computing values of overall vibration attenuation and energy harvesting.

Figure 2.27 presents the results of simulation carried out for $\mu = 0.02$ and $\mu = 0.2$ for the single, centrally positioned E–M oscillator and for 15 oscillators using the locations prescribed in Figure F.5. Load resistance was fixed at $R_1 = 44\ \Omega$. Presented results are normalized to undamped values, $\zeta \to 0$. As anticipated, any increase in mechanical damping is detrimental to energy harvesting objectives. While some increase in ζ improves vibration attenuation, over-damping of the oscillators is observed for $\mu = 0.02$ in Fig. 2.27 (b) indicated by an increase in overall vibration levels for high ζ.

This suggests that overall levels of oscillator damping are adequately met by circuit dissipation and increases in mechanical damping provide negligible improvement in vibration attenuation performance. Thus, it is found that the best design practice to achieve both vibration suppression and energy harvesting is to employ conservative,

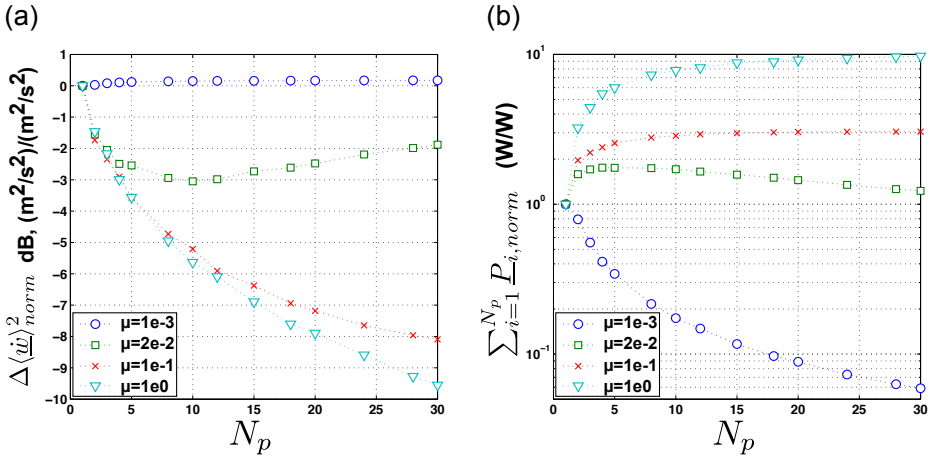

Figure 2.28: (a) Cumulative mean-square panel velocity. (b) Cumulative power output. Data normalized to $N_p = 1$. $R_i = 44.6\ \Omega$.

or mostly undamped, oscillators in tandem with a load resistance which maximizes power harvesting and leads to substantial electrical dissipation.

2.2.2.4 E–M oscillators: population size

It was found that using 15 distributed oscillators significantly improved broadband vibration attenuation capability of the treatment but did not yield a corresponding proportional increase in net electrical power. To study this effect, a mass ratio is selected and the mass divided up into N_p oscillators which are randomly positioned on the panel. The load resistance of each oscillator is kept fixed at $R_1 = 44.6\ \Omega$. The net reduction in mean-square velocity and electrical power from 1–300 Hz are then computed. The results of 50 simulations are averaged, using new random oscillator positions for each run. (The averaging technique is justified by noting that a single simulation for $N_p = 2$ when the oscillators are randomly positioned would not yield conclusive results).

Figure 2.28 presents the results normalized against values computed for a centrally located oscillator, *i.e.* $N_p = 1$. Fig. 2.28 (a) verifies that heavier treatments yield much improved vibration attenuation but only to a point. There is insignificant

improvement from increasing μ from 0.1 to 1; distributing the mass amongst numerous masses begins to converge to a maximum potential for improvement in vibration suppression. For a more reasonable treatment mass ratio, $\mu = 0.02$, an optimum number of devices to best attenuate panel vibration is observed: $N_p \approx 10$.

Figure 2.28 (b) shows that increasing the number of oscillators in a distribution converges to maximum achievable net power output for $\mu = 0.1$ and 1. For such heavy treatments, $N_p = 15$ shows convergence of maximum electrical power. When the mass ratio is $\mu = 0.1$, the maximum increase in electrical power is $3\times$ the amount achievable when employing a single, centrally-positioned device. However, this requires 15 devices, making the approach costly to apply for a small increase in net electrical power. For very lightweight treatments, $\mu = 0.001$, any increase in population size is detrimental to the electrical power output, a synonymous result as observed in the literature for lightweight mass-spring-damper treatments in attenuating plate vibration [83, 84].

In considering the more reasonable treatment mass ratio of $\mu = 0.02$, an optimum number of devices in the distribution is observed, $N_p \approx 7$. This corresponds to nearly the same selection of N_p which maximized the vibration attenuation of the panel. The results of this and earlier sections show that selections of μ, R_1 and the number of E–M oscillators in a given treatment are parameters which may be properly selected to simultaneously optimize vibration suppression and energy harvesting objectives. This is a thorough indication of the analogy of energy harvesters as electromechanical vibration absorbers.

2.2.2.5 Piezoelectric devices: mechanical damping

It was found that increased mechanical damping in E–M oscillators was detrimental to energy harvesting potential and led to small improvements in vibration attenuation capability. However, for continuously distributed devices, increases in the spring layer loss factor were observed to uniformly increase structural attenuation, Section 2.1.2.3. Thus, should the continuously distributed spring now be composed of a transversely

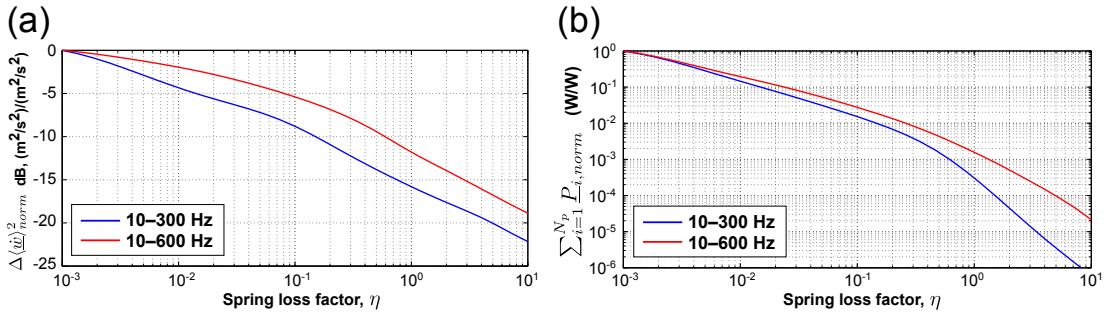

Figure 2.29: (a) Cumulative mean-square panel velocity. (b) Cumulative power output. Data normalized to $\eta = 0.001$. $R_i = 10$ kΩ.

deformable piezoelectric layer, it is anticipated that increases in mechanical damping will reduce energy harvesting capability but uniformly increase the amplitude of vibration attenuation.

This correlation may be studied using the model of Section 2.2.1.2 in simulating the effect of a continuously distributed piezoelectric vibration control device attached to an excited SS panel. Recall that the present device studied, shown in cross-section in Fig. 2.2.1.2, is a circularly corrugated piezoelectric material, appropriately etched, bound by two non-poled PVDF sheets, and topped with a distributed mass layer. The geometric and electromechanical properties of the system and further detail are given in Section H.5.1. The simulation is evaluated in the event that the spring material is negligibly damped and reevaluated for increasing spring layer loss factor, all other parameters remaining the same.

Results are normalized against the undamped case and are plotted in Figure 2.29 (a) for vibration attenuation and (b) energy harvesting for two bandwidths. The frequency range of 10–300 Hz corresponds to the tuning frequency range of the piezoelectric device while 10–600 Hz includes several other SS panel modes and represents a broadband metric of performance. As intuitively predicted, increases in mechanical loss factor uniformly improve vibration attenuation in narrow and broadband evaluations. In a similar fashion to study of electromagnetic energy harvesting, Fig. 2.29 (b) shows that increases in mechanical loss factor of the spring material also leads to

significant decreases in energy harvesting potential. Thus, for maximum results in energy harvesting, damping should primarily be induced through electrical dissipation and not by mechanical design.

2.2.2.6 Piezoelectric devices: electromechanical damping

Piezoelectric stiffening and shunt damping effects resulting from piezoelectric energy harvesting are well understood analytically and regularly observed in practice [35, 36, 49, 43]. From Eq. 2.16, it was observed that changes in the load resistance modified the stiffness of the piezoelectric spring layer while larger areas of the piezoelectric film would amplify electrical damping effects. Given that the coupled external circuit in electromagnetic energy harvesting was observed to yield substantial overall damping for the resonant devices in attenuating structural vibration, it is needed to assess such damping effects as influencing factors for continuously distributed piezoelectric devices. For the present piezoelectric device, this may be best evaluated by an example numerical study.

Consider a SS panel to which one such corrugated piezoelectric vibration control device is centrally positioned. The spring layer uses 7 periods of the piezoelectric film along one length of the device. The electrode potentials are considered to be combined out-of-phase and are attached to an external harvester circuit described by a load resistance, R_1. The device is predicted to exhibit a SDOF transverse natural frequency at 260 Hz, very close to the panel (3,1) mode at 264.1 Hz. The total piezoelectric device represents a mass ratio of $\mu = 0.0117$.

Figure 2.30 plots the untreated panel vibration (dashed plot) along with the panel vibration once the piezoelectric device is attached for a number of load resistances. As expected, the device substantially attenuates the targeted resonance of the panel at 264.1 Hz and produces two split resonances as a result, 244 and 292 Hz. Little difference is observable on a broadband scale by modifying the load resistance to which the piezoelectric electrodes are attached and attention should therefore be directed to the split resonances.

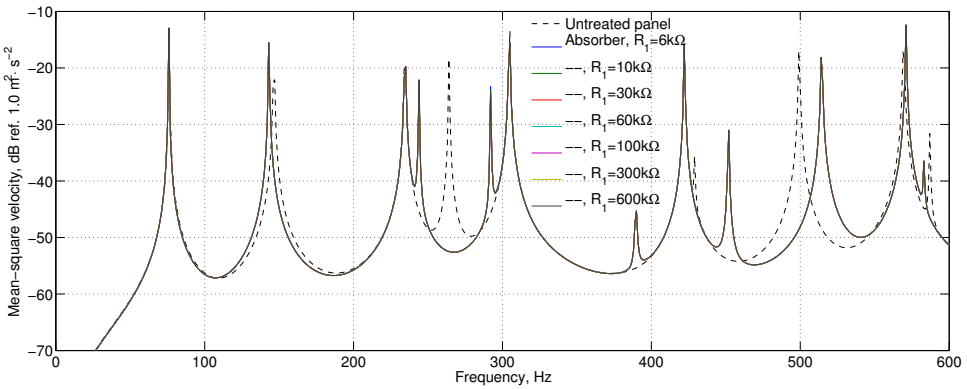

Figure 2.30: Panel mean-square velocity for varying distributed device load resistance.

Figure 2.31 (a) and (b) plot the panel vibration at the two split resonances. (Note that the untreated panel vibration is not included at this level of focus). Very apparent for both of the split resonances is that changes in the harvesting circuit load resistance modify the amplitude and frequency of the split resonances of the host structure. An optimum damping of the split resonances occurs for $R_1 = 30$ kΩ showing roughly an additional 2 dB of vibration attenuation as compared with the load resistance approaching open circuit conditions, $R_1 \to \infty$.

Numerous piezoelectric energy harvesting investigations have observed this feature for the harvesters themselves but the present finding is distinct from prior studies. The effects observed in Fig. 2.31 (a) and (b) are the *indirect* result of piezoelectric stiffening and damping induced by energy harvesting. In other words, the spring layer is directly influenced by the external circuit which stiffens and dampens the dynamics of the spring. In turn, as the characteristics of the piezoelectric device are modified, its influence on the host structure change, changing the split resonance frequencies and magnitudes observed in Figure 2.31. Also it is noted that much less electrically induced damping is observed for the piezoelectric vibration control or energy harvesting device as was predicted to occur for the example electromagnetic device.

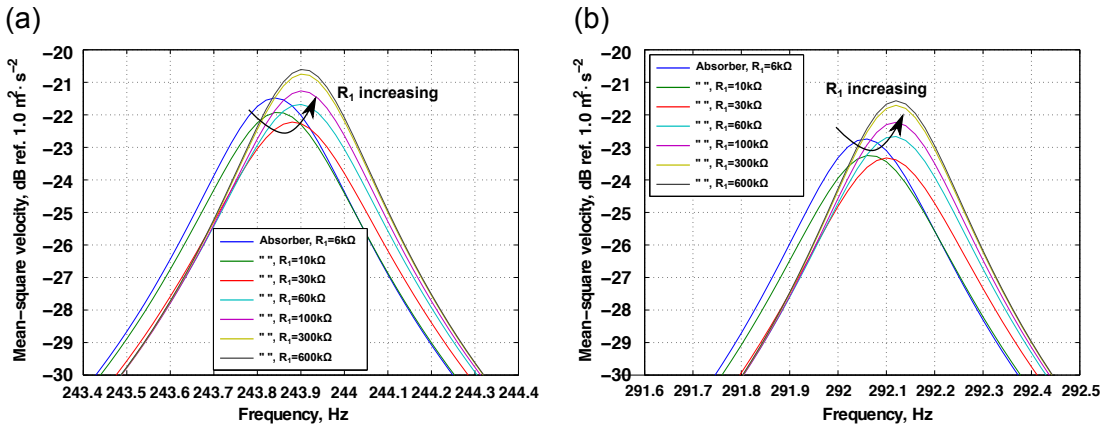

Figure 2.31: Panel mean-square velocity for varying distributed device load resistance, zoom (a) lower split resonance and (b) higher split resonance.

Figure 2.32 plots the harvester electrical response around the two split resonances which represent the peak electrical response over all frequencies. Shifting resonance frequencies are observed as the load resistance is modified. When $R_1 = 30$ kΩ, the electrical power output is maximized; further increases in resistance reduce power output. This is also an identical trend documented in energy harvesting literature. Prior work has shown that cantilever beam harvesters exhibiting low to moderate electromechanical coupling are maximally damped via shunt damping effects when the energy harvested in the external circuit is maximized [27, 35, 85]. Thus, the present continuously distributed device is maximally damped for a load resistance of $R_1 = 30$ kΩ—the best choice for energy harvesting purposes—and therefore dissipates the greatest amount of the panel vibration.

In contrast to existing energy harvesting studies, note that the applied harvester device is no longer oscillating at its natural frequency of 260 Hz but is instead excited at the split resonance frequencies of 244 and 292 Hz. This is the unique effect of applying reactive or resonant devices to a vibrating structure in the event that the devices are capable of exerting an inertial influence on the host structure. This was also found in Section 2.2.2.1 for electromagnetic oscillators and, indeed, would be the case for applying any resonant device to a larger resonant structure. The amplitude to

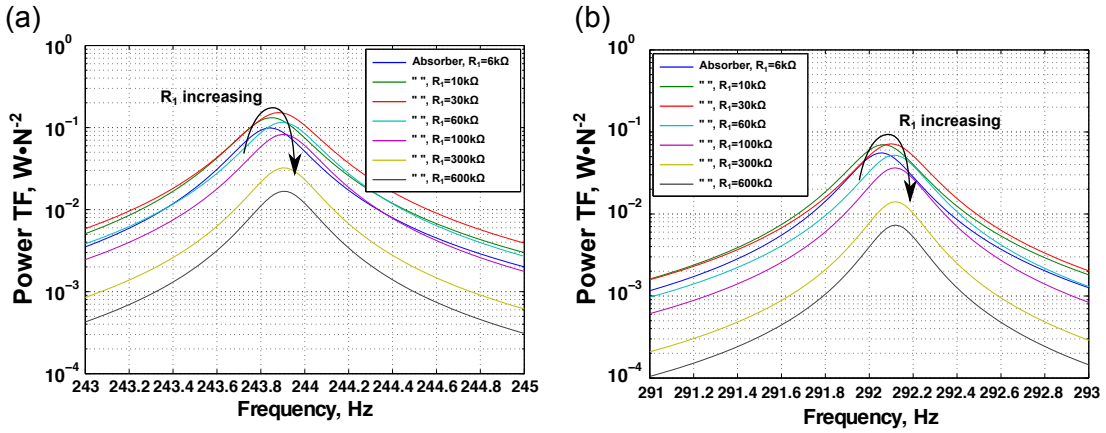

Figure 2.32: Distributed device piezoelectric power output for varying distributed device load resistance, zoom (a) lower split resonance and (b) higher split resonance.

which the applied device influences the host structural response is entirely dependent on the mass ratio of the device, μ. Note that the present piezoelectric device considered is just a 1.17% addition of mass to the structure and shifts the panel resonance frequency from 264.1 Hz to 244 and 292 Hz, indicating great influence from a small increase in total mass. However, recall from Section 2.2.2.1 that for point oscillators this was approximately the mass ratio which maximized energy harvesting potential. Thus, in simultaneously attenuating and harvesting energy from structural vibrations, the principal compromising factor is the added mass of the harvester device[s].

2.2.3 Experiments

2.2.3.1 Model validation: device with corrugated piezoelectric film spring, $t_s = 28$ μm

The assumptions employed in modeling the distributed piezoelectric device approximate the electromechanical coupling effects in a one-dimensional form, Eq. 2.18. It is therefore anticipated that the predicted voltage response from the model will be accurate only in the event that the device is excited by primarily uniform transverse vibration. In other words, a device tuned to the same frequency of a SS panel (1,1) mode and placed at the center of the panel is mostly excited by uniform transverse vi-

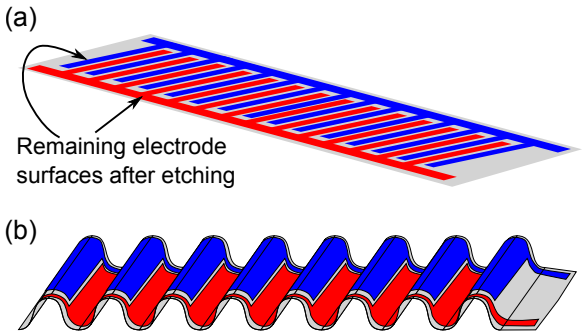

Figure 2.33: (a) Etching of piezoelectric material prior to corrugation and (b) the desired circularly corrugated form.

bration, assuming the span of the device is much smaller than the span of the panel. However, that same device, excited by asymmetric panel modes will likely include more intricate deformation of the actual corrugated spring layer which the model neglects. It is therefore predicted that the model will poorly predict the electrical response of the piezoelectric material in the event of this latter form of excitation. However, energy harvesting potential is maximized around the device SDOF natural frequency and therefore capturing the essence of the voltage response due to uniform transverse excitation is of greatest concern.

A circularly corrugated piezoelectric film spring layer was produced using film of thickness $t_s = 28$ μm, period of $\lambda = 12.7$ mm and other electromechanical properties as given in Table H.1. Prior to corrugation, the piezoelectric film electrodes were carefully etched using a ferric chloride solution, with etch lines every $12.7\pi/4$ mm $\approx$ 10 mm, as illustrated in Figure 2.33 (a). Bonds between the corrugated film and the bounding non-poled sheets of PVDF were made using thin lines of "2-ton" epoxy. Finally, a distributed mass layer was glued to the top non-poled sheet of PVDF film to complete the full device, Figure 2.34. The superposition method of Section 2.1.1.2 was employed to determine equivalent elasticity characteristics of the corrugated spring layer which are provided in Table H.2.

The device was attached to a shaker table and the two pairs of electrode leads

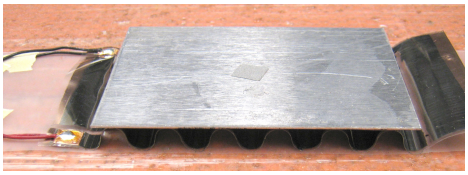

Figure 2.34: Photograph of piezoelectric vibration control device using a circularly corrugated piezoelectric film as the distributed spring layer. Electrical leads are also shown to be attached to the etched surface electrodes of the film.

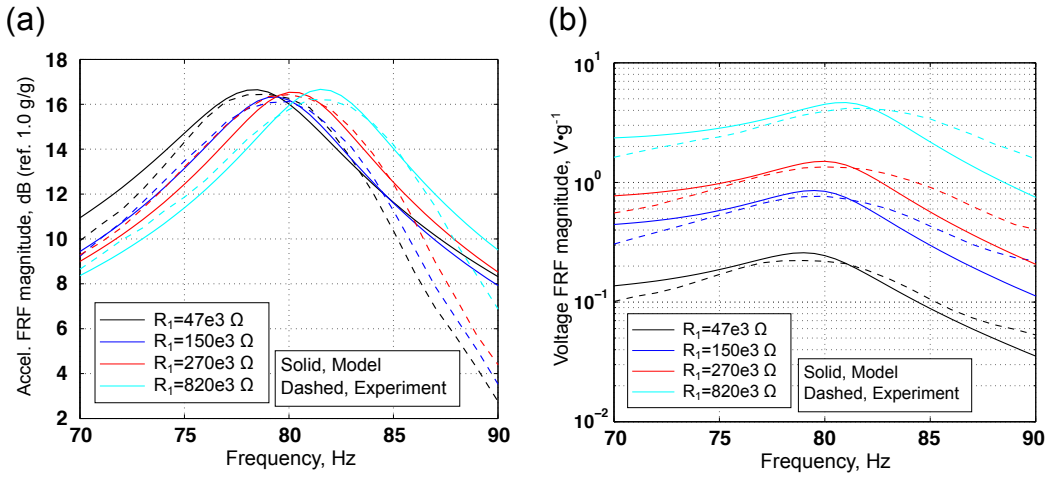

Figure 2.35: Comparison of modeled and measured (a) acceleration FRF magnitudes and (b) voltage FRF magnitudes for piezoelectric corrugated core distributed absorber device for various load resistances, R_1.

were appropriately combined out-of-phase in parallel with the harvester circuit load resistance, R_1. The shaker excited the device with uniform transverse vibration, monitored by an accelerometer on the shaker platform; the amplitude of the shaker table vibration was measured to be 14.2 m·s^{-2} (1.45 g). The velocity of the top mass was measured with a laser vibrometer and acceleration was approximated from $\ddot{w}_{to} = j\omega\dot{w}_{to}$. The acceleration FRF was then computed for various selections of circuit load resistance. The model results were then compared against the measurements, using top and base plate properties as given in Table H.3, and are shown in Figure 2.35.

For smaller values of R_1 (short circuit conditions), the SDOF natural frequency occurs at approximately 78.5 Hz; as the resistance is increased, the coupling through

the piezoelectric material produces a stiffer distributed spring layer and increases the resonance to the open circuit value (*i.e.* $R_1 \to \infty$) at approximately 81.5 Hz. This is a substantial shift in frequency for a piezoelectric material having such low electromechanical coupling as compared with, for example, piezoceramics. However, this may be due to the circularly corrugated design which induces a great bending strain in the film as the mass oscillates transversely at resonance, Fig. 2.22 (b). The model almost exactly predicts the locations of these resonant frequencies for various load resistances but measurements exhibited uniformly more roll-off above resonance. This discrepancy may be explained by employing too small an equivalent elastic loss factor, η_s in Table H.2. Of further note is the near absence of shunt damping effects, indicating the inertial influence of the mass, for this sample, dominates electromechanical coupling effects. Figure 2.35 (b) compares the measured and predicted voltage FRF for the sample. The model fairly accurately predicts the amplitude and shifting resonance frequency of the voltage FRF resonance, trends frequently observed elsewhere in energy harvesting literature.

Finally, a time-domain plot of the response of the device as measured for $R_1 =$ 150 kΩ is given in Figure 2.36 at an excitation frequency of 81 Hz. Shown in Figure 2.36 (a) are the individual voltage outputs for the two electrode pairs generated by etching the corrugated piezoelectric film. The outputs are perfectly out-of-phase and exhibit nearly identical magnitude. This verifies the assumption that the strains exhibited on opposing sides of the piezoelectric film are equal-and-opposite. Proper combination of these voltages yields a substantial increase in output, while directly combining the two signals almost eliminates the net voltage, Figure 2.36 (b).

The response is also observed to be sinusoidal, indicating the linearity of the distributed spring layer as the device transversely oscillates. This is a beneficial finding given that one might assume the bending strain induced in the corrugated spring is substantial for the present amplitude of exciting acceleration of 14.2 m$\cdot$s^{-2} (1.45 g). However, in practice, little displacement from the undeformed configuration

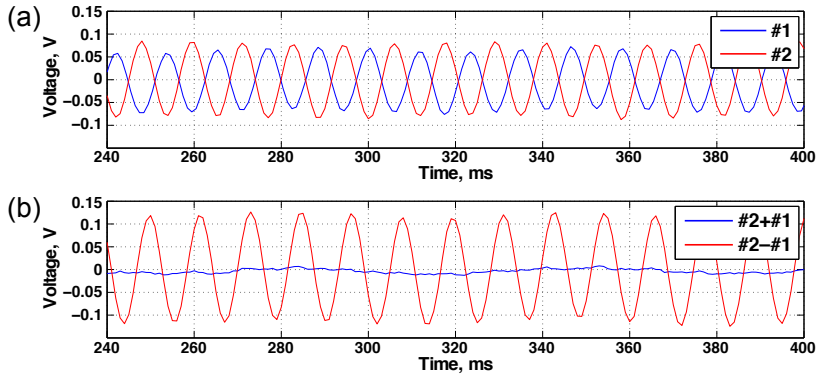

Figure 2.36: Measured time series of corrugated piezoelectric device. (a) Individual electrode outputs and (b) sum and difference of the two signals.

is observed as the device oscillates on the shaker. This may be explained by the fact that the transverse force of the mass deflecting the corrugated spring is distributed over a broader surface as compared to a point vibration absorber which generally deflects its spring to a much greater degree.

While no sensitivity analysis is here performed to determine at what level of input vibration the induced bending strain in the corrugated spring begins to exhibit nonlinear characteristics, the amplitude of vibration presently measured in shaker testing is sufficiently great to assume most realistic scenarios would also exhibit linear elastic and electrical response (a number of realistic ambient vibration acceleration levels are detailed in [86–88]). The linearity of the transverse response suggests model results for the device at its natural frequency should be in reasonable agreement with measurements which is most important for energy harvesting analyses.

2.2.3.2 Model validation: device with corrugated piezoelectric film spring, $t_s = 52$ μm

A second sample was produced using the same corrugated wavelength, $\lambda = 12.7$ mm, but with a thicker piezoelectric film, $t_s = 52$ μm. All other electromechanical characteristics of the film were assumed to be the same as those for the thinner film. The equivalent elasticity parameters for the distributed spring were computed from the

Table 2.4: Equivalent orthotropic plate characteristics of piezoelectric core having $\lambda = 12.7$ mm and $t_s = 52$ μm

E_x (Pa)	E_y (Pa)	E_x (Pa)	ν_{yx}	ν_{yz}	ν_{xz}
4.04e10	3.87e10	4.60e4	0.041	0	0
G_{yz} (Pa)	G_{xz} (Pa)	G_{xy} (Pa)	ρ_s (kg/m^3)	h_s (mm)	η_s
2.66e5	3.23e6	8.03e8	14.2	6.35	0.056

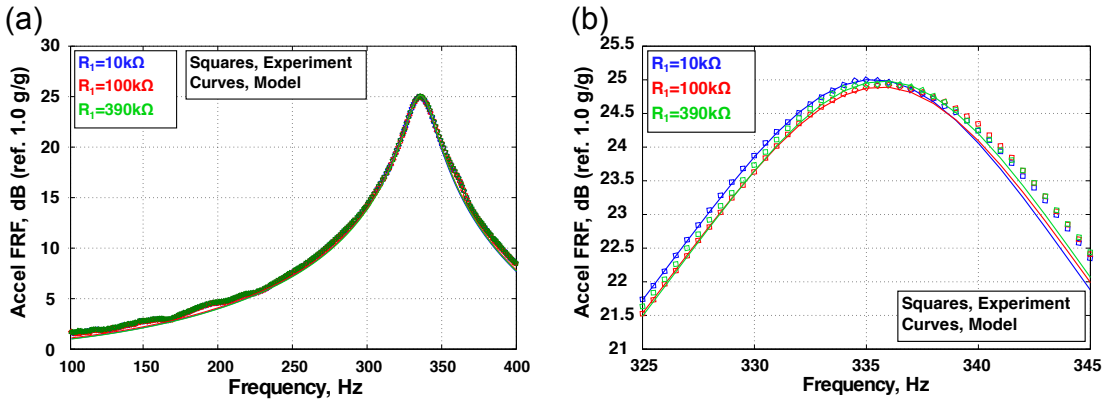

Figure 2.37: Acceleration FRF of piezoelectric device having $t_s = 52$ μm, modeling comparisons. (a) Broadband view and (b) view around resonance.

methods of Chapter D and are given in Table 2.4. The mass layer had characteristics: $a_t = 76.2$ mm, $b_t = 50.8$ mm, $h_t = 0.76$ mm, $E_t = 72e9$ Pa, $\rho_t = 2100$ kg/m^3, $\nu_t = 0.3$, $\eta_t = 0.001$.

In comparing different thicknesses of piezoelectric PVDF film in a biomechanical energy harvesting application, Granstrom et al. [89] observed that the thinner film yielded the greatest levels of harvested power. Though one might anticipate a thicker material, providing more piezoelectric volume per length, would yield the best results, in fact the thinner film is strained to a greater degree and the amplitude of strain is what lends the piezoelectric effect. Thus, considering the corrugated spring layer using a thicker film, it is anticipated that less electromechanical coupling effects should be observed.

Figure 2.37 compares the modeled and measured results of the acceleration FRF in (a) broadband and (b) about resonance frequency ranges. Since almost all of the results overlap, measurements are provided as square symbols. As intuitively ex-

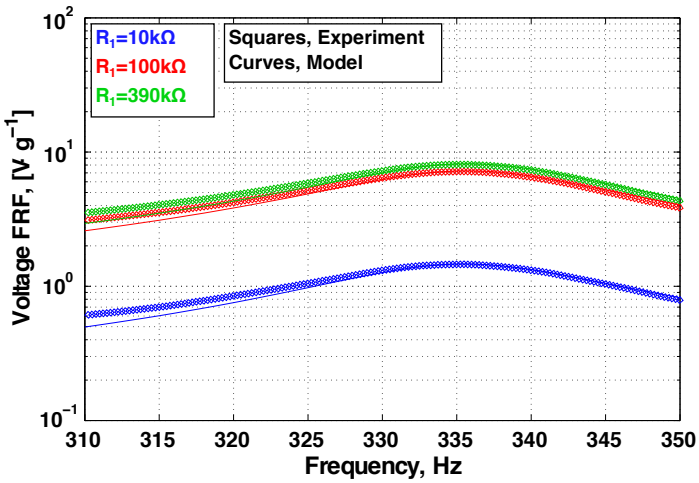

Figure 2.38: Voltage FRF of piezoelectric device having $t_s = 52$ μm, modeling comparisons.

pected, very little piezoelectric stiffening or shunt damping is observed. Even closely observing the FRF just around resonance, Fig. 2.37 (b), there is negligible piezoelectric stiffening induced for the thicker sample. The model accurately replicates these features and exactly predicts the location of the resonances: 335 Hz for short circuit conditions and 336 Hz for open circuit conditions. Figure 2.38 compares the voltage FRF measurements against the model predictions. Since the device is transversely excited, the electromechanical coupling employed by the model is in close agreement with measurements in regards to changes in load resistance.

2.2.3.3 Application: concurrent suppression of and energy harvesting from a vibrating panel

A large SS panel was held within a frame which was suspended. The panel was excited roughly at the center by a shaker and force transducer on one side while a coplanar accelerometer array measured the panel accelerance. A larger piezoelectric distributed device was produced and then attached to the opposing surface of the panel, as shown in Figure 2.39. Figure 2.40 shows a close photograph of the device prior to attachment to the panel surface, showing 12 full periods of the etched, circularly corrugated piezoelectric film of $t_s = 28$ μm and $\lambda = 12.7$ mm.

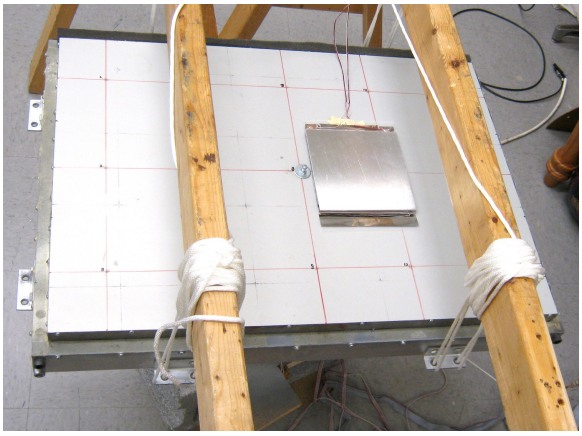

Figure 2.39: Photograph of simply supported panel in mounted structure with piezoelectric device attached to the top surface. The shaker, stinger, force transducer and accelerometer array are positioned on the underside of the panel.

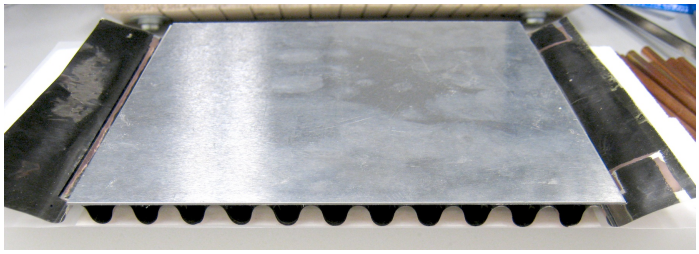

Figure 2.40: Photograph of piezoelectric device with 12 periods of the etched piezoelectric film.

According to Eq. 2.16, for the same film thickness, greater piezoelectric electrode area corresponds to a greater capacitance, C_p, which is found to increase electromechanical damping effects. As such, since the larger device spanned an area 6× greater than the sample used in shaker testing (Fig. 2.34), the larger sample was anticipated to exhibit greater electromechanical influence. The device was predicted to have a SDOF natural frequency of 94 Hz, close to the panel (1,1) mode of 97.5 Hz. Despite being much larger than the samples used for shaker testing, the piezoelectric device had a mass ratio to the panel of just $\mu = 0.0104$.

Material properties of the SS panel, the device top mass and the equivalent elastic characteristics of the distributed spring are given in Section H.6.1. It was discovered

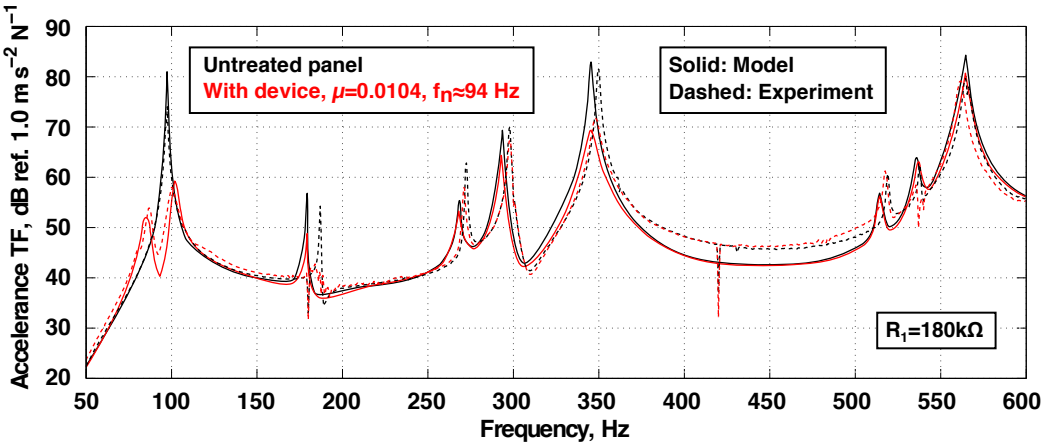

Figure 2.41: Comparison of modeled (solid curves) and measured (dashed curves) accelerance magnitudes of the panel when untreated (black plots) and with the piezoelectric device (red plots). $R_1 = 180$ kΩ.

that the panel was not exactly simply-supported and the model was adjusted so as to include additional rotational springs along the edges as indicated in Chapter A to best fit the model to the measurements of SS panel response.

A comparison of measured and modeled panel accelerance are shown in Figure 2.41 for the untreated panel and after the device was applied for the case of load resistance $R_1 = 180$ kΩ. In terms of model comparison, the greatest disparities are due to the inexact simple supports of the panel, which are seen to shift some of the asymmetric panel modes, for example the (2,1) mode at 186 Hz. However, the model is in very close agreement regarding the amplitude of the panel resonances as well as the magnitude of vibration attenuation achieved following application of the device.

With the piezoelectric device placed closely to the center of the panel, a substantial reduction in the (1,1) panel mode is achieved. By adding a mere 1% additional mass to the panel, the reactive piezoelectric device suppresses the (1,1) mode by more than 20 dB and yields two split resonances, 87 and 100 Hz, a resulting dynamic effect conventionally observed in the application of vibration absorbers to excited systems. The amplitude of attenuation is consistent with modeled results for point E–M oscillators in Section 2.2.2.2, showing the dynamic similarities between the point oscillators

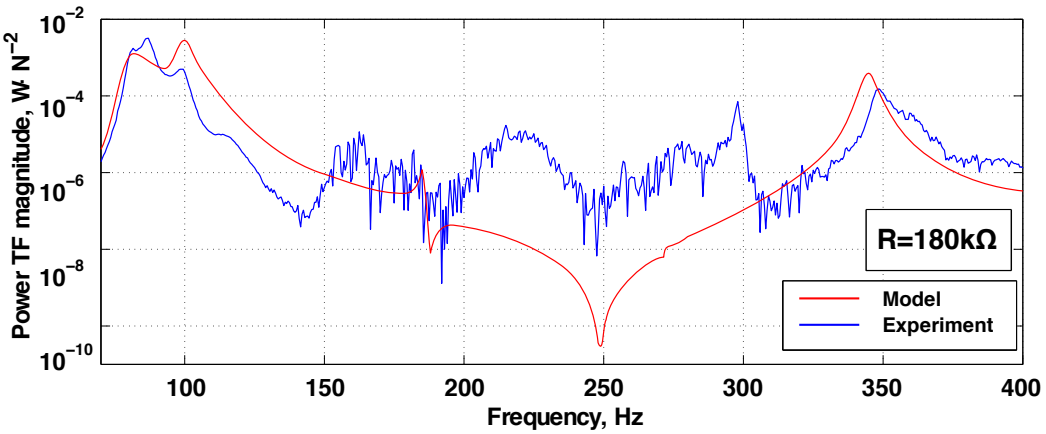

Figure 2.42: Comparison of modeled and measured electrical power TF magnitude of the piezoelectric device. $R_1 = 180$ kΩ.

and the present continuously distributed device when excited at their respective natural frequencies. Being placed along several asymmetric node lines, the device does not significantly attenuate the asymmetric modes but the (3,1) mode at 350 Hz is attenuated by 10 dB due to the device being positioned on an anti-node of the mode.

Figure 2.42 plots a comparison of the measured and predicted electrical power TF for the device. Recall that the assumptions to include electromechanical effects for the piezoelectric devices limit accurate evaluation to when the device is primarily excited by uniform transverse excitation. Thus, given the device placement on the panel, the (1,1) and (3,1) modes both represent excitation conditions under which the device would experience uniform input vibration. In Fig. 2.42 the measured electrical signal around the (1,1) mode at 97.5 Hz and (3,1) mode at 350 Hz show clear electrical response, which the model is in fair agreement with.

When the device is excited by asymmetric panel modes, approximately from 125–325 Hz, the measured response is mostly electrical noise. In contrast, the model predicts a precipitous drop in power TF over this range since it does not take into account the specific geometric intricacies of the corrugated spring. Nevertheless, the model is in fairly good agreement for predictions around the (1,1) and (3,1) modes, which are the main frequencies of interest since these best serve energy harvesting

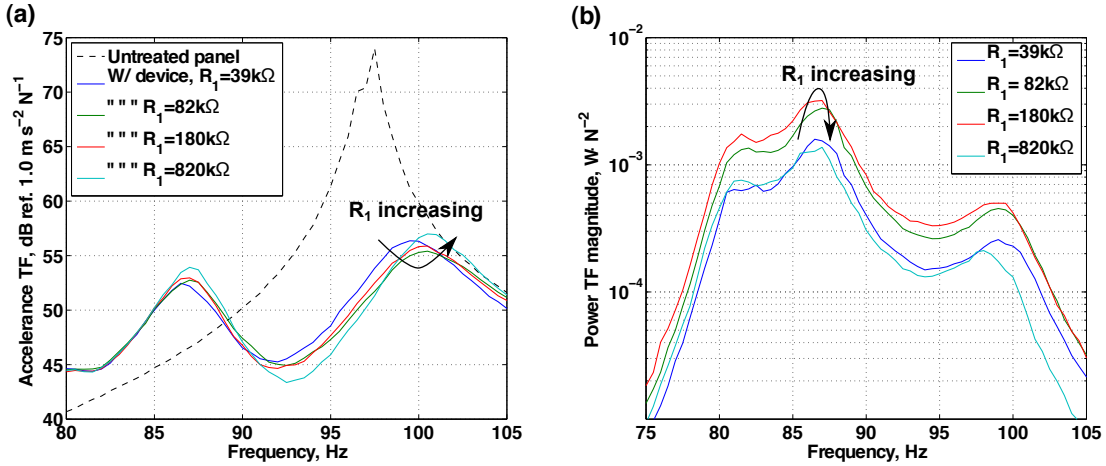

Figure 2.43: (a) Panel accelerance around (1,1) mode and (b) piezoelectric device power TF for a variety of resistances R_1.

objectives. At 86.5 Hz, the peak measured power TF is 3.3 mW·N^{-2}. The model underestimates this output level and predicts greatest electrical power to be produced at 100 Hz which was one of the split resonances.

Figure 2.43 (a) plots the measured panel response around the (1,1) mode for various values of load resistance, R_1. In contrast with the smaller piezoelectric devices used in shaker testing, a notable level of indirect shunt damping is observed for the present larger piezoelectric device. A load resistance of $R_1 = 82$ kΩ further attenuates the 100 Hz split resonance by 2 dB as compared with $R_1 = 820$ kΩ, or effectively open circuit conditions. This corroborates the prediction at the beginning of this section regarding the influence of larger spans of piezoelectric film within the spring layer in light of the governing equations. This is also a remarkable influence induced by the deforming piezoelectric spring layer if one recalls the whole device is just an additional 1% of added mass to the simply-supported panel. Finally, as had been predicted in Section 2.2.2.6, the indirect piezoelectric stiffening and damping is observed, particularly for the split resonance around 100 Hz. For smaller R_1, the piezoelectric spring is softer and the split resonance occurs at 99 Hz; as R_1 increases, the spring is stiffened to such a degree that the split resonance shifts up to 101 Hz.

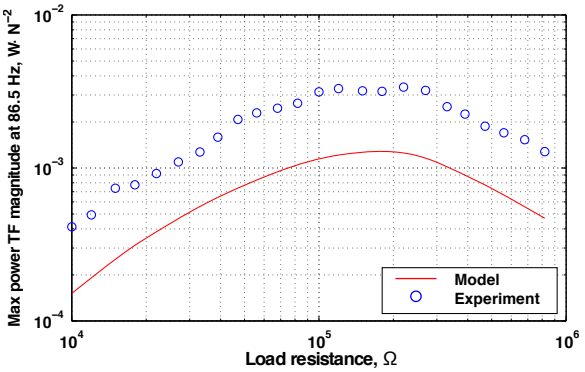

Figure 2.44: Comparison of modeled and measured electrical power TF magnitude of the piezoelectric device at 86.5 Hz for various R_1.

Figure 2.43 (b) plots the change in power TF as R_1 is modified. Peak electrical power is observed in the range of $R_1 \approx 150$ kΩ. This selection of R_1 to maximize energy harvesting objectives is not significantly different than that which optimizes vibration suppression potential. However, the additional 2 dB of suppression of the 100 Hz split resonance is negligible compared to the greater 20 dB attenuation reactively induced by the whole device. The important observation is that there exists a substantial potential for energy harvesting from vibration sources which may be simultaneously attenuated.

Figure 2.44 plots the power TF at 86.5 Hz for various R_1. Since the model predicted the peak electrical power output at 100 Hz instead of 86.5 Hz, the predictions are uniformly less than those measured. However, the trend is identical between measurements and predictions, including the location of the optimum load resistance. Many of the most successful piezoceramic energy harvester prototypes in the literature yield power outputs of this magnitude [85, 90], and it is notable that the present device, using piezoelectric film which is much less electromechanically coupled and less expensive, can achieve similar results.

2.2.4 Concluding remarks

The present energy harvesting literature widely assumes that the harvesters are maximally productive when excited at their tuned natural frequency. This assumption is based on the great majority of energy harvesting applications in which the devices have negligible dynamic influence. Only the effects of resistive shunt damping which results from piezoelectric energy harvesting has been exploited for simultaneous vibration control and energy harvesting. However, by including electromechanical coupling into the generalized analytical model of Section 2.1, it was found that maximum harvested energy could be extracted when the harvesters exert a finite dynamic influence on the host structure which excites them. In this scenario, the harvesters are analogous to electromechanical vibration absorbers which, dependent on their mass relative to the host structure, shift the frequencies of the structural vibration away from the untreated resonance. Thus, it was found that such harvesters could generate greater amplitudes of electrical power when excited off-resonance.

In modeling and measurements, a secondary benefit was observed: the electromechanically stiffened and or damped harvesters could suppress the vibration of the host structure by acting in a manner identical to the classical tuned-mass-damper. Given that much energy harvesting research has been encouraged via structural health monitoring concerns, the suppression of the structural vibration is inherently advantageous. This suggests that the flexibility of resonant structures need not necessarily be a concern but may in fact be exploited for the control of the structure as well as for the generation of useful electric power. Thus, mechanically undamped energy harvesting vibration absorbers meet both objectives by converting the absorbed energy into electrical power the process of which results in a substantial mechanical damping effect to attenuate the structural vibrations.

CHAPTER 3
Summary and Conclusions

The suppression of structural vibration by adding a minimal amount of mass to the system was a key target of this work. By employing electromechanically coupled devices as the vibration control treatments, it was found that energy harvesting objectives may simultaneously be achieved while attenuating the host vibration. With proper design, the two fields of study were bound together in the employment of a single device: an energy harvesting vibration absorber.

A semi-analytical model, based on the generalized Hamilton's principle, was used throughout this work to determine the forced or free response of a system of coupled plates or point mass-spring systems. The versatility and computational efficiency of this model was a significant factor in its development and prolific use. Though the derivation of this model is general and applicable to other studies in the literature, its employment to evaluate the resulting dynamics of continuously distributed vibration absorbers or energy harvesting devices on excited panels was absent from the larger body of related research.

In the design of passive vibration control treatments, the use of continuously distributed spring layers exhibiting both transverse compressibility and high in-plane stiffnesses yields a device capable of resisting structural vibration as well as exhibiting a SDOF natural frequency in conjunction with a distributed mass layer. Such a design uniquely combines the low frequency attenuation benefits of mass-spring systems as well as the higher frequency attenuation capability of traditional constraining treatments. This effect was discovered in the performed analysis and was thereafter validated by experiment with a novel embodiment of such a device employing a circularly corrugated distributed spring layer. To include this form of distributed spring layer into the analytical model, an elastic superposition principle was employed and

was found to provide an accurate representation of both the constraining capabilities and the reactive dynamics of the full vibration control device.

Other features unique to continuously distributed treatments were considered, having yet been neglected in existing research studies. Given the planar span of the distributed top mass, the oscillating mass is capable of exhibiting modal dynamics and this was found to be more useful in passively suppressing the structural vibration than when the mass oscillated in translation. A spring layer having a variable transverse stiffness along the length, in tandem with a softer top mass material, was predicted to provide a broad range of SDOF natural frequencies. The variable stiffness spring was one such feature included in a device designed for the attenuation of a realistic, vibrating ship hull and was observed to be a prime influence in the broadband, reactive vibration attenuation the device produced. Despite being a simple extension of both resistive and reactive vibration control devices, the present combination of these two dynamic systems into one device had not been investigated in prior literature. The resulting invention was a comparatively lightweight device capable of broadband passive vibration control with particular benefit at low frequencies due to the classical vibration absorber effects it produced.

A large proportion of literature in energy harvesting focuses on the vibration control effect achieved via shunt damping that results naturally by the coupling to the external circuit via the electromechanical device. However, as compared to the mechanical authority that a vibration absorber exerts on the host structure, as in the first portion of this research, the shunt damping effect provides negligible attenuation of vibration. To study the potential for energy harvesting vibration absorbers, the modeling formulation used in the first portion of this research was adapted to include electromechanical coupling effects introduced by piezoelectric or electromagnetic materials and external harvesting circuitry. Thus, rather than observing the effects of electromechanical coupling on the harvesters themselves, this new analysis took a broader perspective and considered how the harvesters affected the dynamics of the

structure which originally excited them. A fundamental model of electromagnetic oscillators on an excited, simply-supported panel discovered some features which, to date, have gone unnoticed in energy harvesting literature:

- An optimum mass ratio of the harvester devices exists to yield greatest electrical power output which is not $\mu \to 0$, indicating maximum energy harvesting potential is realized when the harvester devices are capable of dynamically influencing the greater host structure.
- A number of applied devices to the vibrating panel may be computed which, for a given μ, maximizes energy harvesting potential.
- The selection of μ, external circuit load resistance and number of devices to maximize energy harvesting performance is found to occur very closely to those parameters which most attenuate the structural vibration of the panel to which the devices were attached.

Therefore, as harvester devices become more inertially substantial relative to their attached vibrating structures, they inevitably influence the dynamics of the system. Importantly, however, this dynamic influence is not observed to reduce the potential of the harvester to generate electrical power. The opposite is in fact discovered: finite influence of the devices on the host structure is found to nearly simultaneously maximize energy harvesting and vibration suppression goals. While the electrical output around the harvester resonance may be damped due to electromechanical coupling effects, it is found that the maximum achievable power output is greatest when the applied device is capable of dynamically influencing the host structure.

The study was extended to continuously distributed harvester devices designed with corrugated piezoelectric spring layers, an extension from the design cues from the first portion of the research. As continuously distributed devices, fewer such samples would be required in an application to passively attenuate broadband structural vibrations while in turn acting as energy harvesting devices. Indirect observation of

piezoelectric stiffening and shunt damping effects of the external harvester circuit was made by assessing the dynamic influence of the device on the host vibrating structure. It was predicted that very lightweight devices may have substantial vibration attenuation capability and, properly designed, could thereafter yield significant electrical power output.

Several such devices were carefully manufactured in the laboratory and tested to validate the models. The circular corrugations of the piezoelectric film spring are strained in bending when the device resonates at the designed SDOF natural frequency, yielding great electrical potentials across the piezoelectric electrodes. Using a spring layer design that produces high levels of strain compensates for the low electromechanical coupling of the PVDF film, which is amongst the more economical piezoelectric materials available. Despite inducing high levels of bending strain in the corrugated film as the device oscillated at its transverse SDOF resonance, measurements showed a linear electrical response as measured across the harvester load resistance. This validated the modeling assumptions to incorporate the corrugated piezoelectric spring layer as an equivalent continuous layer.

When applied to a large vibrating panel, one such distributed piezoelectric device was observed to significantly attenuate the low frequency structural vibration to which it was tuned. However, the device constituted just a 1% addition of mass to the panel. The amplitude of the measured and modeled attenuation of the panel vibration was consistent with results observed in the prior electromagnetic oscillator analysis, indicating the dynamic similarity of the continuously distributed device with point oscillators around their respective SDOF natural frequencies. Since the resulting split resonances induced by the distributed piezoelectric device were not notably shifted from the original panel resonance, the harvester device was still vibrating at frequencies close to its own SDOF resonance. Therefore, a high amplitude power output was observed at the same time the device was substantially suppressing the structural vibration.

To date, energy harvesting literature has presumed the dynamic influence of harvester devices on the host vibrating system to be negligible. However, the studies and experiments of this research conclusively show that not only are more inertially substantial devices the best choice for energy harvesting, when designed as a tuned-mass-damper the increased dynamic influence of the harvester is inherently beneficial to reduce the vibration of the host structure. Since energy harvesting research has been widely promoted for structural health monitoring purposes, this discovery is significant since the attenuation of the structural vibration intrinsically improves the health of the system. Thus, concurrent attenuation of and energy harvesting not only go hand-in-hand but in certain situations appear to be mutually optimized using the same set of design parameters. The results of this work show that substantially greater dissipation of the structural vibrations may be achieved than present shunt damping methods when the harvesters are designed like electromechanical vibration absorbers.

While present energy harvesting literature has rigorously evaluated the electromechanical effects induced upon the harvesters themselves, this research took a step back to observe the effects that the harvesting devices have on the greater dynamic structure. In doing so, new possibilities for the simultaneous suppression of structural vibration and energy harvesting were discovered. Lightweight, flexible and resonant systems—aircraft or structural panels and space-truss, for example—need not be as "over-engineered" in design. The systems could be exploited for their resonant behavior to generate useful electric power, the process of which suppresses the level of vibration to a more sustainable level.

This suggests the continued exploration of these results. Several opportunities may be proposed:

1. The design of distributed piezoelectric spring layers is pivotal to the extraction of high electrical potentials and additional embodiments should be pursued. Given the low cost of PVDF films relative to other piezoelectric materials, designing

the distributed springs to be highly strained allows the implementation of films at reduced manufacturing expense. This research provided one embodiment of such an economical spring design for energy harvesting purposes but other forms and designs may easily be developed other the course of further studies.

2. Most structural vibration is due to the lowest order modes of the system. Thus, point E–M oscillators should be considered further, particularly with experimentation given their ease of construction. Though continuously distributed devices are best for broadband vibration attenuation, given the primary focus on structural vibrations up to a few hundred Hz, point E–M oscillators can provide much of the same low frequency attenuation performance and consequent energy harvesting potential.

3. Energy harvesting efficiency has been studied in the literature with numerous attempts to define a consistent metric of performance [27, 91, 92]. What has not been considered is an expression for the maximum extractable energy from a vibrating system which is dynamically influenced by the attached harvester devices. This latter case encompasses the broader picture: how much mechanical energy is convertible into electrical power from any given vibrating system?

The third opportunity above is admittedly encouraged by McCoy [93]. Citing an educated estimate of the vast latent energy encompassed in the Gulf Stream on a given day (solar input, waste energy from ship transport, heat capacity of the water, etc.), the author observes that there are numerous neglected energy sources all around us. The greatest inhibitor to taking advantage of ambient energy is the means by which to efficiently convert it from its natural form to electricity. By defining a metric of efficiency for vibrational energy harvesting, sources may be recognized for their electromechanical conversion prospects and thereafter targeted according to the opportunity available.

The driving need for sustainable energy solutions from state, federal and inter-

national bodies encourages innovative solutions. While vibrational energy harvesting has yet been focused on supplying small portable electronics a source of wireless power, the lack of investigation to determine just how much vibrational energy is extractable and convertible to electrical power from a given structure suggests that there is much to learn. Solar power was once the hobby-level distraction of a few tinkerers until industry pushed the envelope on material development and drove down the cost for large-scale solar power plants. This is the state of vibrational energy harvesting: a research novelty with the potential to tip the scale into a much greater opportunity.

APPENDIX A

Modeling formulation by Hamilton's principle

This section provides a more descriptive presentation of the variational energy method used to model a number of systems throughout this work, namely the continuously distributed vibration absorber devices which may simultaneously be employed as energy harvesting systems. The fundamentals of variational calculus are necessary for the reader. From Hamilton's principle may be derived the governing equations of mechanical motion and electrical response for arbitrary electro-mechanical systems. Though this method also may be employed for electromagnetic systems, the present analysis is used for piezoelectric materials. Later work employs the direct approach of Lagrange's equations of motion for electromagnetics. For further reading on these topics, the reader is referred to a number of detailed and helpful texts [60, 94, 95].

A.1 System composition and geometry

The present system of interest is an arbitrary elastic body partially composed of piezoelectric materials, shown in Figure A.1. The non-piezoelectric, or structural, volume of the domain is denoted as Ω_b while the remaining piezoelectric portion is Ω_p. The boundary of the structural surface is denoted as Γ_b. It is assumed that material composition of the structure and of the piezoelectric are distinct.

An arbitrary number of external point forces and point charges are applied on the surface of the system. Electrodes are assumed to cover a portion of the piezoelectric domain surface through which the external charges may either be applied, measured or grounded.

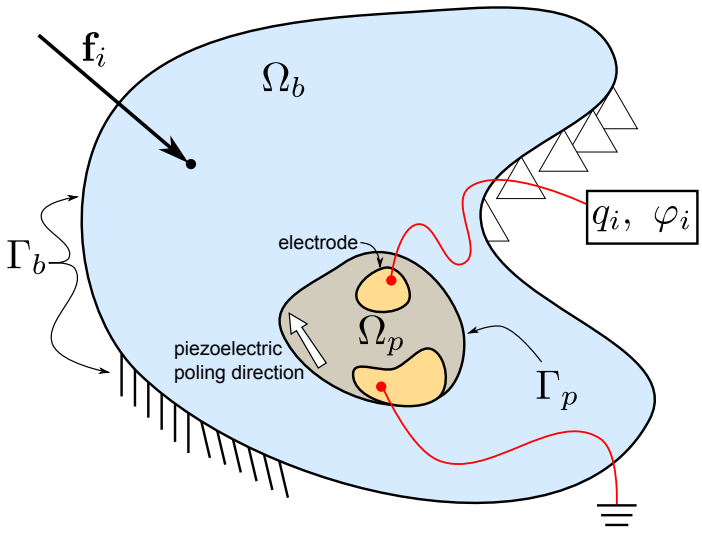

Figure A.1: Arbitrarily bounded and excited electro-elastic body having piezoelectric inclusions.

A.2 Hamilton's principle

The governing equations of motion of the coupled system are determined by employing the generalized Hamilton's principle. A variational approach with the Ritz method is then used to solve the subsequent systems of equations.

For deformable, elastic, electro-mechanical systems, Hamilton's principle may be expressed as

$$\int_{t_1}^{t_2} \left[\delta\left(T - U - U_e + W_e\right) + \delta\overline{W}\right] \mathrm{d}t = 0 \tag{A.1}$$

where δ is the variational operator; T is the total kinetic energy; U is the total potential energy; U_e is the potential energy associated with specific boundary conditons; W_e is the total electrical energy; and $\overline{W}$ is the total contribution of mechanically applied and electrically induced forces and charges, respectively.

These quantities are specified as follows:

$$T = \frac{1}{2}\int_{\Omega_b} \dot{\mathbf{u}}^t \rho_b \dot{\mathbf{u}} \mathrm{d}\Omega_b + \frac{1}{2}\int_{\Omega_p} \dot{\mathbf{u}}^t \rho_p \dot{\mathbf{u}} \mathrm{d}\Omega_p \tag{A.2}$$

$$U = \frac{1}{2}\int_{\Omega_b} \mathbf{S}^t \mathbf{T} \mathrm{d}\Omega_b + \frac{1}{2}\int_{\Omega_p} \mathbf{S}^t \mathbf{T} \mathrm{d}\Omega_p \tag{A.3}$$

$$U_e = \frac{1}{2}\int_{\Gamma_b} \mathbf{u_e^t k_e u_e} \mathrm{d}\Gamma_b \tag{A.4}$$

$$W_e = \frac{1}{2}\int_{\Omega_p} \mathbf{E}^t \mathbf{D} \mathrm{d}\Omega_p \tag{A.5}$$

$$\delta\overline{W} = \sum_{i=1}^{N_f} \delta\mathbf{u}\left(\mathbf{x}_i\right)\mathbf{f}_i - \sum_{j=1}^{N_q} \delta\varphi_j\left(\mathbf{x}_j\right) q_j \tag{A.6}$$

where the following are defined

- $\mathbf{D}$, electrical displacements;
- $\mathbf{E}$, electrical field;
- f_i, i^{th} point force;
- $\mathbf{k_e}$, boundary stiffness matrix;
- N_f, number of applied point forces;
- N_q, number of applied electrical charges;
- q_j, charge on the j^{th} electrode;
- $\mathbf{S}$, strain tensor;
- $\mathbf{T}$, stress tensor;
- $\mathbf{u}$, vector of mechanical displacements;
- $\mathbf{u_e}$, vector of mechanical translational and rotational displacements at the boundaries;
- $\mathbf{x}_i$, co-ordinates of the i^{th} point force;
- $\mathbf{x}_j$, co-ordinates of the j^{th} charge;

- ρ_b, mass density of structural domain;
- ρ_p, mass density of piezoelectric domain;
- φ_j, electrical potential on the j^{th} electrode;
- $(\ )^t$, matrix transpose operator;
- $\dot{(\ )}$, time derivative.

The vector of mechanical displacements is expanded in terms for three-dimensional, Cartesian geometries

$$\mathbf{u}(\mathbf{x},t) = \begin{bmatrix} u_1(x,y,z,t) \\ u_2(x,y,z,t) \\ u_3(x,y,z,t) \end{bmatrix} \tag{A.7}$$

The components of the electrical displacements, electrical field, strain tensor and stress tensor are expressed in the following convention [43]

$$\mathbf{D} = \begin{bmatrix} D_1 \\ D_2 \\ D_3 \end{bmatrix}, \quad \mathbf{E} = \begin{bmatrix} E_1 \\ E_2 \\ E_3 \end{bmatrix}, \quad \mathbf{S} = \begin{bmatrix} S_{11} \\ S_{22} \\ S_{33} \\ 2S_{23} \\ 2S_{13} \\ 2S_{12} \end{bmatrix}, \quad \mathbf{T} = \begin{bmatrix} T_{11} \\ T_{22} \\ T_{33} \\ T_{23} \\ T_{13} \\ T_{12} \end{bmatrix} = \begin{bmatrix} T_1 \\ T_2 \\ T_3 \\ T_4 \\ T_5 \\ T_6 \end{bmatrix} \tag{A.8}$$

The mechanical boundary conditions may be more closely approximated from the classical conditions—simple supports, clamped edges, free suspension—by means of translational and rotational springs along the domain edges. The vector of translation

and rotational displacements is given to be

$$\mathbf{u_e}(\mathbf{x},t) = \begin{bmatrix} u_1(x,y,z,t) \\ u_2(x,y,z,t) \\ u_3(x,y,z,t) \\ \theta_1(x,y,z,t) \\ \theta_2(x,y,z,t) \\ \theta_3(x,y,z,t) \end{bmatrix} \qquad \mathbf{x} \in \Gamma_b \tag{A.9}$$

Therefore, the boundary stiffness matrix is composed as

$$\mathbf{k_e} = \begin{bmatrix} k_{t1} & 0 & 0 & 0 & 0 & 0 \\ 0 & k_{t2} & 0 & 0 & 0 & 0 \\ 0 & 0 & k_{t3} & 0 & 0 & 0 \\ 0 & 0 & 0 & k_{r1} & 0 & 0 \\ 0 & 0 & 0 & 0 & k_{r2} & 0 \\ 0 & 0 & 0 & 0 & 0 & k_{r3} \end{bmatrix} \tag{A.10}$$

To solve for the electrical and structural response of the system, the components of Equations A.2–A.6 must be expressed in terms of the mechanical displacements and electrical potentials. Relating the components of Equation A.8 to these parameters requires the use of constitutive relations of continuum mechanics.

A.3 Constitutive relations

The structural stress-strain relations are expanded by Hooke's Law:

$$\mathbf{T} = \mathbf{c}_b\mathbf{S} \tag{A.11}$$

where $\mathbf{c}_b$ represents the stiffness matrix for the structure. The most general case of materials considered in this work are orthotropic, in which case the stiffness matrix is expanded into a 6×6 matrix of 9 unique components dependent on the material

properties:

$$\mathbf{c}_b = \begin{bmatrix} c_{11} & c_{12} & c_{13} & 0 & 0 & 0 \\ c_{21} & c_{22} & c_{23} & 0 & 0 & 0 \\ c_{31} & c_{32} & c_{33} & 0 & 0 & 0 \\ 0 & 0 & 0 & c_{44} & 0 & 0 \\ 0 & 0 & 0 & 0 & c_{55} & 0 \\ 0 & 0 & 0 & 0 & 0 & c_{66} \end{bmatrix} \tag{A.12}$$

where $c_{ij} = c_{ji}$.

For piezoelectric materials, the stress-strain relations are coupled to field-displacement relations:

$$\begin{bmatrix} \mathbf{T} \\ \mathbf{D} \end{bmatrix} = \begin{bmatrix} \mathbf{c}^E & -\mathbf{e}^t \\ \mathbf{e} & \epsilon^S \end{bmatrix} \begin{bmatrix} \mathbf{S} \\ \mathbf{E} \end{bmatrix} \tag{A.13}$$

where $\mathbf{c}^E$ is the stiffness matrix of the piezoelectric material evaluated at constant electrical field; $\mathbf{e}$ are the piezoelectric constants coupling applied stress to the electrical field; and ϵ^S is the dielectric constant matrix evaluated at constant strain. Further expansion of these latter terms shows that

$$\mathbf{e} = \mathbf{d}\mathbf{c}^E \tag{A.14}$$

$$\epsilon = \epsilon^0 - \mathbf{d}\mathbf{c}^E\mathbf{d}^t \tag{A.15}$$

$$\epsilon^0 = \begin{bmatrix} \varepsilon_{11}^0 & 0 & 0 \\ 0 & \varepsilon_{22}^0 & 0 \\ 0 & 0 & \varepsilon_{33}^0 \end{bmatrix} \tag{A.16}$$

$$\mathbf{d} = \begin{bmatrix} 0 & 0 & 0 & 0 & d_{15} & 0 \\ 0 & 0 & 0 & d_{15} & 0 & 0 \\ d_{31} & d_{32} & d_{33} & 0 & 0 & 0 \end{bmatrix} \tag{A.17}$$

The electrical field-potential relation is

$$\mathbf{E} = \mathbf{L}_\varphi \varphi(\mathbf{x}) = -\Delta\varphi(\mathbf{x}) \tag{A.18}$$

When the electrical field is applied along the poling direction, z-axis, the relation simplifies to

$$\mathbf{E} = \begin{bmatrix} 0 & 0 & -\frac{\partial \varphi}{\partial z} \end{bmatrix}, \quad \mathbf{L}_\varphi = \begin{bmatrix} 0 & 0 & \frac{\partial}{\partial z} \end{bmatrix} \tag{A.19}$$

The strain-displacement relation is expressed as

$$\mathbf{S} = \mathbf{L}_\mathbf{u}\mathbf{u} \tag{A.20}$$

where $\mathbf{L}_\mathbf{u}$ is the linear operator for the specific elasticity problem of interest. In the remainder of the appendices, operators for elasticity problems considering isotropic and orthotropic structural characteristics will be utilized. Thus, for particular assumptions made regarding the constituency of the material under study, specific relations to relate strain to the displacement field are required. Likewise, for the mechanical translational and rotational displacements on the boundaries, $\mathbf{L}_\mathbf{e}$ is the corresponding differential operator such that

$$\mathbf{u}_\mathbf{e} = \mathbf{L}_\mathbf{e}\mathbf{u} \tag{A.21}$$

The total potential energy is then expressed by substitution of Equations A.11, A.13, A.18 and A.20 into Equation A.3.

$$U = \frac{1}{2}\int_{\Omega_b} \mathbf{u}^t \mathbf{L}_\mathbf{u}^t \mathbf{c}_b \mathbf{L}_\mathbf{u}\mathbf{u} \mathrm{d}\Omega_b - \frac{1}{2}\int_{\Omega_b} \mathbf{u}^t \mathbf{L}_\mathbf{u}^t \mathbf{e}^t \mathbf{L}_\varphi \varphi \mathrm{d}\Omega_p + \frac{1}{2}\int_{\Omega_p} \mathbf{u}^t \mathbf{L}_\mathbf{u}^t \mathbf{c}^E \mathbf{L}_\mathbf{u}\mathbf{u} \mathrm{d}\Omega_p \tag{A.22}$$

The external potential energy is given by

$$U_e = \frac{1}{2}\int_{\Gamma_b} \mathbf{u}^t \mathbf{L}_\mathbf{e}^t \mathbf{k}_\mathbf{e} \mathbf{L}_\mathbf{e}\mathbf{u} \mathrm{d}\Gamma_b \tag{A.23}$$

Substitution of Equations A.13 A.18 and A.20 into Equation A.5 yield a new description of the electrical energy

$$W_e = \frac{1}{2}\int_{\Omega_p} \varphi \mathbf{L}_\varphi^t \epsilon^S \mathbf{L}_\varphi \varphi \mathrm{d}\Omega_p + \frac{1}{2}\int_{\Omega_p} \varphi \mathbf{L}_\varphi^t \mathbf{e} \mathbf{L}_\mathbf{u}\mathbf{u} \mathrm{d}\Omega_p \tag{A.24}$$

Finally, substituting Equations A.22 and A.24 into Hamilton's principle, Equa-

tion A.1, and applying the variational operator over the components yields

$$\begin{aligned}
&\int_{t_1}^{t_2} \Bigg\{ \int_{\Omega_b} \delta\dot{\mathbf{u}}^t \rho_b \dot{\mathbf{u}} \mathrm{d}\Omega_b + \int_{\Omega_p} \delta\dot{\mathbf{u}}^t \rho_p \dot{\mathbf{u}} \mathrm{d}\Omega_p \\
&- \int_{\Omega_b} \delta\mathbf{u}^t \mathbf{L}_\mathbf{u}^t \mathbf{c}_b \mathbf{L}_\mathbf{u} \mathbf{u} \mathrm{d}\Omega_b - \int_{\Omega_p} \delta\mathbf{u}^t \mathbf{L}_\mathbf{u}^t \mathbf{c}^E \mathbf{L}_\mathbf{u} \mathbf{u} \mathrm{d}\Omega_p \\
&+ \int_{\Omega_p} \delta\mathbf{u}^t \mathbf{L}_\mathbf{u}^t \mathbf{e}^t \mathbf{L}_\varphi \varphi \mathrm{d}\Omega_p + \int_{\Omega_p} \delta\varphi \mathbf{L}_\varphi^t \mathbf{e} \mathbf{L}_\mathbf{u} \mathbf{u} \mathrm{d}\Omega_p \\
&+ \int_{\Omega_p} \delta\varphi \mathbf{L}_\varphi^t \epsilon^S \mathbf{L}_\varphi \varphi \mathrm{D}\Omega_p - \int_{\Gamma_b} \delta\mathbf{u}^t \mathbf{L}_\mathbf{e}^t \mathbf{k}_\mathbf{e} \mathbf{L}_\mathbf{e} \mathbf{u} \mathrm{d}\Gamma_b \\
&+ \sum_{i=1}^{N_f} \delta\mathbf{u}\left(\mathbf{x}_i\right) \mathbf{f}_i - \sum_{j=1}^{N_q} \delta\varphi_j\left(\mathbf{x}_j\right) q_j \Bigg\} \mathrm{d}t = 0
\end{aligned} \tag{A.25}$$

One simplification may be made to Equation A.25, namely the integration by parts of the first two terms, noting that

$$\delta\mathbf{u}\left(t_1\right) = 0, \quad \delta\mathbf{u}\left(t_2\right) = 0 \tag{A.26}$$

since the displacements at initial and final times are known. Thus, the first two terms become,

$$\begin{aligned}
&\int_{t_1}^{t_2} \left\{ \int_{\Omega_b} \delta\dot{\mathbf{u}}^t \rho_b \dot{\mathbf{u}} \mathrm{d}\Omega_b + \int_{\Omega_p} \delta\dot{\mathbf{u}}^t \rho_p \dot{\mathbf{u}} \mathrm{d}\Omega_p \right\} \mathrm{d}t = \\
&- \int_{t_1}^{t_2} \left\{ \int_{\Omega_b} \delta\mathbf{u}^t \rho_b \ddot{\mathbf{u}} \mathrm{d}\Omega_b + \int_{\Omega_p} \delta\mathbf{u}^t \rho_p \ddot{\mathbf{u}} \mathrm{d}\Omega_p \right\} \mathrm{d}t
\end{aligned} \tag{A.27}$$

For the electromechanical system, the only unknowns remaining are the mechanical displacements and the electrical potentials. The other elements of Equation A.25 are material properties, descriptions of known applied forces and/or charges and mathematical operators. To determine an approximate solution to these governing equations, the Ritz method is employed.

A.4 Ritz method

The Ritz method, or Rayleigh–Ritz method, approximates an unknown function by means of expressing it in terms of a linear combination of generalized co-ordinates and admissible trial functions. The trial functions must be linearly independent, satisfy

essential boundary conditions, form a complete set and be differentiable up to the order of linear operators $\mathbf{L_u}$ and $\mathbf{L}_\varphi$.

For the mechanical displacements and electrical potentials of interest, this approximation is written

$$\mathbf{u}\left(\mathbf{x},t\right) \approx \Psi_{\mathbf{a}}\left(\mathbf{x}\right)\mathbf{a}\left(t\right) = \left[\begin{array}{ccccccc} \psi_a^1\left(\mathbf{x}\right) & \cdots & \psi_a^i\left(\mathbf{x}\right) & \cdots & \psi_a^{N_a}\left(\mathbf{x}\right) \end{array}\right] \left[\begin{array}{c} a_1(t) \\ \vdots \\ a_i(t) \\ \vdots \\ a_{N_a}(t) \end{array}\right] \tag{A.28}$$

$$\varphi\left(\mathbf{x},t\right) \approx \Psi_{\mathbf{v}}\left(\mathbf{x}\right)\mathbf{v}\left(t\right) = \left[\begin{array}{ccccccc} \psi_v^1\left(\mathbf{x}\right) & \cdots & \psi_v^j\left(\mathbf{x}\right) & \cdots & \psi_v^{N_v}\left(\mathbf{x}\right) \end{array}\right] \left[\begin{array}{c} v_1(t) \\ \vdots \\ v_j(t) \\ \vdots \\ v_{N_v}(t) \end{array}\right] \tag{A.29}$$

where $a_i(t)$ is the i^{th} of N_a mechanical generalized co-ordinate and $v_j(t)$ is the j^{th} of N_v electrical generalized co-ordinate. The trial function matrix $\Psi_{\mathbf{a}}$ is noted to be of dimension $3\times N_a$, due to the three unknown mechanical displacements per each mechanical generalized co-ordinate. It is the convention to assume one electrical potential per electrical generalized co-ordinate (electrode) and, as such, $\Psi_{\mathbf{v}}$ is a $1\times N_v$ matrix.

Substituting the assumed solutions of Equations A.28 and A.29 into Equation A.25

gives

$$\int_{t_1}^{t_2}\Bigg\{-\int_{\Omega_b}\delta\mathbf{a}^t\Psi_{\mathbf{a}}^t\rho_b\Psi_{\mathbf{a}}\ddot{\mathbf{a}}\mathrm{d}\Omega_b-\int_{\Omega_p}\delta\mathbf{a}^t\Psi_{\mathbf{a}}^t\rho_p\Psi_{\mathbf{a}}\ddot{\mathbf{a}}\mathrm{d}\Omega_p$$
$$-\int_{\Omega_b}\delta\mathbf{a}^t\left(\mathbf{L}_{\mathbf{u}}\Psi_{\mathbf{a}}\right)^t\mathbf{c}_b\mathbf{L}_{\mathbf{u}}\Psi_{\mathbf{a}}\mathbf{a}\mathrm{d}\Omega_b-\int_{\Omega_p}\delta\mathbf{a}^t\left(\mathbf{L}_{\mathbf{u}}\Psi_{\mathbf{a}}\right)^t\mathbf{c}^E\mathbf{L}_{\mathbf{u}}\Psi_{\mathbf{a}}\mathbf{a}\mathrm{d}\Omega_p$$
$$+\int_{\Omega_p}\delta\mathbf{a}^t\left(\mathbf{L}_{\mathbf{u}}\Psi_{\mathbf{a}}\right)^t\mathbf{e}^t\mathbf{L}_{\varphi}\Psi_{\mathbf{v}}\mathbf{v}\mathrm{d}\Omega_p+\int_{\Omega_p}\delta\mathbf{v}^t\left(\mathbf{L}_{\varphi}\Psi_{\mathbf{v}}\right)^t\mathbf{e}\mathbf{L}_{\mathbf{u}}\Psi_{\mathbf{a}}\mathbf{a}\mathrm{d}\Omega_p$$
$$+\int_{\Omega_p}\delta\mathbf{v}^t\left(\mathbf{L}_{\varphi}\Psi_{\mathbf{v}}\right)^t\epsilon^S\mathbf{L}_{\varphi}\Psi_{\mathbf{v}}\mathrm{d}\Omega_p-\int_{\Gamma_b}\delta\mathbf{a}^t\left(\mathbf{L}_{\mathbf{e}}\Psi_{\mathbf{a}}\right)^t\mathbf{k}_{\mathbf{e}}\mathbf{L}_{\mathbf{e}}\Psi_{\mathbf{a}}\mathbf{a}\mathrm{d}\Gamma_b$$
$$+\sum_{i=1}^{N_f}\delta\mathbf{a}^t\Psi_{\mathbf{a}}^t\left(\mathbf{x}_i\right)\mathbf{f}_i-\sum_{j=1}^{N_q}\delta\mathbf{v}^t\Psi_{\mathbf{v}}^t\left(\mathbf{x}_j\right)q_j\Bigg\}\mathrm{d}t=0 \tag{A.30}$$

The generalized co-ordinates are independent of space and may therefore be removed from the volumetric integrals. Collecting terms then provides

$$\int_{t_1}^{t_2}\Big\{-\delta\mathbf{a}^t\left[\left(\mathbf{M}_b+\mathbf{M}_p\right)\ddot{\mathbf{a}}+\left(\mathbf{C}_b+\mathbf{C}_p\right)\dot{\mathbf{a}}+\left(\mathbf{K}_b+\mathbf{K}_p+\mathbf{K}_e\right)\mathbf{a}-\Theta\mathbf{v}-\mathbf{B}_{\mathbf{f}}\mathbf{f}\right]$$
$$+\delta\mathbf{v}^t\left[\Theta^t\mathbf{a}+\mathbf{P}_p\mathbf{v}-\mathbf{B}_{\mathbf{q}}\mathbf{q}\right]\Big\}\mathrm{d}t=0 \tag{A.31}$$

where the conventional matrices in Equation A.31 are determined by

$$\mathbf{M}_b=\int_{\Omega_b}\Psi_{\mathbf{a}}^t\left(\mathbf{x}\right)\rho_b\Psi_{\mathbf{a}}\left(\mathbf{x}\right)\mathrm{d}\Omega_b \tag{A.32}$$

$$\mathbf{M}_p=\int_{\Omega_p}\Psi_{\mathbf{a}}^t\left(\mathbf{x}\right)\rho_p\Psi_{\mathbf{a}}\left(\mathbf{x}\right)\mathrm{d}\Omega_p \tag{A.33}$$

$$\mathbf{K}_b=\int_{\Omega_b}\left[\mathbf{L}_{\mathbf{u}}\Psi_{\mathbf{a}}\left(\mathbf{x}\right)\right]^t\mathbf{c}_b\mathbf{L}_{\mathbf{u}}\Psi_{\mathbf{a}}\left(\mathbf{x}\right)\mathrm{d}\Omega_b \tag{A.34}$$

$$\mathbf{K}_p=\int_{\Omega_p}\left[\mathbf{L}_{\mathbf{u}}\Psi_{\mathbf{a}}\left(\mathbf{x}\right)\right]^t\mathbf{c}^E\mathbf{L}_{\mathbf{u}}\Psi_{\mathbf{a}}\left(\mathbf{x}\right)\mathrm{d}\Omega_p \tag{A.35}$$

$$\mathbf{K}_e=\int_{\Gamma_b}\left(\mathbf{L}_{\mathbf{e}}\Psi_{\mathbf{a}}\right)^t\mathbf{k}_{\mathbf{e}}\mathbf{L}_{\mathbf{e}}\Psi_{\mathbf{a}}\mathrm{d}\Gamma_b \tag{A.36}$$

$$\mathbf{C}_b=\alpha_b\mathbf{M}_b+\beta_b\mathbf{K}_b \tag{A.37}$$

$$\mathbf{C}_p = \alpha_p \mathbf{M}_p + \beta_p \mathbf{K}_p \tag{A.38}$$

$$\mathbf{P}_p = \int_{\Omega_p} \left[\mathbf{L}_\varphi \Psi_\mathbf{v}(\mathbf{x})\right]^t \epsilon^S \mathbf{L}_\varphi \Psi_\mathbf{v}(\mathbf{x}) \, \mathrm{d}\Omega_p \tag{A.39}$$

$$\Theta = \int_{\Omega_p} \left[\mathbf{L}_\mathbf{u} \Psi_\mathbf{a}(\mathbf{x})\right]^t \mathbf{e}^t \mathbf{L}_\varphi \Psi_\mathbf{v}(\mathbf{x}) \, \mathrm{d}\Omega_p \tag{A.40}$$

$$\mathbf{B_f} = \left[\begin{array}{ccc} \Phi^t_\mathbf{a}(\mathbf{x}_{f_1}) & \cdots & \Phi^t_\mathbf{a}\left(\mathbf{x}_{f_{N_f}}\right) \end{array} \right] \tag{A.41}$$

$$\mathbf{B_q} = \left[\begin{array}{ccc} \Phi^t_\mathbf{v}(\mathbf{x}_{q_1}) & \cdots & \Phi^t_\mathbf{v}\left(\mathbf{x}_{q_{N_q}}\right) \end{array} \right] \tag{A.42}$$

where the damping matrices, $\mathbf{C}_b$ and $\mathbf{C}_p$, are proportional to the mass and stiffness matrices by constants α and β (Rayleigh damping).

Since Equation A.31 must hold for arbitrary variations of the generalized coordinates, $\delta\mathbf{a}$ and $\delta\mathbf{v}$, a system of coupled equation is created:

$$\left(\mathbf{M}_b + \mathbf{M}_p\right)\ddot{\mathbf{a}} + \left(\mathbf{C}_b + \mathbf{C}_p\right)\dot{\mathbf{a}} + \left(\mathbf{K}_b + \mathbf{K}_p + \mathbf{K}_e\right)\mathbf{a} - \Theta\mathbf{v} = \mathbf{B_f f} \tag{A.43}$$

$$\Theta^t \mathbf{a} + \mathbf{P}_p \mathbf{v} = \mathbf{B_q q} \tag{A.44}$$

When the piezoelectric domains of the system are used either as sensors or as energy harvesting systems, no charges are applied to the electrodes and the right-hand side of Equation A.44 is set to zero. The systems of equations must be solved for simultaneously. If the piezoelectrics are used as actuators, then $\mathbf{v}$ are known and the term $\Theta\mathbf{v}$ is moved to the right-hand side of Equation A.43 and the remaining structural response problem is solved.

In the event of harmonic time dependence of the form $\exp(j\omega t)$, then Equations A.43 and A.44 become

$$\left[-\omega^2\left(\mathbf{M}_b + \mathbf{M}_p\right) + j\omega\left(\mathbf{C}_b + \mathbf{C}_p\right) + \left(\mathbf{K}_b + \mathbf{K}_p + \mathbf{K}_e\right)\right]\mathbf{a} - \Theta\mathbf{v} = \mathbf{B_f f} \tag{A.45}$$

$$\Theta^t \mathbf{a} + \mathbf{P}_p \mathbf{v} = \mathbf{B_q q} \tag{A.46}$$

The general energy harvesting systems of equations solved in this work are of the form:

$$\left[-\omega^2 \left(\mathbf{M}_b + \mathbf{M}_p\right) + j\omega \left(\mathbf{C}_b + \mathbf{C}_p\right) + \left(\mathbf{K}_b + \mathbf{K}_p + \mathbf{K}_e\right)\right] \mathbf{a} - \Theta \mathbf{v} = \mathbf{B_f f} \tag{A.47}$$

$$j\omega \Theta^t \mathbf{a} + j\omega \mathbf{P}_p \mathbf{v} + Y_1 \mathbf{v} = 0 \tag{A.48}$$

where the time derivative has been taken on Equation A.46 and the presence of an external circuit admittance, Y_1, is included. In the event of a basic energy harvesting circuit, *i.e.* a constant load resistance R_1, the admittance is $Y_1 = 1/R_1$.

In the absence of either mechanical or electrical forcing, the undamped structural eigenvalue problem is expressed as

$$\left(\mathbf{K}_b + \mathbf{K}_p + \mathbf{K}_e\right) \mathbf{a} = \omega^2 \left(\mathbf{M}_b + \mathbf{M}_p\right) \mathbf{a} \tag{A.49}$$

APPENDIX B

Electromechanical response of thin piezoelectric plates

The basis for the models of Appendices C, D and G is that by continuity of displacements and stresses between the top and bottom plates of the coupled system, the distributed spring layer displacements become expressed fully in terms of the top and bottom plates. Since these bounding plates are both described as thin plates, the expressions for the distributed spring layer displacements are thereafter written in terms of thin plate displacements. Thus, the full problem description in Appendix A need only to be applied in the case of thin plates. This section provides the applicable form of the previous section for thin, Love–Kirchhoff plates. In addition, solutions for metrics of response are provided which serve throughout this work as means by which to evaluate the performance of given distributed vibration control solutions.

B.1 Constitutive relations of thin piezoelectric plates

The dynamics of plates regarded as thin greatly simplifies the analysis of Appendix A. To make this assumption, also termed Love–Kirchhoff (L–K) assumptions and therefore L–K plates, the following are required.

- The plate is elastic, homogeneous and isotropic.
- The transverse deflection of the plate midplane is small compared to the plate thickness; thence, the slope of the midplane is small compared to the thickness; thence, the square of the slope is $\ll 1$. Likewise for higher orders of the strain-displacement relations.
- Straight lines initially normal to the middle plane of the plate remain straight and normal to the middle surface during deformation. The lengths of such lines

is not modified by deformation.

- Transverse stress is negligible compared to other stress components.
- The middle plane remains unstrained after bending.

The displacements of the plate may then be expressed as

$$\mathbf{u}\left(\mathbf{x},t\right) = \begin{bmatrix} u(x,y,z,t) \\ v(x,y,z,t) \\ w(x,y,z,t) \end{bmatrix} = \begin{bmatrix} u_o(x,y,t) - z\frac{\partial w_o(x,y,t)}{\partial x} \\ v_o(x,y,t) - z\frac{\partial w_o(x,y,t)}{\partial y} \\ w_o(x,y,t) \end{bmatrix} \tag{B.1}$$

where components with subscripts o indicate as referenced from the undeformed middle plane of the plate.

Following the L–K assumptions, the strain-displacement relations are

$$\epsilon_x = \frac{\partial u}{\partial x}, \quad \epsilon_y = \frac{\partial v}{\partial y}, \quad 2\epsilon_{xy} = \frac{\partial u}{\partial y} + \frac{\partial v}{\partial x}, \quad 2\epsilon_{yz} = 2\epsilon_{xz} = \epsilon_z = 0 \tag{B.2}$$

Generally, due to the multiple zero entries of the full strain tensor, see Equation A.8, when using the assumptions, the complete set is truncated for convenience:

$$\begin{bmatrix} S_1 \\ S_2 \\ S_6 \end{bmatrix} = \begin{bmatrix} \epsilon_x \\ \epsilon_y \\ 2\epsilon_{xy} \end{bmatrix} \tag{B.3}$$

This is thereafter presented along with the appropriate differential operator as

$$\begin{bmatrix} \epsilon_x \\ \epsilon_y \\ 2\epsilon_{xy} \end{bmatrix} = \mathbf{L_u} \begin{bmatrix} u \\ v \\ w \end{bmatrix} = \begin{bmatrix} \frac{\partial}{\partial x} & 0 & 0 \\ 0 & \frac{\partial}{\partial y} & 0 \\ \frac{\partial}{\partial y} & \frac{\partial}{\partial x} & 0 \end{bmatrix} \tag{B.4}$$

Likewise, the stress tensor relations are expressed in a reduced form. Using Hooke's Law, the stress-strain relations become

$$\begin{bmatrix} T_1 \\ T_2 \\ T_6 \end{bmatrix} = \begin{bmatrix} \sigma_x \\ \sigma_y \\ \sigma_{xy} \end{bmatrix} = \mathbf{c}_b \begin{bmatrix} \epsilon_x \\ \epsilon_y \\ 2\epsilon_{xy} \end{bmatrix} \tag{B.5}$$

For thin plates, the stiffness matrix, $\mathbf{c}_b$, is written

$$\mathbf{c}_b = \begin{bmatrix} \frac{E}{1-\nu^2} & \frac{\nu E}{1-\nu^2} & 0 \\ \frac{\nu E}{1-\nu^2} & \frac{E}{1-\nu^2} & 0 \\ 0 & 0 & \frac{E}{2(1+\nu)} \end{bmatrix} \tag{B.6}$$

As such, it is observed that for thin plates, stress-strain relations are dependent on just two material properties: the Young's modulus, E, and the Poisson's ratio, ν. In a similar fashion for the piezoelectric sub-domain of the system, the stiffness matrix is expressed as

$$\mathbf{c}^E = \begin{bmatrix} \frac{E_p}{1-\nu_p^2} & \frac{\nu_p E_p}{1-\nu_p^2} & 0 \\ \frac{\nu_p E_p}{1-\nu_p^2} & \frac{E_p}{1-\nu_p^2} & 0 \\ 0 & 0 & \frac{E_p}{2(1+\nu_p)} \end{bmatrix} \tag{B.7}$$

where, as before, the subscript p indicates the piezoelectric material.

The electrical field-potential relations for thin plates are much simplified due to the assumption that the electrodes cover the top and bottom span of the plate layer. It is further assumed that the piezoelectric plate is poled through its thickness, in the z-axis. As such, all of the coefficients in the first and second rows of $\mathbf{d}$ must be zero since no flow of current is possible without the presence of the electrodes (and associated external circuitry) to utilize a voltage difference between the electrode surfaces. It is assumed that the potential within the piezoelectric layer varies linearly through its thickness such that

$$\varphi(x, y, z, t) = -z\frac{v(t)}{t_s} \tag{B.8}$$

where t_s is the thickness of the piezoelectric plate. Therefore, the electric field is expressed as

$$\mathbf{E} = \mathbf{L}_\varphi \varphi, \qquad \mathbf{L}_\varphi = \begin{bmatrix} 0 \\ 0 \\ \frac{\partial}{\partial z} \end{bmatrix} \tag{B.9}$$

Thereafter, given the truncated form of $\mathbf{c}^E$ of Equation B.6, the reduced piezoelectric constant matrix is

$$\mathbf{e} = \begin{bmatrix} 0 & 0 & 0 \\ 0 & 0 & 0 \\ e_{13} & e_{13} & 0 \end{bmatrix} \tag{B.10}$$

for

$$e_{13} = \left(c_{11}^E + c_{12}^E\right) d_{31} = \frac{d_{31} E_p}{1 - \nu_p} \tag{B.11}$$

Given Equation B.9, Equation A.39 becomes

$$\mathbf{P}_p = \int_{\Omega_p} \left[\mathbf{L}_\varphi \Psi_\mathbf{v}\left(\mathbf{x}\right)\right]^t \epsilon^S \mathbf{L}_\varphi \Psi_\mathbf{v}\left(\mathbf{x}\right) \mathrm{d}\Omega_p = \int_{\Omega_p} \frac{\epsilon_{33}}{t_s^2} \mathrm{d}\Omega_p = C_p \tag{B.12}$$

where the capacitance of the piezoelectric layer is computed

$$C_p = \frac{a_b b_b}{t_s} \left(\varepsilon_{33} - \frac{e_{33}^2}{c_{33}^E}\right) = \frac{a_b b_b}{t_s} \left(\varepsilon_{33} - d_{33}^2 c_{33}^E\right) \tag{B.13}$$

and a_p and b_p are the planar dimensions of the piezoelectric plate and ε_{33} is the permittivity component evaluated at constant strain.

In the absence of classical boundaries, arbitrarily bounded systems may be modeled using the common approach of applying translational and rotational springs along the plate edges. For the thin structural panel

$$\mathbf{L}_\mathbf{e} = \begin{bmatrix} 1 & 0 & 0 \\ 0 & 1 & 0 \\ 0 & 0 & 1 \\ 0 & 0 & -\frac{\partial}{\partial x} \\ 0 & 0 & -\frac{\partial}{\partial y} \end{bmatrix} \quad \text{at } z = 0 \tag{B.14}$$

and a boundary stiffness matrix composed therefore of just 5 diagonal elements:

$$\mathbf{k}_\mathbf{e} = \begin{bmatrix} k_{tx} & 0 & 0 & 0 & 0 \\ 0 & k_{ty} & 0 & 0 & 0 \\ 0 & 0 & k_{tz} & 0 & 0 \\ 0 & 0 & 0 & k_{rx} & 0 \\ 0 & 0 & 0 & 0 & k_{ry} \end{bmatrix} \tag{B.15}$$

B.2 Ritz method approximation

The mechanical displacements and voltages of the thin piezoelectric plates are approximated by the Ritz method. Assuming the electrodes are continuous over the surface, only one generalized electrical co-ordinate is required per piezoelectric plate. The three mechanical displacements are described in terms of a linear combination of a desired number of generalized co-ordinates per displacement

$$u_0(x,y) \approx \sum_{p=1}^{N_u} U_p \phi_p^u(x,y) \tag{B.16}$$

$$v_0(x,y) \approx \sum_{r=1}^{N_v} V_r \phi_r^v(x,y) \tag{B.17}$$

$$w_0(x,y) \approx \sum_{s=1}^{N_w} W_s \phi_s^w(x,y) \tag{B.18}$$

where U_p, V_r and W_s and $\phi^u(x,y)$, $\phi^v(x,y)$ and $\phi^w(x,y)$ are the generalized co-ordinates and trial functions in the x, y and z axes, respectively. (In this notation, the superscripts u, v and w are merely included to denote the potential for different trial functions sets in each of the axes, and do not represent powers).

In the present work, when simulation involves the modeling of simply supported plates. The choice of trial functions, ϕ^u, ϕ^v and ϕ^w is greatly simplified due to the analytical solution for the boundary value problem of simply supported plates [96].

$$\phi(x,y) = \sin\left[\frac{m\pi x}{a}\right] \sin\left[\frac{n\pi y}{b}\right] \tag{B.19}$$

In the notation of Equation B.19, individual subscripts m and n are denoted for trial functions separable in the x and y co-ordinate axes. In reference to Equations B.16–B.18, these individual subscripts are related to the single subscripts, p, r and s by the following; for example, for N_w and s,

$$s = (m-1)N_y + n, \qquad m = 1, 2, \cdots, N_x, \quad n = 1, 2, \cdots, N_y, \quad N_w = N_x N_y \tag{B.20}$$

In the case of other classical boundary conditions, the hierarchical function set of Beslin and Nicolas [97] is employed. By selection or omission of the first four functions of the set, any combination of the classical boundary conditions may be appropriately accounted for. This function set has been shown to be computationally efficient due to the generation of highly banded matrices for thin plates [98] as well accurate in modeling plates and beams which exhibit material discontinuities along their lengths [99].

The generalized co-ordinates of Equations B.16–B.18 are expressed in vector notation as

$$\mathbf{U} = \begin{bmatrix} U_1 & U_2 & \cdots & U_{N_u} \end{bmatrix}^t \tag{B.21}$$

$$\mathbf{V} = \begin{bmatrix} V_1 & V_2 & \cdots & V_{N_v} \end{bmatrix}^t \tag{B.22}$$

$$\mathbf{W} = \begin{bmatrix} W_1 & W_2 & \cdots & W_{N_w} \end{bmatrix}^t \tag{B.23}$$

Thereafter, the full vector of mechanical generalized co-ordinates is expressed as

$$\mathbf{a} = \begin{bmatrix} \mathbf{U}^t & \mathbf{V}^t & \mathbf{W}^t \end{bmatrix}^t \tag{B.24}$$

For a single thin piezoelectric plate, the generalized co-ordinates of Equation B.24 and one electrical generalized co-ordinate serve as the solution to the systems of Equations A.47 and A.48.

The trial function matrix, $\Psi_{\mathbf{a}}(x, y)$, is expanded to

$$\Psi_{\mathbf{a}}(x, y, z) = \begin{bmatrix} \phi^u(x, y) & 0 & -z\frac{\partial \phi^w(x,y)}{\partial x} \\ 0 & \phi^v(x, y) & -z\frac{\partial \phi^w(x,y)}{\partial y} \\ 0 & 0 & \phi^w(x, y) \end{bmatrix} \tag{B.25}$$

where $\phi^w(x,y)$ is separable such that

$$\phi^w(x,y) = \begin{bmatrix} \phi_1^{w_x}(x)\phi_1^{w_y}(y) & \phi_2^{w_x}(x)\phi_1^{w_y}(y) & \cdots & \phi_m^{w_x}(x)\phi_1^{w_y}(y) \\ \phi_1^{w_x}(x)\phi_2^{w_y}(y) & \phi_2^{w_x}(x)\phi_2^{w_y}(y) & \cdots & \phi_m^{w_x}(x)\phi_2^{w_y}(y) \\ \vdots & \vdots & \vdots & \vdots \\ \phi_1^{w_x}(x)\phi_n^{w_y}(y) & \phi_2^{w_x}(x)\phi_n^{w_y}(y) & \cdots & \phi_m^{w_x}(x)\phi_n^{w_y}(y) \end{bmatrix} \tag{B.26}$$

and where $N_w = N_w = N_x N_y$ as in Eq. B.20.

Assuming the electrical potential varies linearly through the thickness of the piezoelectric domains, only one voltage is necessary to describe the electrical response of each, separated piezoelectric domain:

$$\mathbf{v} = \begin{bmatrix} v_1 & v_2 & \cdots & v_{N_v} \end{bmatrix}^t \tag{B.27}$$

where v_i represents the voltage on the electrode surface of the i^{th} piezoelectric layer. The trial functions of the layers are thereafter expressed as

$$\Psi_{\mathbf{v}}(x,y,z) = \begin{bmatrix} \Psi_v^1(x,y,z) & \Psi_v^2(x,y,z) & \cdots & \Psi_v^{N_v}(x,y,z) \end{bmatrix} \tag{B.28}$$

The piezoelectric voltage response is assumed to be non-zero only at locations along the piezoelectric domain, Ω_p. In this event, the piezoelectric layer trial functions are identical

$$\Psi_v^i(x,y,z) = -z\frac{1}{t_s} \tag{B.29}$$

B.3 System response metrics

Due to L–K assumptions, integrations of Eqs. A.32–A.42 may be carried out through the thickness of the layer analytically since the mechanical response is assumed to vary linearly through the thickness direction. Afterwards, integration need be carried out only in the x and y co-ordinate plane. By the assumption of linearity, the response of the plate is assumed separate in both x and y axes. This separates the integrations into one integral in x and one in y, simplifying analysis considerably. How one wishes to implement this integration depends on the necessary choice of trial functions.

The use of polynomial basis functions may lead to analytically tractable integrations in the (x, y) plane. However, these functions are not as well-suited to simulating all ranges of classical boundary conditions, and the the boundary translational and rotational stiffness approximation would become a necessarily addition to the model. Should the panel be simply supported, closed form solution of the integration may be carried out and solutions to this situation are given by Leissa [96].

For robust trial function sets like that of Beslin and Nicolas [97], the integrations may be reduced to the sum of individual cosines as noted by Dozio [98]. Alternatively, simple numerical integration schemes may be used, for example both **quad** and **quadgk** in MATLAB are apt for this purpose and can be computed with great speed using modern computers, even for high order approximations.

Once the integrations are performed, response of the system is output in terms of the generalized mechanical and electrical co-ordinates, $\mathbf{a}(\omega)$ and $\mathbf{v}(\omega)$, respectively. Transverse plate dynamics are of greatest interest in the study of most troublesome vibration and the associated, coupled radiated noise. To determine the transverse, or out-of-plane, mechanical displacements of the plate follows directly from the Ritz method assumption:

$$w_o(x, y, \omega) = \mathbf{W}(\omega)\phi^w(x, y) \tag{B.30}$$

where $\mathbf{W}$ were the generalized co-ordinates of the out-of-plane displacements and $\phi^w(x, y)$ were the corresponding trial functions. Due to assumptions of time dependence, $\exp(j\omega t)$, out-of-plane velocity and acceleration are easily computed

$$\dot{w}_o(x, y, \omega) = j\omega\mathbf{W}(\omega)\phi^w(x, y) \tag{B.31}$$

$$\ddot{w}_o(x, y, \omega) = -\omega^2\mathbf{W}(\omega)\phi^w(x, y) \tag{B.32}$$

Transverse mean-square velocity is the spatial and temporal average of the out-of-plane velocity over the plate surface

$$\langle \dot{w}(\omega) \rangle^2 = \frac{\omega^2}{2a_b b_b} \int_{-a_b/2}^{+a_b/2} \int_{-b_b/2}^{+b_b/2} \left(\phi^w(x, y)\mathbf{W}(\omega)\right)^* \left(\phi^w(x, y)\mathbf{W}(\omega)\right) \mathrm{d}x\mathrm{d}y \tag{B.33}$$

where a_b and b_b are the lengths of the plate in the x and y axes, respectively. This may be more succinctly expressed as

$$\langle \dot{w}(\omega) \rangle^2 = \frac{\omega^2}{2a_b b_b} \mathbf{W}(\omega)^H \left\{ \int_{-a_b/2}^{+a_b/2} \int_{-b_b/2}^{+b_b/2} \phi^w(x,y)^t \phi^w(x,y) \mathrm{d}x \mathrm{d}y \right\} \mathbf{W}(\omega) \tag{B.34}$$

where $(\ )^H$ is the Hermitian (conjugate) transpose matrix operator.

B.4 Thin shell differential operator

In Chapter G, the response of a thin piezoelectric shell is determined and the corresponding linear differential operator is therefore provided. Due to conventional notation in shell theory, a local co-ordinate system (x, θ, z_p) is defined for the axial, circumferential and radial directions (Figure G.2), having translational displacements of u, v and w, respectively. The linear differential operator for the thin cylindrical shell, with radius h_s, in the local co-ordinate system is

$$\mathbf{L_u} = \begin{bmatrix} \frac{\partial}{\partial x} & 0 & 0 \\ 0 & \frac{1}{h_s}\left(1 - \frac{z_p}{h_s}\right)\frac{\partial}{\partial \theta} & \frac{1}{h_s}\left(1 - \frac{z_p}{h_s}\right) \\ \frac{1}{h_s}\left(1 - \frac{z_p}{h_s}\right)\frac{\partial}{\partial \theta} & \frac{\partial}{\partial x} & 0 \end{bmatrix} \tag{B.35}$$

APPENDIX C

Mechanical vibration analysis of continuously distributed devices for narrow and broadband passive structural vibration attenuation

The dynamic vibration absorber has been studied and employed extensively in its long history. However, few analyses or embodiments of continuously distributed absorbers have been recorded; namely, devices in which both the spring and mass layers are continuous layers. Such devices would be capable of suppressing structural vibration by two dynamic regimes: first, by resisting vibration like constraining-layer treatments and, second, by reactively working against the structure similar to classical mass-spring-dampers. In the following chapter, a model is described which employs the Ritz method to solve the problem of forced response of a host rectangular panel with attached distributed and point absorbers. Several numerical experiments are performed to evaluate the dual dynamic characteristics of continuously distributed vibration absorbers. Studies include segmentation of the devices; modulus and orthotropy ratios of the mass and spring layers, respectively; the effects of utilizing modal dynamics of the continuous mass layers; dampening of an orthotropic spring layer; and variable stiffness characteristics along an otherwise continuous spring layer. It is found that such devices do indeed employ both resistive and reactive effects, making them useful for both low and high frequency passive vibration control. This suggests the nomenclature "vibration absorber" is incomplete and poses the opportunity for new embodiments of a classic device to be created for broadband structural vibration attenuation.

C.1 Introduction

Passive vibration control devices and treatments continue to dominate the available landscape of approaches when it comes to attenuating the vibration of large surfaces, *e.g.* structural or aircraft panels, ship hulls, automotive bodies, and so forth. Active approaches may offer greater maximal performance benefit [100–103], but are almost inevitably more costly to design, implement and maintain. To attenuate the vibration of large surfaces, it is often elected to cover most or all of the troublesome surface. Two classes of passive treatments are employed: those which resist the structural motion by imparting shearing effects and those which reactively work against the structure.

The first class of treatments may be embodied in constraining-layer damping (CLD), free-layer damping, or generally heavily-damped applied mass (ballast) [5]. However, for low frequency vibration and with a concurrent aim of minimizing applied mass to the structure, these treatments are insufficient. The second class is embodied in the classic mass-spring-damper. For surface vibration attenuation, arrays of oscillators have been studied and applied [9–12] but the complexity of this arrangement and multitude of devices required to achieve substantial broadband attenuation makes this solution less convenient. Devices similar to elastic foundations with continuous mass layers have also been considered [13, 14], designed like especially thick CLD. These treatments were found to be very useful around a targeted natural frequency, similar to a series of single degree-of-freedom (SDOF) oscillators.

A few instances appear in literature of plate-like dynamic vibration absorbers [15–17]. However, in most studies, the specific spring layer utilized was not also plate-like but composed of discrete springs. Thus, while the devices may dynamically operate like plates, they only affect the host structure at one or a few points. A true continuous and distributed vibration absorber combines both SDOF dynamics with the modal response of the distributed mass layer through the intermediary of a continuously distributed spring layer; to date, few studies of such devices exist. Fuller and

Cambou [19] considered one device to attenuate beam vibration but did not evaluate comparable constraining-type effects or modal response, preferring instead a more comprehensive analysis based on reactive dynamics. Similarly, Marcotte et al. [20] considered another continuous device for use on a plate but also neglected extensional coupling and modal dynamics.

One such mention of this concept does appear in a thorough literature search, that of the continuously distributed spring–mass by Zhou and Ji [18], but not in a study concerned with vibration control. Instead, analysis was directed at a crowd of people situated together—the continuously distributed spring–mass—over a portion of a structural floor—a rectangular plate—and their free vibration dynamics.

Thus, it appears there are few recorded explorations of the implementation of continuously distributed vibration absorbers designed for surface vibration attenuation. Since such devices may suppress host vibration by both reactive and resistive effects, it is interesting to observe that so little attention has been given to this opportunity. As a lightweight passive vibration control treatment, embodiments of this concept could find wide implementation in a broad range of applications, as mentioned earlier.

This paper presents a brief description of a model based on Hamilton's principle to determine the forced response of a panel to which a number of distributed vibration absorbers and/or point oscillators have been attached. For conciseness and due to the large number of textbook summaries of Hamilton's principle applied in the study of elastic structural dynamics, the description of the analytical formulation is kept at a minimum. The model is then employed to consider a number of features unique to continuous distributed vibration absorbers: segmentation of the devices; orthotropic characteristics of the spring layers; the modulus ratio of the top mass layer with respect to the host structure; and the specific effect of modal dynamics on the performance of a given absorber. The case studies consider the comparable influence of reactive and resistive effects which the devices impart on their host structure. It is found that such continuous devices may indeed unify both passive vibration control

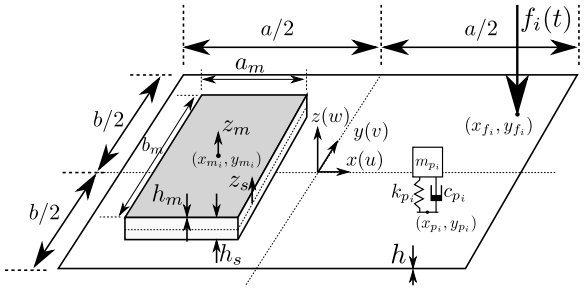

Figure C.1: Thin plate with attached distributed absorbers and mass-spring-dampers

dynamic mechanisms, making the treatments ideal for broadband attenuation at the cost of minimal added mass.

C.2 Governing equations for coupled system forced response

A concise presentation of the model is provided: thorough detail of applying Hamilton's principle and variational energy methods in the study of dynamic, elastic bodies may be found in a number of textbooks [94, 60] as well as a more rigorous explanation in the content of the present system in Appendix A. Consider a thin, rectangular panel to which N_m and N_p distributed vibration absorbers and mass-spring-dampers, respectively, have been attached, Figure C.1. The distributed absorbers are centered at locations (x_{m_i}, y_{m_i}), $i = 1, 2, \ldots, N_m$, while the point oscillators are placed at (x_{p_i}, y_{p_i}), $i = 1, 2, \cdots, N_p$. The host panel, which is arbitrarily bounded, is excited by out-of-plane, harmonic point forces, $f_i(t)$, at locations (x_{f_i}, y_{f_i}), $i = 1, 2, \ldots, N_f$. The global co-ordinate system is defined at the host panel center mid-plane.

The distributed absorbers are assumed to be each composed of a distributed, compressible and continuous spring layer and a thin top plate or mass layer. The transverse deflections of these layers are defined about their undeformed middle planes. The distributed spring layer is assumed to be an equivalent thick and transversely deformable orthotropic plate with known or otherwise determined elasticity parameters.

Hamilton's principle for deformable elastic bodies is

$$\int_{t_1}^{t_2} \left[\delta\left(T-U\right)+\delta W\right] \mathrm{d}t = 0 \tag{C.1}$$

The total kinetic energy, T; potential energy, U; and variation of the applied loads, δW, are defined as

$$\begin{aligned} T \;\; &= \tfrac{1}{2}\rho \int_V \left(\dot{\mathbf{u}}\right)^t \dot{\mathbf{u}} \mathrm{d}V + \tfrac{1}{2}\sum_{i=1}^{N_m} \rho_{m_i} \int_{V_{m_i}} \left(\dot{\mathbf{u}}_{m_i}\right)^t \dot{\mathbf{u}}_{m_i} \mathrm{d}V_{m_i} \\ &\quad + \tfrac{1}{2}\sum_{i=1}^{N_m} \rho_{s_i} \int_{V_{s_i}} \left(\dot{\mathbf{u}}_{s_i}\right)^t \dot{\mathbf{u}}_{s_i} \mathrm{d}V_{s_i} \\ &\quad + \tfrac{1}{2}\sum_{i=1}^{N_p} m_{p_i} \left[\dot{w}_o\left(x_i^p, y_i^p\right) + \dot{z}_{p_i}\right]^2 \end{aligned} \tag{C.2}$$

$$\begin{aligned} U \;\; &= \tfrac{1}{2}\int_V \left(\epsilon\right)^t \mathbf{c}\epsilon \mathrm{d}V + \tfrac{1}{2}\sum_{i=1}^{N_m} \int_{V_{m_i}} \left(\epsilon_{m_i}\right)^t \mathbf{c}_{m_i}\epsilon_{m_i} \mathrm{d}V_{m_i} \\ &\quad + \tfrac{1}{2}\sum_{i=1}^{N_m} \int_{V_{s_i}} \left(\epsilon_{s_i}\right)^t \mathbf{c}_{s_i}\epsilon_{s_i} \mathrm{d}V_{s_i} + \tfrac{1}{2}\sum_{i=1}^{N_p} k_{p_i}\left(z_{p_i}\right)^2 \end{aligned} \tag{C.3}$$

$$\delta W = \sum_{i=1}^{N_f} \delta\mathbf{u}\left(x_{f_i}, y_{f_i}, t\right) \cdot f_i(t) \tag{C.4}$$

where $\mathbf{u}$ is the vector of displacements; ρ is the mass density; m_{p_i} is the mass of the i^{th} mass-spring-damper; z_{p_i} is the relative displacement between the i^{th} mass-spring-damper and the panel; ϵ is the strain tensor; $\mathbf{c}$ is the stiffness matrix; and k_{p_i} is the spring constant of the oscillator. Subscripts m, s and p refer to the top mass layers, spring layers and mass-spring-dampers, respectively; terms without superscripts are related to the host structural panel. The time derivative is denoted by $\dot{(\,)}$ and $()^t$ denotes the matrix transpose operator.

The base plate and distributed top plates are assumed to be Love–Kirchhoff plates having displacements expressed in terms of quantities deviating from the undeformed middle planes.

$$\mathbf{u}(x,y,t) = \begin{bmatrix} u_o - z\frac{\partial w_o}{\partial x} \\ v_o - z\frac{\partial w_o}{\partial y} \\ w_o \end{bmatrix}$$

$$\mathbf{u}_{m_i}(x,y,t) = \begin{bmatrix} (u_o)_{m_i} - z_{m_i}\frac{\partial (w_o)_{m_i}}{\partial x} \\ (v_o)_{m_i} - z_{m_i}\frac{\partial (w_o)_{m_i}}{\partial y} \\ (w_o)_{m_i} \end{bmatrix} \quad i = 1, 2, \ldots, N_m \tag{C.5}$$

where the subscript o indicates the displacement of the middle-plane of the layer, $z = 0$ or $z_i^m = 0$.

The mechanical displacements of the distributed spring layer allow for the transverse flexibility of the layer:

$$\mathbf{u}_{s_i}(x,y,t) = \begin{bmatrix} (u_o)_{s_i} + z_{s_i}(\theta_x)_{s_i} \\ (v_o)_{s_i} + z_{s_i}(\theta_y)_{s_i} \\ (w_o)_{s_i} + z_{s_i}\frac{\partial (w_o)_{s_i}}{\partial z_{s_i}} + \frac{1}{2}(z_{s_i})^2 \frac{\partial^2 (w_o)_{s_i}}{\partial (z_{s_i})^2} \end{bmatrix}$$
$$i = 1, 2, \ldots, N_m \tag{C.6}$$

where θ_x and θ_y are the rotations about the middle-planes in the x- and y-axes, respectively. Application of continuity of displacements and transverse stress between the spring layer and the two bounding plates allows the spring layer mechanical displacements to be expressed in terms of the top plate and bottom plate displacements. Thus, for the complete system, there exist $3 + 3N_m + N_p$ unknown mechanical displacements.

The Ritz method is employed to express the unknown plate displacements in terms of a linear combination of admissible trial functions and generalized co-ordinates.

$$\mathbf{u}(x,y,t) = \Phi(x,y)\,\mathbf{r}(t)$$
$$\mathbf{u}_{m_i}(x,y,t) = \Phi^m(x,y)\,\mathbf{d}_i(t) \qquad i = 1, 2, \ldots, N_m \tag{C.7}$$

where $\Phi(x,y)$ and $\mathbf{r}(t)$ are the M trial functions and the generalized co-ordinates, respectively, for the base panel. Likewise, $\Phi^m(x,y)$ and $\mathbf{d}_i(t)$ are the trial functions

and generalized co-ordinates for the i^{th} mass layer. The generalized co-ordinates of the N_p oscillators are the relative displacements between the oscillator masses and the host panel and may be represented as $\mathbf{z}(t) = \left[z_{p_1}(t) \;\; z_{p_2}(t) \;\; \ldots \;\; z_{p_{N_p}}(t)\right]^t$.

Substitution of the approximate solutions of Eq. C.7 and the generalized co-ordinates of the oscillators into the generalized Hamilton's principle, Eq. C.1, yields a coupled system of equations of the form

$$\begin{bmatrix} \mathbf{M} + \mathbf{M}_s^{base} + \mathbf{M}_p^{base} & \tilde{\mathbf{M}}_s & \tilde{\mathbf{M}}_p \\ \left(\tilde{\mathbf{M}}_s\right)^t & \mathbf{M}_m + \mathbf{M}_s^{top} & \mathbf{0} \\ \left(\tilde{\mathbf{M}}_p\right)^t & \mathbf{0} & \mathbf{M}_p \end{bmatrix} \begin{bmatrix} \ddot{\mathbf{r}}(t) \\ \ddot{\mathbf{d}}(t) \\ \ddot{\mathbf{z}}(t) \end{bmatrix} + \begin{bmatrix} \mathbf{C} + \mathbf{C}_s^{base} & \tilde{\mathbf{C}}_s & \mathbf{0} \\ \left(\tilde{\mathbf{C}}_s\right)^t & \mathbf{C}_m + \mathbf{C}_s^{top} & \mathbf{0} \\ \mathbf{0} & \mathbf{0} & \mathbf{C}_p \end{bmatrix} \begin{bmatrix} \dot{\mathbf{r}}(t) \\ \dot{\mathbf{d}}(t) \\ \dot{\mathbf{z}}(t) \end{bmatrix} + \begin{bmatrix} \mathbf{K} + \mathbf{K}_s^{base} & \tilde{\mathbf{K}}_s & \mathbf{0} \\ \left(\tilde{\mathbf{K}}_s\right)^t & \mathbf{K}_m + \mathbf{K}_s^{top} & \mathbf{0} \\ \mathbf{0} & \mathbf{0} & \mathbf{K}_p \end{bmatrix} \begin{bmatrix} \mathbf{r}(t) \\ \mathbf{d}(t) \\ \mathbf{z}(t) \end{bmatrix} = \begin{bmatrix} \mathbf{Q}(t) \\ \mathbf{0} \\ \mathbf{0} \end{bmatrix} \tag{C.8}$$

Eq. C.8 contains the direct and coupled mass, $\mathbf{M}$, dampening, $\mathbf{C}$, and stiffness, $\mathbf{K}$, matrices. Matrices with subscripts s, m and p represent components related to the spring layers, distributed mass layers and oscillators, respectively; those without subscripts represent the base plate contributions. Matrices with superscript *base* and *top* indicate the components described in terms of the base and top layers co-ordinates, respectively. Matrices with an over ($\tilde{}$) indicate coupling expressions. Since the mass-spring-damper displacements are relative and not absolute, a contribution from the oscillators inertial influence appears directly in the sub-matrix for the mass of the host panel, along with corresponding coupling. The generalized forces, $\mathbf{Q}$, are computed by the evaluation of the base plate trial functions at the location of the applied force locations,

$$\mathbf{Q}(t) = \sum_{i=1}^{N_f} \Phi\left(x_{f_i}, y_{f_i}\right)^t f_i(t) \tag{C.9}$$

In the present work, dampening in the plate layers is included by means of terms proportional to the mass and stiffness matrices. Thus, in general,

$$\mathbf{C} = \alpha\mathbf{M} + \beta\mathbf{K} \tag{C.10}$$

Note that matrices $\mathbf{M}_p$, $\mathbf{C}_p$ and $\mathbf{K}_p$ are diagonal with elements containing the mass, damper coefficient and spring constant of each oscillator, respectively. Eq. C.8 is solved assuming harmonic time dependence of the form $\exp(i\omega t)$ over a range of frequencies, ω.

The out-of-plane mean-square velocity of the panel is useful in evaluating the vibration attenuation capability of applied treatments. If the components of the base panel trial functions and generalized co-ordinates related to out-of-plane displacements, $w(x, y, t)$, are denoted $\Phi^w(x, y)$ and $\mathbf{r}^w(t)$, respectively, then the mean-square velocity is found by

$$\langle \dot{w}(\omega) \rangle^2 = \frac{\omega^2}{2ab} \sum_{m=1}^{M^w} \sum_{n=1}^{M^w} r_m^w(\omega)^* r_n^w(\omega) \int\int (\Phi_m^w)^* \Phi_n^w \mathrm{d}y\mathrm{d}x \tag{C.11}$$

where there are M^w generalized co-ordinates and trial functions for the out-of-plane panel displacement and $()^*$ indicates the complex conjugate. The cumulative mean-square velocity is computed by the sum of values over a bandwidth, BW, of desired frequencies:

$$\langle \underline{\dot{w}} \rangle^2 = \sum_{j=1}^{BW} \langle \dot{w}(\omega_j) \rangle^2 \tag{C.12}$$

Finally, the attenuation of the panel vibration from the untreated levels is expressed as the difference

$$\Delta\langle \underline{\dot{w}} \rangle^2 = \langle \underline{\dot{w}} \rangle^2_{with\ treatments} - \langle \underline{\dot{w}} \rangle^2_{untreated} \tag{C.13}$$

C.3 Case study: Continuity of distributed treatments

This section considers the change in panel vibration attenuation when the applied distributed vibration absorbers are continuous samples or discretized into segments. CLD treatments are known to exert a greater shearing resistance effect, and therefore

increase overall structural dampening, when segmented [68–70]. Thus, since continuous absorber treatments of the present study are coupled to the vibration of the host panel in the same manner as CLD materials, it is useful to compare this effect for devices capable of simultaneous reactive and resistive vibration control.

A simply-supported plate is considered, with a centrally-located distributed vibration absorber. The geometric and material properties of the system are given in Table C.1. The absorber mass ratio, $\mu = \left(a_m b_m (h_m \rho_m + h_s \rho_s)\right) / abh\rho$, was $\mu = 0.0243$, which practically speaking is a very lightweight treatment. Damping is included by means of isotropic loss factors, η, such that $\alpha = 0$ and $\beta = \eta/\omega$. The spring layer properties were assumed to be isotropic, $E_{s,x} = E_{s,y} = E_{s,z} = E_s$ and $G_s = E_s/2(1+\nu_s)$. Computations of mean-square velocity were made from 10 to 600 Hz in 1 Hz increments for the cases of an untreated panel and with the absorber treatments. The first absorber treatment was a continuous device; the second split the device into four equal segments; the third case split the original device into 9 equal segments; and the fourth case split the device into 16 equal segments. In each case of division, the same surface area coverage and μ was maintained. Finally, computations were performed for the case of the panel having a 25×25 grid of mass-spring-dampers equally-spaced over the same surface as the continuous absorber. The applied absorbers or oscillators all exhibited SDOF natural frequencies of 260.9 Hz, very close to the panel (3,1) resonance of 261.1 Hz. Placing the devices centered on the panel is an intuitive method to maximize the benefit of reactive forcing effects since the simply-supported panel has an anti-node at the panel center for the (3,1) vibration mode.

Table C.2 presents the computed values of $\Delta\langle\underline{\dot{w}}\rangle^2$ for two ranges of frequencies. The first bandwidth presented, 200-400 Hz, is targeted around the panel resonance of 261.1 Hz as well as any split resonances that the application of the reactive devices may yield; thus, vibration attenuation in this bandwidth indicates the designed (tuned) benefit. The next bandwidth, 10-600 Hz, would indicate the global or broadband effect of the applied treatments. Further numerical experiments with the model

Table C.1: Geometric and material specifications

Layer	Panel	Top mass	Spring layer
a (mm)	600	90	90
b (mm)	400	90	90
h (mm)	3	2	37
E (Pa)	7.2e10	7.2e10	2e5
ρ (kg/m^3)	2100	2100	9
ν	0.3	0.3	0.4
η	1e-3	1e-3	5e-3
(x_{f_1}, y_{f_1}) (mm)	(144,127)	—	—

Table C.2: Cumulative mean-square velocity reduction, segmentation dependence

# of devices	200-400 Hz	10-600 Hz
1	-3.19	-1.36
4	-4.27	-3.40
9	-2.15	-2.89
16	-1.73	-2.21
625	-1.42	-1.88

indicated that simulations to higher frequencies did not yield any significant change in overall panel vibrational response for the treatments, indicating repeated computation above 600 Hz to be unnecessary.

The distributed absorber segmented into 4 equal pieces best attenuates the structural vibration both in the targeted bandwidth as well over the wider spectrum. For broadband performance, increased segmentation of the distributed absorbers improves the results as compared with the targeted frequency bandwidth; this is indicated by the fact that the distributed devices in 9 and 16 pieces achieve greater broadband as opposed to narrowband control. If the devices operate in the manner of resisting host panel vibration, in addition to the reactive effects, the increased segmentation would lead to greater shearing resistance on the host panel, precisely as shown in literature for segmented CLD treatments.

The point oscillators show the worst overall performance. A frequency spectrum of the panel vibration with the oscillators show that the devices dramatically shift the low frequency panel vibrational response, highly coupling with the other modes, even the asymmetric modes. This makes sense given that the distributed devices,

perhaps placed across asymmetric nodal lines will not couple as well to the asymmetric motion of the panel. However, an individual oscillator will couple to all modes of the structural vibration, so long as it is not placed exactly on a nodal line of the mode in question. Thus, the oscillators yield increased vibrational complexity of the coupled system, to the detriment of both narrowband and broadband vibration attenuation.

In summary, it is observed that some segmentation of the devices is advantageous for both narrow and broadband vibration attenuation. The continuous absorber performs well in suppressing the range of frequencies around its tuned frequency, 260.9 Hz. In contrast, splitting the treatment into either 9 or 16 equal pieces improves global performance with the resultant loss of authority in the tuned frequency range. Thus, dividing the continuous treatment into 4 pieces provides beneficial reactive forcing effects as well as the ability to resist some of the higher order panel vibration.

C.4 Case study: Constraining dynamics

The purpose of this section is to further relate the dynamics of the distributed absorber to those of common CLD treatments. In such products, a low shear strength material is deformed by the host structure but a thin, high modulus material on the other side of the intermediary layer constrains the net motion, resulting in a shear resistance to the host panel vibration. Dissipation of the energy results due to the common use of viscoelastic materials as the intermediary layer. In the case of the distributed vibration absorber, the distributed spring layer may conceivably have a very low shear stiffness relative to the bending stiffnesses, *i.e.* a corrugated spring layer or poroelastic foam spring.

In pursuit of quantifying this effect of orthotropic spring layer characteristics, a ratio of orthotropy is defined (subscript s dropped for convenience from all terms): $\Lambda = [(E_x)^2 + (E_y)^2]^{1/2}/E_z$. Assuming a transversely orthotropic spring layer such that $E_x = E_y = E_t$, the ratio becomes $\Lambda = E_t/E_z$. The remaining necessary parameters to describe the orthotropic elastic parameters are computed as $\nu_{xz} =$

Table C.3: Geometric and material specifications

Layer	Panel	Top mass	Spring layer
a (mm)	600	150	150
b (mm)	400	100	100
h (mm)	2	0.9	80
E (Pa)	7.2e10	7.2e10	—
ρ (kg/m^3)	2100	2100	9
ν	0.3	0.3	—
η	1e-3	1e-3	5e-3
(x_{f_1}, y_{f_1}) (mm)	(144,127)	—	—

$\nu_{zx}E_t/E_z = \nu_{zx}\Lambda = \nu_{yz}$, $G_{yz} = E_t/2(1+\nu_{yz}) = G_{xz}$. In the following numerical studies, $E_z = 2e5$ Pa, $\nu_{yx} = \nu_{xy} = 0.2$, $\nu_{zy} = \nu_{zx} = 0.002$; the last condition being set such that for large Λ the Poisson's ratios would not approach 0.5. Note that very small Poisson's ratios $\nu_{xz} = \nu_{yz} \ll \nu_{zx} = \nu_{zy}$ would indicate near complete decoupling between the cross-planar response of the distributed spring layer and the transverse response of the layer. In conjunction with the top mass layer, this scenario is dynamically identical to the superposition of a layer of springs capable of only vertical displacement and an incompressible sandwich panel. This superposition has been studied extensively by Frostig and Baruch [65] and found to accurately model such compressible orthotropic layers. Note that large Λ also result in greater shearing stiffnesses.

A common practice in the application of CLD materials is the use of a constraining layer of equal or greater Young's modulus as the host structural panel if the principal vibration control bandwidth is in auditory range of about 100 Hz to a few kHz [5]. Thus, this modulus ratio, $\Gamma = E_m/E$, the ratio between the top mass modulus and the base plate modulus, is considered. Since Γ and Λ are independent non-dimensional parameters, the model may be run for a range of these parameters and presented in tandem to show optimal regions of distributed vibration absorber design.

In model simulations, the simply supported panel and centrally-located distributed absorber geometry and properties were those given in Table C.3. Values not indicated for the absorber layers either are unrelated or were mentioned in the earlier paragraphs

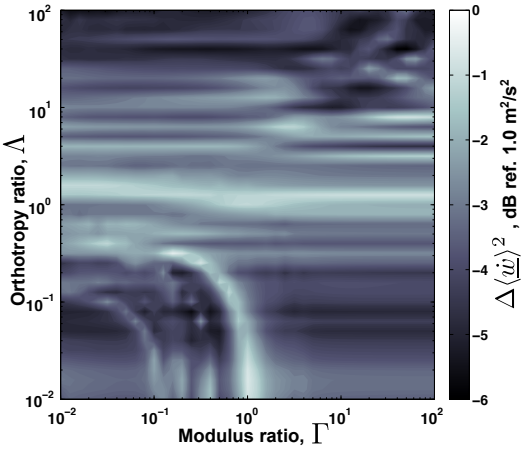

Figure C.2: Reduction in cumulative panel mean-square velocity from applied absorber, orthotropic and modulus ratios dependence

regarding their computation. The panel exhibited a (3,1) mode at 175.1 Hz while the absorber was tuned so as to yield a SDOF natural frequency of 172 Hz. As earlier, placement of the device at the center of the panel was intended to maximize the reactive effect of the absorber working against the panel given the antinode of the vibrational response at the panel center at 175.1 Hz. The distributed vibration absorber constituted a mass ratio of $\mu = 0.0388$. Furthermore, it is noted the present absorber design covers almost twice the surface of the panel (6.25% coverage) as compared to the device of Section C.3 (3.38%), and spans a number of asymmetric nodal lines.

Figure C.2 plots the reduction in cumulative mean-square panel velocity from 10 to 600 Hz over a range of Λ and Γ. In general, it is observed that modification to the modulus ratio does not significantly change the broadband vibration attenuation of the device on the panel. This is intuitive given that the practice of altering Γ in CLD materials is to achieve a more dramatic shearing effect between the host panel through the very thin viscoelastic layer. Compared to a viscoelastic layer, the present distributed spring layer is significantly thicker; thus, no dramatic improved shearing resistance is capable of being transmitted through the thicker intermediary

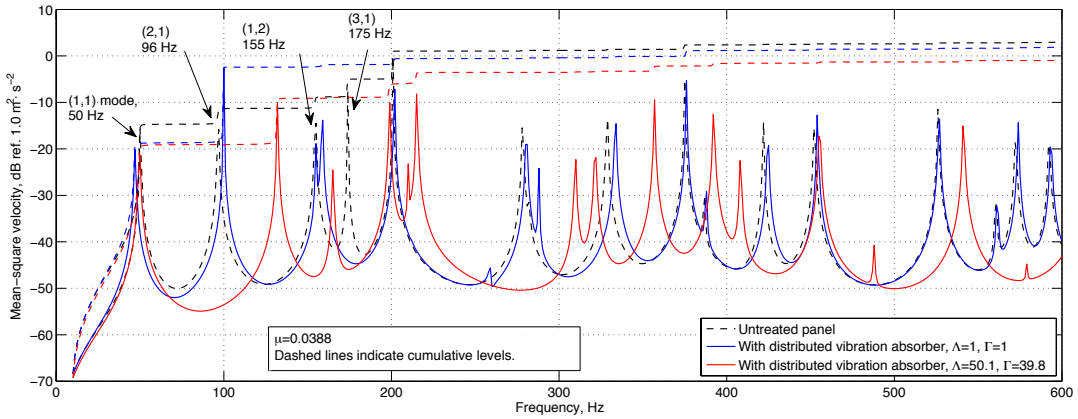

Figure C.3: Panel mean-square velocity, (black) untreated, (blue) with absorber $\Lambda = \Gamma = 1$, (red) with absorber $\Lambda = 39.8$, $\Gamma = 50.1$

layer between host structure and the top plate.

In contrast, it is evident that increased orthotropy ratio, Λ, plays a significant role in improving vibration suppression. However, increased Λ is not uniformly beneficial as there are regions in Fig. C.2 around $\Lambda = 1$ showing average panel vibration attenuation. Again, it is observed that larger values of Λ also indicate high shearing stiffness in the distributed spring layer. In practice, to achieve a device capable of transverse compressibility (yielding a SDOF natural frequency for reactive effects) but also high shearing stiffness is possible by means of corrugated spring layers, such as the conventional sinusoidal or circular corrugations in cardboard. One such embodiment by Cambou [104] appears particularly beneficial both theoretically and experimentally.

The optimum computed ratios were $\Lambda = 39.8$ and $\Gamma = 50.1$. Figure C.3 plots the panel mean-square velocity for this case, alongside the untreated results and the case of $\Lambda = \Gamma = 1$. Cumulative values are plotted as dotted lines. Recall that the absorber exhibited a SDOF natural frequency of 172 Hz, corresponding closely to the panel (3,1) mode at 175.1 Hz. The absorber having $\Lambda = \Gamma = 1$ clearly suppresses the panel vibration at its tuned frequency, but does not dramatically affect the panel response elsewhere, apart from the detrimental amplification of the (2,1) mode at 96.6 Hz. The

absorber having $\Lambda = 39.8$ and $\Gamma = 50.1$ drastically alters the panel response. This is primarily due to its placement at the center of the panel, along which many nodal lines occur. Asymmetric vibration modes are resisted, resulting in higher values of the natural frequencies: *e.g.* (2,1) at 96.6 Hz is shifted to 132 Hz, while (1,2) at 155 Hz is shifted to 165 Hz, and so on. In one sense, much of the panel vibration is redistributed to other frequencies, but on the whole increased broadband vibration suppression is achieved.

C.5 Case study: Modal absorber dynamics

In the history of vibration absorbers, a dynamic feature with little study is the manner in which modal dynamics affect a distributed absorber's net response. In other words, for continuous absorbers how do the modal dynamics of the distributed mass layer change the vibration attenuation performance?

Plate-type dynamic absorbers which covered the full surface of the host structural panel were considered by Aida et al. [16] but tuned by means of a two degree-of-freedom model. For a simply-supported host panel, this seems inadequate since the fundamental vibrational mode of the host panel is not uniform translational motion; however, the spring layer used in [16] were in fact discrete linear springs, more of an elastic foundation in practice, and dissimilar from the present continuous spring layer. Modal response of the attached plate-type absorber was not considered in the earlier work.

In extension of this, Oniszczuk [17] considered the case of plate absorbers utilizing continuous, massless Winkler foundations connected to the host vibrating plate. This scenario lends itself to resonance effects but is still incomplete in satisfying the present case of a continuous spring layer fully-coupled to the host panel and the top mass layer.

In the embodiment of the circular or annular platelike absorber by Snowdon [15], the device operated by means of modal behavior, although the pumping-type motion

Table C.4: Geometric and material specifications

Layer	Panel	Mass #1(#2)	Spring layer
a (mm)	300	90	90
b (mm)	300	90	90
h (mm)	3.7	2	50
E (Pa)	7.2e10	7.2e10 (1.3e9)	2e5
ρ (kg/m^3)	2100	2100	9
ν	0.3	0.3	—
η	1e-3	1e-3	5e-3
(x_{f_1}, y_{f_1}) (mm)	(144,127)	—	—

of the absorber was actually utilized to generate a point force, due to its discrete attachment method. In a similar design, Arpaci and Savci [71] observed the response of beam-type absorbers attached to plate structure via discrete springs. These, too, operated with modal dynamics, as well as translational (or SDOF) resonance, but the discrete attachment locations still differ than the present study. However, the unique observation in [71] was that the modal dynamic of the beam absorber was a more beneficial vibration suppression mechanism than the SDOF oscillation. In relation to the present study, this naturally indicates a pursuit of comparable performance benefit of utilizing the distributed top mass plate modal behavior in conjunction with the distributed spring layer. The clear difference between the present work and [71] is the use of a continuous spring layer as opposed to discrete springs.

To evaluate the difference between utilizing modal and translational dynamics of the distributed absorber, a new system was devised with geometric and mechanical properties as given in Table C.4. The first mass layer was designed so as to exhibit a SDOF natural frequency at the host simply-supported panel (1,1) mode, 229 Hz. The second centrally-located absorber design was modified such that the mass, assumed to be in free suspension, exhibited a "pumping" free vibration mode at 229 Hz. This required a reduced Young's modulus in the second mass layer as compared with the first design. A comparison between the two dynamic behaviors of the devices is shown in Figure C.4, as output from the following simulations, with the distortion of the spring layer superimposed and exaggerated to feature the dynamics involved. Since

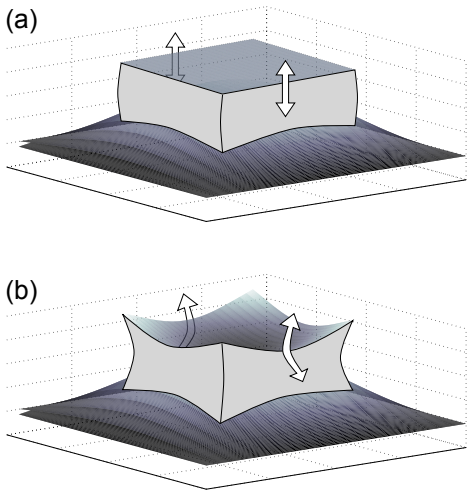

Figure C.4: (a) Translational (SDOF) dynamic of absorber; (b) Modal dynamic of absorber on a SS panel vibrating in (1,1) mode.

Table C.5: Cumulative mean-square velocity reduction, dynamics dependence

Tuned dynamic	10-400 Hz	10-1000 Hz
Translational	-5.72	-1.35
Modal	-7.20	-1.69

all other dimensions and parameters remained the same between the two absorber designs, both devices had a mass ratio of $\mu = 0.0539$. The simulation was run from 10 to 1000 Hz in 1 Hz increments.

Table C.5 presents the reduction in panel mean-square velocity for two bandwidths, that around the (1,1) host panel resonance and the broadband computation. The absorber designed for modal response of the top mass outperforms the translationally absorber design both around the targeted panel resonance and broadband. This exactly corroborates with the findings in [71] for beam absorbers, although in this case the distributed spring layer is completely coupled to the host structural motion. Figure C.5 plots the panel mean-square velocity around the (1,1) simply-supported mode. Very apparent is the split resonance from the addition of the vibration absorbers. Since there is minimal damping in the fully coupled system, the two new resonances are themselves fairly undamped. However, it is observed that the higher

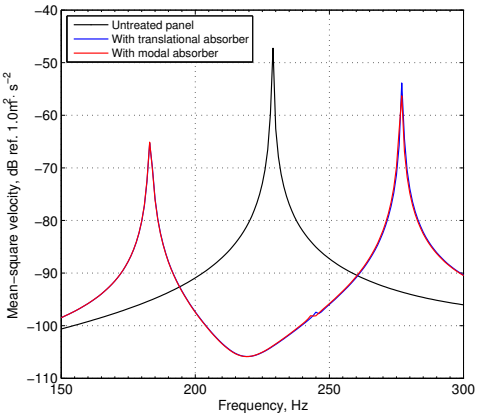

Figure C.5: Panel mean-square velocity, (black) untreated, (blue) with absorber having targeted SDOF resonance, (red) with absorber having targeted modal resonance

of the two resonances, 277 Hz, is suppressed by almost 3 dB more with the modal absorber than the translational dynamic device.

C.6 Case study: Orthotropic and damped spring layers

The potential to alter the frequency response of the host panel by means of a substantial resistance to its flexure suggests that incorporating a highly damped spring layer material will yield significant dissipative effects. While a very thick layer of CLD with a heavy mass on top somewhat represents this scenario, the orthotropy ratio, Λ, indicates that the spring layer would have great bending stiffnesses, which is not the case for a viscoelastic material. Thus, a distributed spring layer with a high orthotropy ratio as well as high dampening may be practically achieved by using a corrugated core layer constructed from plastic, for example, or by laminating a damping material in a composite sheet prior to corrugation, Figure C.6.

The modeling setup of Section C.4 was again employed, this time modifying the orthotropy ratio, Λ, along with the loss factor of the spring layer, η. The reduction in cumulative mean-square panel velocity from 10 to 600 Hz is plotted in Figure C.7 for the computed ranges of Λ and η of the spring layer. Not surprisingly, high levels of

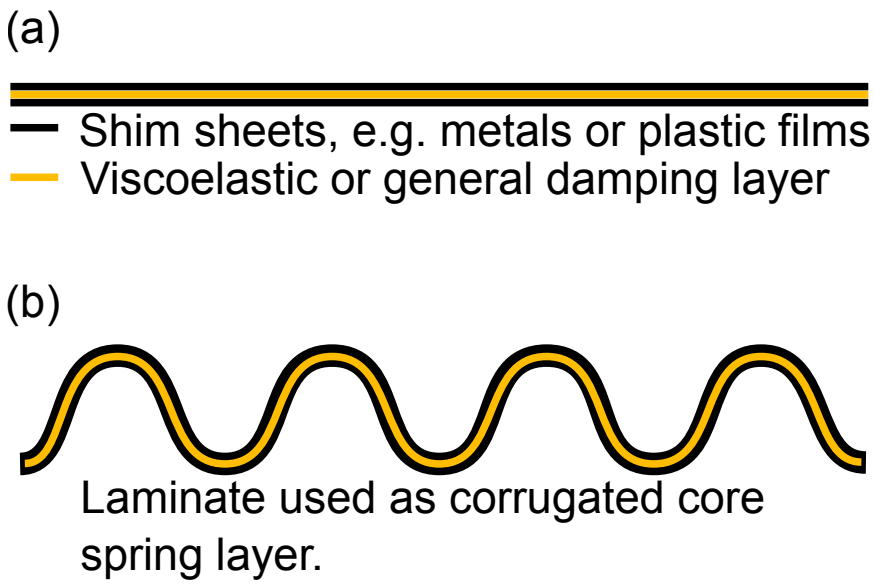

Figure C.6: Laminated core design to increase net dissipative effects. (a) Component lay-up. (b) Corrugation of net laminate material to yield a distributed spring layer.

damping in the absorber spring layer contribution to the greatest reduction in panel mean-square velocity.

More difficult to delineate from the plot due to the large magnitude of vibration suppression predicted is the fact that the optimum ratio of orthotropy is $\Lambda = 7.9$ for $\eta = 10$. However, decreases in η, which would represent more realistic materials opportunities in design, encourages greater ratios of orthotropy in the spring layer. Recall that ratios of orthotropy $\Lambda > 1$ indicate that the bending stiffnesses of the spring layer are greater than the transverse stiffness which determines the SDOF natural frequency. For high bending stiffnesses, greater dampening in the layer would assist in turning the resistive effects of the spring layer into a mechanism of dissipation.

To examine further why both large dampening and high ratios of orthotropy are beneficial in tandem, two scenarios of the above series of simulations are carried out. A moderate loss factor is assumed, $\eta = 0.1$. This may represent a reasonable loss factor achieved from the laminated corrugated core design of Figure C.6 as measured by experiment. Two ratios of orthotropy are considered, $\Lambda = 1$ and $\Lambda = 25$. Figure C.8

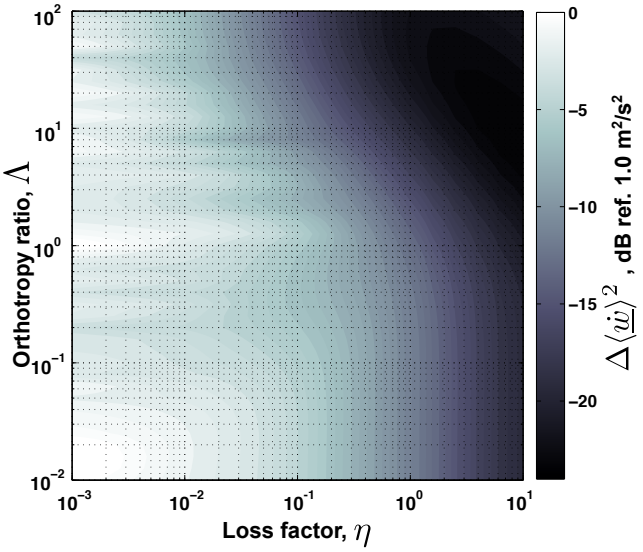

Figure C.7: Reduction in cumulative panel mean-square velocity from applied absorber, orthotropic ratio and loss factor dependency.

plots the panel mean-square velocity over the range of frequencies before computed. Note that the case of $\Lambda = 1$ and insignificant dampening, $\eta = 5e - 3$ was already plotted in Figure C.3. Cumulative values are shown as dashed lines.

In Figure C.3 it was found that the lightly damped absorber device was primarily beneficial at its natural frequency, reactively suppressing the panel vibration dramatically. However, simply increasing the spring layer dampening is found to significantly improve the overall level of vibration attenuation achieved, the blue plot of Figure C.8. Even without increasing the orthotropic characteristics of the spring layer, the spring dissipates significantly greater vibrational energy. Of distinction is the unusually great suppression at the first panel mode, (1,1) at 50 Hz. An illustration may help explain this effect.

Figure C.9 depicts the manner of deformation in the spring layer for the case of the (1,1) mode and the (2,1) mode, shown along a central cross-section of the host panel. When excited by the symmetric first mode, the attached device is excited by structural vibration below its natural frequency and thus moves in-phase with the excitation. As a result, the spring layer of the device is very distorted, stretched in

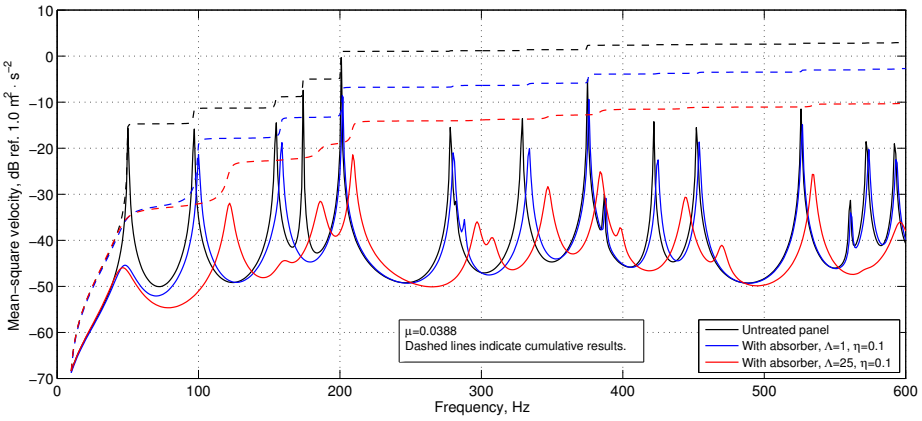

Figure C.8: Panel mean-square velocity, (black) untreated, (blue) with absorber $\Lambda = 1$ and $\eta = 0.1$, (red) with absorber $\Lambda = 25$ and $\eta = 0.1$

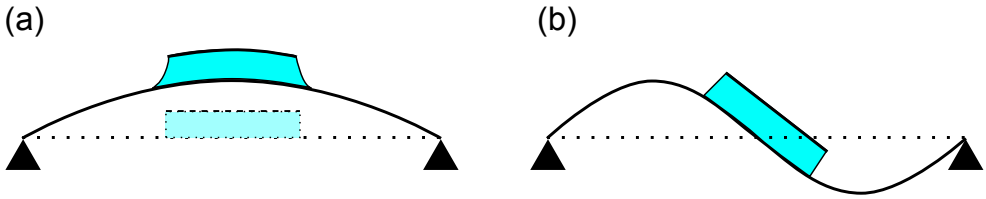

Figure C.9: Centrally-located absorber device in simply-supported panel, cross-section along panel center. Excited by (a) (1,1) mode vibration. (b) (2,1) mode vibration.

both directions. Increasing the dampening of the spring layer lends a great dissipation for the vibration at this frequency. Thus, the (1,1) mode in Figure C.8 is much suppressed from untreated levels. Though the ratio of orthotropy in the spring layer is unity, this dissipative mechanism is clearly a resistive effect.

Yet, this is clearly a resistive effect coincidentally utilized due to the device placement. Note in Figure C.8 that the next two highest modes, (2,1) and (1,2), are asymmetric and are both negligibly attenuated compared to the first mode. With the device centrally-located, as Figure C.9 (b)indicates, there is almost no deformation in the spring layer. Even with a higher loss factor, η, the device is not positioned so as to attenuate these modes. Were the device shifted so as to coincide with the anti-node of the (2,1) mode, much greater vibration suppression could be achieved

due to the same effect of Figure C.9 (a).

Section C.4 found that increased orthotropy ratios increased the resistive effects of the spring layer. Thus, Figure C.8 shows that for $\Lambda = 25$ the asymmetric modes are shifted upwards in frequency. The additional dampening, however, increases dissipative effects. The cumulative result being an increase in dissipative resistive effects. This is in contrast to merely increasing resistive effects (Figure C.3 red plot) or merely increasing dissipative effects (Figure C.8 blue plot).

Despite the opportunities posed, the ultimate challenge is in the material design. Namely, the development of a continuously distributed spring layer having *(1)* highly orthotropy material characteristics, *(2)* transverse compressibility, and *(3)* a high loss factor. Two of the three are not difficult to achieve with many common materials or products; for example, carbon composites are known for having *(1)* and *(3)*, and the classical dashpot damper of course exhibits *(2)* and *(3)*. Novel material design is therefore necessary to find a balance of all three desired features. Again, one such approach is the corrugated design indicated earlier, which utilizes a laminated damping material to help increase the net loss factor.

C.7 Case study: Variable stiffness spring

An advantage in achieving broadband vibration attenuation using an array of mass-spring-dampers is that each may be tuned to a target frequency, and positioned accordingly [105, 10]. For instance, if reduction of the lowest order panel modes is desired with a set limit on total added mass and number of oscillators, even heuristic optimization tactics may be employed to determine optimum tuning and positioning of the oscillators for maximum vibration control [106, 107]. Even active approaches to tuning, sometimes termed adaptive tuning, have been explored with great success [108, 109]. Thus, on the surface it appears that point oscillators have this distinct advantage against the continuous vibration absorber concept.

However, it is not impossible to achieve a continuous spring layer exhibiting unique

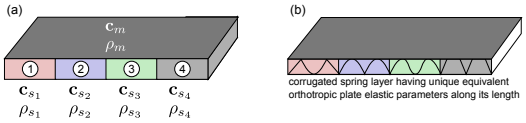

Figure C.10: (a) Continuous vibration absorber having unique stiffnesses along the length, (b) one embodiment of the concept using a corrugated spring layer.

stiffness characteristics along its length. For instance, Figure C.10 (a) presents a generic diagram of such a device, with unique thick plate elasticity parameters, $\mathbf{c}_{s_i}$, and densities, ρ_{s_i}, at certain positions through the spring length. This could be achieved by using several types of poroelastic material or foams, or, in another embodiment, may be met by using a continuous corrugated spring layer having distinct corrugations along the length, Figure C.10 (b). In the latter case, the equivalent thick orthotropic plate characteristics may be determined through homogenization methods [110, 111] in order to include the layer in a continuum domain analysis.

There may be concerns in employing such a variable stiffness spring layer. The first is to determine an appropriate range of variation in the transverse stiffness, that which directly relates to the SDOF natural frequency. The second may be the manner of variation, namely decreasing from one end to the other, or increasing from the ends towards the center, and so on. Finally, the stiffness of the top mass could be of issue; significant rocking or rotation of the mass could result if the mass is very stiff relative to the variable spring layer, and a softer mass layer might be preferable to maximize the utility of the variable stiffness design.

Thus, to consider these possibilities, the analytical model is employed to evaluate the usefulness of the variable spring concept in continuously distributed absorbers. The modulus ratio, Γ, of Section C.4 is required, as is a new non-dimensional parameter to relate to the varying transverse stiffness. (In the following, the subscript s is dropped on terms E, G and ν assuming the reader understands these elasticity parameters are all related to the spring layer). A parameter is defined, the variable stiffness ratio: $\Xi = (\max[(E_z)_i] - \min[(E_z)_i])/\text{mean}[(E_z)_i]$, where $(E_z)_i$ is the trans-

verse stiffness of the i^{th} section of the spring layer. It is assumed that the transverse compressibility of the continuous spring layer to be primarily decoupled from the bending and shear stiffnesses of the layer [65]; in other words, $\nu_{yz} = \nu_{xz} \ll 1$. Large Ξ would represent distributed absorbers with significantly differing SDOF resonance characteristics along the length.

In the following exercise, it is assumed that the variable stiffness characteristics of a given continuous spring layer may be incorporated by piece-wise linear evaluation of the individual segments. Thus, from Eq. C.2 and C.3, for a single continuous device the contribution of kinetic and potential energy for the spring layer is simply the sum of the individual layers

$$T_{spring} = \frac{1}{2} \sum_{i=1}^{5} \rho_i \int_{V_{s_i}} (\dot{\mathbf{u}}_{s_i})^t \, \dot{\mathbf{u}}_{s_i} \mathrm{d}V_{s_i} \tag{C.14}$$

$$U_{spring} = \frac{1}{2} \sum_{i=1}^{5} \int_{V_{s_i}} (\epsilon_{s_i})^t \, \mathbf{c}_{s_i} \epsilon_{s_i} \mathrm{d}V_{s_i} \tag{C.15}$$

while the contribution of the continuous mass layer is evaluated in the same manner as before. As mentioned above, it is also necessary to specify the manner in which the stiffness varies. In the simulations, it is assumed that the stiffness varies, in 5 segments, from "softest" spring to "stiffest", in the manner indicated in Figure C.11. This construction inhibits the potential, for instance, of substantial side-to-side rocking of the device if the stiffest spring layer component was in the middle of the continuous layer. Though rocking would be possible for any form of variable stiffness spring layer, the form utilized in Figure C.11 would result in the least detrimental effects. This is observed in simulation exercises where it is also found that non-uniform stiffness variation—*i.e.* stiffer in the middle with softer sections on either side—tend to result in limited benefit to the variable stiffness design.

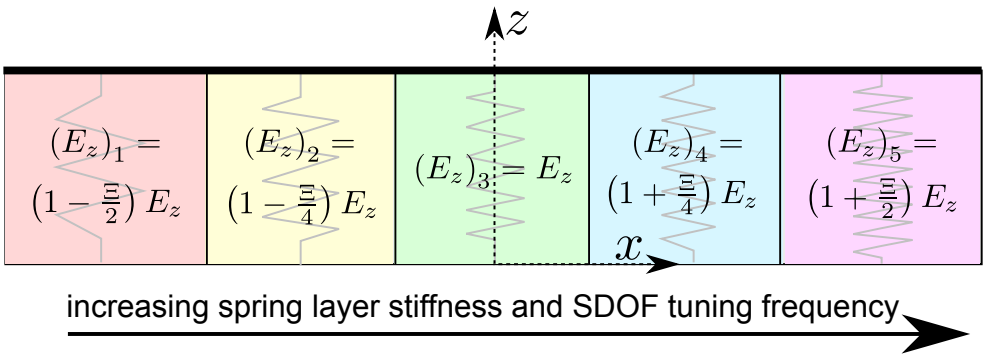

Figure C.11: Piece-wise linear variable stiffness distributed absorber.

Table C.6: Geometric and material specifications

Layer	Panel	Mass	Spring layer
a (mm)	600	180	180
b (mm)	400	150	150
h (mm)	2	1	50
E (Pa)	7.2e10	7.2e10	1.2e5
ρ (kg/m^3)	2100	2100	9
ν	0.3	0.3	—
η	1e-3	1e-3	5e-3
(x_{f_1}, y_{f_1}) (mm)	(144,127)	—	—

In the following model evaluations,

$$(E_x)_i = (E_y)_i = (E_t)_i = 1.2e5 \text{ Pa}$$
$$(\nu_{xz})_i = (\nu_{yz})_i = (\nu_{zx})_i \, (E_t)_i \, / \, (E_z)_i \qquad (\nu_{yx})_i = (\nu_{xy})_i = 0.2 \qquad (\nu_{zy})_i = (\nu_{zx})_i = 2e-5$$
$$(G_{xy})_i = (E_t)_i \, / 2(1 + (\nu_{xy})_i) \qquad (G_{yz})_i = (E_t)_i \, / 2(1 + (\nu_{yz})_i) = (G_{xz})_i \qquad \text{(C.16)}$$

and the remaining parameters for simulation are given in Table C.6. The Young's modulus indicated in Table C.6 for the spring layer corresponds to E_z when $\Xi = 0$, in other words the transverse stiffness of the central element in Fig. C.11. The panel was simply supported and the continuous distributed vibration absorber device was centrally-located. The absorber represented a mass ratio of $\mu = 0.0684$.

Figure C.12 plots the cumulative reduction in the panel mean-square velocity from 10 to 600 Hz for a range of Γ and Ξ. Values of $\Xi > 1$ were not considered as, in practice, too broad of variation in the transverse stiffness would result in significant

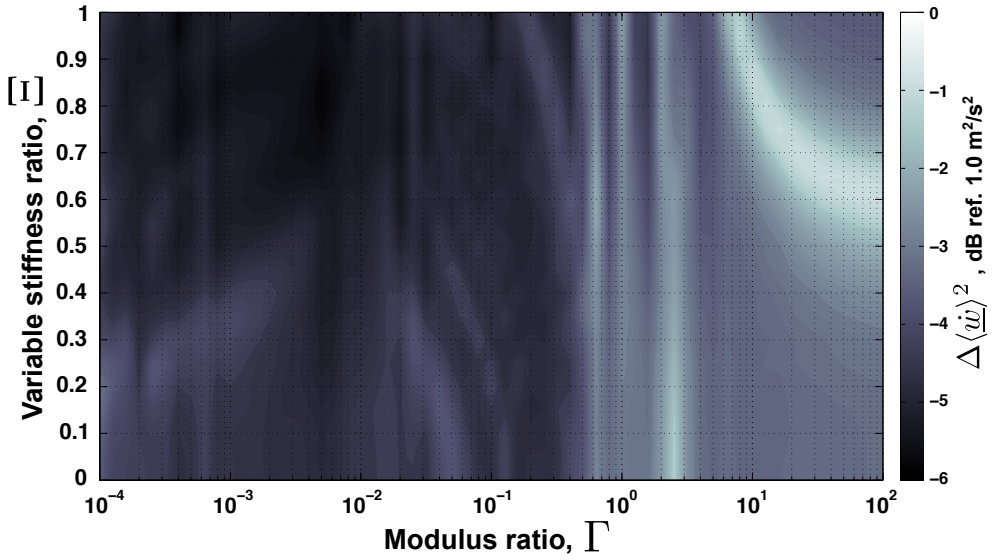

Figure C.12: Reduction in cumulative panel mean-square velocity from applied absorber, variable stiffness and modulus ratios dependence.

rocking of the mass layer, reducing the reactive force component normal to the displacement of the host structure. In this plot, note that $\Gamma = 1$ and $\Xi = 0$ indicate the continuous absorber design using a mass layer of the same Young's modulus as the host panel and a spring layer of uniform transverse stiffness along the length. This mark serves as a reference position against which other regions of the plot may be compared.

Around $\Gamma = 1$, changes in the stiffness ratio do little to improve or modify the capability of the distributed absorber device to attenuate the panel vibration. In fact, increases in the modulus ratio along with increases in Ξ result in a reduction in vibration suppression, observed by the region particularly around $\Gamma = 30$ and $\Xi = 0.7$. However, for narrow bands around $\Gamma = 1$, increased Ξ does in fact steadily increase the global vibration reduction, notably at $\Gamma = 0.8$ and $\Gamma = 1.7$. Thus, changes in the transverse stiffness of the device, accompanied by a small increase or decrease in the modulus ratio, improves the global vibration suppression capability by several dB.

However, most noticably from Figure C.12 is the benefit of both increased Ξ and a

much reduced Γ. When $\Gamma = 10^{-2}$ to 10^{-3}, a variable stiffness spring layer design can provide nearly a reduction of half (-6 dB) of the cumulative panel vibration levels. While large Ξ may result in a broad range of tuned natural frequencies, maintaining a stiff top mass layer is likely to yield a device susceptible to significant rocking. Reduction of the modulus ratio, *i.e.* using a softer material as the continuous top mass layer, allows the full variation of the transverse stiffness to be utilized.

The lack of a visible convergence as Γ is reduced and Ξ is increased may be explained simply by two factors: the use of a cumulative metric of evaluation and piece-wise continuous spring layer assumption. Firstly, in many of the numerical experiments employed, the dual reactive and resistive effects of the continuous absorber designs shift and modify the locations of some of the panel resonances, particularly around the cut-off of the sum at 600 Hz. Thus, as some of these resonances are pushed beyond 600 Hz or pulled back within the considered bandwidth, the cumulative reduction in mean-square velocity is constantly shifted. Were the simulations leading to Figure C.12 instead evaluated at a single frequency, convergence would be very clear. But to evaluate broadband performance of the continuous absorber designs, a broadband metric is necessary. Secondly, having discretized the continuous spring layer into only 5 segments, due to cost of computing the necessary matrices involved in Eq. C.14 and C.15 for each component, creates larger and larger jumps in material properties from layer-to-layer as Ξ is increased. The effects of these discontinuities also inhibits perfect convergence for larger values of Ξ.

The best case of panel vibration suppression indicated in Figure C.12 occurs for $\Gamma = 0.005$ and $\Xi = 0.85$. For the baseline $E_z = 1.2e5$ Pa, this range of SDOF tuning frequencies achieved for $\Xi = 0.85$ was computed using the model to be 124 to 199 Hz. This range is situated precisely around a number of the simply supported panel resonances. Figure C.13 plots the panel mean-square velocity for this optimal design, along with the case of $\Gamma = 1$ and $\Xi = 0.85$, which may be described as a design more susceptible to the rocking effect of the mass layer. Cumulative values of

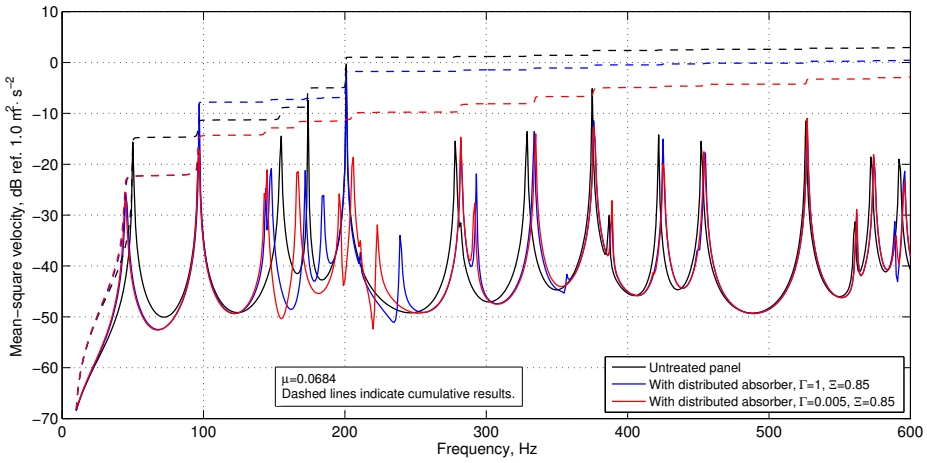

Figure C.13: Panel mean-square velocity, (black) untreated, (blue) with absorber $\Gamma = 1$, $\Xi = 0.85$, (red) with absorber $\Gamma = 0.005$, $\Xi = 0.85$.

panel mean-square velocity are presented as dashed lines.

The absorber design employing $\Gamma = 1$ is seen to adversely amplify the (2,1) mode of the panel at 96.6 Hz but does attenuate the panel resonances over the tuning frequency bandwidth. This design is least capable of suppressing the mode at 200 Hz, though the high-end of the tuning frequency range should correspond almost identically to this frequency.

The absorber employing both the variable stiffness in the spring layer as well as the reduced modulus ratio is observed to be much more beneficial in narrow band and broadband comparison. Even the mode at 96.6 Hz, well outside of the tuning frequency range, is reactively attenuated. Were this simply an effect of mass loading the structure, the frequency of the resonance would correspondingly shift, but this is not observed.

Over the tuning frequency bandwidth, a dramatic reduction in the panel vibration is observed for the absorber having $\Gamma = 0.005$ and $\Xi = 0.85$. Though many of the untreated panel resonances are split due to the reactive effects of the device, these split resonances are each suppressed, nearly equally in fact. Figure C.14 plots the

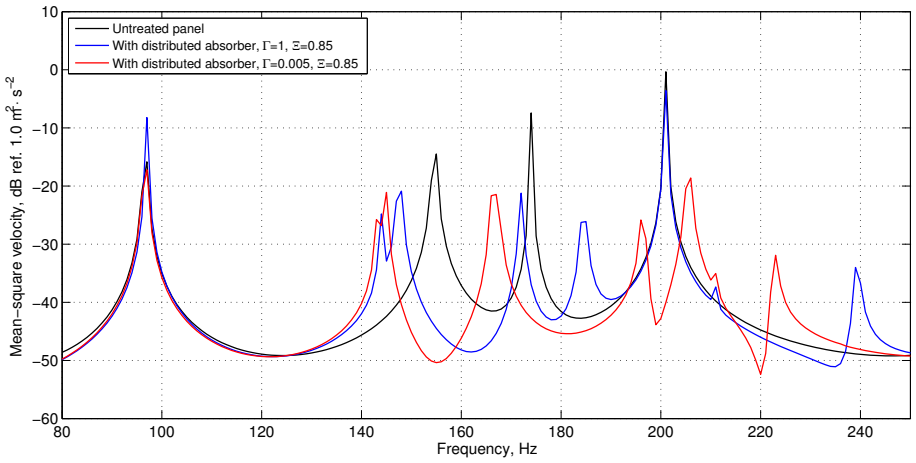

Figure C.14: Panel mean-square velocity (80–250 Hz), (black) untreated, (blue) with absorber $\Gamma = 1$, $\Xi = 0.85$, (red) with absorber $\Gamma = 0.005$, $\Xi = 0.85$.

results of Figure C.13 but zoomed in to the tuned frequency range to better observe the result.

The objective of equalizing split resonances for vibration absorbers on vibrating structures is the hallmark of textbook optimal damping [82]. It appears that reduction of the modulus ratio allows the employment of a variable stiffness spring layer to effectively optimize the dampening of each of the split resonances such that the maximum global vibration reduction is achieved. Figure C.13 shows that cumulatively, up to 200 Hz, the absorber having both $\Gamma = 0.005$ and $\Xi = 0.85$ has reduced the panel vibration levels by more than 11 dB. This is a substantial reduction for a spring layer having minimal damping, $\eta = 5e - 3$, and given the fact that 5 panel resonances occur in the bandwidth.

C.8 Conclusions

In the long history of the vibration absorber, few studies have been reported of the potential benefits of distributed and continuous absorber designs as compared with arrays of conventional mass-spring-dampers, sometimes inconveniently termed “dis-

tributed vibration absorbers." A model based on Hamilton's principle was briefly described to simulate the forced response of a host structural panel to which continuously attached distributed vibration absorber devices and point oscillators were attached. The uniqueness of the present study is that the continuously distributed devices may suppress the host panel vibration by both reactive and resistive means, the prior being the trademark of classical mass-spring systems while the latter is ascribed to common constraining-layer treatments.

The model was employed for a number of scenarios in which the unique vibration absorber dynamics may be specifically explored. First, the continuity of such devices was considered; next, the modulus and "orthotropy" ratios were considered which modified the top mass and distributed spring layer characteristics, respectively; the potential advantage of employing the modal dynamics of the distributed top mass layer were evaluated; the effects of modifying damping in an orthotropic spring layer were studied; and, finally, the use of a spring layer exhibiting variable transverse stiffness was evaluated.

In common with CLD treatments, segmentation of the distributed absorber devices was beneficial in improving narrow- and broadband vibration suppression, but significant segmentation reduced the performance of the devices in working against the host structure. This appears to be a trade-off between the two dynamic regimes: reactance and resistance. The modulus ratio between the top mass layer and the base panel was observed to play a minor role in the vibration attenuation performance of the device. In contrast, the distributed spring layers having larger orthotropy ratios were found to significantly alter the host structural vibration by resisting the motion and redistributing the asymmetric resonances, but more importantly increased the vibration suppression capability of the device.

The benefits of tuning a distributed vibration absorber to operate in the freely-suspended pumping mode of the mass layer were found to be greater than the device when tuned to operate in SDOF resonance. Both narrowband and broadband panel

vibration attenuation were improved when the distributed mass layer oscillated with modal dynamics as opposed to SDOF dynamics. As illustrated in Figure C.4, tuning to the modal operation of the mass layer deforms the distributed spring layer to a greater extent than the translational dynamic. For continuous spring layers exhibiting higher values of dampening, the benefit of this distortion may be exploited to dissipated greater energy and increase narrow and broadband passive control performance.

It was found that distributed devices may be practically useful below their SDOF natural frequency when employing continuous spring layers having a substantial orthotropy ratio and damping. Since the devices move in-phase with structural vibration below the SDOF natural frequency, the device is limited to resisting the structure motion in this bandwidth. Use of more highly damped spring layer material was observed to lend a substantial dissipative effect. The combination of high spring layer orthotropy ratio and damping could be achieved by employing a corrugated spring layer composed of a laminate material containing a viscoelastic layer in the lay-up.

A spring layer having a varying transverse stiffness theoretically allows a continuous absorber device to exhibit a multitude, or bandwidth, of SDOF natural frequencies. Consideration of the range of stiffness variation was taken into account alongside changes in the modulus ratio. It was observed that certain levels of transverse stiffness variation in conjunction with a decreased modulus ratio could lend a substantial increase in broadband vibration suppression. Plots of the predicted panel mean-square velocity for these cases showed that the effect of reducing the modulus ratio assisted in the equalization of the split resonances occurring as a result of the application of the reactive device having multiple natural frequencies. In the absence of dampening in the spring layer, reduction of the modulus ratio for a variably-tuned continuous absorber provides an effective level of dampening to optimize the vibration suppression capability.

In summary, while the dynamic vibration absorber has been studied extensively,

the consideration of distributed and continuous embodiments of the device have been sparse. Modeling of this manifestation of the vibration absorber shows distinct advantages over point mass-spring-damper systems, not least of which is the dual dynamics of reactive and resistive effects. This naturally makes such continuous absorbers more useful in both the tuned and wider bandwidths. New embodiments of a classic device may yield improved broadband passive vibration control opportunities by consideration of the presented results.

APPENDIX D

Modeling and validation of a passive distributed vibration control device using an elastic superposition technique

The modeling of a distributed vibration control device is considered for use in predicting the vibration attenuation benefits and best design practices when such devices are attached to vibrating structures. Exact 3D finite element (FE) analysis is possible but the geometric intricacies of the distributed spring layer and potential lack of symmetries of the device placement on a host structure make such a model expensive to compute, particularly for optimization purposes. Thus, an equivalent 2D model is desirable, whereby conventional Ritz-method solution forms may be implemented. This chapter describes the continuum domain model of interest and explores the applicability of a superposition approach by which a non-continuous distributed spring layer is homogenized into a 2D continuum. Simple FE models are described which allow computation of the required elasticity parameters of the spring layer. An eigenfrequency analysis comparing 3D FE and 2D model results show good agreement in the lowest order natural frequencies over a range of typical device design parameters. A series of experimental validations of the numerical approach is provided which show considerable agreement between laboratory measurements to predicted results. Finally, the extensibility of the superposition approach is considered showing a range of design parameter values around which the technique appears most accurate.

D.1 Introduction

An on-going aim of passive vibration control materials is to simultaneously achieve low and high frequency structural vibration attenuation while contributing only a small additional mass to the host structure. Some successful theoretical or experi-

mental embodiments in this pursuit have featured viscoelastic, poroelastic or vertical discrete spring layers along with some form of distributed mass [13, 112, 113, 14]. A design employing a distributed spring layer composed of a damping or viscoelastic material allows the passive treatment to operate in dual dynamic regimes: at low frequencies like a traditional point vibration absorber as the mass may provide a re-active forcing effect at a natural frequency; and at high frequencies in a manner identical to constraining-layer damping treatments.

One such treatment, originally termed the distributed vibration absorber [19], utilizes a distributed woven, or corrugated, spring layer and a distributed mass layer, Figure D.1. The distributed spring layer is geometrically identical to a number of common sandwich panel designs with the added feature that it is transversely compressible. While full three-dimensional FE analysis may assist in the study of such a device when attached to an arbitrary vibrating structure, the intricacies of the device geometry and any asymmetries in the full system make solution to such a finite element model a computationally expensive task. It is therefore useful to model the coupled system in an equivalent two-dimensional, continuous domain, approximate solutions to which are much more readily achievable, using the Ritz method, for instance.

However, due to the transverse deformability of the vibration control device, application of most sandwich panel theories is limited since they frequently employ incompressibility assumptions in derivation. Practically speaking, most sandwich structures are designed for *strength*, so as to avoid transverse deflection, or buckling. A few methods to include compressibility in the analysis have been explored: for example, higher-order theories (a number of which are summarily reviewed in [114]), the elastic foundation approach [115] and a superposition method [65].

The latter approach superposes incompressible sandwich panel theory with a decoupled compressible core and was found to accurately predict static and dynamic deflection and stress for sandwich panels having both symmetrical and asymmetrical

geometries [116]. This method is hereby explored for the study of the distributed spring layer of the vibration control device.

Although a number of homogenization techniques for corrugated panels are available, a thorough review of available methods is described in [62], the incompressible sandwich panel theory employed in this work follows from the derivation of Libove and Batdorf [110]. The derivation applies to sandwich panels of arbitrary, periodic cross-section and yields the equivalent bending, twisting and shear stiffnesses for an equivalent orthotropic 2D panel. This analysis also included careful laboratory experiments which may be carried out to directly calculate the approximate elasticity parameters. Cheng et al. [111] described the corresponding FE models which may substitute for the experiments and allow for quick calculation of the needed elastic constants.

The equivalent transverse stiffness for the compressible core may be approximated using classical, linear elasticity theory. Thus, the superposition of these two elastic responses may represent the full dynamic characteristics of the distributed spring layer in Figure D.1. Though the superposition approach was derived for core layers having both continuous and non-continuous contact with the facing sheets, for example both honeycomb and foam cores, its application appears to be primarily concerned with foam core materials. As compared with a corrugated sandwich structure like the distributed spring layer of interest, a foam layer more closely resembles a truly continuous material. It does not appear that an investigation has been carried out to evaluate the applicability of this method to core layers of corrugated geometry. The determination of how useful the superposition method may be for corrugated core geometries would be beneficial for future modeling directions.

This paper aims to describe the full modeling approach for the distributed vibration control device and compare results with exact 3D FE models. To do so, an eigenfrequency analysis is performed and computed frequency response functions are compared. Afterwards, the extensibility of the superposition method is assessed by

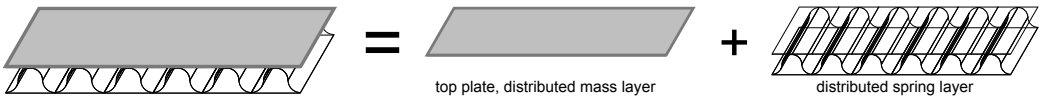

Figure D.1: Components of distributed vibration control device.

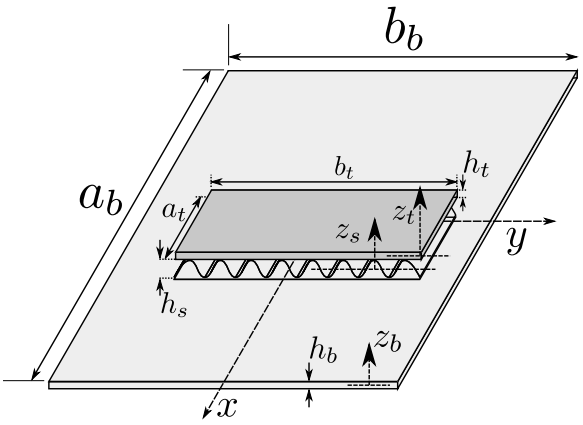

Figure D.2: Vibration control device attached to an arbitrarily bounded and excited base plate (subscripts b, s, t indicate base, spring layer and top plates, respectively).

considering a range of sandwich panel designs, those of significant to insignificant transverse compressibility.

D.2 Modeling methodology

The geometry desired to study is shown in Figure D.2. A vibration control device having a distributed, woven spring layer is attached to a base plate having both arbitrary boundary conditions as well as arbitrary excitation. The vibration control device is composed of two components: a top plate, representing the distributed mass layer, and a transversely flexible, anisotropic spring layer, Figure D.1.

The vibration control device with a distributed spring layer having a woven core exhibits dynamic behavior ascribed to both conventional single degree-of-freedom (SDOF) vibration absorbers and constrained layer damping treatments, Figure D.3 (a) and (b), respectively. In addition, the core layer uses a sandwich design having apparent anisotropic stiffnesses. Therefore, a continuum domain model suitable to assess vi-

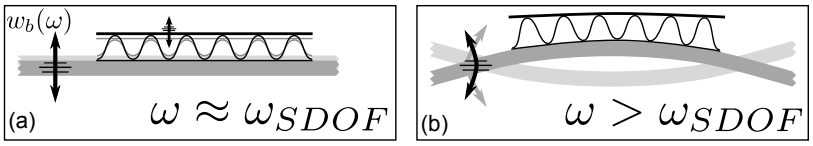

Figure D.3: Device response to host structural vibration above (a) and below (b) the device SDOF natural frequency.

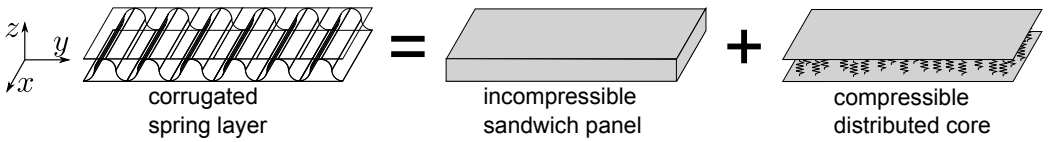

Figure D.4: Approximation of compressible spring layer as the superposition of an incompressible core with a layer of transversely compressible springs.

bration control devices using such a distributed spring layer requires the combination of equivalent anisotropic material properties as well as flexible core characteristics.

In the proposed model, the sandwich structure is considered to be a superposition of an incompressible, orthotropic thick plate and a compressible core of vertical spring elements, Figure D.4. The latter springs are allowed to deflect only in the transverse direction and have no coupling to the incompressible plate response.

D.2.1 Equivalent incompressible core elastic properties calculations

Libove and Batdorf [110] derived a theory for the determination of equivalent orthotropic plate properties for incompressible sandwich panels having an arbitrary

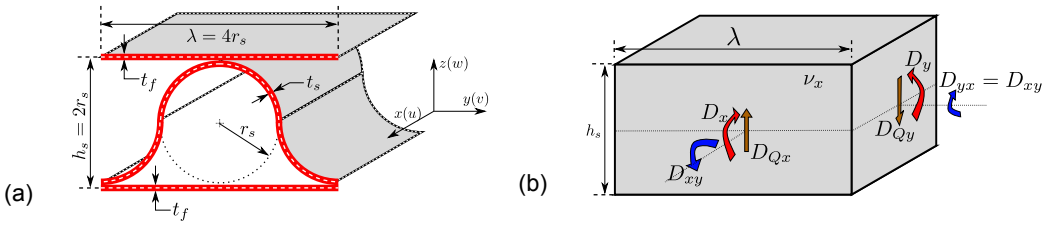

Figure D.5: Periodic geometry of an (a) unit depth circular core sandwich panel transformed into (b) an equivalent, continuous orthotropic thick plate.

core design, thereby transforming the exact core geometry into an equivalent, symmetric and continuous 2D domain, Figure D.5. Included with the derivation were a series of laboratory tests which may be carried out to determine the elasticity constants. Cheng et al. [111] then proposed and validated a set of corresponding FE models to expedite the computation of such elastic properties. The latter FE models are here employed for the present sandwich structure.

The distortion equations for the incompressible sandwich panel are [110]:

$$\kappa_x = \frac{\partial^2 w}{\partial x^2} = -\frac{M_x}{D_x} + \frac{\nu_y M_y}{D_y} + \frac{1}{D_{Qx}}\frac{\partial Q_x}{\partial x} \tag{D.1}$$

$$\kappa_y = \frac{\partial^2 w}{\partial y^2} = -\frac{M_y}{D_y} + \frac{\nu_x M_x}{D_x} + \frac{1}{D_{Qy}}\frac{\partial Q_y}{\partial y} \tag{D.2}$$

$$\kappa_{xy} = \frac{\partial^2 w}{\partial x \partial y} = \frac{M_{xy}}{D_{xy}} + \frac{1}{2}\frac{1}{D_{Qx}}\frac{\partial Q_x}{\partial y} + \frac{1}{2}\frac{1}{D_{Qy}}\frac{\partial Q_y}{\partial x} \tag{D.3}$$

$$\gamma_{yz} = \frac{Q_y}{D_{Qy}} \tag{D.4}$$

$$\gamma_{xz} = \frac{Q_x}{D_{Qx}} \tag{D.5}$$

where M_x and M_y are internal bending moments, M_{xy} is the internal twisting moment, Q_x and Q_y are internal shearing forces, and ν_x and ν_y are the Poisson's ratios coupling the bending responses. These moments and forces are labeled for a unit core cross-section in Figure D.5 (b) having thickness h_s and period length λ. The curvatures and twist, κ_x, κ_y and κ_{xy}, are defined about the middle-plane of the panel and γ_{yz} and γ_{xz} are the transverse shear strains.

The facing sheets and the core layer are considered to be isotropic materials. The FE models to calculate the equivalent stiffnesses for the sandwich structure define a 3D geometry of a certain section of the sandwich core, apply the loads described in the distortion equations and calculate the resulting strains or displacements from key nodes. Shell elements are employed for each model.

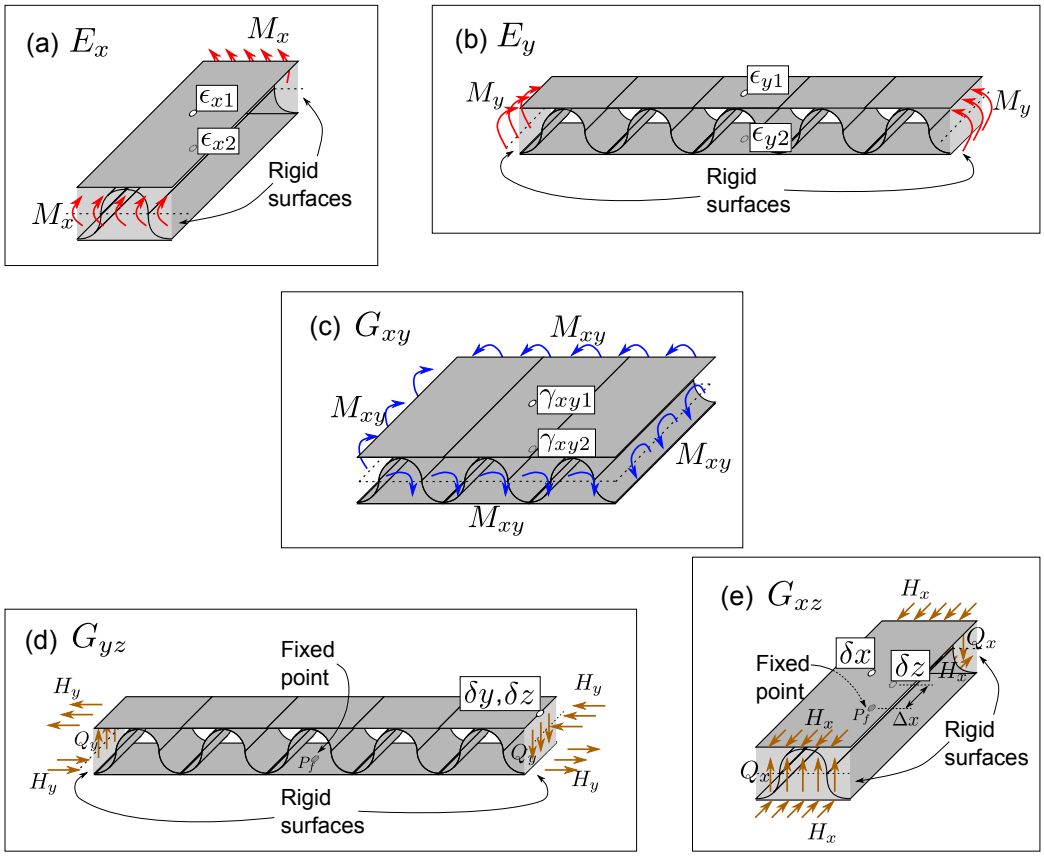

Figure D.6: FE models for computation of (a) E_x, (b) E_y, (c) G_{xy}, (d) G_{yz} and (e) G_{xz}.

The FE models to compute the elastic constants of the incompressible sandwich panel—E_x, E_y, G_{xy}, G_{yz}, G_{xz} and ν_x—are depicted in Figure D.6. The models to compute E_x and G_{xz} use geometries of a single core period with a length of sufficient span so as to ignore end effects. Increasing this length naturally reduces the influence of potential end effects on the center of the specimen, but is more costly to compute due to the increased number of elements. The models to calculate E_y and G_{yz} use multiple periods of the sandwich structure and a depth equal to or greater than the period length. The model to calculate twisting stiffness, G_{xy}, uses a geometry of equal length and depth.

Unit moments per area are applied to rigid end elements in the models to compute

bending stiffnesses. Rigid elements are modeled by using a Young's modulus 6 orders of magnitude greater than the facing sheet value. For the twisting stiffness model, unit moments are applied without rigid end planes, since additional rigidity would inhibit the sample deflection. Unit forces per length are applied to the rigid end elements of the models to compute shearing stiffnesses. The latter two models, Figure D.6 (d) and (e), include fixed points, P_f, on the bottom facing sheets in order to prevent rigid body motion of the sandwich core. In each model, sides of the geometry to which no moments or forces are applied are given boundary conditions of symmetry. This implies that displacements in the co-ordinate axis normal to the plane of symmetry must be zero.

In Figure D.6, the desired outputs of each model are provided in inset boxes. Bending and shearing strains are output at centrally-positioned nodes on the top and bottom facing sheets for the models to compute bending and twisting stiffnesses, respectively. Displacements of the facing sheets from the undeformed configurations are output from the models to compute shearing stiffnesses. In Figure D.6 (e), the transverse deflection, δz, is output from a node spaced Δx away from the centrally-located fixed point, P_f.

Using the strains or displacements the bending and twisting curvatures or shearing strains are calculated as follows [111]:

$$\kappa_x = \frac{\epsilon_{x1} - \epsilon_{x2}}{h_s} \quad \kappa_y = \frac{\epsilon_{y1} - \epsilon_{y2}}{h_s} \tag{D.6}$$

$$\kappa_{xy} = \frac{\gamma_{xy1} - \gamma_{xy2}}{2h_s} \quad \gamma_{yz} = \frac{\delta y}{h_s} + \frac{\delta z}{p} \quad \gamma_{xz} = \frac{\delta x}{h_s} + \frac{\delta z}{\Delta_x} \tag{D.7}$$

These parameters are related to the bending and shear stiffnesses by

$$D_x = -\frac{M_x}{\kappa_x} \quad D_y = -\frac{M_y}{\kappa_y} \quad \nu_x = \frac{\kappa_y}{M_x/D_x} \quad \frac{\nu_x}{D_x} = \frac{\nu_y}{D_y} \tag{D.8}$$

$$D_{xy} = \frac{M_{xy}}{\kappa_{xy}} \quad D_{Qy} = \frac{Q_y}{\gamma_{yz}} \quad D_{Qx} = \frac{Q_x}{\gamma_{xz}} \tag{D.9}$$

Since unit moments per area and unit shear forces were employed in the FE models, Equations D.8 and D.9 are straightforward to calculate.

From the computed stiffnesses may be found the equivalent elastic material properties representing a 2D incompressible, symmetrical orthotropic plate:

$$E_x = \frac{12D_x}{h_s^3} \quad E_y = \frac{12D_y}{h_s^3} \quad G_{xy} = \frac{6D_{xy}}{h_s^3} \tag{D.10}$$

$$G_{yz} = \frac{D_{Qy}}{k_s h_s} \quad G_{xz} = \frac{D_{Qx}}{k_s h_s} \quad \nu_{xy} = \nu_x \quad \nu_{yx} = \nu_y \tag{D.11}$$

where the shear factor is $k_s = 5/6$. Finally, the equivalent density of the anisotropic plate is calculated as the product of the core sheet material density, ρ, multiplied by the ratio of the actual material volume to the volume of the equivalent continuous element. For the circular cross-section, this may be computed as

$$\rho_s = \rho \frac{\pi t_s}{\lambda} \tag{D.12}$$

D.2.2 Equivalent transverse elastic property calculation

To compute the equivalent transverse elastic constant, E_z, representing the distribution of vertical spring elements of the sandwich core layer, Figure D.4, requires one additional FE model. Figure D.7 depicts the model geometry, loading conditions and model output. Since the facing sheets of the sandwich structure do not carry any of the transverse loading in the actual distributed spring layer (recall that the layer is ultimately bounded by a base plate and a top plate), the facing sheets are modeled using rigid elements. A unit force per area is applied to the top facing sheet while the bottom sheet is kept fixed. The boundary planes on each of the four section faces are symmetric as in the earlier FE models; this restricts the sandwich structure to transverse deflection only. The desired output of the model is the transverse deflection of a node of the top facing sheet, δz.

The equivalent transverse elastic parameter may then be computed as

$$E_z = \frac{F h_s}{\delta z} \tag{D.13}$$

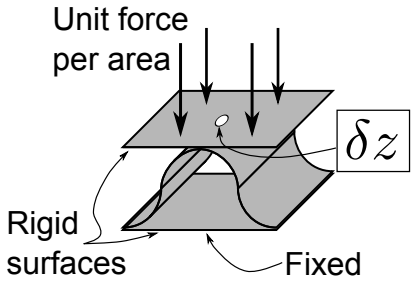

Figure D.7: FE models to compute the transverse elastic constant, E_z.

where F is the force per area applied to the top surface.

D.3 Continuum domain model

D.3.1 Generalized Hamilton's principle for the coupled system

For the sake of conciseness and to focus more on the numerical implementation, a brief description of the mathematical formulation of the model is presented. Greater description of the formulation is contained in Appendix A. The variational method used in the model is based on the generalized Hamilton's principle for deformable mechanical bodies [94]

$$\delta \int_{t_1}^{t_2} \left[(T - U) + \overline{W} \right] \mathrm{d}t = 0 \tag{D.14}$$

where T is the total kinetic energy, U is the total strain energy and $\overline{W}$ are the mechanically applied loads. For each individual layer, these components are calculated from

$$\begin{aligned} U_i &= \frac{1}{2} \int_{V_i} \left(\mathbf{S}^T \mathbf{T} \right)_i \mathrm{d}V_i \qquad K_i = \frac{1}{2} \rho_i \int_{V_i} \left[\dot{u}^2 + \dot{v}^2 + \dot{w}^2 \right]_i \mathrm{d}V_i \\ \overline{W}_i &= \sum_{j=1}^{N_f} [u(x_j)\ v(y_j)\ w(z_j)]_i \cdot [f_x\ f_y\ f_z]_j^T \end{aligned} \tag{D.15}$$

where the subscript $i = b, s, t$ represents the layering convention indicated in Figure D.2, $\mathbf{S}$ and $\mathbf{T}$ are the appropriate strain and stress tensors for the layer, respectively, f represents applied point loads, N_f are the number of applied loads and T is the transpose operator.

The base plate and the top plate are modeled with Love–Kirchhoff assumptions. Thus, the displacement expressions are written in terms of linear Taylor series expansions about the mid-plane displacements. The displacement expressions for the distributed spring layer are linear expansions in the cross-planar co-ordinates and a quadratic Taylor series expansion for the flexural component:

$$\begin{aligned} u\left(x,y,z,t\right)_s &= u_o\left(x,y,t\right) + z_s\theta_x\left(x,y,t\right) \\ v\left(x,y,z,t\right)_s &= v_o\left(x,y,t\right) + z_s\theta_y\left(x,y,t\right) \\ w\left(x,y,z,t\right)_s &= w_o\left(x,y,t\right) + z_s\frac{\partial w_o}{\partial z_s} + \frac{1}{2}z_s^2\frac{\partial^2 w_o^2}{\partial z_s^2} \end{aligned} \tag{D.16}$$

where the subscript o indicates the middle plane of the layer. The orthotropic constitutive relation for the distributed spring layer is expressed as

$$\begin{bmatrix} \sigma_{xx} \\ \sigma_{yy} \\ \sigma_{zz} \\ \tau_{yz} \\ \tau_{xz} \\ \tau_{xy} \end{bmatrix}_s = \begin{bmatrix} \frac{E_x}{1-\nu_{xy}\nu_{yx}} & \frac{\nu_{yx}E_x}{1-\nu_{xy}\nu_{yx}} & 0 & 0 & 0 & 0 \\ \frac{\nu_{xy}E_y}{1-\nu_{xy}\nu_{yx}} & \frac{E_y}{1-\nu_{xy}\nu_{yx}} & 0 & 0 & 0 & 0 \\ 0 & 0 & E_z & 0 & 0 & 0 \\ 0 & 0 & 0 & G_{yz} & 0 & 0 \\ 0 & 0 & 0 & 0 & G_{xz} & 0 \\ 0 & 0 & 0 & 0 & 0 & G_{xy} \end{bmatrix}_s \begin{bmatrix} \epsilon_{xx} \\ \epsilon_{yy} \\ \epsilon_{zz} \\ \gamma_{yz} \\ \gamma_{xz} \\ \gamma_{xy} \end{bmatrix}_s \tag{D.17}$$

Equation D.17 indicates the decoupled nature of the anisotropic sandwich panel dynamics with those of the transversely flexible core. Damping is included in the study by means of an isotropic loss factor, η_i, for each of the three layers in the system.

Continuity of displacements, transverse normal and transverse shearing stresses are applied at the interfaces between the distributed spring layer and the bounding base and top plates. This allows the full system response to be described in terms of the mid-plane displacement components of the base and top plates: $[u_o\left(x,y,t\right)\ v_o\left(x,y,t\right)\ w_o\left(x,y,t\right)]_b$ and $[u_o\left(x,y,t\right)\ v_o\left(x,y,t\right)\ w_o\left(x,y,t\right)]_t$, respectively.

D.3.2 Rayleigh-Ritz solution

To approximate the dynamic response of the system, the Rayleigh-Ritz method is employed for the 6 unknowns. The Rayleigh-Ritz approximate solutions may be

expressed as

$$\begin{aligned}
&(u_o)_t(x,y,t) = \Lambda(x,y)\mathbf{f}(t) \quad (v_o)_t(x,y,t) = \Pi(x,y)\mathbf{g}(t) \quad (w_o)_t(x,y,t) = \Gamma(x,y)\mathbf{h}(t) \\
&(u_o)_b(x,y,t) = \Phi(x,y)\mathbf{p}(t) \quad (v_o)_b(x,y,t) = \Theta(x,y)\mathbf{r}(t) \quad (w_o)_b(x,y,t) = \Psi(x,y)\mathbf{s}(t)
\end{aligned} \tag{D.18}$$

where Λ, Π, Γ, Φ, Θ and Ψ are the admissible trial function sets used in the linear combination, each multiplied by a vector of generalized co-ordinates. The hierarchical trigonometric function set of Beslin and Nicolas [97] is employed as the trial function series since it is convenient for simulation of the classical boundary conditions of plates: simply-supported, clamped and free suspension. Substituting this form of approximate solution into Equation D.14 and assuming a harmonic time dependence yields

$$\left[-\omega^2\left(\mathbf{M_t}+\mathbf{M_s}+\mathbf{M_b}\right)+\left(\mathbf{K_t}+\mathbf{K_s}+\mathbf{K_b}\right)\right]\mathbf{m} = \mathbf{B_f}\mathbf{f} \tag{D.19}$$

with

$$\mathbf{m} = \begin{bmatrix}\mathbf{f} & \mathbf{g} & \mathbf{h} & \mathbf{p} & \mathbf{r} & \mathbf{s}\end{bmatrix}^T \tag{D.20}$$

The matrices to the left-hand side of Equation D.19 represent the mass, $\mathbf{M}$, and stiffness, $\mathbf{K}$, matrices of the three layers, evaluated using the 6 assumed solutions, Equation D.18. The matrices resulting from the distributed spring layer, denoted by subscript s, fully couple the extensional and flexural displacements of the top and base plates. Finally, $\mathbf{B_f}$ are the basis functions evaluated at the location of the applied forces, $\mathbf{f}$.

In the absence of any forcing, an eigenvalue problem is solved yielding the natural frequencies of the coupled system:

$$\left[\mathbf{K_t}+\mathbf{K_s}+\mathbf{K_b}\right]\mathbf{m} = \omega^2\left[\mathbf{M_t}+\mathbf{M_s}+\mathbf{M_b}\right]\mathbf{m} \tag{D.21}$$

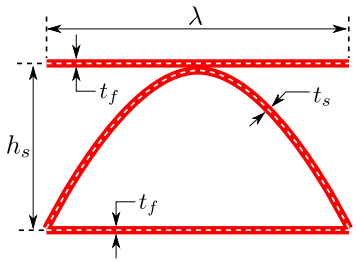

Figure D.8: Periodic geometry of sandwich panel having a half sine wave shape.

Table D.1: Isotropic properties of base and top plates, $i = b, t$, and the facing and core sheets

Layer	a_i m	b_i m	h_i mm	E_i Pa	ν_i	ρ_i kg/m^3	η_i
Base	0.15	0.15	2	2.1e14	0.33	7850	3e-4
Top	0.102	0.102	2	2.1e11	0.33	7850	3e-4
Facing sheet	n/a	n/a	n/a	2.1e11	0.33	7850	3e-4
Core sheet	n/a	n/a	n/a	2.1e11	0.33	7850	3e-4

D.4 Model validation: numerical comparison

D.4.1 Eigenfrequency analysis

The continuum domain model and superposition technique are evaluated by calculating the eigenfrequencies of a sample vibration control device. Two periodic core designs are evaluated: the circular core shown in Figure D.5 and a half sine shape as depicted in Figure D.8. The isotropic properties of the base plate, the top plate, facing sheets and core sheet are provided in Table D.1. The above FE models were employed and the computed equivalent elastic parameters of the sandwich spring layers are presented in Table D.2. It was assumed that the facing sheets of the spring layer are of equal thickness to the core sheet, *i.e.* $t_f = t_s$. In each case, the thickness of the equivalent spring layer was $h_s = 6.35$ mm with a periodic length of $\lambda = 12.7$ mm.

Table D.2: Equivalent orthotropic plate properties of spring layers

Core shape	t_s μm	E_x GPa	E_y GPa	E_z MPa	ν_{xy}	G_{yz} MPa	G_{xz} MPa	G_{xy} GPa
Circular	50.8	2329	2031	1.147	0.0913	8.186	261.4	7.608
Circular	76.2	3451	2996	3.695	0.0877	15.26	204.2	9.836
Half sine	50.8	2189	2312	2.085	0.0434	0.5307	18.93	1.224
Half sine	76.2	3241	3417	7.004	0.0441	1.756	33.98	2.574

Table D.3: Natural frequencies [Hz] as computed by 3D FE analysis and 2D model (percent difference)

Core shape (t_s μm)	Model	Mode 1	Mode 2	Mode 3	Mode 4
Circular (50.8)	3D FE	362.8	536.8	538.5	540.4
	2D	360.0 (-0.7%)	529.6 (-1.3%)	530.3 (-1.5%)	536.3 (-0.7%)
Circular (76.2)	3D FE	652.7	957.7	960.4	964.1
	2D	644.7 (-1.2%)	937.9 (-2.1%)	939.7 (-2.1%)	957.5 (-0.6%)
Half sine (50.8)	3D FE	611.7	683.2	686.3	688.3
	2D	608.1 (-0.5%)	643.8 (-5.7%)	648.3 (-5.5%)	649.2 (-5.6%)
Half sine (76.2)	3D FE	1103	1243	1249	1253
	2D	1087 (-1.4%)	1115 (-10.2%)	1125 (-9.9%)	1127 (-10.0%)

The base plate of the system is considered to be fixed over the full surface. This would represent the case of the vibration control device being attached to a completely rigid surface. A full 3D FE model of the system was constructed using the exact geometry and isotropic material properties of the facing and core sheets, Table D.1. Both the 3D FE and the 2D continuum domain models were evaluated for the first 4 eigenfrequencies and mode shapes of the coupled system and the results are presented in Table D.3. Percentage differences are provided for the 2D domain models, with reference to the 3D FE solutions.

The first four mode shape dynamics, as output from the 2D domain model, are illustrated in Figure D.9. The first, second and third mode shapes exhibit rigid body motion of the device top mass layer: the first mode is back-and-forth rocking of the mass; the second mode shape is rigid body rotation of the mass about the x-axis; the third mode shape is rigid body rotation of the mass about the y-axis. Interestingly, the SDOF oscillation of the top mass layer, that which yields the traditional vibration absorber behavior of the device, does not occur until the fourth mode.

From Table D.3 it is observed that the SDOF natural frequency occurs at almost the same frequency as those for rigid body rotations of the mass layer. The rocking mode shape, however, occurs at a lower frequency, sometimes as much as 30% lower in frequency than the rotational oscillations. This dynamic is caused by the relatively small shearing stiffness, G_{yz}, a feature which such corrugated sandwich panel designs are known to exhibit.

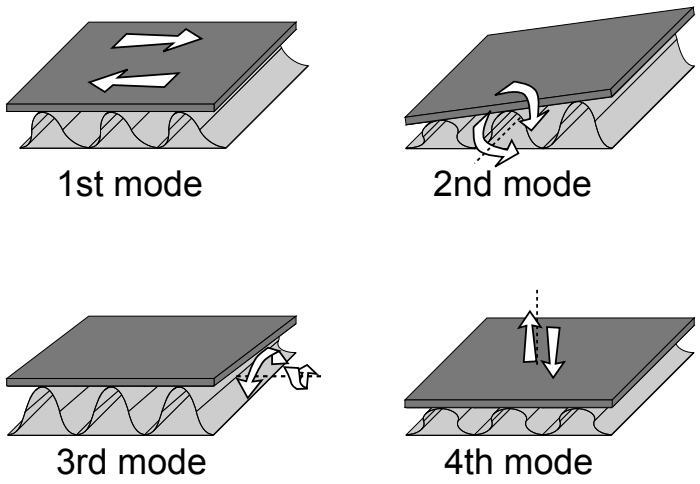

Figure D.9: First four mode shapes of device having a fixed based.

Table D.3 shows that the 2D continuum domain model yields natural frequencies in close agreement with the full 3D FE model, in particular for the device having a circular core spring layer design. The maximum errors between the models occur for the half sine core shape, consistently underestimating the frequency values. This may be attributed to the discontinuous design of the half sine core, each period of the shape beginning with an abrupt shift in the slope of the woven core material. Thus, a localized stiffening effect may be more accurately accounted for in the 3D FE analysis as compared to an equivalent 2D approach which assumes the distributed spring layer to be symmetric and continuous.

D.5 Model validation: experimental comparison

D.5.1 Manufacturing description

With a consideration of numerical validation taken in Section D.4, the numerical superposition approach should additionally be compared against experimental samples. The two corrugated geometries considered in this work, circular and sinusoidal, are in fact not often found in manufactured products to date. The closest embodiment of either is likely conventional corrugated cardboard which is generally mostly

sinusoidal but often reveals a slight "lean" in one direction, generally the result of the rapid manufacturing process as the paper is press through gears to generate the corrugation.

Thus, to actually achieve the corrugated forms of present interest, it was necessary to develop a process by which they could be manufactured. Following the process, it then needed to refine it such that as close to a circular or perfect sinusoid may be achieved. In later portions of this work, it was desired to focus on using steel exclusively in the manufacture of the distributed vibration absorbers, thus the objective became to develop a production method to generate an all-steel device.

The bonding amongst the facing sheets, corrugated layer and the top mass was a concern. Ideally, it would be desired to produce the corrugated layers using an extrusion process, by which a mold could easily maintain any required core cross-section. However, though the extrusion process is used in manufacturing corrugated plastic materials, as sometimes used for outdoor or sidewalk advertising signs, it was found, through contact of multiple manufacturers, that extrusion is not possible down to the sheet thickness desired in the present work. For example, the corrugated plastic sheets produced by such companies may in fact appear identical to the shape of this work, but the sheets are not designed for transverse compressibility. In light of evaluating the superposition approach as a whole, a corrugated plastic sheet would likely only reveal that it is accurately modeled as a traditional incompressible sandwich panel.

Thus, it was necessary to produce, by hand, parts having as consistent a corrugated shape as possible while still retaining a substantial level of core compressibility. The joining together of steel facing and corrugated sheets was also a concern. A number of early trials employing epoxies were successfully performed. But this did not satisfy the goal of achieving all-steel samples, despite providing useful prototype samples with which to begin evaluating the full device dynamics.

Instead, a welding process was necessary. A spot welder was manufactured for

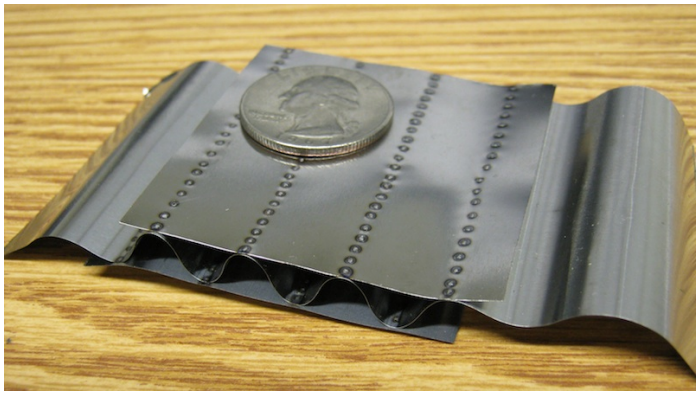

Figure D.10: Welded steel corrugated core sample having consistent circular core shape and minimal, adverse welding effects.

this purpose. With properly sharpened tungsten tips, the equipment was eventually capable of producing non-intrusive welds. Figure D.10 shows a later sample produced over the course of this work, highlighting both the regularity of the corrugated layer as well as the minimal heat affected zone generated by the refined welding technique. Minimizing deformation due to local overheating was vital as was the ability to generate the smallest welded points as possible in order to achieve linear lines connecting the corrugated layer to the facing sheets.

While the present study evaluates the use of considering the corrugated core itself as the superposition of an incompressible sandwich panel and a compressible core, it was found that it was not necessary to always employ the top facing sheet in the manufacture of the parts. Instead, the core was directly welded to the mass layer. This also assisted in reducing the overall mass of the parts which was of benefit in later portions of this work. After a considerable period of practice, adaptation, refinement of the equipment and patience, the distributed absorber devices were ultimately able to be manufactured with great precision from part to part.

D.5.2 Circular corrugated core sample

A sample was produced having a circularly corrugated spring layer and using a top mass layer having material properties and geometry as those given in Table D.4. The

Table D.4: Isotropic properties of base and top plates, $i = b, t$, and the facing and core sheets

Layer	a_i (mm)	b_i (mm)	h_i (mm)	E_i (Pa)	ν_i	ρ_i (kg/m^3)	η_i
Base	300	140	5	2.1e14	0.33	800	3e-4
Top	203	102	2	2.1e11	0.33	4680	3e-4
Facing sheet	n/a	n/a	n/a	2.1e11	0.33	7850	3e-4
Core sheet	n/a	n/a	n/a	2.1e11	0.33	7850	3e-4

Table D.5: Equivalent orthotropic plate properties of spring layer

E_x (Pa)	E_y (Pa)	E_z (Pa)	ν_{yx}	G_{yz} (Pa)	G_{xz} (Pa)	G_{xy} (Pa)	ρ_s (kg/m^3)	h_s (mm)
5.83e11	5.08e11	1.69e5	0.082	3.11e6	9.54e7	6.95e9	20.0	12.7

corrugated material thickness was $t_s = 50$ μm and the layer was constructed with $\lambda = 25.4$ mm. For this sample, the equivalent spring layer properties were computed using the earlier analysis and are provided in Table D.5.

To evaluate the principal dynamic response of the device, an FRF test was simulated in the model and measured in the laboratory. The approximated geometric and material parameters of the shaker platform are given in Table D.4, noting that the Young's modulus of the layer was a best guess. In numerical experiments, it was noted that so long as the modulus was several orders of magnitude greater than any of the moduli in the equivalent spring layer, the comparison with experimental results was favorable. The base plate was presumed to be excited by a centrally-located point force equally at all frequencies. A photograph of the device on the laboratory shaker platform is shown in Figure D.11.

Figure D.12 plots a comparison of the predicted and measured FRF between the platform acceleration and that as measured at the center of the top mass. So long as the device is centrally positioned on the platform surface and the excitation force to the base platform be perfectly out-of-plane, the only major dynamic feature of the FRF results should necessarily be the SDOF natural frequency as the mass layer oscillates vertically. Resonance is predicted to occur at 193 Hz, which corresponds exactly to the measurement. Furthermore, both the magnitude of resonance as well as the roll-off and decay above resonance are in close agreement between the model

Figure D.11: Sample device on shaker platform.

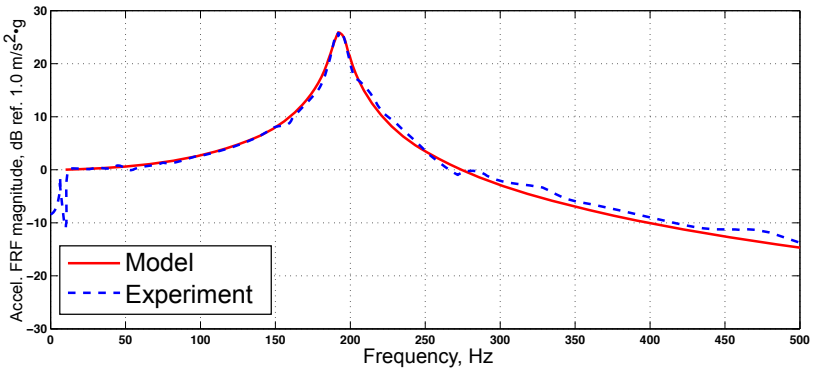

Figure D.12: Comparison of modeled and measured FRF for device employing a standard circularly corrugated spring layer design.

and the measurement.

It is admitted that this alone is not comprehensive validation of the superposition method to realistic experimental results, but individually serves to verify the benefit, in one sense, of considering the transverse oscillation of the distributed absorber device to be fundamental independent of the remaining bending and shear stiffness properties of the continuous spring layer. It may thus be said that part of the superposition approach has been validated.

Table D.6: Properties of the freely suspended panel

a (mm)	b (mm)	h (mm)	E (Pa)	ν	ρ (kg/m^3)	η
305	610	1.5	2.1e11	0.3	7850	1e-3

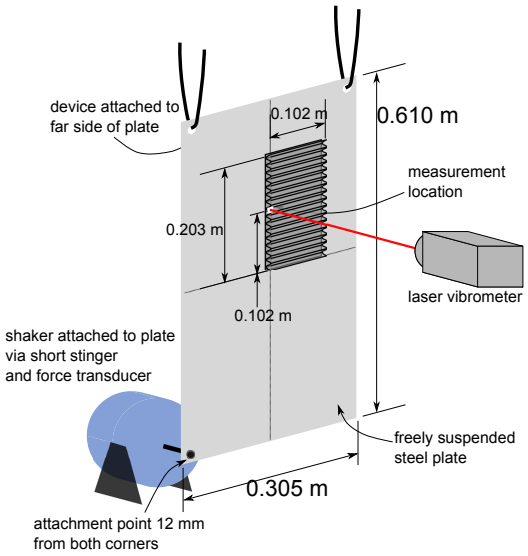

Figure D.13: Freely suspended panel test setup diagram.

D.5.3 Circular corrugated core sample on a vibrating panel

A conclusive evaluation of the superposition approach necessarily comes into play in the comparison of a test which simultaneously considers the transverse and extensional vibration of the device. As these are distributed devices intended for surface vibration suppression, a test performed on a vibrating panel is naturally of most use in comparing model with measurement in pursuit of validation.

A panel was therefore freely suspended in the laboratory from two ends by non-obtrusive elastic wires. At 12 mm from one corner, an electrodynamic shaker was attached via a short stinger. A force transducer was placed in between the stinger and the panel. Reflective tape was attached at a location, (0,102) mm from the plate center, on the reverse side of the panel in order to measure the mobility transfer function of the panel. A diagram of the testing arrangement, including the later attached distributed absorber device, is given in Figure D.13.

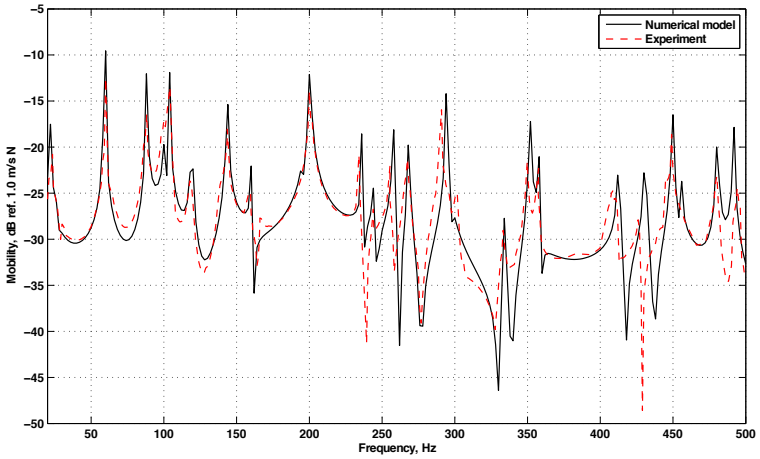

Figure D.14: Mobility transfer function of untreated suspended panel, (black solid) modeled and (red dashed) experimental results.

The measured and predicted untreated panel mobility is plotted in Figure D.14. A substantial number of panel modes are present even up to just 500 Hz. The resonance at 21.6 Hz is the lowest order non-rigid body vibrational mode of the panel. The deviation from the predicted results to the measurements are minimal up to approximately 225 Hz. Below this frequency, the prediction of the location of the resonances is extremely accurate, not deviating by any greater than 0.5 Hz.

Above this point, the limitation on achieving exactly free boundary conditions is observed to slightly modify the frequency response of the panel. Though the magnitude of much of the higher frequency panel mobility is similar between model and experiment, some of the measured locations of the resonances are shifted. This is particularly evident at 291 and 408 Hz. However, though achieving perfectly free boundary conditions is generally an impossibility, the level of agreement between the model and measurement evidenced in Figure D.14 is significant.

Following completion of the untreated vibration testing, the distributed absorber was firmly attached using a very thin layer of hard-curing epoxy. The epoxy requires 24 hours to cure but afterwards adheres to the point of requiring destruction of the attached device, if one desired to thereafter remove it. A photograph of the rear of

Figure D.15: Distributed device attached to rear of suspended panel, showing shaker attachment and force transducer.

the panel with the absorber is provided in Figure D.15. The absorber used was an identical sample to that employed in Section D.5.2, manufactured at the same time as the prior sample for consistency. Thus, the equivalent orthotropic plate properties and mass layer characteristics were the same as those given in Tables D.4 and D.5.

The panel mobility transfer function was again measured following application of the distributed vibration absorber device and is plotted against the modeled result in Figure D.16. Close agreement is found between the numerical prediction and experimental measurement. Below the natural frequency of the device, 193 Hz, the panel vibration is not significantly altered with the exception of the resonance at 49 Hz. This is an asymmetric vibration mode, depending on one's convention of terming free plate modes either (1,1) or (2,2), the "dual-rocking" mode. The ability of the device to substantially suppress this mode is easily explained by its position which spans an anti-nodal line. The very high bending stiffness of the sample, from Table D.5, suggests that it is highly resistive to this form of deformation, which the (1,1) mode tries to impart. Thus, the absorber notably suppresses the magnitude of this resonance.

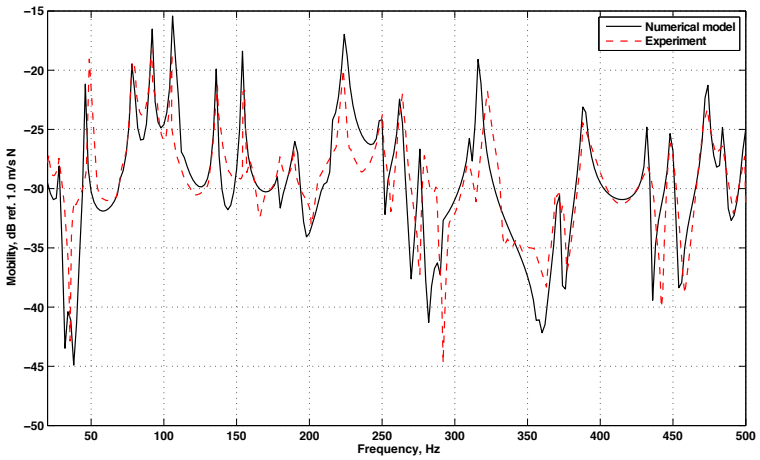

Figure D.16: Mobility transfer function of treated suspended panel, (black solid) modeled and (red dashed) experimental results.

Around the device natural frequency, a panel mode is present at 200 Hz. It is observed that the device "splits" the resonance into two vibrational frequencies at 192 and 222 Hz. This is the conventional dynamic result of applying a lightly-damped re-active device to a vibrating structure. The model is found to be in close agreement with the experimental measurements in regards to the location of these new split resonances as well as the magnitude, with a slight under-prediction at the 222 Hz frequency.

At frequencies greater than the tune SDOF natural frequency of the distributed absorber, the device is found to significantly alter the location of the panel resonances and in some cases provide a level of attenuation from untreated levels. Any attenuation of the panel vibration above the device natural frequency is arguably the result of the resistive effects of the orthotropic spring layer since the re-active effects were observed in Figure D.12 to be significantly less important above the resonance.

The highly orthotropic design of the corrugated spring layer lends a rigorous extensional coupling to the structure and modifies each of the higher order resonances to a unique degree. Results of the model and experiment are in fairly close agreement as to how the spring layer is precisely coupled. Overall, for this modally dense vi-

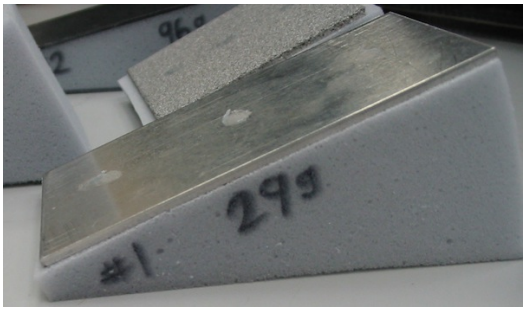

Figure D.17: Photograph of variable stiffness absorber device sample using poroelastic foam.

brational structure and for an attached device exhibiting substantial transverse and extensional coupling to the panel, the model is found to accurately predict the effects of the continuously distributed vibration absorber employing a circularly corrugated spring layer when attached to a vibrating surface.

D.5.4 Variable stiffness concept: continuous spring layer material

In light of later application of the theory and modeling presented in the current and prior chapters, it is necessary to include validations for the variable spring stiffness modeling approach as outlined in Section C.7. To describe the continuous spring in terms of a piece-wise constant spring layer properties, inherently simplifies the reality of manufacturing the parts for applied purposes. Thus, it is necessary to validate this approach against experimental samples.

The most simplified manner by which to attain a variable stiffness distributed spring layer for the devices of interest is to utilize a continuous material, such as poroelastic foam, cut such that the layer varies in thickness along its length. This lends a variation in natural frequency of the top mass, as was observed by Idrisi [117] in the study of inclusion depth in poroelastic media. Figure D.17 shows a photograph of the sample which was tested, showing the variation in foam thickness along the length of the distributed device.

Table D.7: Mechanical and geometric properties of base and top plates, $i = b, t$, and the spring layer

Layer	a (mm)	b (mm)	h (mm)	E (Pa)	ν	ρ (kg/m^3)	η
Base	300	140	5	2.1e14	0.33	800	3e-4
Mass layer	76.2	50.8	3	7.2e10	0.33	2100	1e-3
Spring layer	76.2	50.8	10–50	1.4e5	0.4	9	2e-2

The geometric and mechanical properties used in the model validation are provided in Table D.7. As noted in Section C.7, each discretization along the length of the distributed absorber in the modeling requires new evaluation of the kinetic and potential energy equations. Thus, refined discretization, though certainly increasing accuracy, can quickly become computationally prohibitive. Thus, in the following validation, the spring layer was discretized into 11 portions along the length. As the poroelastic material properties do not change from one region to the next, the spring layer thickness was modified for each of the 11 sections, from 10 to 50 mm. The poroelastic foam was considered to be an isotropic material such that $E_x = E_y = E_z = E$ and $G = E/2(1 + \nu)$.

The experimental sample was prepared and an FRF test was conducted, with similar excitation as for the earlier validations. The corresponding model was simulated and a comparison of the results are provided in Figure D.18 for three discrete points along the center line of the mass layer. Though the sample is continuously varied in stiffness due to the change in material thickness along its length, the three measuring points appear to indicate just two principal natural frequencies of the device: 184 and 233 Hz. The model accurately predicts the location of these two resonances but uniformly over-predicts the amplitude of response, which may be due to employing a smaller damping loss factor than is observed for the poroelastic material.

It is interesting to note that model predictions and measurements both suggest no intermediary resonances occur between the highest and lowest observed natural frequencies. As observed in Section C.7, when a variation of transverse stiffness is present for the continuous spring layer, the advantage of this feature is limited to

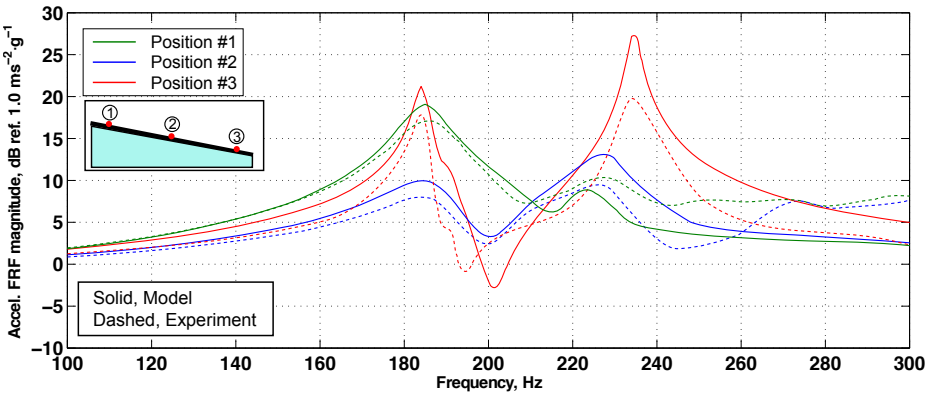

Figure D.18: Comparison of modeled and measured FRF for device employing a variable stiffness poroelastic spring layer.

the stiffness of the top mass layer: softer top mass materials are more compliant and therefore are more able to provide for the full continuum of SDOF natural frequencies that the varying transverse stiffness would yield. In contrast, the stiffness of the sample measured had an aluminum top mass layer. As a result, it is more likely that the top mass was primarily rocking back-and-forth as one end of the device resonated at the lower SDOF natural frequency with the opposite end resonating at the higher natural frequency. This is the disadvantage of using stiffer top mass materials with the variable spring stiffness design; softer mass materials are preferable.

Two additional runs of the model indicate that for foam samples of constant thicknesses 10 and 50 mm, the distributed devices would exhibit SDOF resonances at 350 and 154 Hz, respectively. Thus, the two observed natural frequencies from the variable stiffness sample do not correspond to the SDOF resonances one would encounter for a sample composed of uniform thickness of the thinnest or thickest portion of the variable stiffness design. The continuous variation in stiffness, and the coupling along the length of the sample through both the continuous mass layer and the Poisson's ratio of the spring layer, equalizes the exhibited range of natural frequency. This is by no means a detrimental feature of the variable stiffness concept but one to keep in mind when targeting a broad range of natural frequencies from a

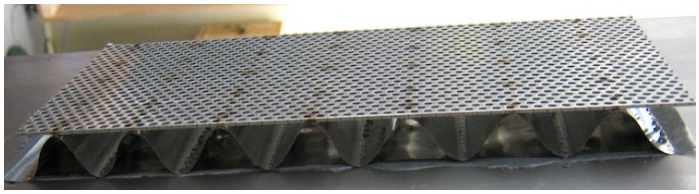

Figure D.19: Photograph of variable stiffness absorber device sample using steel corrugated spring. Corrugated wavelength increasing from left to right.

single device.

D.5.5 Variable stiffness concept: corrugated spring layer

Utilization of the variable stiffness design for the corrugated spring layer is of utmost importance later in this work, so evaluation of the utility of incorporating it along with the superposition approach is next to be considered. In general regard to achieving a variable stiffness design of the continuous spring layers, it is anticipated that using layers of different total thickness is less beneficial than using a spring layer of equal thickness along the length. This follows from the reasoning that samples of variable thickness, like that shown in Figure D.17 for the poroelastic spring layer, will not lend as much re-active force normal to the host structural vibration. Instead, the mass will rock and oscillate in such a way as to yield components of the re-active force which operate both to coupling with the extensional and well as flexural motion of the base vibration. Thus, maintaining a constant thickness along the distributed spring layer is preferable while the variable stiffness design is employed.

For the corrugated spring layer of concern, a variable transverse stiffness design may easily be achieved using a constant thickness of the spring layer merely by increasing or decreasing the peak-to-peak distance of the corrugations along the length of the sample. One such sample was created, using three distinct wavelengths, $\lambda = 25.4$, 31.8 and 38.1 mm, and is shown in Figure D.19 attached in a later test to a plate. Two wavelengths of the 25.4 and 31.8 mm increments are used and three wavelength are used for the broader $\lambda = 38.1$ mm.

Table D.8: Isotropic properties of base and top plates, $i = b, t$, and the facing and core sheets

Layer	a_i (mm)	b_i (mm)	h_i (mm)	E_i (Pa)	ν_i	ρ_i (kg/m^3)	η_i
Base	300	140	5	2.1e14	0.33	800	3e-4
Top	203	102	2	2.1e11	0.33	4680	3e-4

Table D.9: Equivalent orthotropic plate characteristics of core having $\lambda = 25.4$ mm

E_x (Pa)	E_y (Pa)	E_x (Pa)	ν_{yx}	ν_{yz}	ν_{xz}
4.43e11	3.87e11	7.17e4	0.079	0	0
G_{yz} (Pa)	G_{xz} (Pa)	G_{xy} (Pa)	ρ (kg/m^3)	h_s (mm)	η
2.20e6	3.74e7	1.12e10	48.6	12.7	0.05

By maintaining a constant spring layer thickness, this design reduces the potential for the design to rock and generate substantial non-normal re-active forces which would not contribute to suppressing the host structural vibration. The spring layer is observed to begin as a circular core but by merely elongating the wavelength, without correspondingly increasing the thickness, naturally changes the form to a more sinusoidal shape.

The material properties and geometric properties of the device are as given in Table D.8. The core sheet was of a laminate design, constructed in three layers: first a layer of steel shim $t_s = 38.1$ μm; then a thin, $t_s = 20$ μm damping layer; and another steel layer of $t_s = 38.1$ μm. The equivalent material properties of this laminate material were evaluated using the simple MATLAB routines and method provided in the text by Voyiadjis and Kattan [118]. After which, the equivalent spring layer material properties were computed and are presented in Tables D.9–D.11.

As before, the experimental sample was prepared and an FRF test was conducted. The corresponding model was simulated and a comparison of the results are provided in Figure D.20 for three discrete points along the center line of the mass layer. The

Table D.10: Equivalent orthotropic plate characteristics of core having $\lambda = 31.8$ mm

E_x (Pa)	E_y (Pa)	E_x (Pa)	ν_{yx}	ν_{yz}	ν_{xz}
2.81e11	2.48e11	3.94e4	0.077	0	0
G_{yz} (Pa)	G_{xz} (Pa)	G_{xy} (Pa)	ρ (kg/m^3)	h_s (mm)	η
1.69e6	1.99e7	9.71e9	61.5	12.7	0.05

Table D.11: Equivalent orthotropic plate characteristics of core having $\lambda = 38.1$ mm

E_x (Pa)	E_y (Pa)	E_x (Pa)	ν_{yx}	ν_{yz}	ν_{xz}
1.93e11	1.72e11	1.09e4	0.074	0	0
G_{yz} (Pa)	G_{xz} (Pa)	G_{xy} (Pa)	ρ (kg/m^3)	h_s (mm)	η
1.42e6	1.35e7	9.75e9	68.6	12.7	0.05

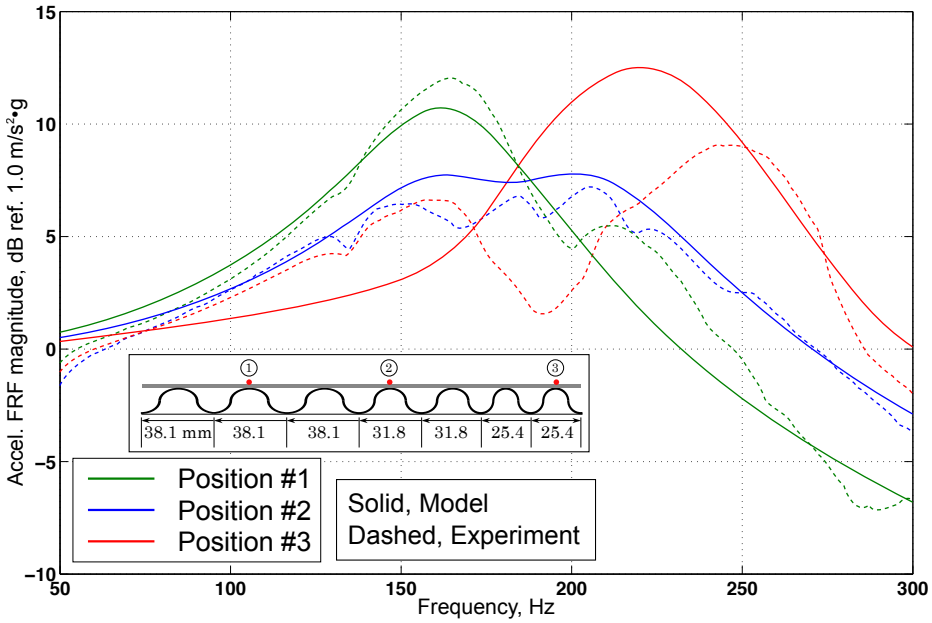

Figure D.20: Comparison of modeled and measured FRF for device employing a variable stiffness corrugated spring layer.

distinct segmentation of the corrugated spring layer into three regions of unique stiffness characteristics results in different dynamics than those evidenced in Figure D.18 for the layer achieving variable stiffness by means of a changing thickness. However, like the poroelastic layer of varying thickness, the variably corrugated sample also exhibits two primary natural frequencies, 161 and 248 Hz.

The model accurately predicts the lowest resonant response of the device at 161 Hz. However, the predicted highest resonant frequency is notably less in frequency and greater in magnitude than the measurement. This is perhaps explained by a limitation in perfectly maintaining the corrugated shape of the experimental sample as the wavelength of the corrugated period was decreased. This manufacturing difficulty

is partially observable in Figure D.19 for the shortest wavelength of the corrugated core which appears to be neither circular nor sinusoidal in form, but a mixture of the shapes. It is believed that this manufacturing deviation led to the shortest wavelength of the spring layer to be stiffer than was provided for in the modeling and thus the measured resonance occurred at 248 Hz as opposed to the prediction at 223 Hz. However, the response of the device at measurement position #2 is also fairly accurately predicted by the model to be a "smeared" resonant response spanning the lowest and highest resonances.

D.6 Extensibility of superposition modeling methodology

To assess the validity of the superposition approach, the model is evaluated for a range of the parameter t_s/h_s for both core designs. Thus, small values of t_s/h_s are representative of highly compressible core layers, while larger ratios would yield primarily incompressible sandwich layers. The output of interest is the comparison of the SDOF natural frequency of the vibration control device as predicted by both the 2D continuum domain model and an exact 3D FE model. The eigenfrequency problem of Equation D.21 was solved, using base plate, top plate, facing and core sheet geometries and properties as given in Table D.1.

A range of ratios t_s/h_s were considered, in each case also maintaining the same facing sheet thickness, $t_f = t_s$, as well as $h_s = 6.35$ mm. Furthermore, the thickness of the top mass layer was modified for each value of t_s/h_s such that $h_t = 0.002\,(t_s/h_s) \cdot (1e3)$ mm. This latter constraint kept the SDOF natural frequency within a conventional bound, ∼50 to 5,000 Hz, whereas maintaining $h_t = 0.002$ mm would yield unreasonable natural frequency estimates of >20 kHz as t_s/h_s increased.

Figure D.21 plots the percentage difference between the 2D and 3D FE model results. For both core designs, the errors between SDOF natural frequency predictions are minimized around a ratio of $t_s/h_s = 4e-3$ to $1e-2$. At the low extreme of t_s/h_s, the transverse stiffness of the spring layer is very small, representing a manufactured

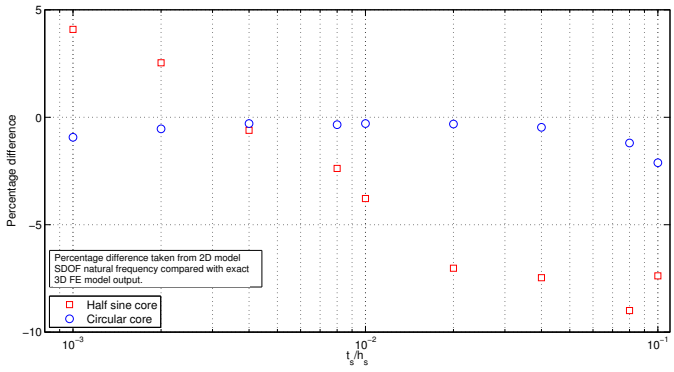

Figure D.21: Percentage difference between 2D and 3D FE model SDOF natural frequencies.

component which would be described as fragile. At the opposite extreme, the values of $t_s/h_s \approx 1e-1$ represent a more conventional sandwich panel designed for strength and durability.

For the circular core, in both extremes of t_s/h_s, the superposition approach begins to under-predict the transverse natural frequency of the device since the applicability of the method is stretched to its limits and errors rapidly increase. In the former case, buckling dynamics begin to play a major role; in the latter case, true incompressibility of the panel makes the assumption of a compressible core an inaccurate assumption. Furthermore, in the vicinity of $t_s/h_s \approx 1e-1$, the SDOF natural frequency is no longer one of the lowest order mode shapes as localized end effects take precedence.

For the half sine core shape, errors in the approach are much more prevalent, particularly for the extremes of t_s/h_s. As was discussed in Section D.4.1, this is likely due to the discontinuity in the core cross-section. The exact 3D FE model is capable of taking into account such localized stiffening while the equivalent, continuous 2D domain must neglect such features. Thus, the superposition method of modeling the distributed spring layer has a range of usefulness, approximately $t_s/h_s = 4e-3$ to $1e-2$, and one should take care to avoid utilizing it for either extreme of very "soft" or "stiff" core designs.

Furthermore, the circular core cross-section, lacking discontinuities in the woven shape, uniformly yields 2D model results in greater agreement with exact 3D FE analysis than the half sine core shape. This indicates that not only is there a window of greatest geometric applicability to the superposition approach but also, perhaps, a limitation based on the number and type of discontinuities in the woven core shape.

D.7 Conclusions

In this paper, a continuum domain model of a distributed vibration control device was proposed which has the advantage of reduced computational expense as compared with full 3D FE analysis. Crucial to the model is the homogenization of a distributed spring layer into the superposition of an incompressible sandwich panel and a compressible core. The methods to employ this approach and its validity as compared with exact 3D FE analysis were explored.

The continuum domain model was found to be in very close agreement in an eigenfrequency analysis with 3D FE models of select vibration control device designs. Most evident are dynamics of the device which are not otherwise observed for one-dimensional, mass-spring-damper systems, indicating that the device is capable of also suppressing structural motion through constraining-type effects as the spring layer extensionally deforms. The ability to both re-actively work against and resistively suppress structural motion suggests that the distributed vibration control devices should be useful over a broader range of frequencies than either point oscillators or constraining treatments alone.

Experimental validation was carried out for a distributed absorber sample employing the circularly corrugated spring layer design. First, FRF measurements were taken and compared against modeled results. The SDOF resonance frequency of the device was found to match exactly. The validation of the full complexity of the re-active and resistive device was made by comparison of a vibrating panel test with an attached distributed device. Measured and predicted results were in close agreement over a

broad range of structural modal resonances, featuring a number of unique features of the device's coupling to the structure. The lightly-damped nature of the vibration absorber was found to split a panel resonance into two additional frequencies, as is conventional with spring-mass oscillators. The resistive effects of the orthotropic spring layer was observed to alter the location and amplitude of some of the higher order panel resonances, typical of constraining layer treatments. Good agreement was found across the full bandwidth of evaluated frequencies for the modally dense structure.

The utility of the superposition approach was evaluated by considering a range of potential design parameters for the distributed spring layer. Transverse natural frequency comparisons were made between the 3D FE and 2D models. It was observed that in the extremes of either significant transverse deformability or incompressibility, the 2D model solutions diverged from the exact 3D FE results. For highly compressible core designs, buckling response and nonlinear effects due to significant transverse normal and shearing stresses are a concern. For very stiff core layers, standard incompressible sandwich panel theories are most suitable. Thus, a range of appropriate distributed spring layer designs exists to which this analysis is useful and accurate.

When utilizing the continuum domain model to assess the potential vibration suppression capability of such devices attached to structures, one is advised to consider the limitations of the superposition approach. However, it was observed that the circular core shape uniformly yielded 2D model results in closer agreement to 3D FE analysis as compared to the half sine corrugated shape. Therefore, a greater range of usefulness may be engaged for core cross-sections lacking discontinuities in the periodic geometry.

APPENDIX E

Development and testing of passive continuous vibration absorbers on a ship hull surface

This chapter describes the design of continuously distributed devices for use as a passive vibration control treatment on a realistic ship hull. Primary objectives for the test were to achieve a similar or greater level of broadband vibration attenuation as compared with an existing damping tile treatment and to reduce the applied weight of the designed devices as much as possible. Earlier studies of continuously distributed absorbers encouraged the employment of three main spring layer features: variable stiffness, orthotropic characteristics and a damped laminated spring material. Such design maximized the tuned and broadband utility of each device, also corresponding to a project goal of a "one-size-fits-all" solution. The important metric for the tests was the passive vibration attenuation provided by the devices on a simulated ship hull as compared with using the damping tiles. It was found that, at frequencies < 500 Hz, the designed devices lended a similar degree of vibration suppression compared to the tiles. At higher frequencies, the damped material and increased mass of the tiles yielded greater attenuation benefit than the absorber devices. However, the absorbers totaled a 20% savings in mass as compared with the tiles, which was a particular advantage given the comparable performance at frequencies < 500 Hz. In summary, the conclusions from earlier studies of continuously distributed vibration absorbers were applied to a realistic vibration problem and led to the design of device found to yield significant reactive and resistive passive vibration control benefit.

E.1 Problem background and motivation

Modern transportation systems are rigorously integrated with the latest computer technologies. While consumer-scale integration of the newest electronic devices occurs

at a lightning pace, the adoption of such technology in industrial or military sectors occurs at a more progressive pace. This is frequently due to concerns of sensitivity. For instance, modern notebook or laptop computers were generally not physically robust enough when immediately applied in military environments. As a result, Panasonic Toughbooks® were developed and now are widely employed throughout military and law enforcement industries.

Vibration in maritime vessels produces similar concerns. Attached machinery which shakes hull panels, or even propagating waves from one end of the ship to the other, can yield substantial levels of vibration. In regards to aircraft carriers, the noise from aircraft jet engines easily couples to the hull structure and thereafter produces propagating waves throughout the hull, which later couple to the interior acoustic environment to yield very high cabin noise levels. All of this amounts to a serious concern from the perspective of the Navy, who observed a 250% increase in disability payments for post-career Navy personnel due to hearing loss from 1999 to 2004 [119]. This study also found that the standard 6 month deployment onboard an aircraft carrier exposed crew members to such high continuous levels of noise that 12% of the crew experienced permanent hearing threshold impairment.

Since it is not necessarily possible to attenuate the source of vibration itself, *i.e.* remove the machinery causing the vibration or halt aircraft launches, remedial efforts must be made to alleviate the vibration of the structural panels of the ship hulls. Thus, the principal sponsor for this work, Newport News Shipbuilding (NNS) of Huntington Ingalls Industries, formerly Northrop Grumman Shipbuilding, Newport News (NGSB-NN), desired to develop a passive vibration control solution capable of significant attenuation benefit. As with all transportation systems, added weight requires greater power for propulsion or, alternatively, reduced range of transit. Thus, minimization of the mass of the devices was a primary goal; particularly to develop a solution of reduced weight compared to the existing treatment solution. To categorize the type of vibration of concern, since most of the hull panels are identical—welded

along the edges to stiffeners—and little vibration is transmitted from one panel to the next, the main vibration present is low order clamped panel vibration, typically in a range < 400 Hz.

To attenuate the structural vibration of the ship hulls, heavily-damped mass layers (ballast) were being employed, in the form of tiles applied directly to the hull surface wherever vibration was noticed. These solutions reduce vibration levels by shear resistance, not by the reactive means ascribed to conventional mass-spring-dampers. Thus, while the tiles provide notable mid to high frequency vibration control, significant mass must be added to substantial reduce the low, modal vibration of the ship hull panels. NNS desired a new approach to passively attenuate the vibration of their latest maritime vessel designs, inspiring a portion of this project.

E.2 Test facility description and project goals

The testing was decided to be performed at the NNS facility in Newport News, Virginia. On location is an elaborate and flexible laboratory complex, ideal for the present testing needs. Mock ship hulls are available, closely replicating conditions onboard a class of maritime vessels. These hulls are constructed by a series of panels and stiffeners, each panel being welded to stiffeners along all edges, as illustrated in Figure E.1.

While hull panels varied from wall to wall, a number of repeated sizes were present. The most frequently used panel size was a painted steel panel measuring 1.016 m by 0.559 m by 4.76 mm, welded along the edges. The welding along the boundaries may closely replicate classically clamped boundary conditions.

To evaluate the vibrational frequencies of greatest concern, NNS conducted a series of tests. An electrodynamic shaker was attached to both a nearby stiffener and later to the panel center itself. An array of accelerometers was placed over the panel surface. Excitation at both locations showed that the panel vibrated primarily at three frequencies: 81, 115 and 191 Hz. Modal analysis of the structure showed

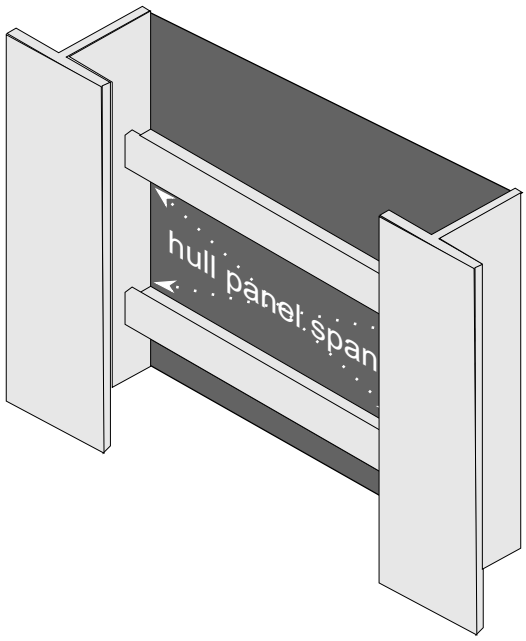

Figure E.1: Illustration of individual hull panel welded to series of stiffeners along the edges.

that these were similar to the 3 lowest order modes for a clamped panel of the given dimensions. The measured operational deflection shapes corroborated this result.

With this data and analysis, it was clear that the principal vibration of concern was flexural motion of the panel. The necessity for substantial mass of damping tiles to attenuate this vibration therefore makes sense. The tiles provide a shear resistance to the extensional motion of the host structure; however, extensional vibration of distributed structures occurs primarily at high frequencies where shearing effects are of greater importance. Thus, in general, the only way to provide low frequency vibration control with a resistive treatment, like the damping tiles, is to merely load the structure down with mass. The low order clamped plate flexural vibration would best be alleviated by means of a treatment which operated reactively like a traditional vibration absorber.

In discussions with NNS representatives, it was determined that the desired solution be “one-size-fits-all”. The advantage of the damping tiles was that each were

the same, orientation of the tiles was irrelevant, and application could be quickly performed using standard epoxies. This flexibility was of great importance to NNS, in addition to the fact that the designed solution must be mount-able using the same epoxy used for the tiles. Optimization of placement of potential treatments or the specific design for target frequencies was therefore not preferable.

Full or substantial coverage of the ship hull panels is generally the mode of application when vibration is a concern. This was also a desired element to design and testing of a new surface vibration control treatment. Quick calculation using the damping tile and test panel characteristics found that full coverage of the panel with the damping tiles would yield a mass ratio $\mu = 25$–40%, depending on the thickness of the tile. Lastly, it was noted that due to availability, cost and recyclability, the use of steel in the design of the new treatment, in as much as is possible, was preferable.

In summary, the main project objectives were:

1. Develop a passive vibration control device, primarily constructed from steel, for broadband attenuation on an excited clamped plate, simulating a realistic maritime ship hull panel;

2. The primary vibrational frequencies of concern were 81, 115 and 191 Hz;

3. Complete or considerable coverage of the panel was necessary;

4. No constrictive optimization should be performed in developing a solution which may yield a treatment suitable for only specific applications, orientations, etc.;

5. The treatment must provide improved low and broadband reduction in vibration as compared with the existing damping tile treatment; and

6. The design must total a mass ratio of $\mu < 25\%$.

E.3 Development of continuous distributed vibration absorber devices

E.3.1 Treatment design analysis

The analysis of continuously distributed vibration absorbers in Chapter C served as a useful point from which to begin design of appropriate devices to meet the project goals. The areas of interest from the earlier study could be directly applied to the need of developing a lightweight and broadband vibration control solution.

Since the vibration of the clamped panel was determined to be primary flexural for the lowest frequencies of interest, a solution which operated reactively would be better suited than a treatment capable only of supplying shear resistance to the panel vibration. To achieve a "one-size-fits-all" treatment, a design exhibiting one SDOF natural frequency would be prohibitive and not likely to meet project goals. Thus, employing a continuous spring layer exhibiting a varying transverse stiffness along the length of the device would allow for a broader range of SDOF resonance.

While it was found in Section C.7 that only so much of a variable stiffness range was beneficial, allowing for the greatest possible range would be of greatest interest in designing one device for the broadest range of reactive attenuation. Additionally, though the spread of 81 to 191 Hz was common, it was admitted that this frequency bandwidth was not always that of interest since panels changed in size from one area of the ship hull to the next. Thus, the variable stiffness spring layer design would be employed to the greatest extent practicable.

The necessity for full surface coverage was of concern, particularly given the results of Section C.3 which found that segmented coverage provide improved narrow and broadband vibration suppression. After consultation with NNS representatives, it was decided that segmentation of a treatment would be satisfactory, namely because the damping tiles themselves are available only in standard sizes.

Orthotropic distributed spring layers were observed to improve vibration attenuation in Section C.4. Though the type of vibration to suppress on the hull surface

were the fundamental clamped plate modes, this feature of spring layer design could still be employed, particularly to increase broadband control.

A reduced modulus ratio, Γ, between the top mass the host panel, though not as beneficial in conjunction with a higher orthotropy ratio, Λ, was found to be of benefit in Section C.7 for spring layers of varying stiffness. However, the material limitation of steel made achieving lower Γ difficult. Exhaustive searches were performed for a variety of new products, most often made of stainless steels, which yielded steel sheets of greater flexibility than solid steel. These were achieved by meshing, sintering and/or layering techniques.

One such product, Dynapore [120], was located. The product was composed of stainless steel sheets having a meshed construction, ideally suited for the filtering purposes. However, in light of the present objectives, the Young's modulus of such sheets was measured to be significantly lower than sheet steel: $E \approx 60$ GPa for Dynapore as compared with $E = 193$ GPa of stainless steel sheets [120]. Though some samples of the material were acquired, the expense of a large sheet of the material was a concern. Ultimately, though reduced Γ was found to improve the benefit of variable tuning in the spring layer by effectively increasing the dampening of the vibration absorber device, the cost of Dynapore was determined to be too prohibitive. Projections indicated that using Dynapore as the top mass layer, as opposed to solid or perforated stainless steel sheets, would increase material costs by almost two orders of magnitude. Since the use of steel was initially chosen by NNS to keep cost down, there was no reason to unnecessarily pursue this expensive route and Dynapore was discarded as a possibility.

Modal dynamics were found to be beneficial in distributed surface vibration attenuation as opposed to solely employing SDOF dynamics. However, this came at the cost of optimizing the design—indeed, changing the theoretical material properties—in order to achieve such a device in the simulation. Thus, modal dynamics fell under the category of inappropriate optimization methods and, as such, were not considered.

In summary, the design of the continuous distributed vibration absorber device would employ the concepts of a variable stiffness and orthotropic spring layer as well as segmented manufacture into a common size and shape. Stainless steel was furthermore chosen over standard carbon steels due to rust-proofing.

E.3.2 Experimental construction and evaluation

The orthotropic spring layer described in Section D.5 utilizing a circularly corrugated design was employed for a number of reasons. Achieving an orthotropic spring layer exhibiting a transverse SDOF natural frequency necessitates a "soft" spring layer design. Corrugated layers are one such means by which to achieve this in a semi-continuous form, particularly if the requirement for steel material in manufacturing is made.

Manufacture of corrugated materials frequently employs the use of adhesives to hold the corrugated layer to the bounding layers, or facing sheets. To eliminate adhesives, a spot welding device was constructed for the purpose of manufacturing distributed spring layers of a circular corrugated design truly using nothing more than steel. Many experimental samples were made in order to refine the manufacturing process, particularly to reduce the heat affected zone since very thin steel layers were implemented.

Numerical experiments, employing the modeling of Chapter D, found that to achieve a target SDOF natural frequency range of roughly 100 Hz for a given mass layer, approximated from the target μ, would require the spring layer to be composed of stainless steel 35 to 60 μm in thickness. This is on the order of shim metal thickness. When composed into a distributed spring layer via spot welding, the corrugated layer proved to be more robust than the use of shim metal may suggest. Figure E.2 provides a photograph of a sample spring layer produced later in the project once the spot welding process was refined.

Section D.5.2 found that the circularly corrugated spring layer yielded a lightly

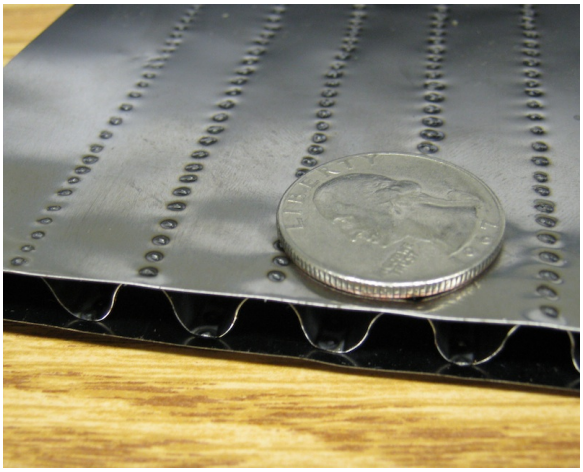

Figure E.2: Photograph of spot welded distributed spring layer sample.

damped SDOF natural frequency for the final device. Though the variable stiffness design would help to broaden the utility of the devices, a spring layer of very low dampening would not be beneficial in achieving the same order of broadband passive vibration attenuation that the damping tiles were anticipated to yield. After discussion with NNS on this issue, it was determined that using the laminated spring layer design as described in Section D.5.5 was admissible for the project, despite the inclusion of a non-steel material into the design.

Following an extensive period of manufacturing to achieve consistent spring layer construction from part to part, one sample was produced for panel testing. This sample employed a variable spring layer design with the laminated spring layer material. The top mass layer was a perforated steel.

Early on in the project, perforated masses were found to be highly beneficial in achieving target tuning frequencies of devices since the variation of perforation directly modified the mass density of the sheet. Since thicknesses of desired materials are available in finite increments, perforated materials allowed to very accurately achieve the desired tuning frequency once a top mass material thickness was determined. Acoustically, perforated mass layers have the benefit of reduced structural-acoustic coupling as the mass layer oscillates like a piston in the SDOF resonance, as opposed

Table E.1: Geometric and material specifications

Layer	a (mm)	b (mm)	h (mm)	E (Pa)	ρ (kg/m^3)	ν	η	(x_{f_1}, y_{f_1}) (mm)
Panel	305	610	1.8	2.1e11	7800	0.3	1e-3	(150,-300)
Top mass	152	191	1.2	2.1e11	5460	0.3	1e-3	—

to the greater coupling of a solid mass layer.

The sample piece constructed then had the varying equivalent elastic properties as provided in Tables D.9–D.11. The resonance frequencies predicted, and validated by experiment, were found to span the range of approximately 160 to 245 Hz. To properly evaluate the vibration attenuation benefit of such a device, a vibrating structure with a number of flexural modes in this bandwidth was necessary.

A freely suspended steel panel was employed as the vibrating test surface. This panel had the geometric and material properties are given in Table E.1. The device was centered on the position (-40,25) mm, as referenced from the center of the panel. A diagram of the test setup is shown in Figure E.3. Free suspension of the panel was achieved by hanging the panel with two elastic ropes. There are few methods to truly achieve free boundary conditions in plate vibrations testing, but this is a common means of *mostly* meeting assumptions of free suspension. Due to the tensile loading along the edge attached to the cables, in general, this makes the boundary less than ideally free.

An electrodynamic shaker was attached at a corner of the panel. White noise was driven into the shaker to excite the low order modes. A force transducer mounted in between the shaker attachment and the panel itself measured the exact input excitation. Within the bandwidth of interest, namely the range of SDOF resonances exhibited by the sample distributed absorber device, the suspended panel was predicted to have a number of vibrational modes, given in Table E.2. Provided also are the measured natural frequencies and the corresponding error relative to the prediction. It is likely that error exists in this case due to the imperfect satisfaction of the boundaries.

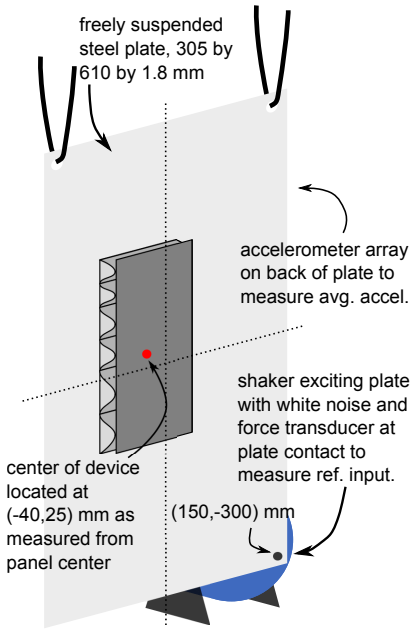

Figure E.3: Diagram of vibrating panel test to evaluate a distributed absorber design.

Table E.2: Plate natural frequencies within bandwidth of interest (% error)

Mode	(1,4)	(2,4)	(1,5)	(3,4)	(3,5)
Predicted	163	198	204	237	250
Measured	161(-0.012)	197 (-0.005)	199 (-0.0245)	232 (-0.0211)	252 (+0.008)

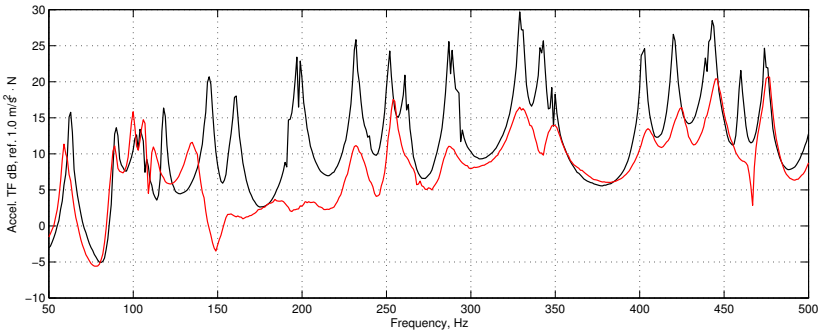

Figure E.4: Accelerance TF of untreated panel and with one distributed, variably-tuned absorber device.

Global acceleration of the panel was measured using an array of accelerometers on the panel. This was performed both before and after application of the distributed device. Figure E.4 plots the average accelerance transfer function (TF) of the untreated panel and with the device, $\mu = 0.106$. Below the tuned range of the device, the panel vibration is not substantially attenuated. However, over the range of tuning, a dramatic suppression of the panel vibration is observed. Beginning at approximately 150 Hz and continuing to 240 Hz, the vibration of the panel is globally suppressed. In other words, the vibration is attenuated to the degree that no split resonances even occur, as would be common for traditional vibration absorber devices.

This result is a significant feature of variably tuning the distributed spring layer and was observed in Section C.7. The variation in tuning of the device helped to suppress the generation of split resonances over the tuned range of natural frequencies. However, the previous analysis was for mostly undamped spring layer material. In contrast, the present laminate spring layer has a much higher equivalent loss factor, at room temperature $\eta^s \approx 0.1$ [121], due to the viscoelastic material within the material. Thus, though split resonances are likely to occur due to the reactive forcing effect of the absorber, the heavy damping of the spring layer attenuates those new resonances. As a result, the total effect is global vibration suppression over the tuning frequency range.

Furthermore, at higher frequencies, this increased dampening likely plays a role in the suppression of vibration above the tuned range. Since the device does not reactively work against the structure to the same degree in the higher frequency bandwidth as it would in its tuned bandwidth—recall that the FRF magnitude of the device as modeled and measured in Section D.5.5 declined steadily and continually above resonance—the resistive effects of the spring layer in tandem with the laminated and damped spring material attenuate the vibration in this range.

Such broadband vibration suppression capability, with particular effectiveness over the tuned frequency range, makes this distributed vibration absorber design ideal for achieving the objectives as outlined by NNS. In conjunction with a damped spring layer material, the variable stiffness design is found to be of clear benefit.

E.4 Design of final devices

Final discussions to confirm testing plans with NNS set in place a specific lay-up pattern for the devices. The pattern in shown in Figure E.5. Nine identical pieces were to be constructed and applied in the positions indicated. Thus, the span of the distributed mass and spring layers were thereafter specified. This allowed for a more direct path to achieve the target mass ratio, μ, since it eliminated many possibilities due to part availability. Furthermore, it was decided to excite the panel at the center point, as had been done in earlier testing carried out by NNS.

Taking into account the targeted frequencies of the ship hull panel to be test—81, 115 and 191 Hz—a series of numerical experiments were carried out to determine the appropriate spring and mass layer characteristics in order to achieve an appropriate tuning frequency range. The final design of the distributed spring layer used a circular and sinusoidal corrugated form, changing in peak-to-peak wavelength, λ, from 25.4 mm to 31.8 mm to 38.1 mm. A cross-section of one of the devices is provided in Figure E.6.

The laminated core material was composed of stainless steel and a laminated

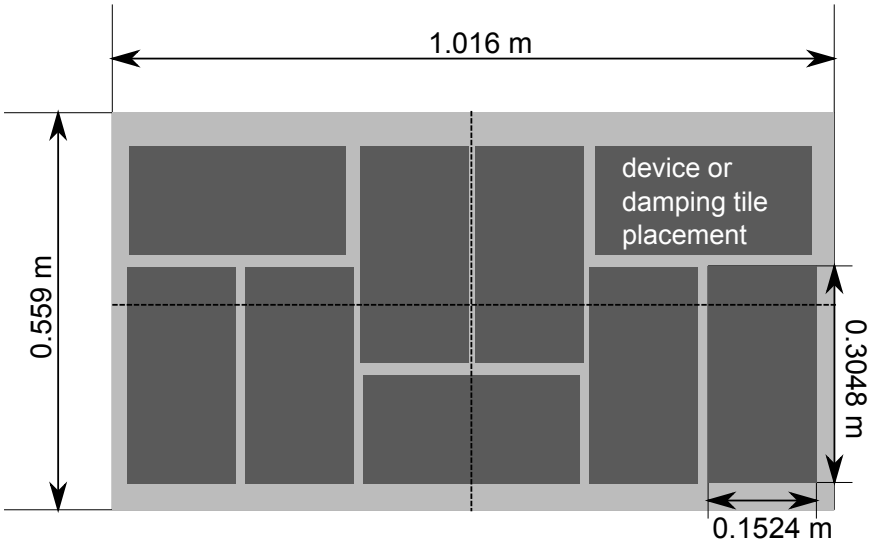

Figure E.5: Layout of continuously distributed devices on hull panel.

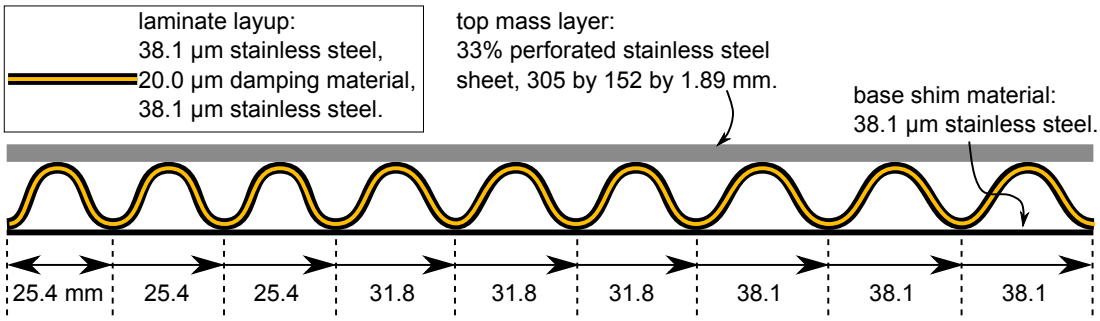

Figure E.6: Cross-section of final device design, exaggerated cross-sectional thickness.

Table E.3: Properties of stainless steel mass layer

Layer	h_t (mm)	E (Pa)	ρ (kg/m^3)	ν	η
Mass	1.89	1.9e11	5360	0.3	0.001

Table E.4: Approximated properties of clamped ship hull panel

Layer	a_b (m)	b_b (m)	h_b (mm)	E (Pa)	ρ (kg/m^3)	ν	η
Panel	1.016	0.559	4.76	2.1e11	7800	0.3	0.004

damping material. This laminated layer was described in Section D.5.5 and the corresponding equivalent orthotropic plate elasticity constants presented in Tables D.9–D.11. As three distinct wavelengths were used in the construction of the device, the equivalent continuous spring layer was discretized into three segments.

The mass layer selected was a stainless steel, 33% perforated sheet. Properties of the layer are given in Table E.3. In conjunction with the distributed spring layer, each device was predicted to exhibit a range of SDOF natural frequencies from 90 to 220 Hz.

Prior to the test, a simulation of the performance of the distributed vibration absorbers on the ship hull panel was performed. This numerical evaluation set a bar of potential vibration attenuation to anticipate. The ship hull was assumed to have isotropic properties as given in Table E.4. An expected source of deviation from the assumed mechanical properties is the fact that the actual panel is painted, generally a feature which lends itself to greater damping levels, particularly at high frequencies. Thus, the loss factor, η, of the panel was set to a value greater than usual for plain steel. As compared with the assumed parameters of the clamped panel, the full distributed absorber treatment would constitute a mass ratio of $\mu = 0.16$.

Figure E.7 plots the output of the numerical model of global vibration attenuation capability of the device treatment on the excited clamped panel. The panel is excited 3 mm off-center with the devices attached to the panel surface in the manner shown in Figure E.5. Attachment is assumed to be perfect, although, in practice the devices would be applied using a thin, but solidly-curing, epoxy layer. Vibration attenuation

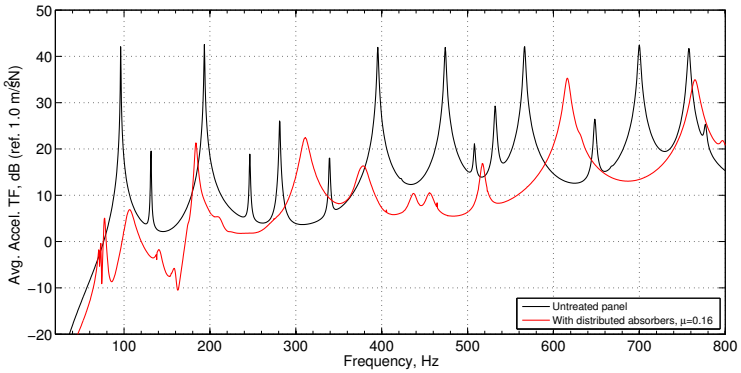

Figure E.7: Predicted global vibration attenuation of devices on ship hull panel.

is characterized in terms of the global accelerance TF, which was to be measured in practice using a large array of accelerometers.

The untreated panel exhibits very small amplitude asymmetric modal vibration as compared with the symmetric modes. Were the excitation precisely at the panel center, none of the asymmetric modes would be evident in Figure E.7. Using the assumed parameters of the clamped panel in Table E.4, the first three natural frequencies of the panel are found to be 96.1, 131 and 193 Hz. This is in reasonably close agreement with the measured frequencies of 81, 115 and 191 Hz. The deviation between the measured and predicted frequencies represents the inevitable unknowns encountered in using an existing environment for laboratory testing purposes, as opposed to careful construction of the test designed so as to conform the model.

Figure E.7 shows that the applied devices substantially attenuate the panel vibration over the tuned frequency range, primed for the 3 principal frequencies of importance. The first panel resonance at 96 Hz is attenuated by almost 40 dB. The asymmetric panel mode at 131 Hz is also attenuated but the untreated amplitude is 20 dB lower than the first mode, indicating its reduced influence in terms of the general global vibration response. The third, and symmetric, mode, 193 Hz, is attenuated by more than 20 dB. The suppression of these three frequencies quantifies the tuned vibration control benefit of the devices. The cumulative reduction in the

accelerance TF from 20 to 200 Hz was predicted to be -16.6 dB.

Above the tuning frequency range, the use of the damped laminate spring material in the corrugated spring layer design substantially helps to attenuate the panel vibration as the devices resist the motion of the panel. There is indeed global vibration suppression observed around the range of 350 to 550 Hz. The modes at these frequencies are not of significantly high order to be dominant by shearing effects, but since the devices do not predominantly operate by reactive forces above the tuned range, the predicted results suggest that, nevertheless, the devices provide a substantial resistance to the extensional motion of the panel in vibration.

This may be furthermore amplified if the device placement crosses nodal lines of any given mode still traditionally deemed to be flexural vibration. As such, the device would be stretched in both directions. Since the equivalent shearing and in-plane bending stiffnesses of the orthotropic spring layers, Tables D.9–D.11, are significant compared to the transverse stiffness, this lends itself to the notable higher frequency attenuation effects predicted from the model. Such orthotropic spring layer characteristics were found to be dramatically beneficial in Section C.4 and this is also observed in Figure E.7. The predicted cumulative reduction in accelerance TF from 20 to 800 Hz was predicted to be -8.1 dB.

Nine of the devices, as needed in the placement layout in Figure E.5, were produced with three more prepared in the event of accidental damage. The devices were generally quite robust and durable but naturally, due to the softer transverse stiffness, were capable of being crushed if too much pressure was applied in applying them to the treated surfaces. Photographs of the produced devices are shown in Figure E.8 and E.9. These devices along with a host of testing equipment were collected together for the testing at NNS.

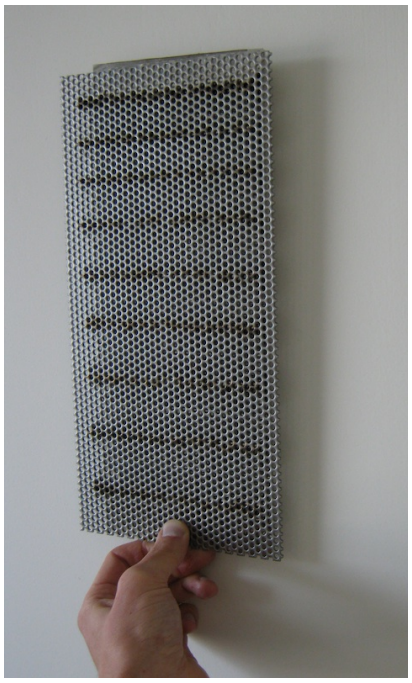

Figure E.8: Photograph of sample device used for NNS testing.

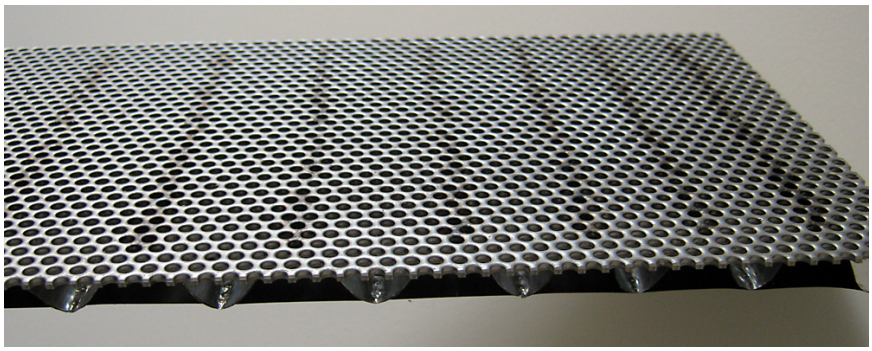

Figure E.9: Close-up of device showing minimal heat affected zone from welding manufacture process.

E.5 Testing procedures and untreated panel vibration

Just prior to official testing, the specific area of mock ship hull, which had been earlier tested and prepared by NNS representatives, became unavailable due to prioritization of the facilities for additional testing. However, other hull sections were still open for testing, many of which contained the same hull panel size as planned for.

Unfortunately, the remaining example panels conforming to the original 1.016 m by 0.559 m by 4.76 mm size included a welded rib stiffener running along the back of the panel. The presence of a substantial mechanical difference in the panel like a stiffener was anticipated to dramatically alter the frequency response of the panel from the earlier measured results. Namely it was expected that the stiffener would increase the first modal clamped plate frequency as well as perhaps cause a redistribution of the higher modes since the stiffener ran the full length of the longer dimension of the panel.

Photographs of the testing arrangement are not available but Figure E.10 provides a diagram of the testing arrangement used. The reverse side was simply the untreated surface or the device layout of Figure E.5. A 50 pound Ling Dynamics electrodynamic shaker was suspended and attached to the test panel using a long, polymer stinger. The use of a polymer material for the stinger reduces the potential for dynamics of an overly-stiff rod to become coupled with the structural response of the panel. A PCB 208 A03 force transducer was positioned between the stinger and the panel for global vibration accelerance TF measurement. The attachment to the panel was slightly off-center, roughly by a few mm from exact center.

An array of 19 PCB 330A accelerometers were randomly positioned over the surface of the panel, on the side attached to the shaker. The layout of the accelerometers is shown in Figure E.11. Random placement of the sensors ensures that the modal vibration of importance should be well- and equally-represented in the resulting measurements. Grid arrangements of accelerometers may very well be detrimental since it is likely that a portion of the sensors may be placed along nodal lines. Figure E.11

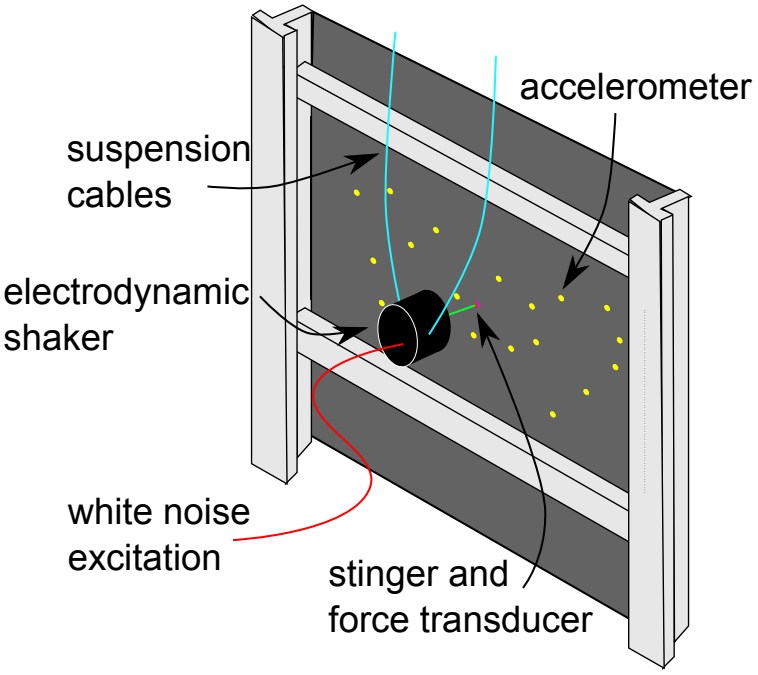

Figure E.10: Front side of test setup at NNS to evaluate clamped panel vibration attenuation from distributed absorbers.

also shows the approximate location of the welded stiffener that was present on the final tested panel.

The excitation into the shaker was white noise filtered from 20 to 2000 Hz, with a multi-meter voltage reading available to ensure that constant RMS voltage was maintained throughout all testing. The untreated panel was therefore excited in this manner and the global acceleration levels measured. Figures E.12 and E.13 plot the measured accelerance TF and acceleration autospectra, respectively.

It is immediately evident that the principal frequencies of the new clamped panel had shifted from those measured by NNS from the earlier panel. The (1,1) clamped mode natural frequency is observed at 100 Hz as compared with 81 Hz of earlier testing. Due to the stiffening weld in the panel, the (2,1) mode, originally 115 Hz, is observed to be split into two individual frequencies, 138 and 144 Hz. The third mode of the panel, (3,1), shifted down in frequency from 191 to 189 Hz. Note also that

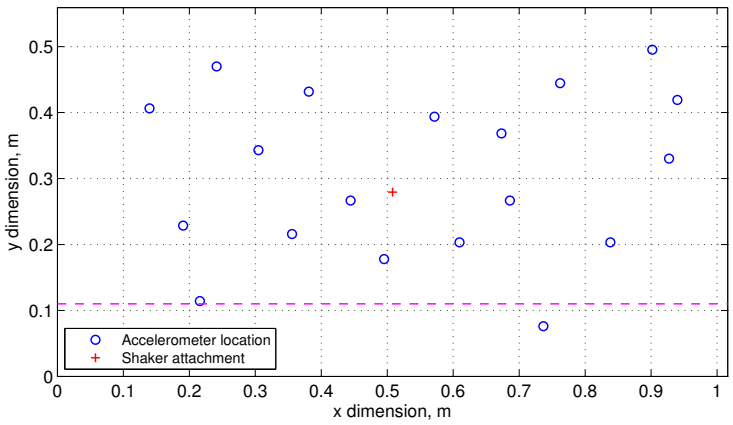

Figure E.11: Accelerometer array positioning on clamped panel showing approximate location of stiffener as pink dashed line.

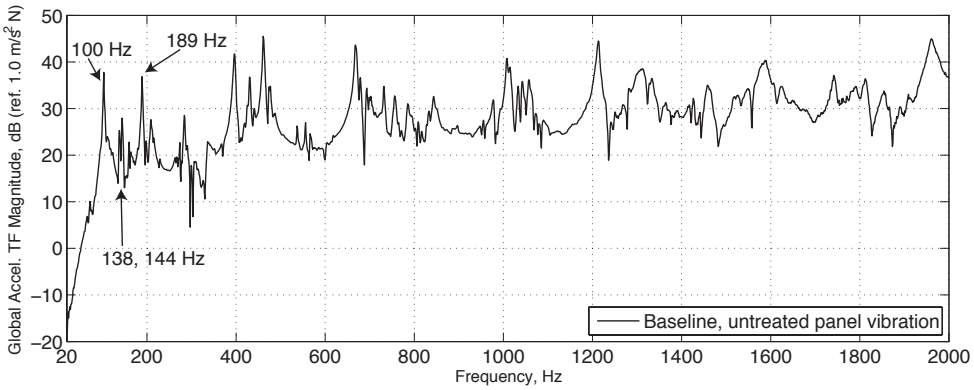

Figure E.12: Untreated clamped panel accelerance TF.

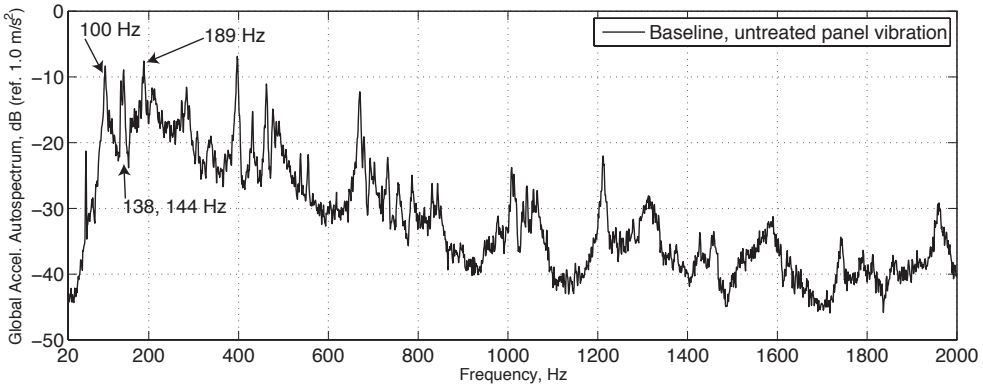

Figure E.13: Untreated clamped panel acceleration autospectra.

though the panel is a lightly-damped steel, the combination of the painted surface as well as the shaker suspension inhibits the input of energy into the lowest order panel modes. In general, were the shaker connected to a fixed platform as it excited the panel, one would anticipate that the (1,1) and (3,1) modes would be dramatically more excited than that shown in Figures E.12 and E.13. The suspension of the shaker results in the shaker itself vibrating at these lowest frequencies, reducing the overall energy able to be input in the panel.

Despite the rearrangement of the lowest order frequencies targeted for attenuation, recall that a principal objective was to design a device useful in all such low frequency vibration situations: one-size-fits-all. The change of testing scenario therefore presented an ideal challenge for the designed devices. The variable stiffness design and the include laminated damping material of the corrugated spring layer were developed in order to provide for a much broader range of useful vibration attenuation than a treatment designed for operation at a specific frequency.

From the autospectra plot of Figure E.13, it is clear that vibration levels above 500 Hz are substantially less than the fundamental clamped panel vibration, with the primary exception of the resonance at 668 Hz. Thus, to evaluate a global level of vibration attenuation, it is sufficient to focus on the range from approximately 20 to 500 Hz since the plate was difficult to excite above this bandwidth. The project

sponsor also corroborated this prioritization of focus to vibrational response less than 500 Hz.

E.6 Testing of continuously distributed vibration absorbers

To apply the distributed vibration absorbers to the rear of the panel, a specified epoxy material was used. The adhesive was PhillyBond TA-30, a epoxy and hardener mix which required 24 hours for solid curing. Though the material cured to a significant stiffness, it lended a small dampening effect between the applied material and the structural surface, as per design. The absorbers were therefore applied as desired by NNS in the manner indicated in Figure E.5. To faciliate optimal curing of the adhesive, approximately a 24 hour period elapsed between application and the testing of the devices, in addition to the fact that the environment was well-ventilated. The devices represented a mass ratio of $\mu = 0.16$ to the host panel using the assumed panel properties in Table E.4.

The test method was repeated once the distributed devices were firmly attached to the clamped panel. Figure E.14 plots the comparison of untreated panel vibration with that measured following application of the distributed devices. The devices, designed for reactive performance from 90 to 220 Hz, are seen to provide substantial vibration suppression in this bandwidth. However, as compared with the modeled result of Figure E.7, less suppression of the principal clamped mode (1,1) at 100 Hz is seen in the experiment.

There may be a simple explanation for the disparity of performance at the lowest frequency of importance. Manufacture of the distributed devices was performed by hand, by the author. Substantial experience with the spot welding device for constructing the corrugated spring layers was cultivated over the course of the project which led to exceptionally consistent all-metal spring designs, *e.g.* as shown in Fig. E.2. Despite extensive construction experience, it was known that it was difficult to consistently achieve the exact target tuning frequency when using the laminated

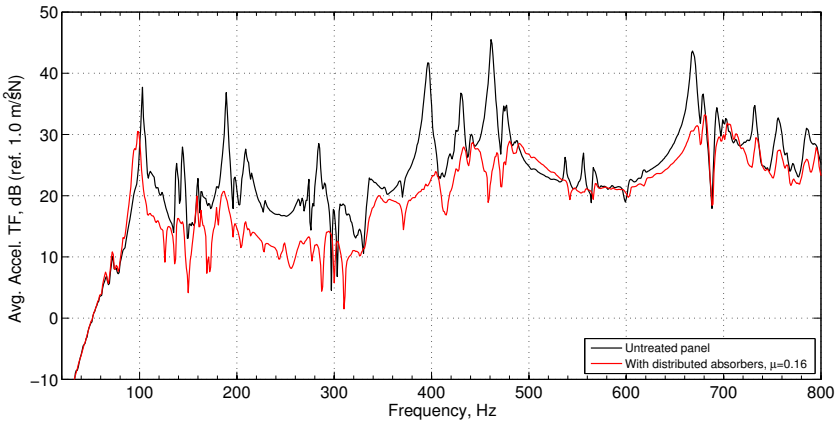

Figure E.14: Comparison of (black) untreated panel accelerance TF and that with the distributed absorbers (red).

spring design, as opposed to a single sheet comprising the corrugated spring layer. Thus, the tuning frequencies are reported as a *range* from 90 to 220 Hz as opposed to individually testing each device. (Testing each device on a firm shaker platform for actual tuning frequencies would inevitably require a strong tensile force to remove them from the platform, likely damaging the spring layer; thus, no such prior testing occurred).

In reality, the low end of the tuning bandwidth may have varied from approximately 90 to as high as 125 Hz, from the author's experience. Likewise, the high end of the bandwidth may have varied from 210 to as much as 280 Hz. Over-stiffening of the spring layer was found to be much more common than under-stiffening, in manufacturing practice. Thus, not all of the devices may have been prime for reactively attenuating vibration as low as 90 or 100 Hz, therefore justifying an observed reduced performance at this low end in Figure E.14. A more professional manufacture of the devices would likely alleviate this concern in the future.

Despite the over-prediction of vibration reduction at the (1,1) modal frequency, the remainder of the tuning frequency bandwidth is substantially attenuated. The asymmetric (2,1) mode at 138/144 Hz is globally suppressed as is the (3,1) mode at

191 Hz. This is a testament to the reactive nature of the continuously distributed vibration absorbers in suppressing surface flexural vibration. The measured cumulative accelerance TF from 20 to 200 Hz was found to be -5.5 dB. This compares with the predicted performance of -16.6 dB in Section E.4. The manufacturing difficulties mentioned above may well serve as explanation for this disparity as the principal difference in vibration suppression between the modal and measurement are those achieved at the (1,1) panel mode.

A major difference between the trends of predicted results in Figure E.7 and measured results in Figure E.14 is the amplitude of the resonances. This deviation may be easily explained by an under-predicted level of damping that the surface paint layer imparts to the panel vibration and the suspension of the excitation, mentioned in Section E.5. It is particularly anticipated that were the shaker rigidly mounted, as opposed to suspended, the peak magnitudes of the plate response would have been much greater; this therefore would have yielded reductions in the panel response of closer magnitude to the predicted results.

At higher frequencies, a combination of the damped laminate spring layer, the resistive effects of the orthotropic spring layer and the overall mass loading of the treatment lend a substantial global vibration suppression. From 200 to 300 Hz, a global reduction of approximately 6 dB is measured. The resonances at 396, 431 and 461 Hz are each dramatically attenuated. Even the resonance at 668 Hz is suppressed by 12 dB. Such magnitude of broadband vibration suppression also verifies that the devices are capable of operating both reactively and resistively.

The measured cumulative accelerance TF from 20 to 800 Hz was discovered to be -5.4 dB. This is fairly close to the predicted value of -8.1 dB. In light of the difficulties of hand manufacture and the changing test environment from earlier plans, this level of measured global vibration suppression is substantial for such a lightweight treatment. Furthermore, the model, though suggesting an overly-optimistic benefit at the (1,1) vibration mode, is in fairly close agreement for the broadband performance of the

devices, despite the many unknowns in achieving an ideal testing scenario.

For past embodiments of the continuously distributed vibration absorber using a poroelastic foam spring layer, this amplitude of vibration attenuation was not achieved above the tuning frequency range [72]. This is primarily due to the low elastic coupling between the poroelastic foam material and the host structure. Acting principally as an equivalent layer of vertical springs, the foam lends itself to negligible extensional coupling to the host structure as compared with the highly orthotropic characteristics of the corrugated spring layer design developed in the present work.

In another respect, the present continuously distributed absorbers are plainly operating in both reactive and resistive dynamic regimes since it is well known and recorded that above the tuned natural frequency, vibration absorbers are significantly less beneficial [9]. Achieving broadband vibration suppression with traditional mass-spring-dampers is only possible by making the absorbers heavy and sufficiently damped, thus increasing their overall quality factor [122]. However, adding significant mass to the structure was, in this project, a principal feature to avoid. Thus, the design of the distributed devices themselves are seen to span the gap between reactive effects of point vibration absorbers and resistive effects of constraining treatments.

E.7 Testing of damping tile treatment

To compare the performance of the distributed absorbers to the present solution used by NNS for vibration attenuation, damping tiles were prepared and cut to the form required for an identical surface coverage application, indicated in Figure E.5. The tiles, 12.7 mm in thickness each, totaled a mass ratio of $\mu = 0.2$. Thus, the distributed absorbers represented a weight savings of 20% compared with the tiles.

The distributed absorber treatment required official removal from the ship hull surface. This task requires facilities operators to effectively hammer and chisel the devices from the hull, due to the extreme hold with which the epoxy makes between attached substrates and the structural surface. Following removal, the surface re-

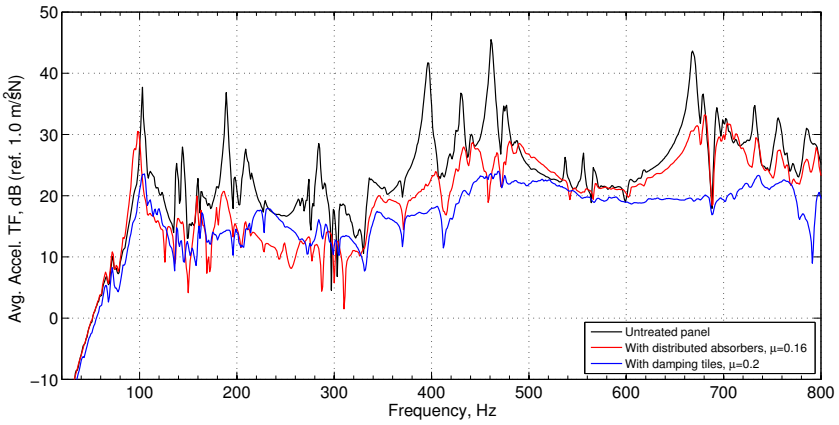

Figure E.15: Comparison of panel vibration (black) untreated; (red) with distributed absorbers; and (blue) with damping tiles.

quired sanding down to remove all remaining epoxy, and finally a re-painting.

After this process was completed, the author returned for the testing of the damping tile treatment. Test procedures were followed as before. Baseline vibration measurements were first taken. Though the autospectral content of the vibration had changed in magnitude from the first series of tests, namely due to the sanding and repainting of the surface, the accelerance TF was almost identical to the first tests. This ensures that an accurate evaluation of the damping tiles and the distributed absorbers could be made in comparing their relative vibration attenuation performance.

Once the baseline measurements were taken, the tiles were applied using the same epoxy and configuration as the absorbers. The same 24-hour time period elapsed between application and the testing of the panel vibration after tile application. Figure E.15 plots the panel vibration when untreated, with the distributed absorbers and with the damping tiles.

The tiles, being a heavily-damped polymer material, are only capable of suppressing low frequency panel vibration by means of mass loading the structure. Though the tiles were segmented, which was found in the present work and in past literature to increase low frequency vibration suppression capabilities of resistive vibration con-

Table E.5: Cumulative reduction (dB) in accelerance TF from untreated clamped panel vibration

	Tuned Range	Global Range
Evaluation	20–200 Hz	20–800 Hz
Model w/ devices	-16.6	-8.1
Measured w/ devices	-5.5	-5.4
Measured w/ tiles	-7.5	-9.1

trol treatments [68–70], little shearing effects are possible in the fundamental clamped panel modes which are dominated by in-phase flexural vibration.

Thus, in the absorbers' tuned frequency range, 90 to 220 Hz, the increased mass and dampening of the tiles is observed to suppress nearly the same order of vibration as the distributed absorber devices. Above this bandwidth, shear resistance effects imparted by the tiles are more important, as the bending wavelengths of the panel are reduced and the modal density of the plate vibration is increased. The more influential shear resistance explains the considerable vibration suppression of panel vibration that the tiles provide in the range of 600 to 800 Hz.

However, from approximately 20 to 500 Hz, little improvement in vibration suppression is achieved with the heavier tiles as compared with the continuously distributed absorbers. The cumulative reduction in accelerance TF compared with untreated panel vibration levels is summarized in Table E.5 for the variety of cases considered in this Chapter.

The principal reason for improved vibration suppression of the damping tiles as compared with the distributed absorbers over the tuned frequency bandwidth, as seen in Table E.5, is the increased mass loading on the structure. The (1,1) mode is attenuated by the tiles approximately 6 dB more than the absorber devices. Were manufacturing difficulties more easily overcome for the corrugated and laminated spring layer of the continuous absorbers, this disparity should not only have been reduced but ideally reversed.

The broadband cumulative reduction of the tiles shows a marked improvement over the absorbers, -9.1 dB compared with -5.4 dB, which is primarily due to the

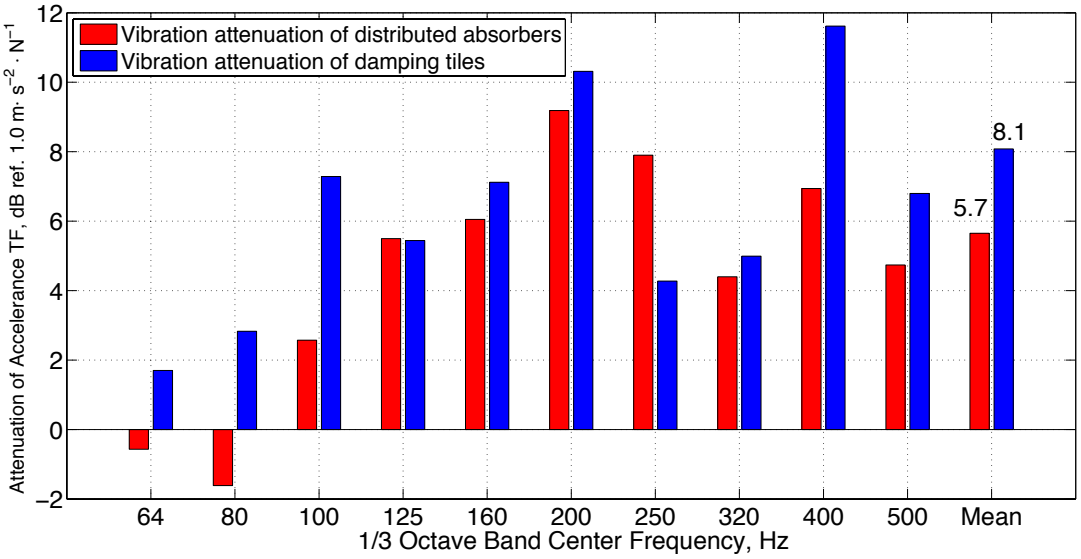

Figure E.16: One-third octave band attenuation of panel vibration.

significant and damped shear resistance, by design, the tiles impart to the panel vibration from approximately 400 to 800 Hz. This is observed in Figure E.15 by the global vibration reduction in this bandwidth.

Finally, as a more traditional comparison, Figure E.16 plots the attenuation of the panel accelerance in one-third octave bands. There is a 1 dB or less difference in performance between the distributed absorbers and the damping tiles from 125–320 Hz, with the exception of the 250 Hz one-third octave band where the absorbers are seen to provide 3.7 dB more attenuation. The difference of the mean levels of vibration attenuation in one-third octave bands from 64–500 Hz is just 1.7 dB, in favor of the damping tiles of 20% greater mass.

Overall, however, this is not a significant difference in performance between the absorbers and tiles. Since the tiles were 20% heavier than the absorbers, this indicates that the distributed absorbers are a versatile passive vibration control device and help to span the divide between interest in attenuating a single frequency and the need to attenuate all frequencies. With the improvement of manufacturing methods, tuned and global vibration attenuation would most likely improve. Considering

low frequency vibration attenuation, as the bandwidth of troublesome frequencies becomes narrower, it is anticipated that the distributed devices would be of greater benefit per added mass given their reactive effects like classical vibration absorbers.

E.8 Conclusions

This chapter presented the development of continuously distributed vibration control devices for testing on a realistic marine hull surface. The objectives of the project sponsor could be summarized as achieving equal or improved vibration suppression from a typical hull panel as compared with the existing damping tile treatment, for a reduced cost in weight. Furthermore, the dominant use of steel for the absorber devices was desired and a device usable for a variety of vibration control scenarios, "one-size-fits-all", was vital.

Development followed the principal features regarding continuously distributed absorbers which were observed in Chapters C and D. It was determined that orthotropic spring layers, lending resistive effects to the net vibration suppression potential, were clearly beneficial in achieving broadband control as opposed to less extensionally-coupled materials like poroelastic foam.

To broaden the reactive usefulness of the absorber design, a variably stiffened spring layer was incorporated. This spring layer was furthermore composed of a damped laminated spring material which lent for significantly greater transverse and extensional damping than solely employing steel materials. The product of the development stage was a device capable of substantial reactive and resistive vibration attenuation.

A number of test samples of the device were produced and one such sample was evaluated on a vibrating plate in free suspension. Measurements indicated the clear benefit of the three main features of the distributed spring layer: variable stiffness, orthotropic characteristics and the laminated spring material. While classical mass-spring-dampers often yield split resonances in the host structure vibrational response

around the tuned device frequency, the continuously distributed absorber design did not produce this effect, instead globally attenuating the free panel vibration over the tuning frequency range.

Following confirmation from the project sponsor regarding test protocol and procedure, a number of the final devices were constructed with the greatest manufacturing consistency possible. The ship hull panel to be tested was unfortunately changed prior to testing although this served to evaluate the versatility of the developed devices. Baseline vibration tests were carried out along with tests employing the continuously distributed absorbers.

Significant tuned and broadband vibration suppression was observed for the devices applied to the panel. The modeled vibration suppression over-predicted the magnitude of suppression capable for the first panel mode as compared with measurements. However, the difficulties encountered in manufacture explain the disparity in part. Global vibration attenuation of the devices on the panel was also substantial, clearly indicating the the devices are simultaneously reactive absorbers and resistive treatments.

Testing with the existing passive vibration control solution of the project sponsor, a heavily-damped tile material, found the that from approximately 20 to 500 Hz both the absorbers and tiles provided a comparable reduction in panel vibration. In the range of excitation which mattered most in this application, <500 Hz, there was <2 dB difference in the mean attenuation capability between the treatments. Depending on the bandwidth of excitation frequencies of interest, the advantage of the distributed devices in providing a lightweight alternative to the damping tiles could become more apparent.

In summary, a robust passive vibration control device was developed to attenuate surface vibration both in the low frequency regime where reactive forces are beneficial as well as into higher frequencies where resistive effects are of greater influence. While most vibration control treatments fall into either the prior or latter class in

terms of their dynamics, the present continuously distributed device employs both dynamic regimes. This increased versatility also allows the device to achieve substantial broadband vibration attenuation at a fraction of the applied weight of either one of the vibration control device classes, reactive or resistive.

APPENDIX F

Dynamic response of surfaces to which discrete electromagnetic oscillators are attached

Many energy harvesting devices employ mass-spring-damper dynamics ascribed to the classical vibration absorber. Proper design suggests that when host structural motion excites the devices at resonance, maximum electrical power output is produced. When applied to lightweight structures, this condition no longer holds since the response of the structure and the attached harvesters is dynamically coupled. In this regime, the devices become true vibration absorbers that alter the oscillations of the structure which may consequently inhibit energy harvesting capability. This paper presents an analysis of distributed single- and two-degree-of-freedom, linear electromagnetic oscillators attached to a harmonically excited, lightweight panel. The coupled Euler–Lagrange equations of motion are solved and the simultaneous goals of vibration attenuation of the host panel and energy harvesting from attached devices are considered for a variety of scenarios. It is found that the concurrent objectives are not necessarily exclusive but care must be taken to attain low mechanical damping for the oscillators, to use treatments of low mass ratio and to properly distribute the oscillators over the structural surface.

F.1 Introduction

The interest in converting ambient vibrational energy into useful electrical power has led to a broad range of devices employing electromechanical coupling. Whether embodied as cantilevered specimens [123–125], mass-spring oscillators [31, 33, 126, 34], or surface-attached treatments [127, 128], the devices are excited by the host structural vibration and external circuits are utilized to quantify the net electrical power output. A frequent assumption in the fundamental analysis of basic oscillator-

type harvesters is that the devices are excited by way of base vibration [76, 36, 39, 25, 129]. But as energy harvesting concepts are applied to the vibration of lightweight structures, this mathematical model is no longer appropriate.

When the mass of the harvester begins to approach the mass of the host structure, the vibrations of both are coupled and new dynamic governing equations must be considered to properly model the result. While the complexity of this new analysis is greater than the earlier approximations of base excitation, the coupled dynamics provide the potential to achieve two distinct objectives: vibration suppression of the host structure and energy harvesting from the devices attached to it. This may be important, for example, on aircraft panels where passive vibration control treatments help to generate a more pleasing cabin environment and the attached electromechanical devices may simultaneously power embedded sensors for structural monitoring purposes. The unification of both goals into the manifestation of a single treatment would therefore be of benefit.

While other present literature employs the phrase "simultaneous vibration suppression and energy harvesting" [35, 52], the context for the vibration control in those works is due to piezoelectric shunt damping once the devices are attached to external circuits. In this analysis, vibration attenuation is achieved through a combination of damping effects via external circuits and re-active effects, the latter of which are those resulting from the classical dynamics of vibration absorber devices working against the host structure.

This paper presents a simple model based on Euler–Lagrange equations of motion for the vibration of a simply-supported rectangular panel to which a number of electromagnetically (E–M) coupled single- (SDOF) or two-degree-of-freedom (2DOF) oscillators are attached. The E–M mass-spring-dampers are attached to external circuits and the electrical governing equations are solved simultaneously with the mechanical problem to determine output electrical power potential. Metrics of global vibration suppression and energy harvesting over a bandwidth of frequencies are uti-

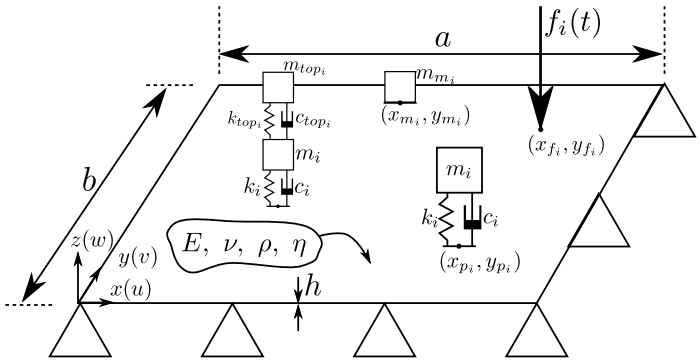

Figure F.1: Mechanical geometry of the present analysis.

lized and a number of scenarios are considered: single oscillators, random distributions of oscillators and the effects of internal damping. This analysis is intended to show that the dual objectives of energy harvesting and vibration attenuation are not inherently opposed and that there exists a unique potential to develop robust treatments which may serve both ends.

F.2 Model formulation

A thin, simply-supported rectangular panel is considered, to which N_p SDOF or 2DOF mass-spring-dampers have been attached at positions (x_{p_i}, y_{p_i}), Figure F.1. The host panel is excited by N_f out-of-plane harmonic point forces, $f_i(x_{f_i}, y_{f_i}, t)$. The attached oscillators exhibit an electromagnetic coupling as, in one conceivable embodiment, the magnetic mass, m_i, moves along the axis of a conductive coil inducing a flow of electrical current through an external circuit (Figure F.2) [34]. In the case of the 2DOF oscillators, it is assumed that only one of the oscillating sub-systems exhibits electromagnetic coupling. In the present analysis, the response of the oscillator spring is assumed to remain within a linear regime.

The Lagrangian of the system is

$$L = T - V + W_m \tag{F.1}$$

The total kinetic energy, T, is the sum of the contributions from the host panel and

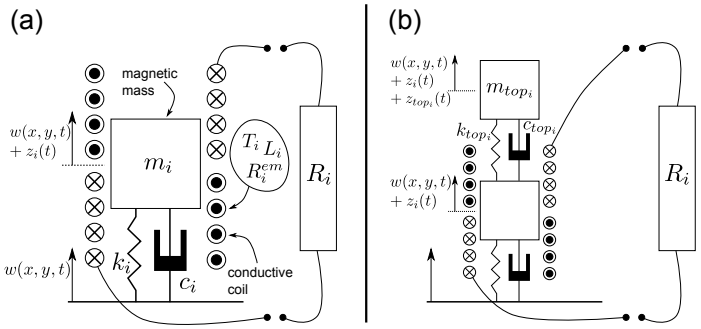

Figure F.2: Schematics of (a) SDOF E–M oscillators and (b) 2DOF oscillators, here showing electromagnetic coupling for the bottom oscillator sub-system.

the attached oscillators

$$T = \frac{1}{2}\rho \int_\Omega \dot{\mathbf{u}}^t \dot{\mathbf{u}} \mathrm{d}\Omega + \frac{1}{2}\sum_{i=1}^{N_p} m_i \left[\dot{w}\left(x_{p_i}, y_{p_i}\right) + \dot{z}_i\right]^2$$
$$+\frac{1}{2}\sum_{i=1}^{N_p} m_{top_i}\left[\dot{w}\left(x_{p_i}, y_{p_i}\right) + \dot{z}_i + \dot{z}_{top_i}\right]^2 + \frac{1}{2}\sum_{i=1}^{N_m} m_{m_i}\dot{w}^2\left(x_{m_i}, y_{m_i}\right) \tag{F.2}$$

where the displacements of the panel are $\mathbf{u} = [u(x,y,z,t)\ v(x,y,z,t)\ w(x,y,z,t)]^t$; ρ is the panel mass density; m_i is the mass of the i^{th} mass-spring-damper attached to the panel at (x_{p_i}, y_{p_i}); z_i is the relative displacement between the i^{th} mass-spring-damper sub-system and the panel; z_{top_i} represents the relative displacement between the top oscillator, of mass m_{top_i}, and the bottom oscillator of the 2DOF system; and m_{m_i} is the mass of the i^{th} concentrated mass attached to the panel at (x_{m_i}, y_{m_i}). The time derivative is denoted by $\dot{()}$ and $()^t$ denotes the matrix transpose operator.

The total potential energy, V, is

$$V = \frac{1}{2}\int_\Omega \epsilon^t \mathbf{c} \epsilon \mathrm{d}\Omega + \frac{1}{2}\sum_{i=1}^{N_p} k_i z_i^2 + \frac{1}{2}\sum_{i=1}^{N_p} k_{top_i}\left(z_{top_i}\right)^2 \tag{F.3}$$

where ϵ is the strain tensor of the panel; $\mathbf{c}$ is the stiffness matrix of the panel; k_i is the spring constant of the bottom oscillator; and k_{top_i} is the spring constant of the top oscillator.

The electromagnetic energy in the coils, W_m, is

$$W_m = \frac{1}{2}\sum_{i=1}^{N_p}\left[L_i \dot{q}_i^2 + T_i \dot{q}_i z_i\right] \tag{F.4}$$

where L_i is the internal inductance of the coils of the i^{th} oscillator; q_i is the charge passing through the coils; and $T_i = B_i l_i$ is transducer constant for the oscillator, calculated as the product of the magnetic flux density, B_i, and the length of the conductive coils l_i. If the top mass of a 2DOF oscillator is electromagnetically-coupled, one replaces the term z_i in Equation F.4 with z_{top_i}.

The dissipation function for the coupled system is the sum of the contributions of mechanical damping in the panel and of attached circuitry to the electromagnetic oscillators. It is here assumed that the external circuits are composed of resistive loads, R_i, such that the total dissipation function is

$$D = \frac{1}{2}c\int_{\Omega}\dot{\mathbf{u}}^t\dot{\mathbf{u}}\mathrm{d}\Omega + \frac{1}{2}\sum_{i=1}^{N_p}c_i\dot{z}_i^2 + \frac{1}{2}\sum_{i=1}^{N_p}c_{top_i}\left(\dot{z}_{top_i}\right)^2 + \frac{1}{2}\sum_{i=1}^{N_p}\left(R_i + R_i^{em}\right)\dot{q}_i^2 \tag{F.5}$$

where c is the viscous damping coefficient of the panel; c_i is the damping coefficient of the bottom oscillator; c_{top_i} is the damping coefficient of the top oscillator; and R_i^{em} is the internal resistance of the conductive coil. The damping ratio of the oscillators is defined as $\zeta_i = c_i/2\sqrt{m_i k_i}$. In the present study, $c_i = c_{top_i}$.

The Euler–Lagrange governing equations for the coupled system are

$$\begin{aligned}
\frac{\mathrm{d}}{\mathrm{dt}}\left[\frac{\partial L}{\partial\dot{\mathbf{u}}}\right] + \frac{\partial D}{\partial\dot{\mathbf{u}}} - \frac{\partial L}{\partial\mathbf{u}} &= \mathbf{F}\\
\frac{\mathrm{d}}{\mathrm{dt}}\left[\frac{\partial L}{\partial\dot{z}_i}\right] + \frac{\partial D}{\partial\dot{z}_i} - \frac{\partial L}{\partial z_i} &= 0\\
\frac{\mathrm{d}}{\mathrm{dt}}\left[\frac{\partial L}{\partial\dot{z}_{top_i}}\right] + \frac{\partial D}{\partial\dot{z}_{top_i}} - \frac{\partial L}{\partial z_{top_i}} &= 0\\
\frac{\mathrm{d}}{\mathrm{dt}}\left[\frac{\partial L}{\partial\dot{q}_i}\right] + \frac{\partial D}{\partial\dot{q}_i} - \frac{\partial L}{\partial q_i} &= 0
\end{aligned} \tag{F.6}$$

where $\mathbf{F}(t) = \sum_{i=1}^{N_f}\mathbf{f}_i(\mathbf{x}_{f_i}, t)\mathbf{u}(\mathbf{x}_{f_i})$ are the generalized forces.

For the thin, isotropic panel of interest and considering harmonic excitation:

$$\mathbf{u} = \begin{bmatrix} -z\frac{\partial w(x,y,\omega)}{\partial x} \\ -z\frac{\partial w(x,y,\omega)}{\partial y} \\ w(x,y,\omega) \end{bmatrix} \qquad \epsilon = \begin{bmatrix} \epsilon_x \\ \epsilon_y \\ 2\epsilon_{xy} \end{bmatrix} \qquad \mathbf{c} = \begin{bmatrix} \frac{E}{1-\nu^2} & \frac{\nu E}{1-\nu^2} & 0 \\ \frac{\nu E}{1-\nu^2} & \frac{E}{1-\nu^2} & 0 \\ 0 & 0 & \frac{E}{2(1+\nu)} \end{bmatrix} \tag{F.7}$$

where E is the Young's modulus and ν is the Poisson's ratio. A Ritz method solution form for the panel displacement is assumed:

$$w(x,y,\omega) = \sum_{n=1}^{N} a_n(\omega)\Psi_n(x,y) \tag{F.8}$$

where $\mathbf{a}(\omega) = [a_1(\omega)\ a_2(\omega)\ \cdots\ a_N(\omega)]^t$ are the N generalized co-ordinates and $\Psi(x,y) = [\Psi_1(x,y)\ \Psi_2(x,y)\ \cdots\ \Psi_N(x,y)]$ the admissible trial functions of the panel out-of-plane displacement. Substituting the above components into the Euler–Lagrange equations F.6 (a–d) and assuming the bottom oscillator is electromagnetically coupled yields

$$\begin{aligned} &\left[-\omega^2\left(M_{mn}+H_{mn}+G_{mn}+P_{mn}\right)+j\omega C_{mn}+K_{mn}\right]a_m(\omega) \\ -\omega^2&\left[\sum_{i=1}^{N_p} m_i\Psi_m(x_{p_i},y_{p_i})z_i(\omega)+\sum_{i=1}^{N_p} m_{top_i}\Psi_m(x_{p_i},y_{p_i})z_{top_i}(\omega)\right] = F_m(\omega) \\ &m=1,2,\ldots,N;\ n=1,2,\ldots,N \end{aligned} \tag{F.9}$$

$$\begin{aligned} -\omega^2 m_i\sum_{m=1}^{N}\Psi_m(x_{p_i},y_{p_i})a_m(\omega)&+\left[-\omega^2 m_i+j\omega c_i+k_i\right]z_i(\omega) \\ -\omega^2 m_{top_i}z_{top_i}(\omega)&-j\omega T_i q_i(\omega)=0 \\ i&=1,2,\ldots,N_p \end{aligned} \tag{F.10}$$

$$\begin{aligned} -\omega^2 m_{top_i}\sum_{m=1}^{N}\Psi_m(x_{p_i},y_{p_i})a_m(\omega)&-\omega^2 m_i z_i(\omega) \\ +\left[-\omega^2 m_{top_i}+j\omega c_{top_i}+k_{top_i}\right]&z_{top_i}(\omega)=0 \\ i&=1,2,\ldots,N_p \end{aligned} \tag{F.11}$$

$$\begin{aligned} j\omega T_i z_i(\omega)+\left[-\omega^2 L_i+j\omega\left(R_i+R_i^{em}\right)\right]q_i(\omega)&=0 \\ i&=1,2,\ldots,N_p \end{aligned} \tag{F.12}$$

In the event that the top oscillator is electromagnetically coupled, the term $-j\omega T_i q_i(\omega)$ of Eq. F.10 is transferred to Eq. F.11 and the term z_i in Eq. F.12 is replaced with z_{top_i}. The following are specified

$$M_{mn} = \rho h\int_0^a\int_0^b\left[\Psi_m\Psi_n+\frac{h^2}{12}\left(\frac{\partial\Psi_m}{\partial x}\frac{\partial\Psi_n}{\partial x}+\frac{\partial\Psi_m}{\partial y}\frac{\partial\Psi_n}{\partial y}\right)\right]\mathrm{d}x\mathrm{d}y \tag{F.13}$$

$$K_{mn} = \frac{Eh^3}{12\left(1-\nu^2\right)} \int_0^a \int_0^b \left[\frac{\partial^2 \Psi_m}{\partial x^2} \frac{\partial^2 \Psi_n}{\partial x^2} + \nu \left[\frac{\partial^2 \Psi_m}{\partial x^2} \frac{\partial^2 \Psi_n}{\partial y^2} + \frac{\partial^2 \Psi_m}{\partial y^2} \frac{\partial^2 \Psi_n}{\partial x^2} \right] + \frac{\partial^2 \Psi_m}{\partial y^2} \frac{\partial^2 \Psi_n}{\partial y^2} + 2\left(1-\nu\right) \frac{\partial^2 \Psi_m}{\partial x \partial y} \frac{\partial^2 \Psi_n}{\partial x \partial y} \right] \mathrm{d}x\mathrm{d}y \quad \text{(F.14)}$$

$$C_{mn} = \alpha M_{mn} + \beta K_{mn} \quad \text{(F.15)}$$

$$H_{mn} = \sum_{i=1}^{N_p} m_i \Psi_m\left(x_{p_i}, y_{p_i}\right) \Psi_n\left(x_{p_i}, y_{p_i}\right) \quad \text{(F.16)}$$

$$G_{mn} = \sum_{i=1}^{N_p} m_{top_i} \Psi_m\left(x_{p_i}, y_{p_i}\right) \Psi_n\left(x_{p_i}, y_{p_i}\right) \quad \text{(F.17)}$$

$$P_{mn} = \sum_{i=1}^{N_m} m_{m_i} \Psi_m\left(x_{m_i}, y_{m_i}\right) \Psi_n\left(x_{m_i}, y_{m_i}\right) \quad \text{(F.18)}$$

$$F_m(\omega) = \sum_{i=1}^{N_f} f_i(x_{f_i}, y_{f_i}, \omega) \Psi_m(x_{f_i}, y_{f_i}) \quad \text{(F.19)}$$

Equations F.9–F.12 are composed of $N + 2N_p$ generalized co-ordinates for the system employing SDOF oscillators and $N + 3N_p$ co-ordinates for 2DOF oscillators. The mass ratio is defined as

$$\mu = \frac{\sum_{i=1}^{N_p} \left[m_i + m_{top_i}\right]}{abh\rho} \quad \text{(F.20)}$$

As a metric to evaluate the global vibration levels of the panel, the mean-square out-of-plane velocity is computed as

$$\left\langle \dot{w}\left(\omega\right)\right\rangle^2 = \frac{\omega^2}{2ab} \sum_m^N \sum_n^N a_m^*(\omega) a_n(\omega) \int_0^a \int_0^b \Psi_m^*(x,y) \Psi_n(x,y) \mathrm{d}x\mathrm{d}y \quad m = 1, 2, \ldots, N;\ n = 1, 2, \ldots, N \quad \text{(F.21)}$$

where $()^*$ denotes the complex conjugate. The current through the i^{th} load resistance, R_i, is determined by $\dot{q}_i(\omega) = i_i(\omega)$. The voltage over the resistance is therefore computed as $v_i(\omega) = i_i(\omega) R_i$ and the average power is $P_i(\omega) = |v_i(\omega)|^2 / 2R_i$.

Table F.1: Panel specifications.

a (mm)	b (mm)	h (mm)	E (Pa)	ν	ρ (kg/m^3)	η	(x_{f_1}, y_{f_1}) (mm)
600	400	2	7.1e10	0.3	2100	1e-3	(100, 100)

Table F.2: Oscillator specifications.

ζ_1	T_1 (T·m)	L_1 (μH)	R_1^{em} (Ω)	(x_{p_1}, y_{p_1}) (mm)
1e-2	10	100	5	(300,200)

To compare the mean-square velocity or average power over a bandwidth of frequencies, the cumulative values are defined by

$$\langle \underline{\dot{w}} \rangle^2 = \sum_{r=1}^{R} \langle \dot{w}\,(\omega_r) \rangle^2 \qquad \underline{P_i} = \sum_{r=1}^{R} P_i(\omega_r) \tag{F.22}$$

where R is some determined range of frequencies. The attenuation of the panel vibration from the untreated levels is expressed as the difference

$$\Delta \langle \underline{\dot{w}} \rangle^2 = \langle \underline{\dot{w}} \rangle^2_{with\ oscillators} - \langle \underline{\dot{w}} \rangle^2_{untreated} \tag{F.23}$$

F.3 One centrally-located oscillator

To initially evaluate the simultaneous aims of vibration suppression and energy harvesting from the same device using the model, a single electromagnetic oscillator was positioned at the center of the simply supported panel. Geometric and material properties of the system are provided in Table F.1. Damping of the panel was included by means of an isotropic loss factor, η, such that in Eq. F.15, $\alpha = 0$ and $\beta = \eta/\omega$. The oscillators were either a SDOF device, a 2DOF device with E–M coupling on the bottom sub-system or a 2DOF device with coupling on the top oscillating mass. In the event of the 2DOF device, it was assumed that the total mass ratio, μ, was split with 70% of the mass as the bottom oscillator and 30% of the mass as the top oscillator. Properties of the oscillator electrical and electromechanical characteristics are provided in Table F.2.

The SDOF oscillators were tuned to have a natural frequency of 50 Hz; as such, the individual mass, m_i, and spring constant, k_i, changed with each run of the sim-

ulation as μ was modified. For the 2DOF oscillators, the bottom oscillator natural frequency was maintained at $\sqrt{k_i/m_i}/2\pi$ =61 Hz, while for the top sub-system $\sqrt{k_{top_i}/m_{top_i}}/2\pi$ =143 Hz. Collectively, the 2DOF oscillator natural frequencies become 50 Hz and 174 Hz [130].

Numerical simulations of the forced response of the panel were computed from 1–300 Hz in 1 Hz increments. This bandwidth contains the first 7 modes of the panel: 49.9 Hz (1,1); 96.0 Hz (2,1); 154 Hz (1,2); 173 Hz (3,1); 200 Hz (2,2); 276 Hz (3,2); and 280 Hz (4,1). The metrics of cumulative power, Eq. F.22 (b) and reduction in the panel mean-square velocity, Eq. F.23 were computed for a range of μ and R_1.

Figure F.3 plots the metrics of vibration suppression (top row) and energy harvesting (bottom row) for the case of adding the SDOF oscillator (first column), 2DOF oscillator with bottom E–M coupling (second column) and 2DOF oscillator with top E–M coupling (third column). Improved vibration attenuation is achieved by means of the heaviest devices as well as the least load resistances. Greatest suppression is attained with the SDOF oscillator but increases in R_1 are seen to decrease the benefits. However, for smaller μ, the SDOF oscillator is less susceptible to a reduction in attenuation performance for changes in R_1.

From the bottom row of Figure F.3, optimized output power is not achieved for the same range of μ and R_1 as for vibration attenuation. Instead, for the SDOF oscillator the greatest power is generated for $\mu = 2.2e-2$ and $R_1 = 44.6\ \Omega$: $\underline{P_1} = 10.4\ \mu$W. For practical passive vibration control treatments, this μ is very small and indicates that for simple energy harvesting systems, *i.e.* few devices attached to the structure, the careful limitation of additional mass is important. Too much mass, while increasing the devices' influence on reducing the host vibration levels, actually inhibits the ability of the device to convert the input kinetic energy into electrical power. On the opposite extreme, too little mass also reduces the energy harvesting potential, though to a degree this may be offset by greater R_1.

Neither of the two cases of 2DOF oscillators achieve this magnitude of power

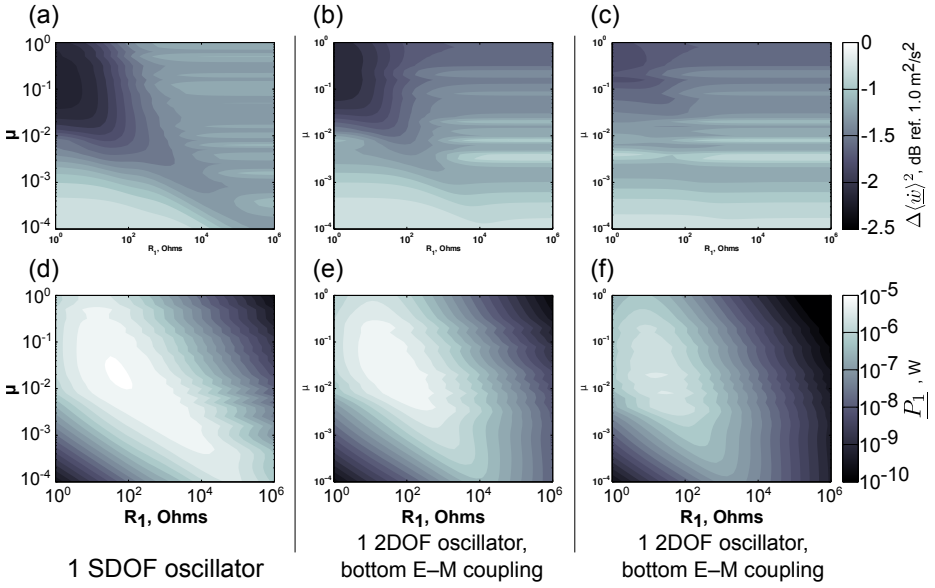

Figure F.3: Vibration suppression for case of the panel having a (a) SDOF oscillator, (b) 2DOF oscillator with bottom E–M coupling and (c) 2DOF oscillator having top E–M coupling. Energy harvesting for panel having a (d) SDOF oscillator, (e) 2DOF oscillator with bottom coupling and (f) 2DOF oscillator with top coupling.

output. Though the increased dynamic complexity of the device may help explain why it is less useful in generating significant electrical power, this same feature might also be argued as a benefit. The second natural frequency of the device, 174 Hz, was designed so as to match a symmetric mode shape of the panel, 173 Hz; thus, whether operating at 50 Hz or 174 Hz, the device was intended to be of greater electrical benefit than the SDOF device which is principally useful at 50 Hz. However, it appears that the presence of the non-E–M-coupled mass in the 2DOF oscillator is ultimately a detriment to the generation of electrical power in that it serves to reduce the net power input into the component which is coupled to the external circuit.

Figure F.4 plots the panel mean-square velocity for the scenarios of optimum energy harvesting potential, $\mu = 2.2e-2$ and $R_1 = 44.6\ \Omega$. As is anticipated for vibration absorber devices, the targeted untreated panel natural frequency of 50 Hz is split into two resonances, determined by the mass ratio of the treatment [82]. It is evident that the external circuit serves as a damping mechanism for the devices,

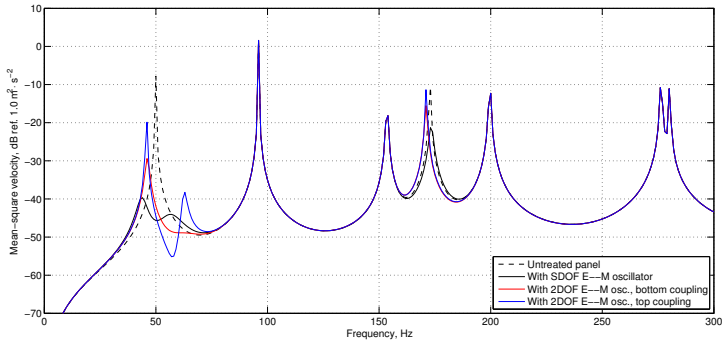

Figure F.4: At optimum energy harvesting configuration, mean-square velocity of the panel untreated (black dashed), with the SDOF device (black curve), with the 2DOF device with bottom coupling (red curve) and the 2DOF device with top coupling (blue curve).

particularly in the case of the SDOF oscillator which almost equally dampens the split resonances around 50 Hz. The 2DOF oscillators do not have the same order of influence on the host panel as the SDOF device, since the split resonances for the 2DOF devices are much less damped. The oscillators are positioned at the center of the panel, and as such only symmetric modes are capable of being suppressed. The only other symmetric mode in the bandwidth of interest, 173 Hz, is in fact attenuated by 10 dB by the SDOF oscillator but predominantly just shifted in frequency by the less influential 2DOF oscillators.

F.4 Randomly positioned oscillators

In practice, it is well-known that a single vibration absorber device will have little authority at passively controlling the broadband vibration of a distributed structure. Thus, a solution may be to apply a greater number of absorbers over the structural surface having total mass satisfying a designated limit on μ. The simulations were then evaluated using a random distribution of 15 oscillators, having positions indicated as in Figure F.5. The only restriction on the position of the oscillators was that the random distribution be confined from $a/6 < x_{p_i} < 5a/6$ and $b/6 < y_{p_i} < 5b/6$.

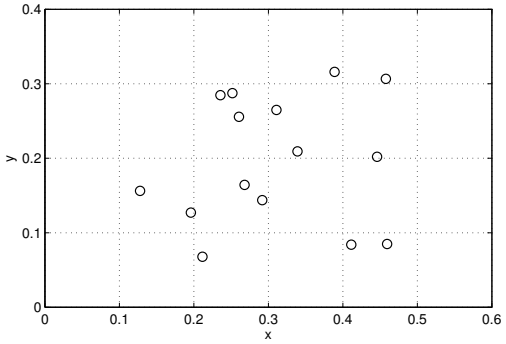

Figure F.5: Randomly selected locations of the 15 oscillators.

Since the panel was supported at the edges, oscillators placed too close to the panel extremities would be of little use since they may be poorly excited.

The range of μ and R_i was again varied, maintaining the same R_i for each oscillator. The natural frequencies of the devices were the same as in Section F.3. The mass of the oscillators was evenly distributed, such that $m_i = abh\rho\mu/15$, and the same 70/30 bottom/top split of mass was chosen for the 2DOF oscillators. Since the devices were no longer positioned on a nodal line of asymmetric panel modes, they were capable of attenuating vibration over the full 1-300 Hz bandwidth of interest, despite being tuned to just 50 Hz or 50 and 174 Hz for the 2DOF oscillators.

Figure F.6 plots the results of varying μ and R_i in achieving reduction in panel mean-square velocity and in generating electrical power. Unlike with a single oscillator, using numerous devices is beneficial in reducing the panel vibration almost exclusively by employing greater mass ratios. From $\mu = 10\%$, which is a common practical ceiling for lightweight structures like aircraft panels, the benefit in attenuation is reduced by 6 dB or more by decreasing the mass ratio to 1%. This effect is partially alleviated by increasing R_i, but only to a point. As was shown in Figure F.4, since the oscillators are lightly-damped, $\zeta_i = 1e-2$, R_i plays the principal role of changing the mechanical damping of the devices. Changing R_i after reducing μ helps to optimize damping of the structure, but ultimately greater mass is required

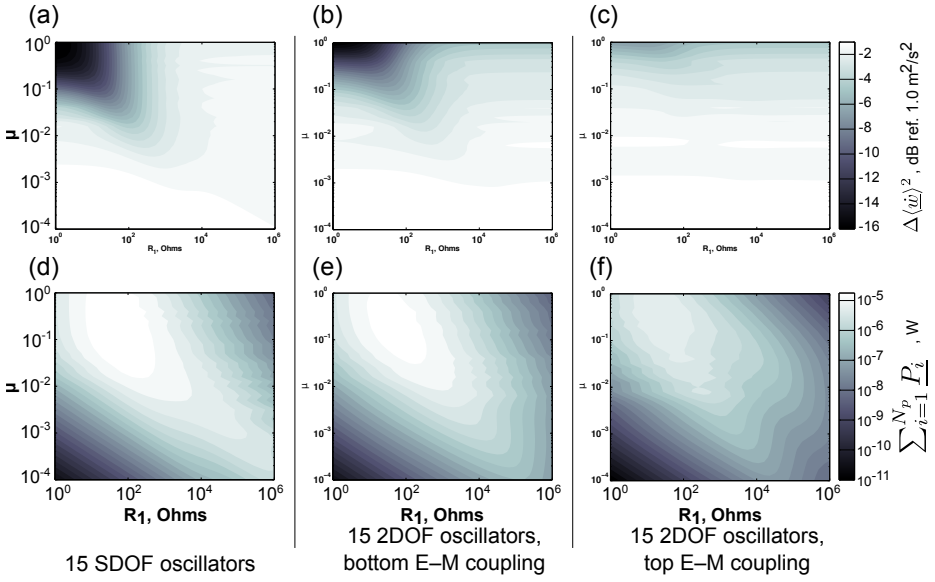

Figure F.6: Vibration suppression for case of the panel having 15 (a) SDOF oscillators, (b) 2DOF oscillators with bottom E–M coupling and (c) 2DOF oscillators having top E–M coupling. Energy harvesting for panel having 15 (d) SDOF oscillators, (e) 2DOF oscillators with bottom coupling and (f) 2DOF oscillators with top coupling.

to globally reduce the panel vibration.

Once again, the 2DOF oscillators are much less useful in suppressing panel vibration than the SDOF devices. This is clearly the case when the 2DOF oscillators have top E–M coupling. Since the external circuits serve as a means not only to generate electrical power but to passively dampen the structure, effectively by shunt damping methods, the collection of SDOF E–M oscillators serve as a useful means to optimize structural dampening. Ultimately, the rapid decrease in vibration attenuation as μ is reduced is explained by the same conflicting dynamics evidenced in Section F.3 for a single 2DOF oscillator. In the single 2DOF oscillator case, the top mass dynamics interfere with the useful vibration-attenuating effects of the bottom mass, and vice versa. For a random distribution of oscillators, this creates an amalgam of dynamic complexity, inherently reducing the overall effectiveness of the treatment in attenuating the panel vibration. As a result, for a dispersed oscillator treatment, achieving optimum vibration suppression is only achieved by loading the structure

with significant mass.

While optimum vibration reduction for the distribution of oscillators is achieved within a narrow confine of significant added mass, the energy harvesting metric is not as significantly constricted. However, Figure F.6 shows that there is no longer a considerable difference between the result of the SDOF oscillators and the 2DOF oscillators having bottom coupling over the range of μ and R_i. While this could be a sign of improved usefulness of the 2DOF devices, it is probably more a testament to the overall reduced effectiveness of the SDOF treatment when employing a multitude of dynamic devices, for the same explanation described above regarding vibration attenuation.

A mass-spring-damper device on a vibrating panel is of greatest benefit when it "absorbs" the maximum amount of structural vibration, the same objective of energy harvesting devices. The increased complexity of the array of devices inhibits the global capability of the array to absorb vibration since they affect one another through the panel. Thus, reduced effectiveness in vibration suppression intrinsically reduces the effectiveness in energy harvesting. Note that were each individual device as effective as generating electrical power as the individual device in Section F.3, the cumulative power should be roughly 15 times the earlier result. As it is, the maximum cumulative power of the SDOF oscillators, Fig. F.6 (d), is 26.1 μW, much short of the potential maximum of 15 times the single oscillator results in Section F.3: $15 \times \underline{P_1} = 15 \times (10.4) = 156$ μW.

F.5 Internal oscillator damping

All previous simulations employed oscillators having negligible internal damping ratios, $\zeta_i = 1e-2$. This is the same characteristic often adjusted in tandem with the tuning frequency for vibration absorbers to achieve optimum global structural attenuation. It was observed in Sections F.3 and F.4 that dampening of the attached oscillators, and therefore of the structural vibration, was achieved through the means

of the attached circuitry and load resistances, R_i. Thus, it would be useful to assess the comparative influence of ζ_i and R_i in improving vibration suppression and energy harvesting capabilities.

Using the optimum R_i for two values of mass ratio, $\mu = 2e - 2$ and $\mu = 2e - 1$, as computed in earlier sections, the model was reevaluated over a range of ζ_i. The earlier metrics of Eqs. F.22 (b) and F.23 were employed, although output data were normalized to the results for undamped oscillators. The case of a centrally-located SDOF oscillator was considered, as was the random distribution of the 15 oscillators, using the positions of Figure F.5. All other mechanical and geometric parameters remained the same as in prior sections.

Figure F.7 plots the results for normalized change in cumulative mean-square velocity from undamped results (top row) and the normalized change in total power (bottom row). Results for a single oscillator are shown in the left column and for the 15 SDOF oscillators in the right column. For a single SDOF oscillator, the reduction of panel vibration is optimized for a damping ratio $\zeta = 1.9$ at $\mu = 2e - 2$ and $\zeta = 2.8$ at $\mu = 2e - 1$. Consequently, from Figure F.7 (c), it is observed that the generated power output is significantly reduced, by almost two orders of magnitude for $\mu = 2e - 1$. This is intuitive since an over-damped oscillator is less capable of vibrating at all frequencies compared with the mostly undamped device.

For the application of a multitude of oscillators, no increase in internal damping for $\mu = 2e - 2$ improves vibration attenuation or energy harvesting capabilities. The heavier treatment of devices, $\mu = 2e - 1$, is more capable of suppressing vibration for large ζ, but at the expense of generating electrical power. As is generally the case in passive vibration control of distributed structures, heavy mass loading is one simple means of attenuating the vibration but this is an inappropriate approach for applications requiring lightweight control strategies, and appears also to be disadvantageous for energy harvesting purposes.

Figure F.8 (a) compares the panel mean-square velocity corresponding to opti-

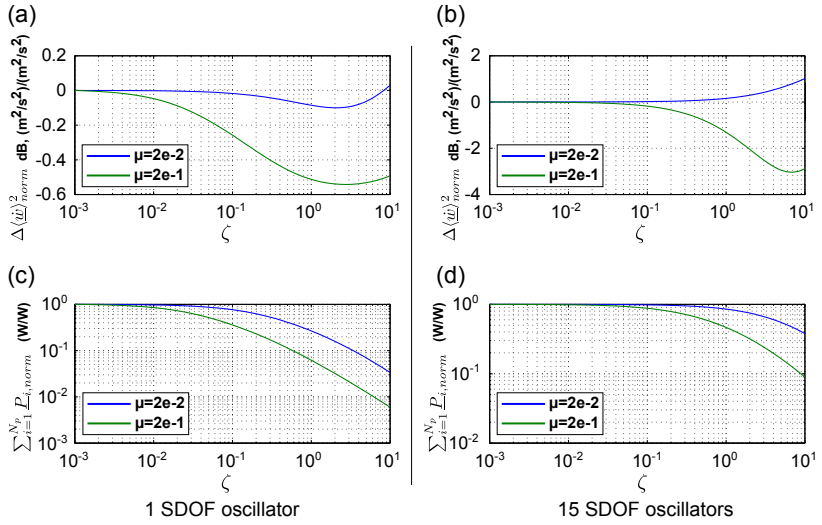

Figure F.7: Vibration suppression for case of the panel having (a) 1 SDOF oscillator, (b) 15 SDOF oscillators. Energy harvesting for panel having (d) 1 SDOF oscillator, (e) 15 SDOF oscillators. Variation of ζ with results normalized to undamped data.

mum vibration suppression and energy harvesting conditions when applying a single, centrally-located oscillator, $\mu = 2e-2$. Figure F.8 (b) provides the oscillator responses. The over-damped oscillator, $\zeta = 1.9$, is capable of attenuating both of the symmetric panel modes over the frequency bandwidth of interest, notably the (3,1) mode at 173 Hz. As a consequence, it is observed that the oscillator response, Fig. F.8 (b) blue curve, is much repressed and is clearly less suited for energy harvesting purposes. In contrast, the lightly-damped device, $\zeta < 1e-2$, is dampened only due to the shunt damping effects of the external circuit. Interestingly, while the broadband panel vibration attenuation of the over-damped oscillator is best, the lightly-damped oscillator attenuates the first panel mode 15 dB greater than the over-damped device. This is clear evidence that the fundamental dynamic concept of energy harvesting devices is to create the classical, undamped mass-spring system, which becomes damped not through mechanical means but by way of external circuits. As a lightweight treatment, this is an ideal method for achieving both objectives of vibration suppression and electrical power.

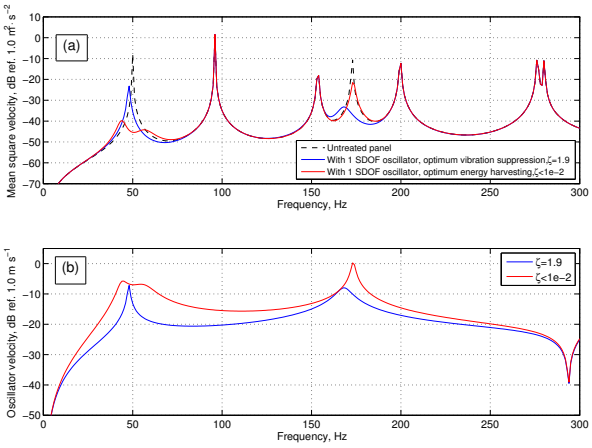

Figure F.8: (a) Mean-square velocity of the panel for $\mu = 2e-2$, untreated (black dashed), with the centrally-located SDOF device $\zeta = 1.9$ (blue curve) and the SDOF device $\zeta < 1e-2$ (red curve). (b) Oscillator velocity $\mu = 2e-2$, the SDOF device $\zeta = 1.9$ (blue curve) and the SDOF device $\zeta < 1e-2$ (red curve).

F.6 Distributed SDOF oscillators

In Section F.4 it was found that a multitude of SDOF oscillators provided significant vibration suppression primarily at the cost of applying a heavy treatment to the host panel. As a consequence to this distributed treatment of oscillators, it was found that while energy harvesting potential was maximized close to the same regime of μ as for best vibration suppression, ultimately the ability of the multitudinous treatment to generate electrical power was less effective than for the single device. This was quantified by a comparison of the maximum electrical output of the individual oscillator multiplied by the number of randomly distributed oscillators, which may serve as a theoretical maximum power achievable; this theoretical limit was much greater than that actually achieved by the randomly distributed treatment.

To further explore the trade-off of numerous oscillators in yielding best simultaneous vibration suppression and net electrical power output, the model was again employed for a variety of μ using $R = 44.6\ \Omega$, and varying the number of applied devices. Rather than applying the devices in an orderly fashion, a random distribu-

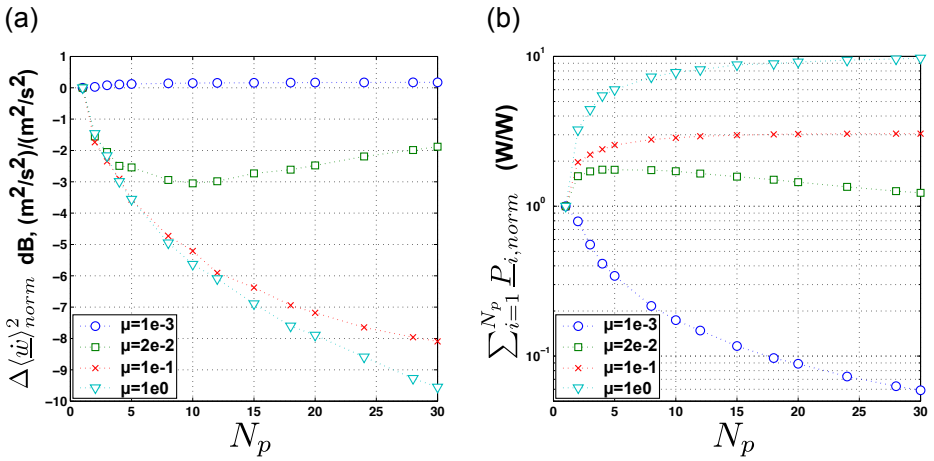

Figure F.9: (a) Cumulative mean-square panel velocity. (b) Cumulative power output. Data normalized to $N_p = 1$. $R_i = 44.6\ \Omega$.

tion was utilized, but 50 runs of the model for each value N_p were performed and averaged such that a sufficient combination of positions were explored. For example, using only one model evaluation of a random distribution of $N_p = 2$ would not yield conclusive results; so the average of 50 model evaluations was taken. In the case of $N_p = 1$, the SDOF oscillator was positioned at the panel center.

The results were normalized to data computed for $N_p = 1$ and are presented in Figure F.9. The reduction in panel vibration, Fig. F.9 (a), is a goal best met using heavy treatments, as several times indicated before. However, it is found that the advantages of increased mass are reduced as the treatment approaches the mass of the host panel. From $\mu = 1e-1$ to $\mu = 1e0$, there is an insignificant improvement in vibration suppression. Distributing this heavier mass amongst a multitude of oscillators does not appear to drastically alter this effect.

For more realistic mass ratios for lightweight structures, $\mu \leq 1e-1$, the reduction of panel vibration is not necessarily increased using numerous oscillators. In fact, for $\mu = 2e-2$ an optimum number is observed, $N_p = 10$. A -3 dB reduction in cumulative mean-square velocity is achieved for this value as compared with the single SDOF oscillator. Distributing the mass amongst an additional number of oscillators

decreases the authority of the treatment in passively suppressing the structural vibration suggesting, again, that too many dynamic elements on the host structural ultimately deter each other from their collective performance.

Figure F.9 (b) presents the second objective of generating electrical power over the frequency bandwidth of interest. Any increase in the number of oscillators for the very lightweight treatment, $\mu = 1e-3$, quickly reduces its potential to convert the panel kinetic energy to useful electrical power. The heaviest treatment, $\mu = 1e0$, though seen to increase its power output as N_p increases, ultimately converges to a maximum value, roughly an order of magnitude increase over $N_p = 1$. A similar effect is observed for $\mu = 1e-1$, which converges to a maximum power output limit of 3 times that achievable for a single oscillator.

In contrast, for the treatment of $\mu = 2e-2$ a number of oscillators is found to achieve best energy harvesting potential, roughly $4 \leq N_p \leq 8$. Nearly an increase of 2 times the power output of $N_p = 1$ is predicted. Since this falls close to the range of optimum N_p which was determined to best improve vibration suppression performance, this serves as evidence that energy harvesting and global vibration attenuation are not always mutually exclusive goals. Proper distribution of the total mass of the treatment amongst a number of oscillators, and best selection of μ, may lead to a condition which maximizes both objectives.

F.7 Conclusions

A simple model of the forced vibration of a host panel and attached single- or two-degree-of-freedom electromagnetically-coupled oscillators was employed for the purposes of evaluating the simultaneous goals of global vibration attenuation and energy harvesting. When applying dynamic devices to lightweight structures, the assumption that the energy harvester does not influence the host structure is no longer valid and the coupled vibrational response must be considered. Basic analysis of the model was made using first a single attached oscillator and then for a random distribution of

oscillators. In both cases, the 2DOF devices were of reduced benefit for both simultaneous goals than the SDOF devices. Greater total treatment mass led to the best suppression of panel vibration but this did not correspond to optimum conditions for energy harvesting.

It was observed that altering the internal damping of the oscillators reduced energy harvesting capability but could, in some instances, improve vibration suppression performance. In general, the external circuit, through a shunt damping effect, supplied sufficient damping for the oscillators; for a centrally-located SDOF device, optimum energy harvesting characteristics actually yielded better attenuation of the first panel vibrational mode than optimum global vibration suppression parameters.

Finally, it was observed that the distribution of the applied oscillator treatment into a number of discrete devices was capable of simultaneously improving both the objectives of vibration attenuation and energy harvesting for small treatment mass ratios, $\mu = 2e - 2$. A first hypothesis regarding the simultaneous objectives may predict that their aims are incompatible, that achievement of one must come at the detriment to the other. However, proper selection of the total applied mass and the distribution of the devices across the structural surface may yield improved results for both goals. For lightweight structures in which energy harvesters are attached to also help attenuate structural vibration, this result may be of significant benefit.

APPENDIX G

Modeling and validation of a distributed device for simultaneous reactive vibration suppression and energy harvesting

Distributed devices or treatments are a mainstay of passively suppressing structural vibrations. In some cases, piezoelectric materials were included within the devices to utilize them as actuators. Interest in energy harvesting encourages a reassessment of these devices, using the piezoelectric materials as a means to convert input vibrational energy into electrical power. A numerical model of one such device, exhibiting mass-spring-damper dynamics, attached to a vibrating host structure is described and validated against 3D finite element (FE) analysis. The model is utilized to evaluate the simultaneous goals of passive vibration attenuation and energy harvesting of devices on a lightweight, clamped panel. The objectives are found to be partly in opposition, particularly when the total mass of the added devices becomes more substantial. This feature is widely neglected in employing mass-spring systems as energy harvesting devices, where the mass of the device is insubstantial relative to the main structure. As a result, compromises or alternatives may be explored to achieve both goals: the implementation of materials exhibiting greater electromechanical coupling; minimization of total applied mass to the host structure; and re-tuning attached devices to exhibit natural frequencies not exactly equal to those of the host structure.

G.1 Introduction

The interest in converting ambient vibrational energy into a useful electrical power source has fostered a range of practical implementations and numerical modeling strategies. In many embodiments, the devices employ dynamics identical to tradi-

tional mass-spring-dampers (vibration absorbers) historically used for passive and active vibration control purposes.

Due to the significant in-phase strains possible, cantilevered beams designed to operate at the first modal frequency are often employed, in tandem with attached piezoelectric or piezoceramic layers. Devices described or studied by Roundy and Wright [123], Lefeuvre et al. [131], and Erturk et al. [125] have shown an appreciable potential in converting vibrational energy into usable power. Though it is of little or no interest in energy harvesting applications, in the case of cantilevered beam harvesters, the beams supply a reactive bending moment back to the host structure. With a contrasting focus, cantilever beam vibration absorbers utilize this bending moment to suppress the vibration of their host structure [132]. The gap between employing a cantilevered beam as an energy harvesting device and as a vibration control device exists between the assumption of relative inertial influence: energy harvesting devices tend to be of little or effectively no mass compared to the host structure (*e.g.* harvester on a bridge), whereas the vibration control device is more substantial (*e.g.* mass-spring-damper on an aircraft panel).

The disparity between the fields of vibration control and energy harvesting is apparent in the modeling methodology. In a fundamental analysis, vibration control studies consider two- or multi-degree-of-freedom systems [82]; in energy harvesting, a single degree-of-freedom (SDOF) system with base excitation is evaluated [39]. Thus, it is presumed, in a large proportion of energy harvesting studies, that the harvester does not affect the vibration of the greater host structure to which it will ultimately be attached.

With a growing interest in power harvesting has come the desire to convert ambient vibration from a broad array of sources. Yet, in some of these cases, it may no longer be appropriate to assume the attached devices are a negligible inertial influence to the host structure, for instance a harvester on a lightweight aircraft panel. Thus, a new analysis must be made for devices employing energy harvesting technology that

may also modify the vibrational response of the host structure, or devices generally intended for the simultaneous purposes of vibration suppression and power harvesting.

To avoid confusion, a note should be made regarding the use of the phrase "simultaneous vibration suppression and energy harvesting". Elsewhere in literature, this concept appears in regards to the damping and stiffening effects of the external load resistance across a piezoelectric electrodes as the harvester oscillates [35, 133]. The observed damping effects are primarily considered to be affecting the harvester itself—*e.g.* the bimorph cantilevered beam dynamics—as opposed to the structural dynamics of a larger system. This justifies the implicit modeling assumption that the device is excited by base vibration or a unit force (*i.e.* an infinite energy source).

In the present analysis, the base structure, *i.e.* a structural panel, is externally excited and harvesters, in the form of mass-spring systems, are thereafter attached. The piezoelectric materials are not fully attached to the host structure, but are contained within some manifestation of a distributed spring layer. Thus, the vibration suppression effect is due to the attached devices reactively or resistively working against the motion of the host structure. One similar embodiment of this design appears in the literature in the event that the cantilever beam harvesters are the wings of an aircraft [52]. The present work is distinguished from the prior in that the harvester devices exhibit reactive and resistive dynamics as opposed to only resistive. In other words, the present harvester designs of interest work against the host structure by reactive forces like vibration absorbers as well as resist the structural vibration like constraining treatments.

A passive vibration control device is considered, termed smart foam by Gentry et al. [134], which utilizes a distributed poroelastic spring layer in which a curvature of piezoelectric film is embedded. Smart foam was intended to serve as a combined passive and active acoustic-structural device and was successfully employed in active noise control experiments [77, 78]. Marcotte et al. [20] studied this device with the addition of a distributed top mass layer, the resulting embodiment then combining

passive vibration absorber dynamics alongside the potential of active control. In the context of energy harvesting and passive vibration control, the smart foam design is considered in that it may reactively suppress the vibrations of the host structure but also may generate electrical power as the embedded piezoelectric film is strained within the deformed spring layer.

This chapter briefly describes an analytical model based on the generalized Hamilton's principle of a distributed device, like smart foam, when applied to an excited, vibrating structure. The model is validated by comparison with the results from 3D FE analysis and is found to be much more computationally efficient to solve as compared with FE analysis. The model is then employed to consider the simultaneous capability of smart foam samples to reduce vibration levels of a lightweight clamped panel as well as harvest electrical energy. Though the simultaneous objectives are not mutually exclusive, potential trade-offs exist and are discussed.

G.2 Model formulation

G.2.1 Mechanical domain description

For conciseness and to focus primarily on the results of the model simulations, only essential elements of the present variational formulation are provided. Greater detail on the generalized Hamilton's principle is available in a number of texts [94, 60] as well as a recent, similar derivation of this variational method for energy harvesting using piezoelectric plates in the context of the finite element method [135]. Further summary of the analytical method is provided in Appendix A.

Consider a system composed of a base plate to which one or more piezoelectric vibration control devices are attached, Figure G.1. The attached devices are each composed of a distributed spring layer and a distributed top plate; the spring layer itself is a composite of a continuous material and a piezoelectric layer. In the following analysis, subscripts b, s, p and t refer to the base plate, the distributed spring layer, the embedded piezoelectric layer and the distributed top plate, respectively. The

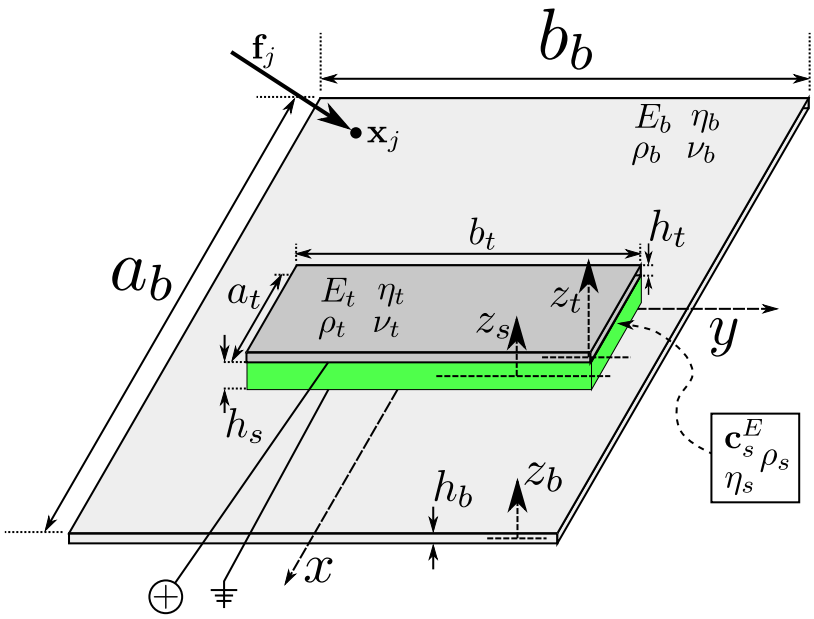

Figure G.1: Geometry and material properties of the model.

origin of the global co-ordinate system is defined at the base plate center point and the (x, y) plane corresponds to the base plate mid-plane, $z_b = 0$. The base plate is arbitrarily bounded and may be excited by a number of localized point forces, $\mathbf{f}_j(\mathbf{x}_j)$.

The base plate and distributed top plate are assumed to be Love–Kirchhoff plates having displacements expressed in the form

$$\mathbf{u}(\mathbf{x}, t)_{i=b,t} = \begin{bmatrix} u_{io}(x, y, t) - z_i \frac{\partial w_{io}(x,y,t)}{\partial x} \\ v_{io}(x, y, t) - z_i \frac{\partial w_{io}(x,y,t)}{\partial y} \\ w_{io}(x, y, t) \end{bmatrix} \tag{G.1}$$

where the second subscript o indicates the displacement in the middle-plane of the plate, $z_b = 0$ or $z_t = 0$.

For simplification of the analysis, the distributed spring layer is approximated as a superposition of a thick, transversely deformable, orthotropic plate and a thin, cylindrical shell which exhibits piezoelectric properties, Figure G.2.

The mechanical displacements of the thick orthotropic plate allow for the trans-

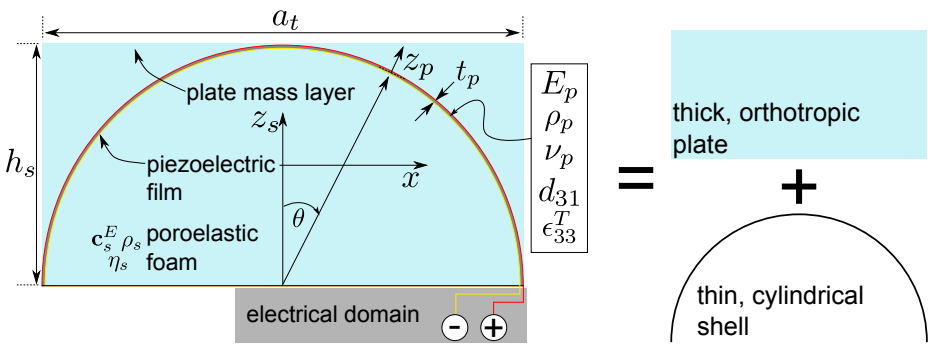

Figure G.2: Layout of distributed spring layer, the superposition of a thick plate and thin shell.

verse flexibility of the layer:

$$\mathbf{u}\left(\mathbf{x},t\right)_s = \begin{bmatrix} u_{so}\left(x,y,t\right) + z_s\theta_x\left(x,y,t\right) \\ v_{so}\left(x,y,t\right) + z_s\theta_y\left(x,y,t\right) \\ w_{so}\left(x,y,t\right) + z_s\frac{\partial w_{so}(x,y,t)}{\partial z_s} + \frac{1}{2}z_s^2\frac{\partial^2 w_{so}(x,y,t)}{\partial z_s^2} \end{bmatrix} \tag{G.2}$$

where θ_x and θ_y are the rotations about the middle-planes in the x- and y-axes, respectively. Application of continuity of displacements and transverse stress between the spring layer and the two bounding plates allows the spring layer mechanical displacements to be expressed in terms of the top plate and bottom plate displacements,

$$\mathbf{u}\left(\mathbf{x},t\right)_s = \begin{bmatrix} \frac{1}{2}\left[u_{to}+u_{bo}\right] + \frac{1}{4}\left[h_t\frac{\partial w_{to}}{\partial x} - h_b\frac{\partial w_{bo}}{\partial x}\right] + \frac{1}{h_s}z_s\left\{\left[u_{to}-u_{bo}\right] + \frac{1}{2}\left[h_t\frac{\partial w_{to}}{\partial x} + h_b\frac{\partial w_{bo}}{\partial x}\right]\right\} \\ \frac{1}{2}\left[v_{to}+v_{bo}\right] + \frac{1}{4}\left[h_t\frac{\partial w_{to}}{\partial y} - h_b\frac{\partial w_{bo}}{\partial y}\right] + \frac{1}{h_s}z_s\left\{\left[v_{to}-v_{bo}\right] + \frac{1}{2}\left[h_t\frac{\partial w_{to}}{\partial y} + h_b\frac{\partial w_{bo}}{\partial y}\right]\right\} \\ \frac{1}{2}\left[w_{to}+w_{bo}\right] + \frac{1}{h_s}z_s\left[w_{to}-w_{bo}\right] \end{bmatrix} \tag{G.3}$$

It is assumed that the inertial influence of the shell is negligible compared to the host spring layer material; in practice, the piezoelectric film may constitute 5% or less of the mass of the whole spring layer. Following this assumption, the displacements of the embedded piezoelectric film correspond to those of the thick orthotropic plate, evaluated over the surface defined by the film. This assumption would not be valid, however, in the event that the embedded piezoelectric material was more substantial

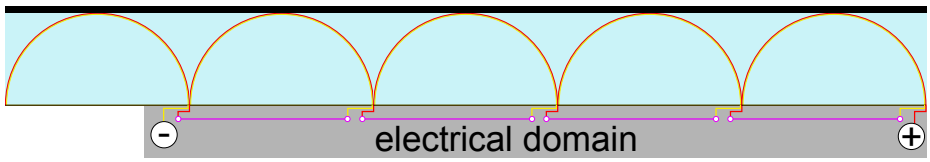

Figure G.3: Smart foam sample containing a periodic embedded piezoelectric film for improving voltage output, showing voltages added in series.

relative to the host spring layer. In the latter case, rather than assumptions of superposition, it may be more appropriate to determine equivalent elasticity characteristics of the full spring layer using homogenization or experimental techniques [136, 137].

In this manner, for n attached vibration control and energy harvesting devices, the coupled system mechanical displacements constitute $3 + 3n$ unknowns: u_{bo}, v_{bo} and w_{bo} for the base structure, and u_{to}, v_{to} and w_{to} for each device.

G.2.2 Electrical domain description

In the present analysis, the following assumptions are taken: *(i)* continuous electrodes cover the top and bottom surfaces of each piezoelectric domain; *(ii)* the piezoelectric materials are poled in the thickness direction, z_p; and *(iii)* the only non-zero electric field component varies linearly through the thickness of the material. As a result of assumption *(i)*, only one voltage is necessary to describe the electrical response of each piezoelectric domain.

In the following study, smart foam samples containing a single half-circular segment of embedded piezoelectric film are considered. A simple means by which to increase the collective output of voltage is to utilize a multitude of periods of the film and connect the individual voltage outputs in series. Figure G.3 shows an example implementation of this design. Furthermore, other embedded shapes of piezoelectric material may be employed which may be more effective in converting the transmitted strain to electrical energy.

G.2.3 Approximate solution

The mechanical displacements and voltages are estimated to be the linear combination of admissible trial functions and generalized co-ordinates:

$$\mathbf{u}\left(\mathbf{x},t\right)_{i=b,t} = \left(\Psi_m\left(\mathbf{x}\right)\mathbf{m}\left(t\right)\right)_i \tag{G.4}$$

$$\mathbf{v}\left(\mathbf{x},t\right) = \Psi_v\left(\mathbf{x}\right)\mathbf{z}\left(t\right) \tag{G.5}$$

where $\Psi_m\left(\mathbf{x}\right)$ and $\Psi_v\left(\mathbf{x}\right)$ are the admissible trial functions and $\mathbf{m}\left(t\right)$ and $\mathbf{z}\left(t\right)$ are the generalized co-ordinates for the mechanical and electrical domains, respectively. The generalized co-ordinates and trial functions number N_b and N_t for the base and top plates, respectively. Given the assumptions of continuous electrodes covering the top and bottom surfaces of the piezoelectric material, it is convenient to represent the generalized electrical co-ordinate as a single parameter, $z(t)$.

Substituting these solutions into the generalized Hamilton's principle, assuming an harmonic time dependence of the form $e^{i\omega t}$, and assuming there is no external electrical excitation on the piezoelectric electrodes, yields a coupled systems of equations describing the mechanical and electrical response for a passive vibration control and/or energy harvesting device attached to an excited host structure [135]:

$$\begin{bmatrix} Y^c + j\omega C_p & j\omega\Theta^t \\ -\Theta & \mathbf{K} + j\omega\mathbf{C} - \omega^2\mathbf{M} \end{bmatrix} \begin{bmatrix} z \\ \mathbf{m} \end{bmatrix} = \begin{bmatrix} 0 \\ \mathbf{F} \end{bmatrix} \tag{G.6}$$

where the components of Eq. G.6 are described in Appendix A. For n attached devices, the coupled system of equations contains $3N_b + 3nN_t$ mechanical generalized co-ordinates and n electrical generalized co-ordinates. The attached circuit admittance, Y^c, for energy harvesting devices is a simple load resistance, $Y^c = 1/R_1$.

The generalized co-ordinates and electrical responses are computed from Eq. G.6 as

$$\mathbf{m} = \left[\mathbf{K} + j\omega\mathbf{C} - \omega^2\mathbf{M} + j\omega\left(Y^c + j\omega C_p\right)^{-1}\Theta\Theta^t\right]^{-1}\mathbf{F} \tag{G.7}$$

$$z = -\left[Y^c + j\omega C_p\right]^{-1}\left(j\omega\Theta^t\right)\left[\mathbf{K} + j\omega\mathbf{C} - \omega^2\mathbf{M} + j\omega\left(Y^c + j\omega C_p\right)^{-1}\Theta\Theta^t\right]^{-1}\mathbf{F} \tag{G.8}$$

For a given distributed piezoelectric vibration control and energy harvesting device, the frequency response function (FRF) of the top plate transverse acceleration to the base plate transverse acceleration is computed as

$$\left|\mathrm{FRF}_{accel}\left(\omega\right)\right| = \left|\frac{w_{to}(x_1, y_1, \omega)}{w_{bo}(x_2, y_2, \omega)}\right| = \left|\frac{\Psi_{m_{w_{to}}}(x_1, y_1)\mathbf{m}_{w_{to}}(\omega)}{\Psi_{m_{w_{bo}}}(x_2, y_2)\mathbf{m}_{w_{bo}}(\omega)}\right| \tag{G.9}$$

where $\Psi_{m_{w_{to}}}$ and $\mathbf{m}_{w_{to}}$ are the trial functions and generalized co-ordinates related to the top plate transverse displacement, respectively; $\Psi_{m_{w_{bo}}}$ and $\mathbf{m}_{w_{bo}}$ are the trial functions and generalized co-ordinates related to the base plate transverse displacement, respectively; and (x_1, y_1) and (x_2, y_2) are the points of evaluation. The voltage FRF ($\mathrm{V{\cdot}g^{-1}}$) of a device is computed as

$$\left|\mathrm{FRF}_{volt}\left(\omega\right)\right| = \left|\frac{z(\omega)}{-\omega^2\Psi_{m_{w_{bo}}}(x_2, y_2)\mathbf{m}_{w_{bo}}(\omega)}\right| \tag{G.10}$$

Considering the FRF responses in light of Eq. G.7, the mechanical response of the system is damped and shifted in frequency by the specific of circuit admittance and piezoelectric characteristics. The significance of this effect is modulated by the magnitude of the electromechanical coupling terms, Θ. The same frequency shift is observed in the electrical response but the magnitude of the voltage FRF is predicted to continually increase with increasing R_1 to short circuit conditions.

In considering the vibration attenuation capability of a device on a larger host structure, the mean-square out-of-plane velocity ($\mathrm{m^2{\cdot}s^{-2}}$) of the base plate is determined by

$$\left\langle \dot{w}_{bo}\left(\omega\right)\right\rangle^2 = \frac{\omega^2}{2a_b b_b}\int_{-a_b/2}^{+a_b/2}\int_{-b_b/2}^{+b_b/2}\left(\Psi_{m_{w_{bo}}}(x, y)\mathbf{m}_{w_{bo}}(\omega)\right)^*\left(\Psi_{m_{w_{bo}}}(x, y)\mathbf{m}_{w_{bo}}(\omega)\right)\mathrm{d}x\mathrm{d}y \tag{G.11}$$

where $()^*$ denotes the complex conjugate. Recalling that the spring layer mechanical displacements were expressed in terms of the bounding plate displacements, the

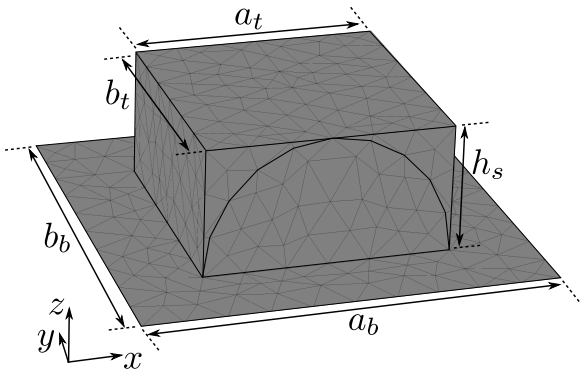

Figure G.4: FE model mesh of vibration control and energy harvesting device.

transverse generalized co-ordinates of the base plate, $\mathbf{m}_{w_{bo}}$, contain terms related to the spring layer as well as coupling terms related to the top mass displacements. Furthermore, the electromechanical coupling, Θ, is expressed in terms of mechanical displacements of the bounding plates as well as the electrical response itself. As a result, the presence of the piezoelectric spring layer slightly dampens and shifts in frequency the response of the base and top plates to varying degrees as the external load resistance is modified.

G.3 Model validation: numerical comparison

The present model is compared against the results computed from a 3D FE model using the COMSOL software package [138]. As was recommended by Leroy et al. [139], due to the thinness of the embedded piezoelectric film relative to the foam layer, the film is modeled as a two-dimensional surface (shell elements). Acoustic coupling within the poroelastic foam is ignored since vibration suppression and energy harvesting capabilities are the metrics of present interest. The poroelastic material is modeled using tetrahedral solid elements while the base plate is constructed using shell elements. A diagram of the 3D FE mesh is shown in Figure G.4 which used approximately 8,000 total elements.

A smart foam sample employing the half-circular embedded piezoelectric film

Table G.1: Geometric and mechanical properties of the layers

Layer	a (m)	b (m)	h (m)	E (Pa)	ν	ρ (kg/m^3)	η
Base	0.10	0.10	0.005	2.1e14	0.33	7850	3e-4
Top	0.06	0.06	0.002	7.1e10	0.33	2100	3e-4
Spring layer	0.06	0.06	0.03	1.9e5	0.4	9	4e-2

Table G.2: Mechanical and electrical characteristics of the embedded piezoelectric film

t_s (m)	E_p (Pa)	ν_p	ρ_p (kg/m^3)	η	d_{31} (m/V)	ϵ_{33}^T (F/m)
28e-6	5.4e9	0.18	1780	1e-3	23e-12	$12\epsilon_0$

shape is centrally located on a base plate having free boundaries. The base plate is excited by a centrally-located, out-of-plane, unit harmonic force, $f_z(0,0,0,\omega) = 1$ N. Geometric and material properties of the layers are provided in Table G.1; properties of the embedded piezoelectric film are provided in Table G.2 [140]. The base plate is modeled as being exceptionally stiff in order to excite the attached device equally at all frequencies and to avoid modal effects of the base structure within the frequency range of interest. The foam layer is assumed to have identical elastic properties regardless of orientation; *i.e.* $E_x = E_y = E_z = E$ and $G_{yz} = G_{xz} = G_{xy} = E/2(1+\nu)$. Damping for all layers is included by means of an isotropic loss factor, η.

Figure G.5 compares the present model predictions of out-of-plane acceleration FRF and those computed by the FE model for three values of load resistance, R_1. In each plot, a resonance effect is evident at 224 Hz, with the FE and present models in perfect agreement of the frequency. This represents the single degree-of-freedom (SDOF) resonance of the device.

As the load resistance on the electrodes is increased, the SDOF resonance frequency is seen to moderately shift from 224 Hz at $R_1 = 1.8$ kΩ to 225 Hz at $R = 560$ kΩ. In addition to the minor shift in frequency, both the FE model and the present numerical model concur that the amplitude of the resonance increases as load resistances increases; the magnitude increases from 25.4 at $R_1 = 1.8$ kΩ to 33.9 at $R_1 = 560$ kΩ. This is a one-third increase in the magnitude of the resonance (+2.5 dB). This suggests that as a distributed vibration control treatment, different

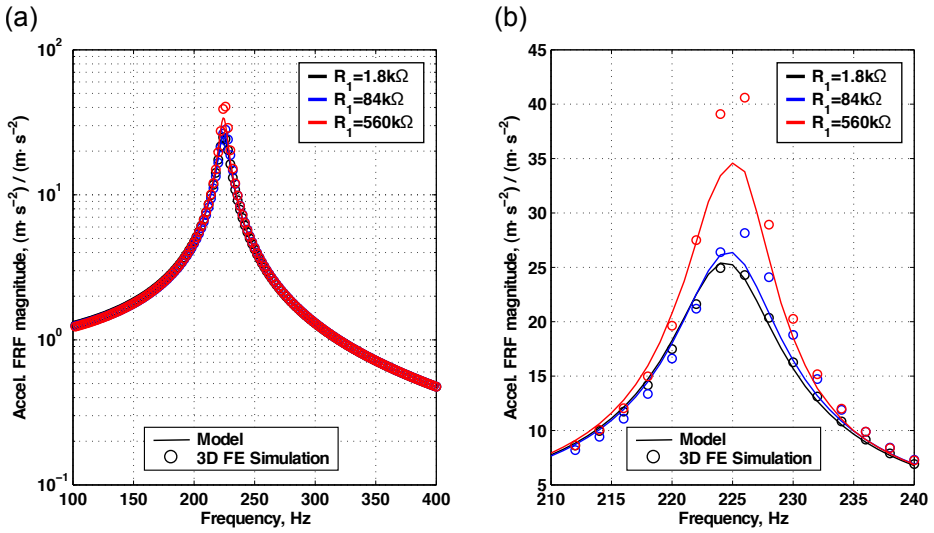

Figure G.5: (a) Comparison of acceleration FRF magnitudes for $R_1 = 1.8$ kΩ, 84 kΩ and 560 kΩ, full spectrum. (b) Around resonance.

load resistances (in this case, larger resistances) would improve the ability of the device to reactively work against the host structural vibration.

Voltage FRF predictions are compared in Figure G.6 for four values of R_1. The same resonance effect witnessed in the acceleration FRF is observed for the voltage output, also at 224 Hz, but increasing to 225 Hz for $R_1 = 560$ kΩ. For greater load resistances, the increased time constant, $R_1 C_p$, serves to reduce the voltage output at higher frequencies while the lower frequency components continue to increase. Both models corroborate this feature. Overall, both the 3D FE model and the present numerical model are in close agreement, with a maximum of 15% error (in the acceleration FRF at resonance for $R_1 = 560$ kΩ), but an average error of <1%. To provide a measure of the computational benefit of employing the present continuum domain model, the 2D continuum domain model completed each FRF prediction over 225 times faster than the 3D FE model.

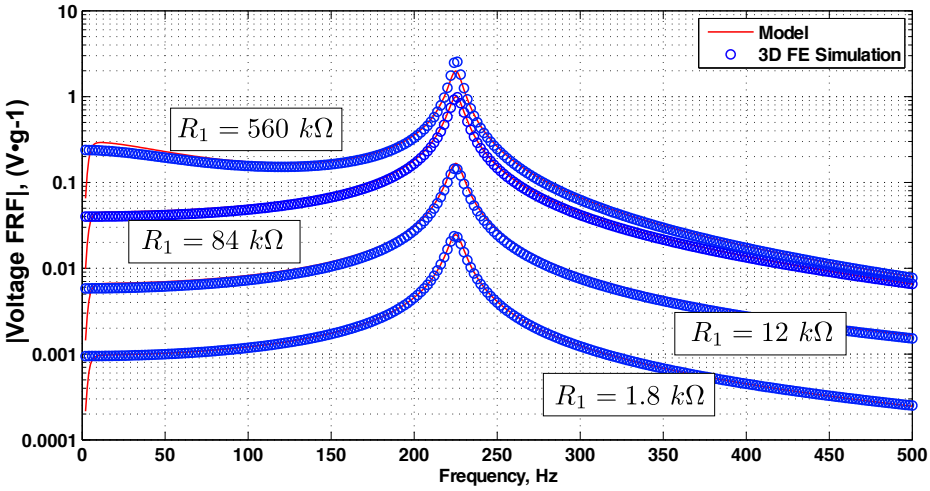

Figure G.6: Comparison of voltage FRF magnitudes, solid curves from the present model results and circles from the FE model.

Table G.3: Geometric and mechanical properties of the plate and original-sized devices

Layer	a (m)	b (m)	h (m)	E (Pa)	ν	ρ (kg/m^3)	η
Base	0.60	0.40	0.003	7.1e10	0.33	2100	3e-4
Device 1 & 2 Top	0.06	0.06	0.002	7.1e10	0.33	2100	3e-4
Device 1 Spring	0.06	0.06	0.075	1.9e5	0.4	9	4e-2
Device 2 Spring	0.06	0.06	0.03	1.9e5	0.4	9	4e-2

G.4 Application: devices on a vibrating panel

Recalling the focus of this work, the goal of the present variational model is to serve as a computationally efficient means by which to assess and optimize the simultaneous capabilities of passive vibration suppression and power harvesting for distributed piezoelectric devices. To explore some of the utility of the model, consider a clamped plate to which two smart foam devices are attached. The geometry of the model and device layout is shown in Figure G.7 with tabulated geometric and mechanical properties in Table G.3. As before, the distributed spring layer is considered to have similar isotropic thick plate elasticity parameters. The properties of the embedded piezoelectric film are the same as those provided in Table G.2. The plate is excited by an out-of-plane unit point force, $f_z\,(0.18, -0.16, 0, \omega) = 1$ N.

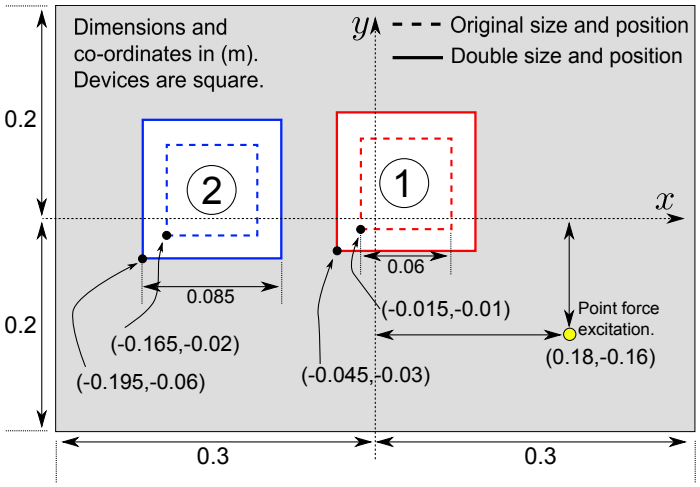

Figure G.7: Diagram of modeled geometry and device placement.

Both of the attached devices were square and both were attached to load resistances of $R_1 = 10$ kΩ. Device 1 was designed so as to exhibit a SDOF natural frequency of 141 Hz, very close to the first natural frequency of the clamped panel (144 Hz). Device 2 was designed to have a SDOF natural frequency of 224 Hz, almost identical to the second natural frequency of the panel (223 Hz). The devices were positioned on the panel so as to be most useful in reactively suppressing the vibrations of the clamped panel to which they were tuned.

The base plate out-of-plane mean-square velocity is computed for three cases: the untreated panel, after attaching the original-sized devices and for when the areas of the devices were doubled, as in Figure G.7. Note that doubling the area of the devices does not alter the SDOF natural frequencies, but should, presumably, increase the collective power output of the devices and/or improve vibration suppression performance. The mass ratio (defined as the total device mass divided by the untreated panel mass) was 2.5% while doubling the surface coverage of the devices doubled the mass ratio to 5.0%.

Figure G.8 plots the mean square velocity of the clamped base plate for the untreated and two additional scenarios with the attached devices. Characteristic of

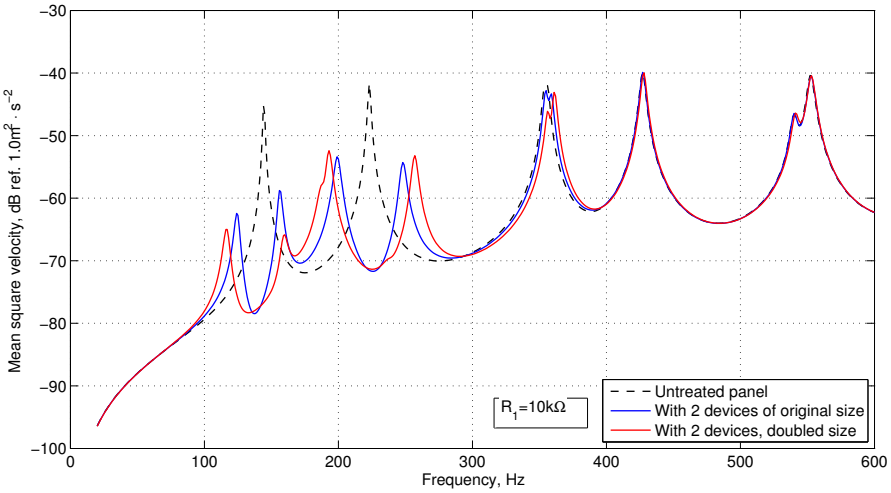

Figure G.8: Mean square velocity of untreated panel (black dash), with original-sized devices (blue curve) and with double-sized devices (red curve).

vibration absorbers, the devices significantly reduce the panel vibration at their respectively tuned SDOF natural frequencies, transferring some of the energy to frequencies above and below the untreated panel resonances. Doubling the area of the devices serves to further reduce the magnitude of the split clamped panel resonances around 120 and 157 Hz, but does not appreciably reduce the magnitude of the split resonances of the second mode. However, the added mass does further spread the second mode split resonances away from the untreated resonance, exactly as per the results of classical, analytical treatment of point vibration absorbers [82]. Above the devices' SDOF natural frequencies, they do little to suppress the panel vibration, the latter of which almost completely converges to the magnitude of untreated vibration levels by the fourth untreated panel resonance, 427 Hz.

The amplitude of the average power for the devices, $|v(\omega)|^2/2R_1$, is plotted in Figure G.9. Only one load resistance is considered here, $R_1 = 10$ kΩ, and this may not represent the optimal choice of resistance. However, the important elements to consider are potential trade-offs between vibration suppression capability and energy harvesting potential.

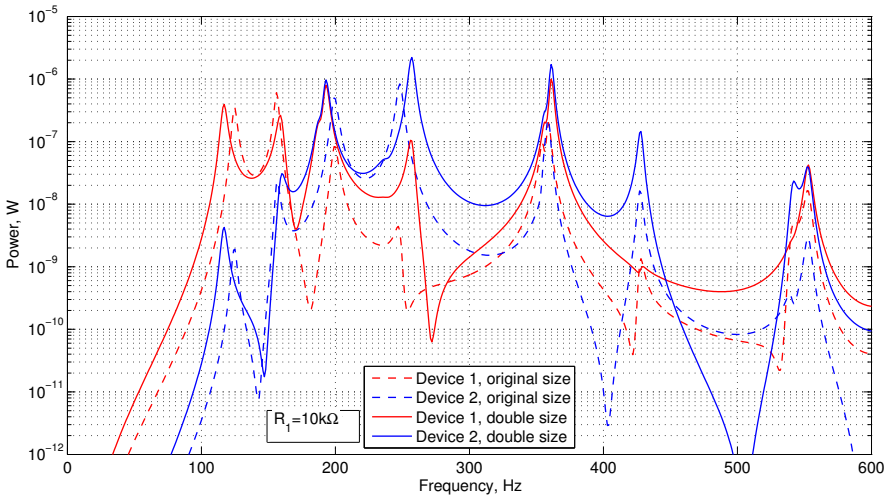

Figure G.9: Power of original-sized Device 1 (red dash) and Device 2 (blue dash) and of double-sized Device 1 (red curve) and Device 2 (blue curve).

From Figure G.9, below 300 Hz, it is observed that both devices output greater power around their respective tuned SDOF frequencies, albeit now conforming to the location of the split resonances. From Device 1, greatest power is achieved around the untreated panel resonance at 144 Hz; and from Device 2, greatest power is output around the untreated resonance at 223 Hz. However, since the nature of lightly-damped SDOF vibration absorbers is to split the energy around the original, targeted vibrational frequency, the result is that now the absorbers are no longer of oscillating at their individual natural frequencies which would yield significantly greater electrical output.

This issue is perhaps not commonly regarded in most energy harvesting applications (*e.g.* transducers to be applied to roadways or bridges) when the mass ratio of the device is negligible compared to the mass of the vibrating structure. In such conditions, the natural frequency of the main structure is not perceptibly shifted and the power harvesting device oscillates at the designed frequency. In the case of devices designed for simultaneous vibration suppression and energy harvesting, maintaining the lowest mass ratio possible is vital. Otherwise, the resonant frequencies of the

host structure are pushed further away from the optimal operating frequency of the energy harvesting device.

For instance, the doubling of surface coverage of the devices (solid curves in Fig. G.9) does not noticeably improve the electrical power output, despite a greater volume of piezoelectric material present for charge collection. In fact, Device 1 produces less electrical power at 157 Hz once the area is doubled. Note also from Figure G.8 that the vibration of the panel at this frequency is better attenuated with the doubling of size of the devices. Thus, better performance at suppressing the host panel vibration inherently reduces the effectiveness of the device in terms of producing electrical power. This trade-off may be most notably observed by the fact that both devices output an equal or greater amount of power at the third panel resonance, 357 Hz, at which neither of the devices were best designed to operate.

G.5 Conclusions

Interest in the capture and conversion of ambient kinetic energy into an electrical power source has resulted in a wide range of innovative electromechanical and electromagnetic devices. Modeling methods have been equally diverse with the general aim of assisting in the optimization of device design or energy conversion. A variational numerical model was here described for the purpose of evaluating the simultaneous reactive vibration suppression and energy harvesting capabilities of a class of devices attached to vibrating host structures. Such devices would employ a distributed top mass layer and a distributed spring layer, the latter of which exhibits piezoelectric properties.

The model was compared against a 3D FE model showing close agreement in both mechanical and electrical response of the devices. The model was then employed to evaluate the simultaneous vibration control and power harvesting potential of similar devices on a clamped panel. Similar to point vibration absorbers, the reactive forcing nature of the device significantly suppressed the panel vibration at the tuned natural

frequencies, splitting the original untreated panel resonances. This result implies that the attached devices no longer oscillate with greatest amplitude at the frequencies to which they would be most useful for energy harvesting purposes.

Increasing the area coverage of the devices improved the ability to suppress the panel vibration but showed no appreciable improvement in power harvesting, despite the greater volume of piezoelectric material present. While many energy harvesting devices use an identical, dynamic concept to that of tuned mass-spring-damper systems, the underlying assumption is that the devices are not effective at reducing the vibration of the host structure. Thus, it is assumed that the added mass to the structure is negligible. In the present model, it was observed that for a treatment of devices totaling a 5% mass ratio to the panel mass, a clear trade-off existed between vibration suppression potential and the ability to efficiently convert the remaining kinetic energy into electrical power. The panel resonant frequencies were observed to shift away from the untreated frequencies, as per classical analysis, thereby reducing the effectiveness of the devices since they were tuned to the original, untreated panel resonances.

A few conclusions may be drawn in light of the results:

- The lowest possible mass ratio of the devices to the host structure is important; this reduces the shift in the host panel resonances when tuned reactive devices are attached.

- The devices may improve wider-band vibration suppression by means of improved mechanical coupling to the structure. Extensionally stiffer spring layers may help to improve global vibration reduction performance by means of constraining layer-type effects, while still providing for energy harvesting capabilities from transverse vibration response.

- The use of more electromechanically coupled piezo materials within the distributed spring layer should yield improved power output. Alternatively, using

a greater volume of lightweight piezoelectric film, as in a multitude of periodic film shapes (Fig. G.3), may achieve similar results.

- For improved energy harvesting, by further study it may be determined that the devices should be designed so as to exhibit SDOF natural frequencies not exactly equal to the host structural resonances since this reduces the disparity between the split host panel resonances and the original device natural frequency.

While passive, reactive vibration suppression and energy harvesting techniques may be important goals to achieve simultaneously, the optimal design of devices or systems for this purpose will involve the careful assessment and weighing of the inherent trade-offs.

APPENDIX H

Development, modeling and testing of continuously distributed devices for concurrent vibration suppression and energy harvesting

Fundamental studies in vibrational energy harvesting consider the electromechanically coupled devices to be excited by uniform base vibration. Yet as harvester devices are applied to lighter weight vibrating systems, coupled structural dynamics must be taken into account. Since the attached devices are mass-spring systems, this new field of application poses the opportunity to simultaneously suppress the vibration of the host structure via reactive forces while converting the "absorbed" vibration into electrical power. This paper presents a general analytical model for the coupled electro-elastic dynamics of a vibrating panel to which distributed energy harvesting devices are attached. One such device is described which employs a distributed, piezoelectric spring layer for conversion of the oscillating potential energy into electrical power via an external circuit. The model is validated by comparison of elastic and electric FRF results. Tests on a randomly excited panel show that the device is capable of significant vibration suppression, like a conventional mass-spring-damper, and concurrently generates an electrical power TF of 3.3 $\mathrm{mW{\cdot}N^{-2}}$. Adjustment of the load resistance in the harvester circuit shows that it directly manipulates the stiffness and dampening of the piezoelectric spring layer, thereby tailoring its dynamic influence on the vibrating panel. The results finally show that optimal vibration suppression and energy harvesting objectives occur for nearly the same load resistance in the harvester circuit.

H.1 Introduction

Vibrational energy harvesting aims to convert ambient vibration into useful electric power by means of novel electromechanical transducers. Mass-spring systems are frequently employed whereby piezoelectric materials may serve as the spring. Such reactive devices are a mainstay in passive vibration control applications since the oscillators work against a host structure or system at a tuned natural frequency.

A typical numerical model in energy harvesting analysis considers the harvester to be excited by base vibration, neglecting the device's influence on the host structure [36, 38, 39]. However, structural dynamic coupling is the foundational assumption in vibration control modeling. The discrepancy exists since early energy harvesting studies considered sources of vibration of massive inertial influence relative to the harvester, for instance bridge vibrations [25] or wireless sensor vibrations having MEMS harvesters [141], which most of the first prototypes would have no dynamic influence upon.

As material advancements are made and practical applications of energy harvesting are demonstrated, there has arisen an interest to convert most any source of vibrational energy into electrical power. However, some applications involve vibrating systems which are more likely to be dynamically influenced by applied harvester devices. Therefore, when the attached devices become more inertially substantial relative to the host structure, a new analysis of the coupled electro-elastic dynamics must be considered.

This poses a new opportunity. Since the harvester devices exhibit reactive (resonant) dynamics like mass-spring systems, might they be employed as "vibration absorbers" in a passive vibration control sense while also generating electrical power? So long as the device is relatively undamped, and therefore conversion of potential to kinetic energy in the oscillator remains mostly conservative, this appears to be a practical possibility.

Many of the present successful piezoelectric energy harvesting devices to date have

been developed using cantilevered beam designs [142, 37, 85]. The advantage of these embodiments are the large strains induced along the beam as it oscillates in the first mode, which therefore yield large electrical signals. However, in vibration control applications, cantilever beam vibration absorbers are not frequently employed since they induce bending moments upon the structures to which they are attached [132]. Most vibration control applications require devices to exert reactive *forces* as opposed to *moments* in order to work against either the 1D motion of a simple structure or the flexural motion of a vibrating surface.

This paper describes a study of one such device developed for this purpose. The device exhibits a single degree-of-freedom (SDOF) resonance but is also suitable to attenuate the vibration of surfaces since it employs continuously distributed mass and spring layers. In addition, the spring layer is constructed of a corrugated piezoelectric material such that, as it deforms at the device resonance, it generates a significant electric potential which is then connected to an external energy harvesting circuit. The design of the passive device is similar to the manifestation achieved for actuating purposes by Fuller and Cambou [19] using a circularly corrugated piezoelectric spring layer earlier patented by Tibbetts [80].

A model based on the generalized Hamilton's principle is briefly presented which describes the coupled electro-elastic dynamics of a vibrating rectangular panel to which a number of such distributed piezoelectric vibration control devices are attached. The model is validated by comparison against experimental measurements of a piezoelectric device's elastic and electrical dynamics on a shaker table. An experimental setup is then described in which a large, lightly-damped and simply supported panel is excited by random vibration. A second piezoelectric device is applied to this panel to consider its capability to simultaneously suppress the panel vibration and generate electrical power when the piezoelectric electrodes are attached to an external circuit.

The model is found to accurately predict the vibration suppression capability of

the device as well as the electrical response around the device SDOF resonance. Like other energy harvesting devices studied, changes of the load resistance in the harvester circuit affect the stiffening and damping of the distributed piezoelectric spring layer which therefore affect its influence in reactively suppressing the panel vibration. For the lightweight piezoelectric device applied, it is found that the dual objectives are not contradictory and appear to be best met when employing nearly the same load resistance in the harvester circuit.

H.2 Model description

H.2.1 Mechanical domain description

Consider a system composed of a base plate to which one or more distributed piezoelectric vibration control devices are attached, Figure H.1. The attached devices are each composed of a distributed spring layer and a distributed top plate. The spring layer itself is a continuous layer exhibiting piezoelectric characteristics. In the following analysis, subscripts b, s and t refer to the base plate, the continuous spring layer and the distributed top plate, respectively.

The origin of the global co-ordinate system is defined at the base plate center point and the (x, y) plane corresponds to the base plate mid-plane, $z_b = 0$. The base plate is arbitrarily bounded and may be excited by a number, N_f, of localized point forces, $\mathbf{f}_j(\mathbf{x}_j)$ where $j = 1, 2, \ldots, N_f$ and $\mathbf{x}_j = (x_j, y_j, 0)$.

The base plate and distributed top plate are assumed to be Love–Kirchhoff (L–K) plates having displacements expressed in the form

$$\mathbf{u}(\mathbf{x}, t)_{i=b,t} = \begin{bmatrix} u_{io}(x, y, t) - z_i \frac{\partial w_{io}(x,y,t)}{\partial x} \\ v_{io}(x, y, t) - z_i \frac{\partial w_{io}(x,y,t)}{\partial y} \\ w_{io}(x, y, t) \end{bmatrix} \tag{H.1}$$

where the second subscript o indicates the displacement in the middle-plane of the plate, $z_b = 0$ or $z_t = 0$.

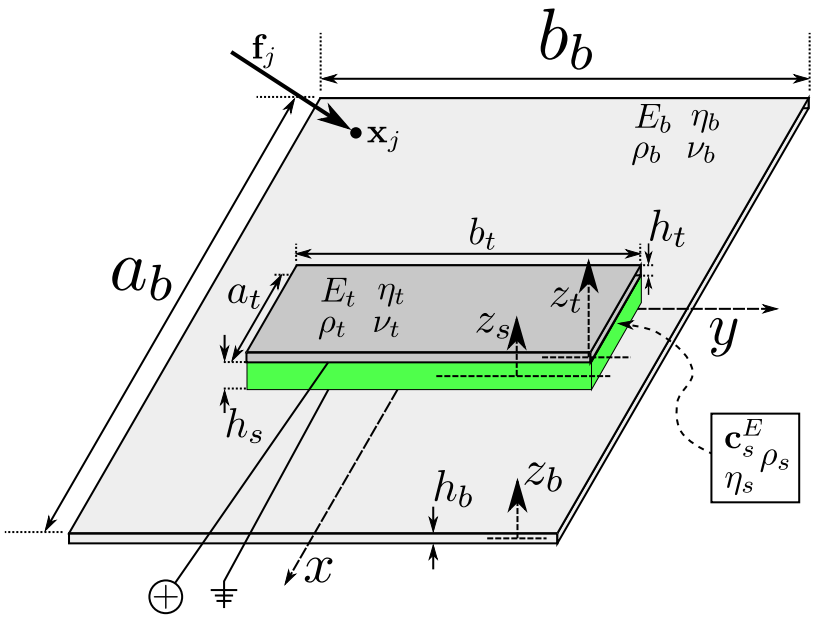

Figure H.1: Geometry and material properties of base plate structure with attached piezoelectric vibration control devices.

The distributed spring layer is considered to be a thick, transversely deformable, orthotropic plate. Elastic properties of the layer, as described by the stiffness matrix $\mathbf{c}_s^E$ evaluated at constant electric field, are assumed to either be known or are able to be computed approximately. The mechanical displacements of the thick orthotropic plate allow for the transverse compressibility of the layer:

$$\mathbf{u}\left(\mathbf{x},t\right)_s = \begin{bmatrix} u_{so}\left(x,y,t\right) + z_s\theta_x\left(x,y,t\right) \\ v_{so}\left(x,y,t\right) + z_s\theta_y\left(x,y,t\right) \\ w_{so}\left(x,y,t\right) + z_s\frac{\partial w_{so}(x,y,t)}{\partial z_s} + \frac{1}{2}z_s^2\frac{\partial^2 w_{so}(x,y,t)}{\partial z_s^2} \end{bmatrix} \tag{H.2}$$

where θ_x and θ_y are the rotations about the middle-planes in the x- and y-axes, respectively. Application of continuity of displacements and transverse stress between the spring layer and the two bounding plates allows the spring layer mechanical displacements to be expressed in terms of the top plate and bottom plate displacements,

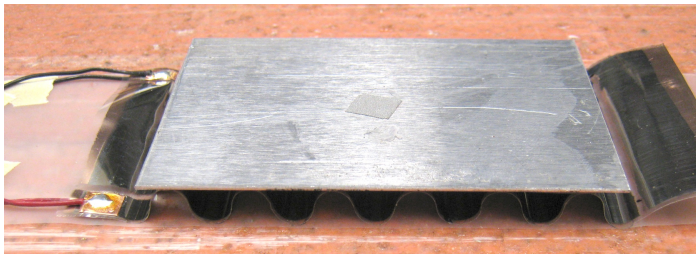

Figure H.2: Photograph of piezoelectric vibration control device using a circularly corrugated piezoelectric film as the distributed spring layer. Electrical leads are also shown to be attached to the etched surface electrodes of the film.

$$\mathbf{u}\left(\mathbf{x},t\right)_s = \begin{bmatrix} \left(\frac{1}{2}\left[u_{to}+u_{bo}\right]+\frac{1}{4}\left[h_t\frac{\partial w_{to}}{\partial x}-h_b\frac{\partial w_{bo}}{\partial x}\right]\cdots \\ +\frac{1}{h_s}z_s\left\{\left[u_{to}-u_{bo}\right]+\frac{1}{2}\left[h_t\frac{\partial w_{to}}{\partial x}+h_b\frac{\partial w_{bo}}{\partial x}\right]\right\}\right) \\ \left(\frac{1}{2}\left[v_{to}+v_{bo}\right]+\frac{1}{4}\left[h_t\frac{\partial w_{to}}{\partial y}-h_b\frac{\partial w_{bo}}{\partial y}\right]\cdots \\ +\frac{1}{h_s}z_s\left\{\left[v_{to}-v_{bo}\right]+\frac{1}{2}\left[h_t\frac{\partial w_{to}}{\partial y}+h_b\frac{\partial w_{bo}}{\partial y}\right]\right\}\right) \\ \left(\frac{1}{2}\left[w_{to}+w_{bo}\right]+\frac{1}{h_s}z_s\left[w_{to}-w_{bo}\right]\right) \end{bmatrix} \tag{H.3}$$

H.2.2 Electrical domain description

Depending on the specific embodiment of piezoelectric spring layer under study, one must appropriately select how to include electromechanical coupling effects in the analysis. The present inclusion of piezoelectric material in the spring layer is in the form of a circularly corrugated layer. A photograph of the full device is shown in Figure H.2 and a diagram of the cross-sectional geometry is given in Figure H.3 (a). As the full vibration control device oscillates transversely at its SDOF natural frequency, bending strain is induced in the corrugated piezoelectric material. However, on a given surface electrode, these strains are out-of-phase from one half period of the corrugation to the next, Figure H.3 (b). Thus, studies by Gentry-Grace [143] showed that etching of the electrode every half period allowed for maximum control authority when the corrugated layer was used as an actuator. In fact, this design was patented earlier by Tibbetts [80].

Therefore, the circularly corrugated piezoelectric spring layer electrodes are etched,

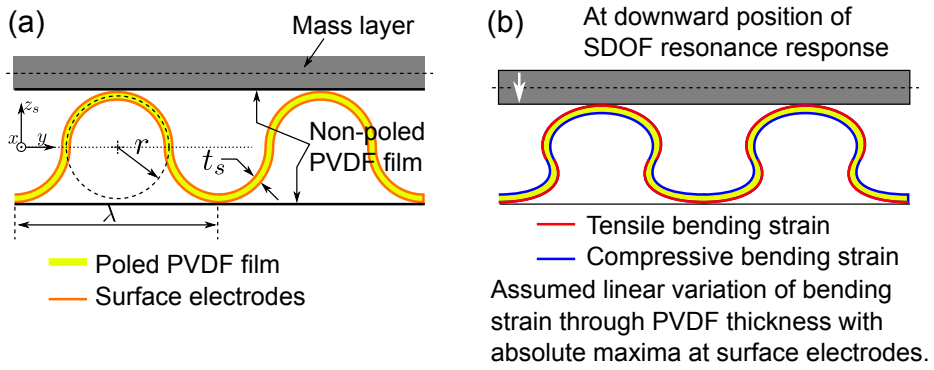

Figure H.3: (a) Undeformed cross-sectional geometry of circularly corrugated piezoelectric spring layer with exaggerated electrode thickness and arbitrary top mass layer. (b) Illustrated cross-sectional response when top mass layer is displaced downward during SDOF resonant vibration. Bending strain is assumed to vary linearly through the thickness of the PVDF film.

as shown in Figure H.4 (a), and then woven into the form shown in Figure H.4 (b). Note that the portions of the electrodes which are etched correspond to the undeformed centerlines of the full spring layer, $z_s = 0$. The two resulting electrical biases are then combined out-of-phase to yield the maximum voltage output. Analytical representation of electromechanical coupling effects is provided in the following section.

H.3 Generalized Hamilton's principle

For the sake of conciseness, rigorous derivation of Hamilton's principle for deformable electro-elastic bodies is not here presented due to the availability of useful texts [94, 60] and a similar summary [135] elsewhere. Only unique forms of the resulting equations are hereafter explained with specific mathematical operators provided in H.8.

For the case of a single applied piezoelectric vibration control device, there exist 6 unknown mechanical displacements:

$$\mathbf{u}\left(\mathbf{x},t\right)_b = \left[\begin{array}{ccc} u_{bo} & v_{bo} & w_{bo} \end{array}\right]^T \qquad \mathbf{u}\left(\mathbf{x},t\right)_t = \left[\begin{array}{ccc} u_{to} & v_{to} & w_{to} \end{array}\right]^T \tag{H.4}$$

From Eq. H.3, the mechanical displacements of the continuous spring layer are also expressed using these unknowns. Due to the assumptions regarding the electrical

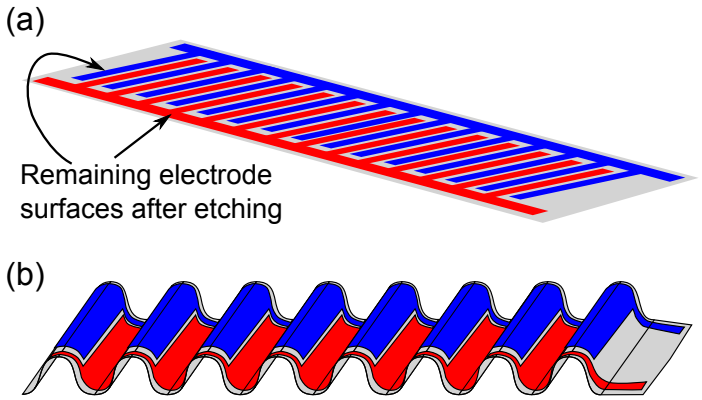

Figure H.4: (a) Etching of piezoelectric material prior to corrugation and (b) the desired circularly corrugated form.

characteristics of the piezoelectric material, only one unknown is required to describe this response, v_p.

The mechanical displacements are then approximated to be the linear combination of admissible trial functions and generalized co-ordinates:

$$\mathbf{u}\left(\mathbf{x},t\right)_{i=b,t} = \left(\Psi\left(\mathbf{x}\right)\mathbf{m}\left(t\right)\right)_i \tag{H.5}$$

where $\Psi\left(\mathbf{x}\right)$ are the admissible trial functions and $\mathbf{m}\left(t\right)$ are the generalized co-ordinates. The co-ordinate dependence may be truncated as per convention $\left(\mathbf{x}\right) = \left(x,y,0\right) \rightarrow \left(x,y\right)$ since these displacements are defined using L–K assumptions.

Substituting the approximate Ritz solutions into the generalized Hamilton's principle and assuming: that only the base plate is excited by point forces; an harmonic time dependence of the form $\exp(j\omega t)$; and that the electrodes of the piezoelectric material are attached only to an external resistive load, R_1, yields a coupled system

of electromechanical equations of the form:

$$\left\{ \begin{bmatrix} \frac{1}{R_1} & \mathbf{0} & \mathbf{0} \\ -\Theta_{s,t} & \mathbf{K}_t + \mathbf{K}_{s,t} & \tilde{\mathbf{K}}_{s,b} \\ -\Theta_{s,b} & \tilde{\mathbf{K}}_{s,t} & \mathbf{K}_b + \mathbf{K}_{s,b} \end{bmatrix} + j\omega \begin{bmatrix} C_p & \Theta_{s,t}^T & \Theta_{s,b}^T \\ \mathbf{0} & \mathbf{C}_t + \mathbf{C}_{s,t} & \tilde{\mathbf{C}}_{s,b} \\ \mathbf{0} & \tilde{\mathbf{C}}_{s,t} & \mathbf{C}_b + \mathbf{C}_{s,b} \end{bmatrix} \right. \\ \left. -\omega^2 \begin{bmatrix} 0 & \mathbf{0} & \mathbf{0} \\ \mathbf{0} & \mathbf{M}_t + \mathbf{M}_{s,t} & \tilde{\mathbf{M}}_{s,b} \\ \mathbf{0} & \tilde{\mathbf{M}}_{s,t} & \mathbf{M}_b + \mathbf{M}_{s,b} \end{bmatrix} \right\} \begin{bmatrix} v_p(\omega) \\ \mathbf{m}_t(\omega) \\ \mathbf{m}_b(\omega) \end{bmatrix} = \begin{bmatrix} 0 \\ \mathbf{0} \\ \mathbf{F}(\omega) \end{bmatrix} \tag{H.6}$$

where matrices $\mathbf{K}$, $\mathbf{C}$, $\mathbf{M}$ and Θ are the stiffness, damping, mass and electromechanical coupling terms, respectively; C_p is the capacitance of the piezoelectric film; and matrices having subscript (s,i) with $i = b,t$ indicate components ascribed to the spring layer written in terms of the base plate, b, or the top plate, t, displacements. Those marked by $\tilde{(\ )}$ indicate elastic coupling terms due to the spring layer. Note that electromechanical coupling is due to the spring layer; yet, because the spring layer mechanical displacements are written in terms of the base and top plate responses, the coupling is seen to directly affect the host structural vibration as well as the response of the top mass layer of the vibration control and energy harvesting device. All components of Equation H.6 are detailed in Section H.8 for implementation.

In the present study, the electromechanical coupling terms are determined by

$$\Theta_{s,t} = N_c\left(h_s\right) \frac{2h_s}{\pi t_s} \frac{d_{31} E_z^s}{h_s} \int_x \int_y \Psi_{w_{to}} \mathrm{d}y \mathrm{d}x \tag{H.7}$$

$$\Theta_{s,b} = N_c\left(h_s\right) \frac{2h_s}{\pi t_s} \frac{d_{31} E_z^s}{h_s} \int_x \int_y -\Psi_{w_{bo}} \mathrm{d}y \mathrm{d}x \tag{H.8}$$

where $\Psi_{w_{to}}$ and $\Psi_{w_{bo}}$ are the trial functions of the top and base plate transverse displacements, respectively. Eqs. H.7 and H.8 are the result of assuming the elastic transverse displacements are decoupled from the in-plane responses and the assumption that the piezoelectric spring layer electromechanical coupling is only related to transverse displacement. These equations have further been tailored to reflect a

more intuitive representation of the linear transverse strain induced in the corrugated piezoelectric film. Though the spring layer is deformed transversely, the piezoelectric coefficient d_{31} related to bending is employed, as opposed to d_{33} which is related to through-thickness deformation. Secondly, a weighting term is applied, $N_c \frac{2h_s}{\pi t_s}$, which is the product of the number of corrugations, N_c, and the ratio of the equivalent continuous area to the actual corrugated cross-sectional area of the spring layer. These modifications have been made following empirical observation of the devices' electrical response in the laboratory but in fact reflect an intuitive connection to the bending strain of the corrugated spring as it is transversely deformed.

The frequency response function (FRF) of the top plate transverse acceleration to the base plate transverse acceleration is computed as

$$|\mathrm{FRF}_{accel}(\omega)| = \left| \frac{-\omega^2 w_{to}(x_1, y_1, \omega)}{-\omega^2 w_{bo}(x_2, y_2, \omega)} \right| = \left| \frac{\Psi_{w_{to}}(x_1, y_1)\mathbf{m}_{w_{to}}(\omega)}{\Psi_{w_{bo}}(x_2, y_2)\mathbf{m}_{w_{bo}}(\omega)} \right| \tag{H.9}$$

where $\mathbf{m}_{w_{to}}$ and $\mathbf{m}_{w_{bo}}$ are the generalized co-ordinates related to the top plate and base plate transverse displacements, respectively; and (x_1, y_1) and (x_2, y_2) are the points of evaluation. The voltage FRF ($\mathrm{V{\cdot}g^{-1}}$) of a device is computed as

$$|\mathrm{FRF}_{volt}(\omega)| = \left| \frac{v_p(\omega)}{-\omega^2 \Psi_{w_{bo}}(x_2, y_2)\mathbf{m}_{w_{bo}}(\omega)} \right| \tag{H.10}$$

In considering the vibration attenuation capability of a device on a larger host structure, the average mean-square out-of-plane velocity ($\mathrm{m^2{\cdot}s^{-2}}$) of the base plate is determined by

$$\langle \dot{w}_{bo}(\omega) \rangle^2 = \frac{\omega^2}{2a_b b_b} \int \int \left(\Psi_{w_{bo}}(x, y)\mathbf{m}_{w_{bo}}(\omega) \right)^* \left(\Psi_{w_{bo}}(x, y)\mathbf{m}_{w_{bo}}(\omega) \right) \mathrm{d}x\mathrm{d}y \tag{H.11}$$

where $()^*$ denotes the complex conjugate. The mean-square acceleration, using the harmonic time dependence assumption, is then $\langle \ddot{w}_{bo}(\omega) \rangle^2 = \omega^2 \langle \dot{w}_{bo}(\omega) \rangle^2$. The accelerance TF for the vibrating structure is the transfer function between the global, or mean-square acceleration, and the input force response.

Average electrical power over the energy harvesting load resistance is computed:

$$P(\omega) = \frac{|v_p(\omega)|^2}{2R_1} \tag{H.12}$$

Table H.1: Mechanical and electrical characteristics of the piezoelectric film

t_s (m)	E_p (Pa)	ν_p	ρ_p (kg/m^3)	η	d_{31} (m/V)	$\epsilon_{33}^{\mathbf{T}}$ (F/m)
28e-6	5.4e9	0.18	1780	1e-3	23e-12	$12\epsilon_0$

Table H.2: Equivalent orthotropic plate characteristics of piezoelectric core having $\lambda = 12.7$ mm and $t_s = 28$ μm

E_x (Pa)	E_y (Pa)	E_x (Pa)	ν_{yx}	ν_{yz}	ν_{xz}
2.47e10	2.12e10	5.78e3	0.045	0	0
G_{yz} (Pa)	G_{xz} (Pa)	G_{xy} (Pa)	ρ_s (kg/m^3)	h_s (mm)	η_s
7.49e4	1.77e6	2.69e8	7.12	6.35	0.08

When the device is placed on the host panel, similar to the accelerance TF, the power TF is the ratio of the electrical power to the input force.

H.4 Experimental validation

H.4.1 Device description and characterization

The device shown in Figure H.2 was produced using piezoelectric film of thickness $t_s = 28$ μm having characteristics as given in Table H.1 [140]. Both surface electrodes were carefully etched as per the design of Figure H.4 using a fine-tipped watercolor brush and ferric chloride solution. Afterwards, the film was constrained in the circularly corrugated form of period $\lambda = 12.7$ mm using thin lines of quick-drying epoxy and facing sheets of non-poled PVDF film into the circularly corrugated form having 5 full periods. Elastic homogenization techniques were used to determine equivalent orthotropic thick plate elasticity parameters to characterize the spring layer stiffness matrix, $\mathbf{c}_s^E$ [144, 65, 111]. These equivalent material properties are given in Table H.2 and were computed using the methods proposed in Chapter D. Note that the transverse parameter, E_z, is many orders of magnitude less than the cross-planar bending stiffnesses, E_x and E_y, and that there is no coupling between them, $\upsilon_{yz} = \upsilon_{xz} = 0$. This indicates that transverse dynamics of the layer are similar to a layer of vertical springs, as per [65], not coupled to the remaining dynamics of the layer.

The device was fixed to a stiff shaker table platform for FRF testing. Evident in

Table H.3: Mechanical and geometric properties of base and top plates, $i = b, t$

Layer	a_i (mm)	b_i (mm)	h_i (mm)	E_i (Pa)	ν_i	ρ_i (kg/m^3)	η_i
Base	300	140	5	1.0e14	0.33	800	3e-4
Mass layer	76.2	50.8	0.76	2.1e11	0.33	7850	1e-3

Figure H.2 are the lead attachments connected to the etched surface electrodes noting that four connections are required given the four unique segments of the electrode after etching. Table H.3 presents the top mass layer and approximate base plate characteristics. The shaker excited the specimen only in the transverse direction and, as such, was anticipated only to excite the SDOF resonance response of the device. In the model, the base plate was assumed to have free boundary conditions and be excited by a centrally-located unit point force. For FRF computation, $(x_1, y_1) = (0, 0)$ and $(x_2, y_2) = (0, 0)$.

H.4.2 FRF test results and model validation

A comparison of the measured and modeled acceleration FRF is given in Figure H.5 (a) for four values of load resistance, R_1. The device is observed to exhibit a principal SDOF resonance, akin to a 1D mass-spring-damper system. For smaller values of R_1, the natural frequency occurs at approximately 78.5 Hz; as the resistance is increased, the coupling through the piezoelectric material produces a stiffer distributed spring layer and increases the resonance to the open circuit value (*i.e.* $R_1 \to \infty$) at approximately 81.5 Hz. This is a substantial shift in frequency for a piezoelectric material having such low electromechanical coupling as compared with, for example, piezoceramics. However, this may be due to the circularly corrugated design which significantly strains the film as the mass oscillates vertically at resonance. The model almost exactly predicts the locations of these resonant frequencies for various load resistances but measurements exhibited uniformly more roll-off above resonance. This lapse in the model may be explained by employing too great of a loss factor, η_s in Table H.2, for the equivalent spring layer elastic material properties.

It is also noted that there is no noticeable shunt damping effect due to dissipa-

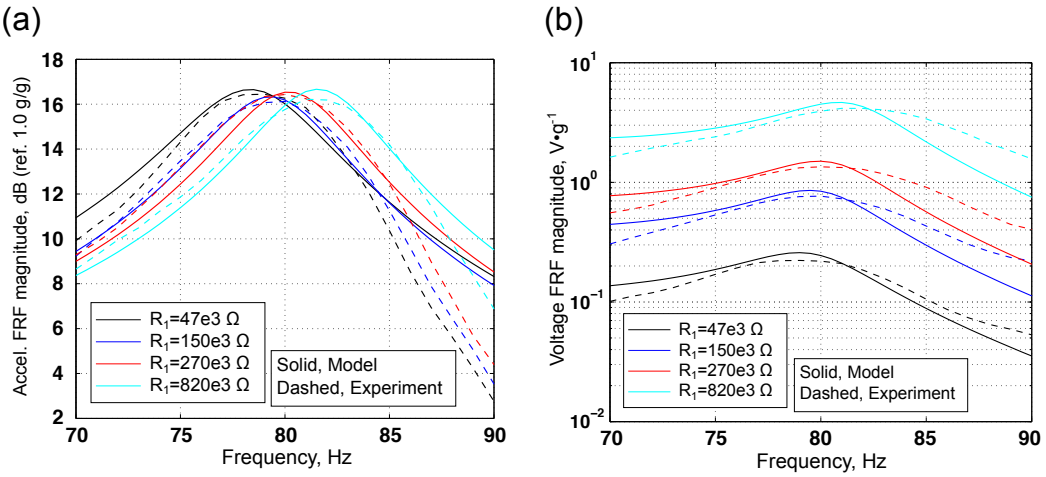

Figure H.5: Comparison of modeled and measured (a) acceleration FRF magnitudes and (b) voltage FRF magnitudes for piezoelectric corrugated core distributed absorber device for various load resistances, R_1.

tion in the electrical circuit. The inertial influence of the top mass layer dominates dissipative circuit effects. Therefore, for this particular specimen, the damping of the device is mostly a function of the elastic characteristics of the PVDF film itself as opposed to electromechanical coupling.

Figure H.5 (b) compares the measured and predicted voltage FRF for the sample. The model fairly accurately predicts the amplitude and shifting resonance frequency of the voltage FRF resonance. Similar to past work in piezoelectric energy harvesting [85], the voltage FRF is measured and predicted to both increase in overall amplitude as well as in frequency as the load resistance of the energy harvesting circuit is increased.

Finally, a time-domain plot of the response of the device as measured for $R_1 = 150$ kΩ is given in Figure H.6 at an excitation frequency of 81 Hz. Shown in Figure H.6 (a) are the individual voltage outputs for the two electrode pairs generated by etching according to the design in Figure H.4. The outputs are perfectly out-of-phase and of nearly identical magnitude. This verifies the assumption that the strains exhibited on opposing sides of the piezoelectric film are equal-and-opposite. Proper combination

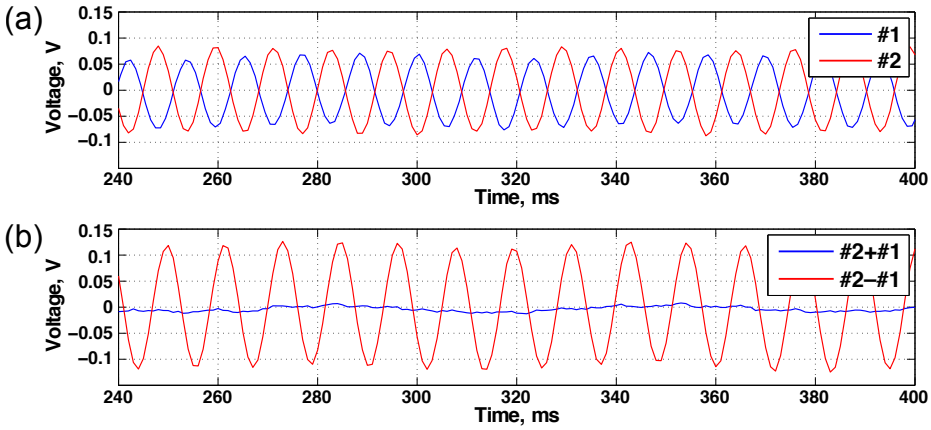

Figure H.6: Measured time series of corrugated piezoelectric device. (a) Individual electrode outputs and (b) sum and difference of the two signals.

of these voltages yields a substantial increase in output, while directly combining the two signals almost eliminates the net voltage, Figure H.6 (b).

The response is also observed to be sinusoidal, indicating the linearity of the distributed spring layer as the device transversely oscillates. Though bending and shearing dynamics of the piezoelectric spring layer may yield measured electrical responses of greater complexity, the linearity of the transverse response suggests model results for the device at its natural frequency should be in reasonable agreement with measurements which is most important for an accurate energy harvesting analysis.

H.5 Analysis of distributed device design for energy harvesting and vibration suppression purposes

H.5.1 Dampening of distributed spring layer

H.5.1.1 Mechanical damping considerations

Devices intended to suppress surface vibration are frequently designed so as to dissipate the energy which they intercept. However, energy harvesting devices are generally designed so as to have negligible dissipative effects. Indeed the shunt damping effect of harvester circuits when operating at maximal power output can be a detriment to performance in that objective [35].

Table H.4: Geometric and mechanical properties of the layers

Layer	a (mm)	b (mm)	h (mm)	E (Pa)	ρ (kg/m^3)	ν	η	(x_{f_1}, y_{f_1}) (mm)
Base	600	400	3	7.2e10	2100	0.33	1e-3	(144,127)
Top	90	90	1	7.2e10	2100	0.33	1e-3	—

Table H.5: Equivalent orthotropic plate characteristics of piezoelectric core

E_x (Pa)	E_y (Pa)	E_x (Pa)	ν_{yx}	ν_{yz}	ν_{xz}
4.04e10	3.44e10	3.62e4	0.041	0	0
G_{yz} (Pa)	G_{xz} (Pa)	G_{xy} (Pa)	ρ (kg/m^3)	h_s (mm)	η
1.73e5	4.67e6	1.69e8	15	6.35	0.001

Thus, consideration of the spring layer mechanical dampening should be made as it initially appears to be a factor promoting one objective while inhibiting the other. For this purpose, a simply-supported panel is considered to which a centrally-located distributed absorber device is attached. The spring layer of the device is a circularly corrugated layer, using a piezoelectric film thickness of 63.5 μm and a wavelength of $\lambda = 12.7$ mm. Mechanical and geometric properties of the system are provided in Table H.4; equivalent continuous spring layer elasticity constants are provided in Table H.5 as computed from the method of Chapter D; and the remaining piezoelectric film properties are those of Table H.1. The device represents a mass ratio of $\mu = 0.0117$ and has a SDOF natural frequency of 260 Hz, very close to the panel (3,1) modal resonance at 264.1 Hz. The load resistance during computation was fixed at $R_1 = 10$ kΩ. Note that the circularly corrugated piezoelectric film uses 7 periods of the film to cover the span of the continuous device.

The model was evaluated over a range of spring loss factors, η. Metrics of reduction of the cumulative panel mean-square velocity and cumulative power were made for two bandwidths, 10 to 300 Hz and 10 to 600 Hz. Results were normalized to the nearly undamped case, $\eta = 1e-3$, and are presented in Figures H.7 and H.8.

Intuitively, Figure H.7 shows that increased dampening in the spring layer benefits both narrow and broadband vibration attenuation. The effect is more apparent around the bandwidth where the device works reactively, near to its tuning frequency

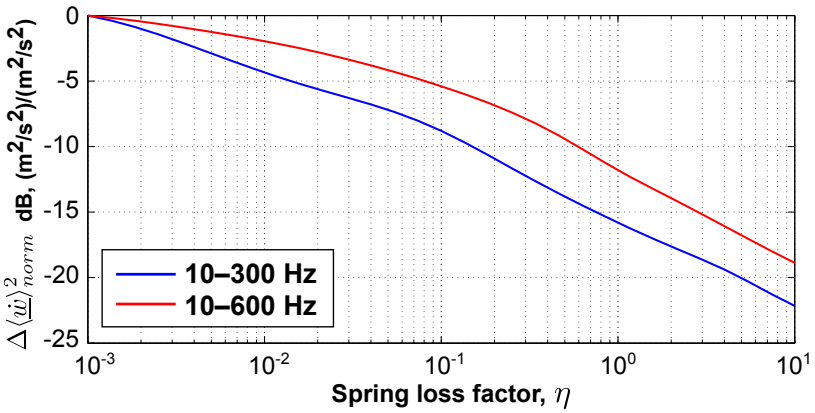

Figure H.7: Vibration suppression dependency on distributed spring layer loss factor, normalized to undamped case.

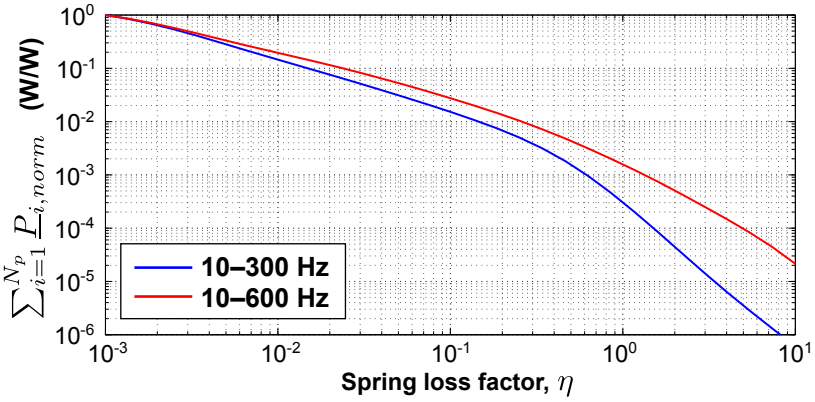

Figure H.8: Energy harvesting dependency on distributed spring layer loss factor, normalized to undamped case.

of 260 Hz. Also, as may be expected, as Figure H.8 indicates, any increase in dampening inhibits power harvesting potential. In general, energy harvesting devices are designed so as to be as lightly damped as possible in order to most efficiently convert the captured kinetic energy into electrical power. Thus, dissipated energy is lost electrical power.

In this sense, it is no surprise that the case of dampening in the continuously distributed spring layer presents a contradiction in terms of objectives. However, as mentioned at the beginning of this section, structural dampening caused by con-

nected harvester circuits is an unavoidable effect in the electro-mechanical conversion process; this effect is witnessed most prevalently at optimal power harvesting conditions [35, 85]. Thus, a design goal may be to develop a spring layer with minimal mechanical dampening such that increases in dampening are achieved through the electrical circuits as the natural result of energy harvesting, instead of through damped materials via the conventional mechanism of Joule heating.

A note should be made regarding the results shown for vibration attenuation as mechanical damping of the spring layer increased, Figure H.7. In Section F.5, continually increasing the damping of the electromagnetic oscillators improved vibration attenuation capability but only up to the point whereupon they effectively became overdamped. This led to an observed optimum mechanical damping ratio which was best suited for the corresponding load resistance, thus collectively yielding best electrical and mechanical overall damping.

However, Figure H.7 shows no such convergence or optimum damping of the spring layer. The explanation for this is that the present continuously distributed spring layer is capable of both transverse as well as extensional deformation, whereas the oscillators are one-dimensional systems. Thus, as the loss factor of the distributed spring layer increases, this increases the resistive effects of the vibration control device which is a useful broadband vibration suppression feature. In contrast to the EĐM oscillators, increases in the loss factor of the distributed spring would not exhibit an optimum value since the dynamics of the continuously distributed device are more complex than the simpler mass-spring-damper systems.

H.5.1.2 Electromechanical damping considerations

In extension of an analysis of the dampening of the distributed device by means of materials selection, it is valuable to examine the effects of piezoelectric stiffening and dampening due to varying load resistance. While the level of dampening and stiffening of the oscillating device may be substantial, as in the case of a bimorph piezoceramic energy harvesting beam for optimal power output [85], it is not necessarily the case

that the effect translates to a viable improvement in narrow or broadband panel vibration attenuation.

Furthermore, it may be recognized that the piezoelectric stiffening effect, in modifying the SDOF resonance of the device, observed in Figure H.5 (a), will thereafter modify the way in which it couples to the host structural vibration. The split resonances due to the reactive effect of the absorber device may shift as a result.

The same model as the previous section was utilized. In the simulations, mechanical dampening of the spring layer was held fixed, $\eta = 1e-3$, while the load resistance varied. The mean-square velocity of the panel is plotted in Figure H.9 for a variety of load resistances, R_1. Very little differences are apparent amongst the variety of cases of panel mean-square velocity with the absorbers and, in a global sense, they appear identical and overlaid. This is partially due to two key factors: first, the very low mass ratio of the device and minimal amount of piezoelectric film within the spring layer; second, the piezoelectric film has a low electro-mechanical coupling as compared with a more conventional material for energy harvesting, like piezoceramics. Therefore, as the load resistance is varied, it is not anticipated that the structural response will alter drastically.

However, a closer look at the two split resonances of the reactively suppressed panel (3,1) mode—264 Hz split into 244 and 292 Hz—shows that the changing load resistance does have a direct effect on these two responses. Figure H.10 (a) provides a zoomed in plot of the lower split resonance, using a finer computed frequency resolution for convenience. Note that the untreated panel vibration is not shown in Figure H.10 due to the shift in location of the resonance with the attachment of the devices.

Figure H.10 (a) shows that, as the load resistance increases, the split resonance is dampened to varying degrees. Around 3e4 Ω an optimal level of dampening occurs. While existing piezoelectric energy harvesting literature suggests that the optimal level of dampening due to the choice of resistive load occurs under the same conditions

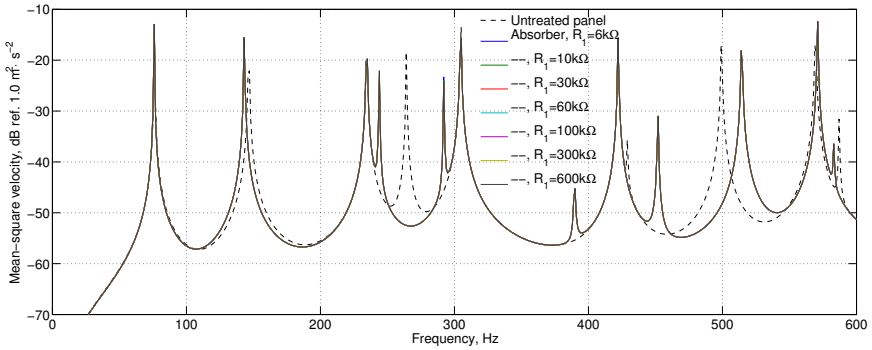

Figure H.9: Panel mean-square velocity for varying distributed device load resistance.

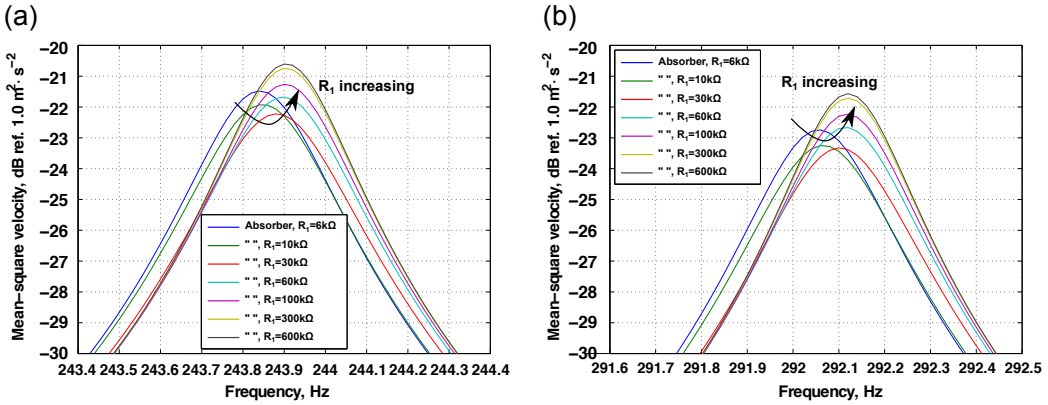

Figure H.10: Panel mean-square velocity for varying distributed device load resistance, zoom (a) lower split resonance and (b) higher split resonance.

as optimal power output [35], it should be recalled that this was the case for the energy harvester beam itself, and not in regards to coupling to another structure's vibrations. However, for the choice of $R_1 = 3e4\ \Omega$, the magnitude of the resonance is attenuated by roughly 1.5 dB greater than for some other selections of resistance.

Figure H.10 (b) plots a zoomed plot of the panel mean-square velocity around the higher of the two split resonances, at 292 Hz. The same effect is observed as for the lower of the split resonances, again with best structural dampening achieved around $R_1 = 3e4\ \Omega$. Closer to 2 dB reduction in mean-square velocity is achieved for best resistance selection in this instance.

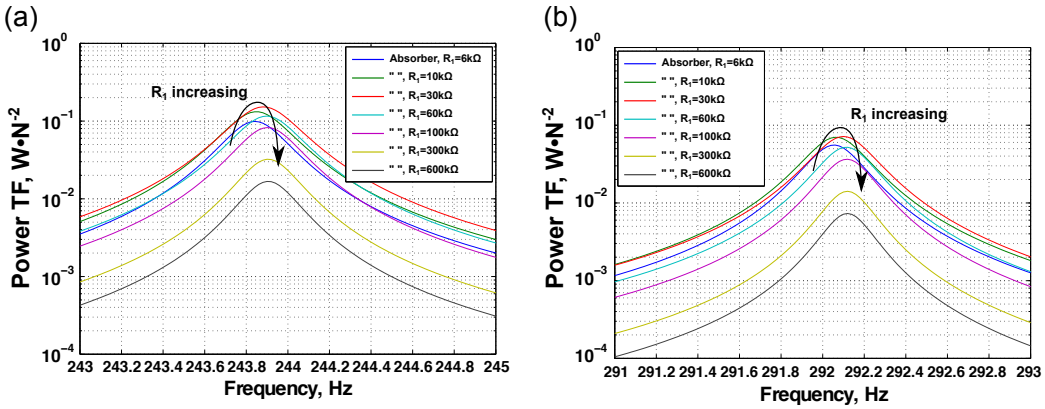

Figure H.11: Distributed device piezoelectric power output for varying distributed device load resistance, zoom (a) lower split resonance and (b) higher split resonance.

The varying power output of the device is shown in Figures H.11 (a) and (b) for the same bandwidths. It is seen that the maximum power from the device also occurs in the range of 3e4 Ω. From this result may be deduced the following. Since the mechanical dampening of the spring layer is less than that induced by the circuit, the distributed device itself is most damped via the harvester circuit under conditions of maximum power output. Thence, the greatest level of vibration attenuation of the host panel around the tuned bandwidth occurs simultaneously for the load resistance which maximizes the energy harvesting potential of the same applied device. This is one direct sign of the simultaneous achievement of reactive vibration suppression and energy harvesting goals. It is also an indirect observation of shunt damping effects: the panel split resonances are modified in amplitude and frequency as the piezoelectric spring layer is stiffened and damped to varying degrees.

Figure H.12 plots the full spectrum power output for reference. The additional large peak in output at 515 Hz is due to excitation of the distributed device by the (1,3) vibrational mode of the structure. Since the device does not span any of the nodal lines of this mode, it is uniformly excited, indeed nearly to the same extent as around its tuned frequency bandwidth, such that power output at 515 Hz is almost of the same order as the tuned range.

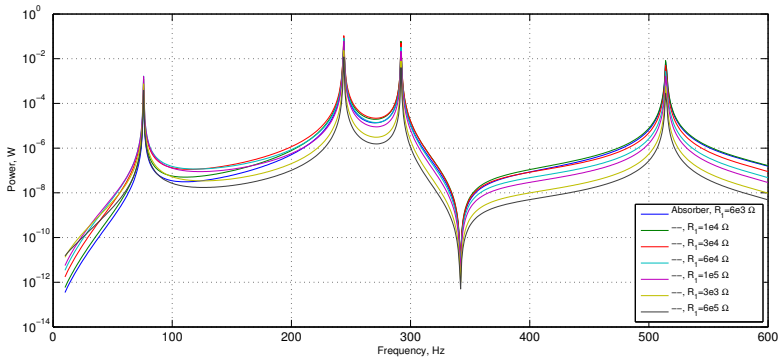

Figure H.12: Distributed device piezoelectric power output for varying distributed device load resistance.

A final zoomed plot around this frequency highlights an additional feature of importance. Figure H.13 plots the power output around the (1,3) panel mode as load resistance is varied. While maximum power was generated around the tuning frequency range for load resistances near to 3e4 Ω, it is seen that around 514.4 Hz optimal power output occurs for load resistances closer to 1e4 Ω. It is also observed that no change in frequency is predicted as load resistance is varied. Thus, the optimal power output at 514.4 Hz occurring for a different load resistance than around the tuning frequency range is likely the natural consequence of the induced dampening effects unique to the choice of R_1.

Note that in this analysis, the contribution of mass of the applied device was very low, $\mu = 0.0117$. Even for such a small addition of mass, the reactive nature of the device greatly shifted the frequencies of the host panel around the device's tuned range. These features reveal a number of important points regarding distributed devices to be designed for the concurrent purposes of passive vibration suppression and energy harvesting. Namely,

1. The presence of a reactive device inherently modifies the dynamics of the host structure such that the operational frequencies of the structure no longer coincide with the tuned frequency for which the device was originally intended.

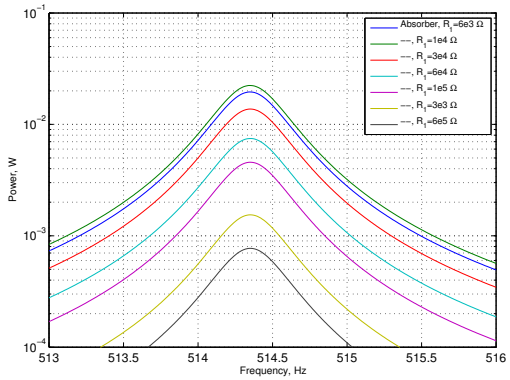

Figure H.13: Distributed device piezoelectric power output for varying distributed device load resistance, zoom higher panel mode.

2. For a mechanically undamped device, optimal electrical dampening occurs for a choice of load resistance equal to that of optimal power harvesting conditions.

3. In the case of (2), since the device dampening is primarily dependent on the electrical circuit dissipation, shunt damping serves as the best means to reactively attenuate structural vibration in the tuned frequency bandwidth.

4. However, the reactive device is not oscillating at its optimal (tuned) frequency, see (1), and there may be other frequencies of excitation which, in fact, yield even greater power output for a load resistance not equal to conditions of (3).

H.5.2 Alternative placement of piezoelectric film in the harvester and vibration control devices

An interesting possibility is considered in light of the results of Section C.5. It was found that the modal response of a continuously distributed vibration absorber top mass layer was more beneficial to vibration attenuation than the use of the translational SDOF device resonance.

The modal dynamic is the freely-suspended plate bending mode depicted in Figure H.14. In this mode, there are no nodal lines of strain; in other words, the strain on the surface of the plate is fully in-phase on the top surface and fully in-phase

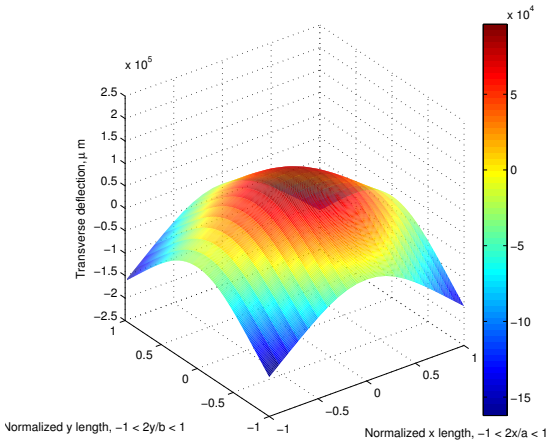

Figure H.14: Freely-suspended plate bending mode without nodal lines.

on the bottom surface (though the two surfaces are out-of-phase with reference to each other). This is due to the fact that this operational deflection shape is the superposition of the free-free beam fundamental bending mode shape in both x and y co-ordinate axes.

Were a piezoelectric layer attached to the top surface of the mass layer which was vibrating in this mode shape, the surface strain distribution, being all in-phase, may be of benefit for energy harvesting purposes. This is the same reason that cantilever beam harvesters are designed to oscillate in the fundamental beam mode shape. Avoidance of strain nodes is crucial to implementation of the most straightforward electrical circuits and electrode etching requirements [145].

Thus, with the top mass vibrating in this low order modal dynamic, no etching of the applied piezoelectric film electrodes would be necessitated. However, it must be evaluated whether the bending of the top mass in this dynamic is substantial enough as compared with, for reference, the host panel bending. If the latter were greater than the prior, there would be no benefit to piezoelectric material on the top mass layer and, therefore, it may likely be best to design spring layers utilizing the piezoelectric material.

Table H.6: Geometric and material specifications

Layer	a (mm)	b (mm)	h (mm)	E (Pa)	ρ (kg/m^3)	ν	η	(x_{f_1}, y_{f_1}) (mm)
Base	300	300	3.7	7.2e10	2100	0.3	1e-3	(144,127)
Top	90	90	2	7.2Γe10	2100	0.3	1e-3	—
Spring layer	90	90	50	2e5	9	0.4	5e-3	—

H.5.2.1 Comparison using smart foam sample

To study this feature, a series of model simulations were carried out in which a simply-supported panel was excited, having a centrally-located distributed vibration absorber device. Three cases were considered: the absorber utilizing the piezoelectric material in the spring layer like smart foam (Figure H.2); the piezoelectric film being directly attached to the host panel, immediately beneath the distributed spring layer of the absorber; and the absorber top mass having a layer of piezoelectric film on top. It was anticipated that comparison between the second and third arrangements should give a clear indication as to whether the bending of the host panel is thoroughly transmitted through the spring layer to couple to the modal dynamic of the top mass. Note that the volume of piezoelectric material used for each of the three cases is roughly equivalent, though the curvature of the smart foam design uses slightly more than the latter two.

Variations in the load resistance, R_1, and in the modulus ratio, Γ, are evaluated with the corresponding metrics of the reduction of cumulative mean-square velocity around the tuning frequency of the distributed absorber (10 to 300 Hz) and broadband (10 to 1000 Hz). It is noted that the host panel exhibits a (1,1) mode at 228.9 Hz and the SDOF oscillation of the absorber was tuned to 228 Hz. Geometric and material characteristics of the layers are given in Table H.6 while the piezoelectric material and electric properties are those of Table H.2. The smart foam device represented a mass ratio of $\mu = 0.0538$.

Figures H.15–H.17 plot the results of simulation for the case of the piezoelectric film in the spring layer, beneath the device on the panel and when the film is applied to the top surface of the top mass, respectively. Plots in the left column provide

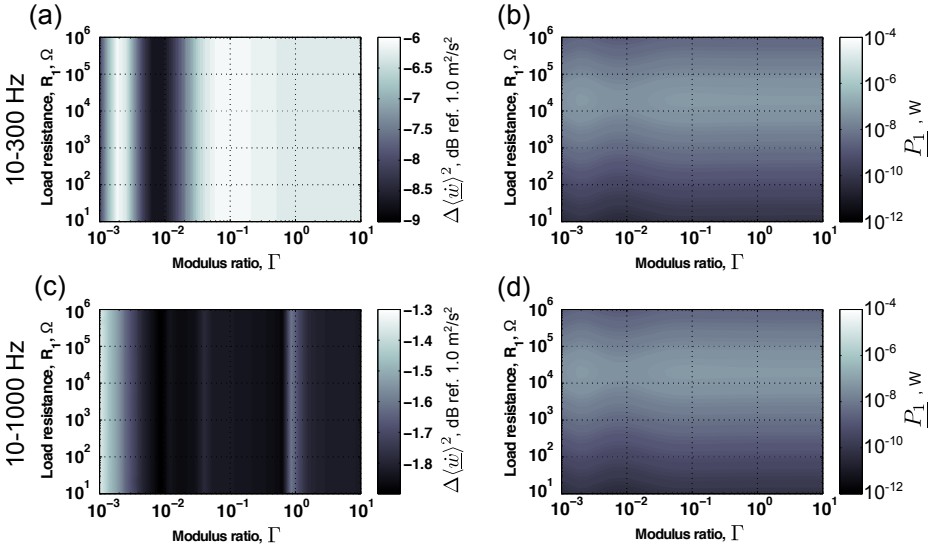

Figure H.15: Smart foam with piezoelectric film in smart foam spring layer. (a) Narrowband reduction in cumulative mean-square velocity. (b) Narrowband cumulative power. (c) Broadband reduction in cumulative mean-square velocity. (d) Broadband cumulative power.

the reduction in cumulative mean-square velocity; plots in the right column provide the cumulative power. The top rows are computations evaluated near the tuning frequency range, 10 to 300 Hz, while the bottom rows are computations over the full spectrum, 10 to 1000 Hz.

In each case, Figures H.15–H.17 (a) show that a modulus ratio of approximately $\Gamma = 0.006$ yields substantial narrowband reduction in the panel mean-square velocity. This, in fact, corresponds to the case of the device top mass oscillating in the freely suspended mode illustrated in Figure C.4. Thus, this corroborates the findings of Section C.5 that continuously distributed vibration absorbers are more beneficial when designed so as to oscillate modally as opposed to translationally. This also appears to yield the best improvement in broadband vibration attenuation as well, considering Figures H.15–H.17 (c), though other ranges of Γ yield nearly equivalent levels of vibration suppression.

When the piezoelectric film applied to the top mass layer, Figure H.17 (a) shows that an optimal level of resistance, $R_1 \approx 14$ kΩ, further increases the narrowband

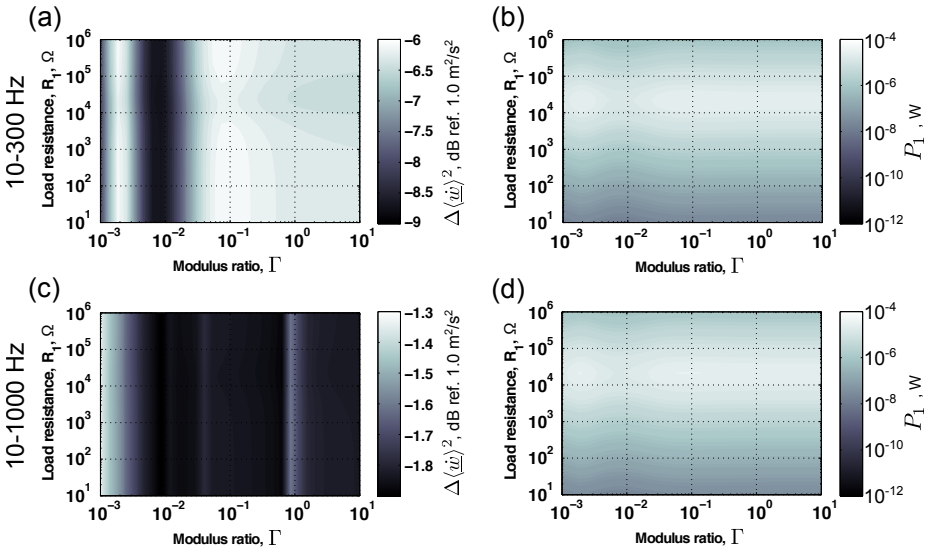

Figure H.16: Piezoelectric film applied to panel surface beneath smart foam device. (a) Narrowband reduction in cumulative mean-square velocity. (b) Narrowband cumulative power. (c) Broadband reduction in cumulative mean-square velocity. (d) Broadband cumulative power.

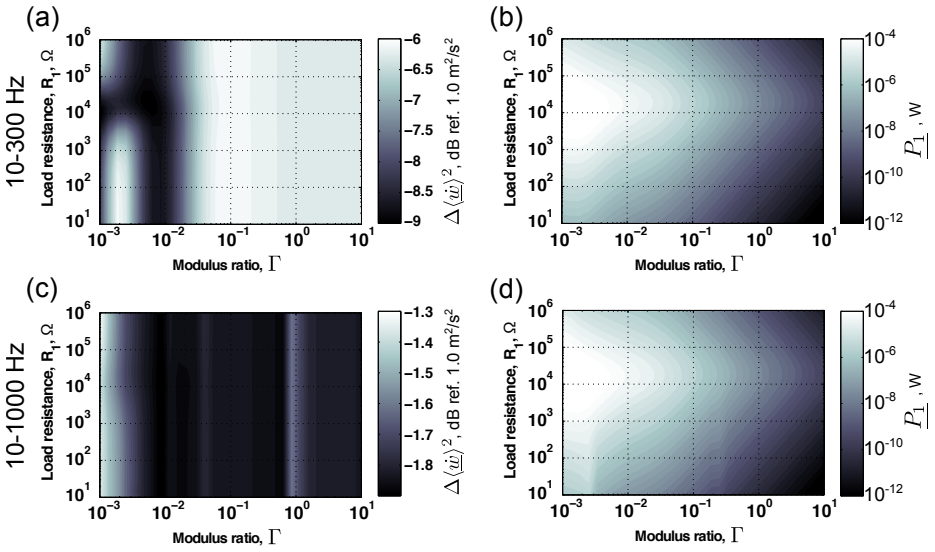

Figure H.17: Piezoelectric film applied to smart foam device top mass surface. (a) Narrowband reduction in cumulative mean-square velocity. (b) Narrowband cumulative power. (c) Broadband reduction in cumulative mean-square velocity. (d) Broadband cumulative power.

vibration suppression. Thus, as the mass layer oscillates modally, an optimum load resistance is determined to best attenuate the structural motion, by means of increasing the electrical damping effects.

Figures H.15–H.17 (b) and (d) do not show major variations from within each case, but the cases comparatively exhibit significantly different power outputs. The piezoelectric film in the smart foam spring layer is the least effective manner by which to generate useful electrical power. This indicates that comparatively the embedded film is much less strained as the smart foam device works against the host vibrating panel. Thus, this is a poor energy harvesting device design, not surprising given the original application of smart foam was for acoustic actuation.

Figures H.16 and H.17 (b) and (d) show that when the piezoelectric film is directly applied to either the base structure or top mass layer, much greater power output is possible. However, when the piezoelectric film is applied to the mass layer, and the modulus ratio of the top mass is selected so as to allow the mass layer to operate in the freely suspended modal dynamic, the greatest power output is possible. The optimum computed values are $\Gamma = 0.00135$ and $R_1 = 14.7$ kΩ when the piezoelectric film is directly applied to the top mass.

Using these optimum values, Figures H.18 and H.19 plot the panel mean-square velocity of the higher of the two split resonances of the original untreated panel response and the power output, respectively. Figure H.18 represents a zoomed plot of nearly identical results as computed for Section C.5 Figure C.5, since the earlier modeling scenario was the same with the exception of the presence of a piezoelectric material.

Figure H.18 shows that the higher split resonance may be attenuated to a greater degree with the piezoelectric film on the modally-oscillating top mass as compared with the film on the host panel itself or when present in the smart foam spring layer. Since each of the modeling scenarios involves the top mass oscillating in the modal dynamic, this suggests that the additional reduction in panel mean-square velocity

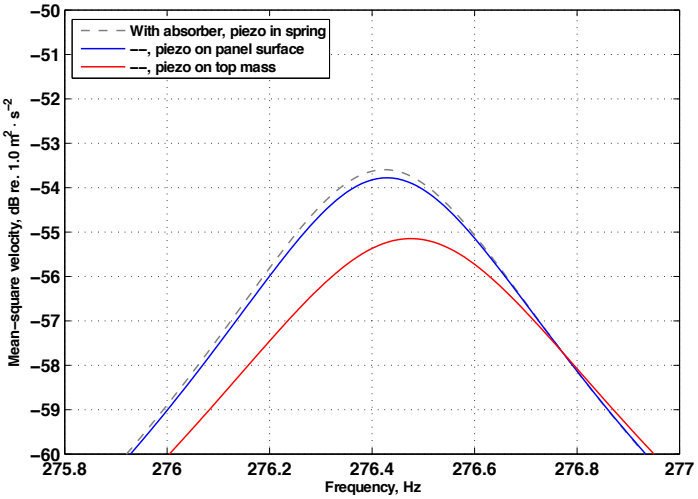

Figure H.18: Comparison of panel mean-square velocity, higher split resonance, for changing location of piezoelectric film application. $\Gamma = 0.00135$ and $R_1 = 14.7$ kΩ.

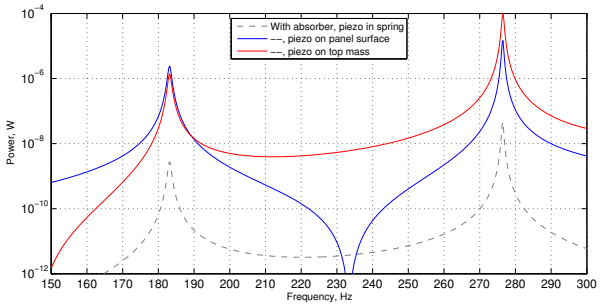

Figure H.19: Comparison of power across load resistance, $R_1 = 14.7$ kΩ, changing location of piezoelectric film application. $\Gamma = 0.00135$.

possible with the piezoelectric film applied to the top mass layer is due to dissipative effects in the external harvester circuit.

Figure H.19 reveals a clear benefit of applying the piezoelectric film to the top mass layer in terms of generating maximum electrical power. The application of the film in the smart foam spring layer does not substantially strain the film, and a smaller power output results. Applying the film to the host panel is, in fact, a reasonable means by which to extract power from the strained piezoelectric material. The modally-oscillating top mass is found to be the most useful surface of application of the piezoelectric material for both energy harvesting as well as vibration suppression purposes.

However, the use of the circularly corrugated spring layer may substantially increase the total power output possible due to the greater volume of and straining of the spring layer. In the smart foam construction, the film is supported by an encasing poroelastic layer, thus minimizing the transmitted strain to the film. In contrast, the piezoelectric film supports itself in the corrugated spring layer design; thus, all strain of the spring layer is necessarily transmitted through the piezoelectric film leading to greater electromechanical energy conversion.

H.5.2.2 Comparison using circularly corrugated piezoelectric spring layer

While the comparison made to a smart foam sample employed roughly equivalent amounts of piezoelectric film per case—whether the film was on the top mass, embedded in the foam or applied directly beneath the device—the device using the circularly corrugated spring layer is of greater interest to this work. Liao and Sodano [27] point out that the efficiency of a power harvesting device is interconnected with the amplitude of electromechanical coupling which it exhibits. Since the circularly corrugated sample is substantially more coupled by means of a greater mass of piezoelectric material per volume, as compared with a smart foam sample, it is worthwhile to repeat the analysis of the previous section to assess how the greater electrome-

Table H.7: Geometric and material specifications

Layer	a (mm)	b (mm)	h (mm)	E (Pa)	ρ (kg/m^3)	ν	η	(x_{f_1}, y_{f_1}) (mm)
Base	300	300	3.7	7.2e10	2100	0.3	1e-3	(144,127)
Top	90	90	0.9	7.2Γe10	2100	0.3	1e-3	—

Table H.8: Equivalent orthotropic plate characteristics of piezoelectric core

E_x (Pa)	E_y (Pa)	E_x (Pa)	ν_{yx}	ν_{yz}	ν_{xz}
4.60e10	3.96e10	2.37e4	0.044	0	0
G_{yz} (Pa)	G_{xz} (Pa)	G_{xy} (Pa)	ρ (kg/m^3)	h_s (mm)	η
2.05e5	1.53e7	2.56e8	13.3	6.35	0.005

chanical coupling affects vibration attenuation and energy harvesting results.

Thus, the analysis was repeated using the base plate and top mass layer geometric and material properties as provided in Table H.7; the piezoelectric material and electric properties are those of Table H.1 with the exception that $t_s = 52$ μm; and the equivalent elasticity parameters of the spring layer having wavelength $\lambda = 15$ mm were computed using the methods of Chapter D and are provided in Table H.8. The absorber exhibited a SDOF natural frequency of 227 Hz; represented a mass ratio of $\mu = 0.0229$ and used 6 circular corrugations of the piezoelectric film along its length. In evaluating the response of the system when the piezoelectric film was applied to either the top plate surface or the base plate surface, the spring layer was assumed to be composed strictly of non-poled PVDF film.

Figures H.20–H.22 plot the results of simulation for the case of the piezoelectric film in the spring layer, beneath the device on the panel and when the film is applied to the top surface of the top mass, respectively. As in the prior section, plots in the left column provide the reduction in cumulative mean-square velocity; plots in the right column provide the cumulative power; the top rows are computations evaluated near the tuning frequency range, 10 to 300 Hz, while the bottom rows are computations over the full spectrum, 10 to 1000 Hz.

Unlike the smart foam sample of the prior section, the circularly corrugated piezoelectric spring layer exhibits significantly greater electromechanical effects and is the

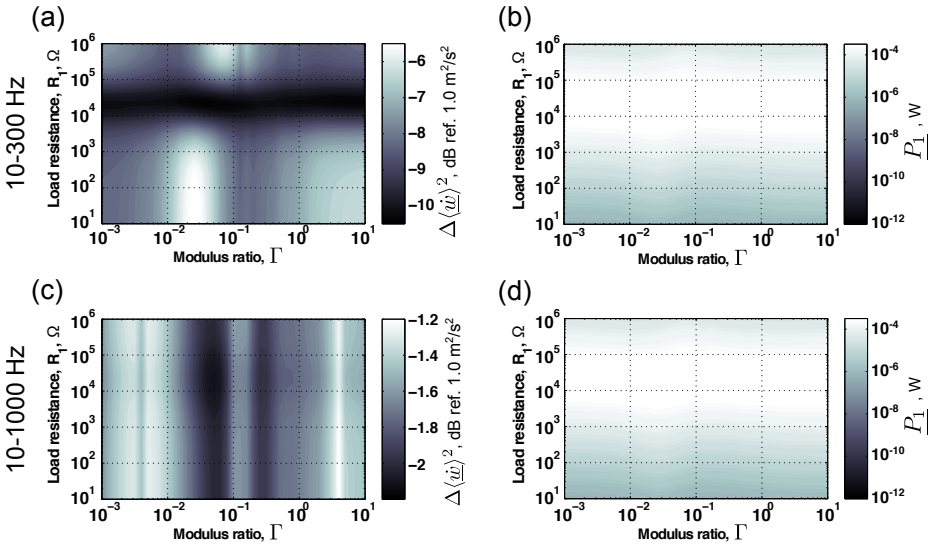

Figure H.20: Device having piezoelectric film in spring layer. (a) Narrowband reduction in cumulative mean-square velocity. (b) Narrowband cumulative power. (c) Broadband reduction in cumulative mean-square velocity. (d) Broadband cumulative power.

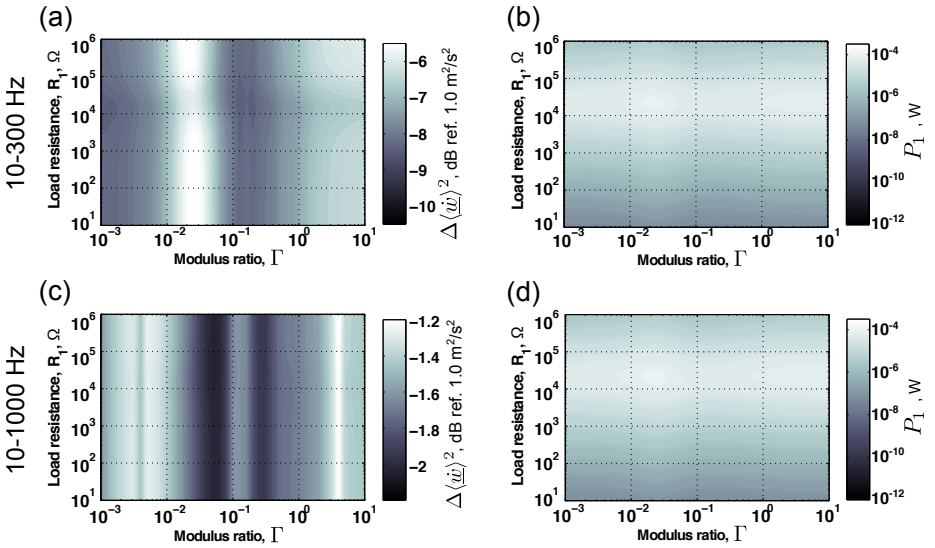

Figure H.21: Piezoelectric film applied to panel surface beneath device. (a) Narrowband reduction in cumulative mean-square velocity. (b) Narrowband cumulative power. (c) Broadband reduction in cumulative mean-square velocity. (d) Broadband cumulative power.

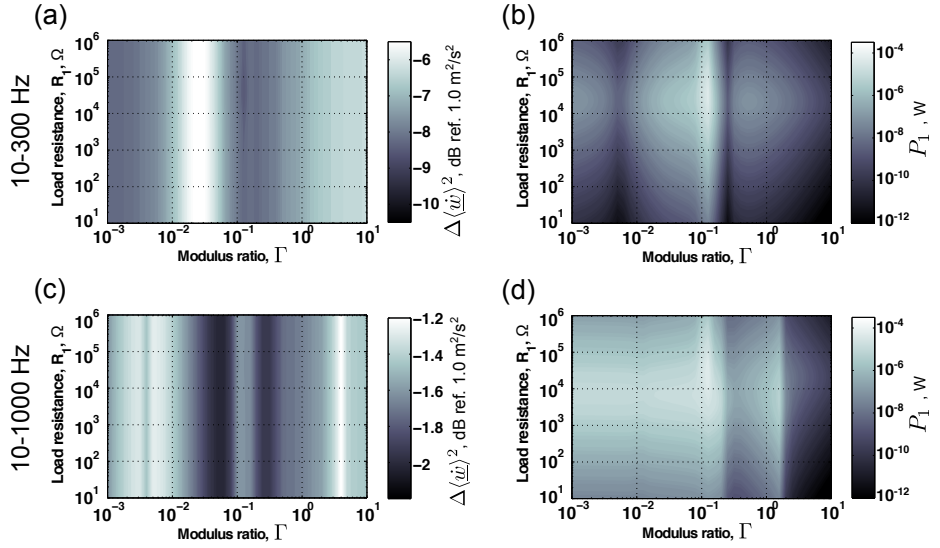

Figure H.22: Piezoelectric film applied to device top mass surface. (a) Narrowband reduction in cumulative mean-square velocity. (b) Narrowband cumulative power. (c) Broadband reduction in cumulative mean-square velocity. (d) Broadband cumulative power.

best solution for all scenarios: narrow and broadband vibration suppression and energy harvesting. An optimum modulus ratio is observed for narrowband vibration attenuation in all cases, Figures H.20–H.22 (a), $\Gamma \approx 0.1$ which contrasts to a best selection observed for broadband vibration attenuation, Figures H.20–H.22 (c), $\Gamma \approx 0.05$. When $\Gamma \approx 0.1$, the top mass layer of the device would exhibit the freely suspended pumping modal dynamic of Figure H.14 at the tuned natural frequency of the device, 227 Hz. As was found in the previous section and in Section C.5, designing the device such that the top mass oscillates modally as opposed to translationally is best suited for passive vibration suppression.

An explanation may be proposed as to the reduction in optimum Γ for broadband vibration attenuation as compared with the optimum for narrowband results. Due to the greater electromechanical coupling of the present spring layer design, there is a greater amount of piezoelectric damping and stiffening induced in the spring layer at the device resonance. This stiffening effect therefore inhibits the top mass from being excited to vibrate modally; to offset this constraint, the optimum modulus

ratio for broadband vibration attenuation is less than that which yields the modal dynamic at 227 Hz. It may be found that a modulus ratio of $\Gamma \approx 0.05$ indicates the top mass exhibits the pumping modal dynamic at approximately 170 Hz. Lower modulus ratio were observed in Section C.4 to be well-suited for passive broadband vibration suppression. The combination of the piezoelectric stiffening effects of the present device and the design of the top mass such that it oscillates modally appear to suggest the best compromise is to lower Γ than the narrowband optimum selection such that broadband attenuation may be maximized.

In the previous section, it was observed that placement of the piezoelectric film on the top mass layer would maximize narrow and broadband vibration suppression. However, the greater electromechanical coupling of the corrugated spring layer yields substantial electrical damping from the harvester circuit, which comparatively outweighs the damping effects induced should the film be placed on the top mass.

Given the greater electromechanical coupling induced by the corrugated piezoelectric spring layer, an optimum load resistance is computed to suppress vibration in Figure H.20 (a) and (c):$R_1 \approx 20$ kΩ. This indicates the device is most electrically damped for this selection of resistance, thus reducing the panel vibration to the greatest degree.

What's more, it is observed that this load resistance also corresponds to the best choice for energy harvesting purposes: Figure H.20 (b) and (d). Section H.5.1.2 discovered this effect as well in evaluating electromechanical damping effects induced in the piezoelectric spring layer which thereupon modified how the harvester device influenced the structural vibrations. It is found in literature that for moderately electromechanically coupled piezoelectric energy harvesters that maximum damping of the harvester structure corresponds to the maximum electrical power output [27].

This is again evidence that energy harvesting from and suppression of structural vibrations need not be mutually exclusive. Prior energy harvesting analyses which ignore the structural dynamic coupling of applying resonant devices to a greater

Table H.9: Mechanical and geometric properties of base and top plates, $i = b, t$

Layer	a_i (mm)	b_i (mm)	h_i (mm)	E_i (Pa)	ν_i	ρ_i (kg/m^3)	η_i
Base	711	508	6.35	7.2e10	0.33	2100	1e-3
Mass layer	150	150	1.3	7.2e10	0.33	2100	1e-3

vibrating system, be it a bridge or structural panel, may be missing a larger picture of the possibilities. Given that vibrational energy harvesting has significantly been spearheaded by structural health monitoring concerns, the ability to simultaneously attenuate the vibrations of a structure and convert the absorbed energy into electrical power intrinsically benefits the health of the structure.

H.6 Vibration suppression of and energy harvesting from an excited panel

H.6.1 Experiment description

A simply supported panel was then used for testing another piezoelectric vibration control device. The panel itself was a part of a larger mounted structure with the panel extending off of the structure by means of thin shims to replicate simple supports as closely as possible. The mechanical and geometric information of the panel and the device top mass layer are provided in Table H.9. It was observed that the edges of the panel support were not exactly classical simple supports but additionally constrained the rotation of the edges. This was compensated for in the modeling by including additional edge stiffnesses in computation. This is achieved by assuming the edge is further constrained by rotational springs as described in [146] and [98] and analytically detailed in Appendix A. However, due to the inexact boundaries along the edges of the test panel, it was not possible to perfectly match eigenfrequency predictions of the panel with those measured.

The mounted structure and the panel were both suspended as shown in Figure H.23. An electrodynamic shaker was attached to a bored hole at the center of the panel through a short stinger. A PCB 208 A03 force transducer was positioned between the stinger and the panel. An array of 30 PCB 330A accelerometers were

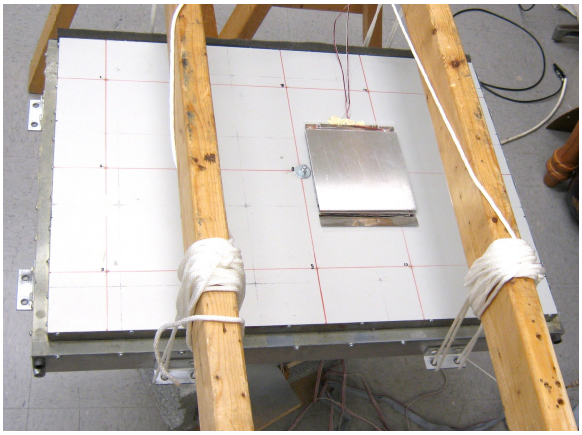

Figure H.23: Photograph of simply supported panel in mounted structure with piezoelectric device attached to the top surface. The shaker, stinger, force transducer and accelerometer array are connected to the underside of the panel.

randomly positioned on the underside of the panel, with the top surface left clear for later application of the piezoelectric device. The global accelerance TF was computed by the average accelerance TF between each accelerometer and the force transducer.

The piezoelectric spring layer design was the same as for the earlier shaker test sample, having piezoelectric film characteristics as given in Table H.1 and equivalent elastic parameters as provided in Table H.2. A close-up photograph of the device attached to the panel is shown in Figure H.24. The device was much larger than the specimen used in FRF testing of Section H.4 and included 12 periods of the circular corrugation. However, despite the larger size, the mass ratio of the device relative to the mass of the panel was only $\mu = 0.0104$, or just over 1%. In practical terms, this is an unusually lightweight device to employ for vibration control purposes but also meets the general objective in energy harvesting of attaching devices of negligible inertial influence to the host structure. Though the device was not measured on the shaker platform, for the justified reason that removing such devices from the platform often resulted in the destruction of the piezoelectric film layer, the SDOF natural frequency of the device was predicted by the model to be approximately 94 Hz. This was very close to the (1,1) mode of the simply supported panel which was measured

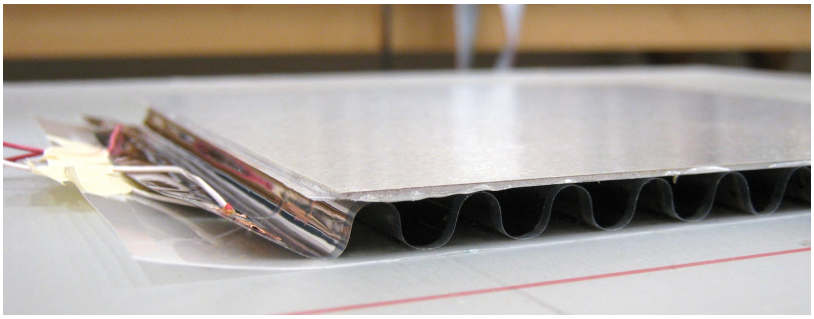

Figure H.24: Photograph of the piezoelectric vibration control device attached to the panel.

and computed to be 97.5 Hz.

H.6.2 Panel experimental results and model comparison

The panel accelerance TF was initially measured with nothing attached to the top surface. Afterwards, the center of the piezoelectric device was attached at (93,0) mm relative to the panel center. The device was attached by means of a thin double-sided tape. The tests were repeated varying the load resistance, R_1, in the energy harvesting circuit to which the electrical leads from the etched electrodes were attached. The out-of-phase voltages from the electrodes were appropriately combined so as to yield the maximum electrical signal. By experimental trials, it was found that $R_1 = 180$ kΩ yielded the greatest electrical power TF. The untreated panel accelerance TF and that with the applied piezoelectric device are shown in Figure H.25 comparing predicted results and measurements.

The model very closely predicts the untreated panel response with the exception of the location of some resonances. This is attributed to the inexact simply supported boundary conditions of the panel. It is apparent that the connection of the shaker to the panel is not exactly at panel center since several of the asymmetric modes are excited, for instance the (2,1) mode at 186 Hz. After observation of this feature, the model was appropriately adjusted to simulate the point force excitation at (4,4) mm relative to panel center. The two lowest-order symmetric panel resonances—the (1,1)

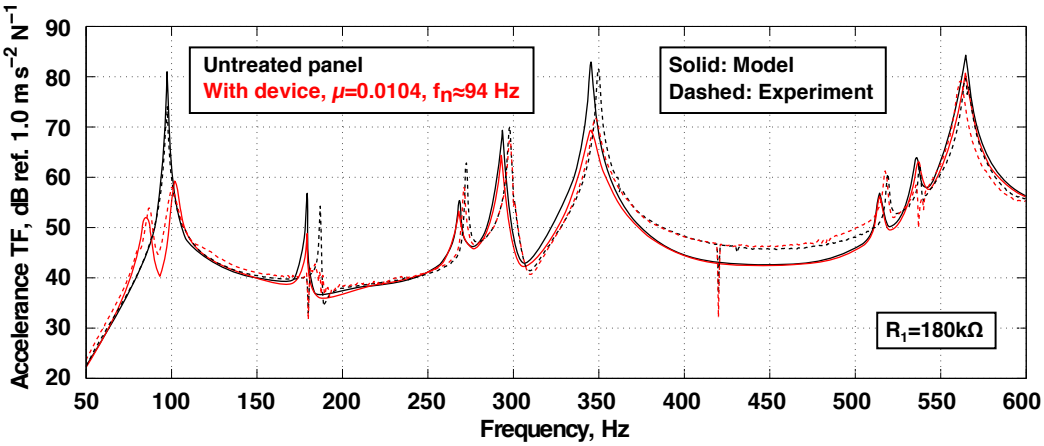

Figure H.25: Comparison of modeled (solid curves) and measured (dashed curves) accelerance TF magnitudes of the panel when untreated (black plots) and with the piezoelectric device (red plots). $R_1 = 180$ kΩ.

mode at 97.5 Hz and the (3,1) mode at 350 Hz—are thoroughly excited by the shaker and these are the resonances for which the piezoelectric device was designed and appropriately positioned.

Following application of the device, the panel vibration of the (1,1) mode is observed to be significantly attenuated. The resonance at 97.5 Hz is predicted to be suppressed by approximately 20 dB and the measurements show nearly this exact attenuation. Two split-resonances at 87 and 100 Hz are generated by application of the reactive device. This is a dynamic ascribed to conventional 1D vibration absorbers [82] and is seen to also be the case for the distributed system of interest. This further exemplifies the reactive nature of the piezoelectric device in suppressing the panel response. The (3,1) panel resonance at 350 Hz is attenuated by more than 10 dB but this is not due to the direct "tuning" of the device for this frequency. Instead, the reactive suppression of the symmetric (3,1) mode is conveniently achieved by the mostly central placement of the device on the panel surface. Over the bandwidth of frequencies computed, the model is in very close agreement with the measurements, despite minor misalignment of panel resonances due to the inexact simple supports.

While the device is observed to dramatically suppress the panel vibration for being

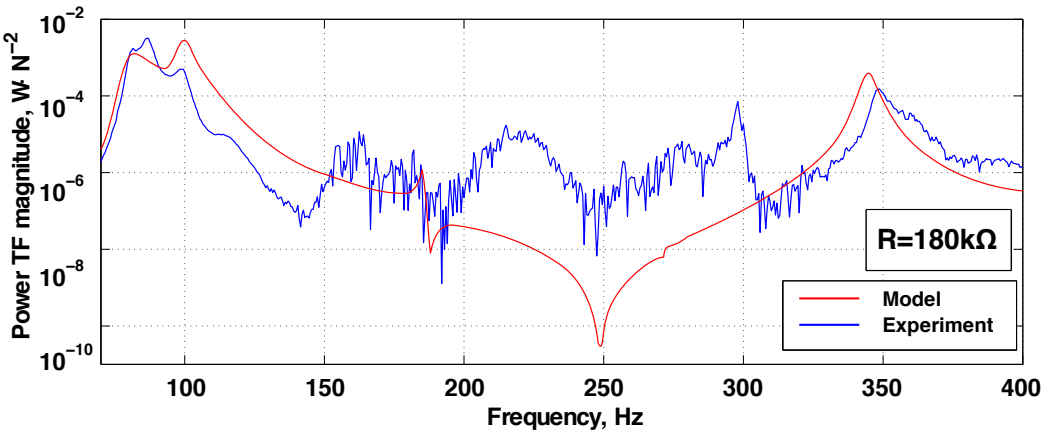

Figure H.26: Comparison of modeled and measured electrical power TF magnitude of the piezoelectric device. $R_1 = 180$ kΩ.

such a lightweight treatment, the second objective pursued is the achievement of useful electrical power output from the device. For a load resistance of $R_1 = 180$ kΩ, the power TF magnitude is shown in Figure H.26. For the two symmetric modes in this bandwidth, (1,1) and (3,1), the measurements show very clear maxima in the electrical power response. While the model is close in replicating the magnitude of the power around the device SDOF natural frequency, 94 Hz, it slightly under estimates the peak response. Measurements at 86.5 Hz observed a power TF magnitude of 3.3 mW·N^{-2}.

In addition, the measurements showed that electrical response for the device when excited by panel asymmetric modes yielded stray electrical signals, and thus the noisy response observed between 120 and 320 Hz. However, the model does not take into account the precise geometry of the circularly corrugated spring layer and, instead, predicts a precipitous electrical signal drop in this bandwidth. Nevertheless, for the two symmetric modes, for which the piezoelectric device is primarily excited by uniform transverse panel vibration, the model is in reasonable agreement with the measurements.

Figure H.27 (a) plots the measured panel response around the (1,1) mode for a variety of load resistances, R_1. Changing the load resistance is here observed to influ-

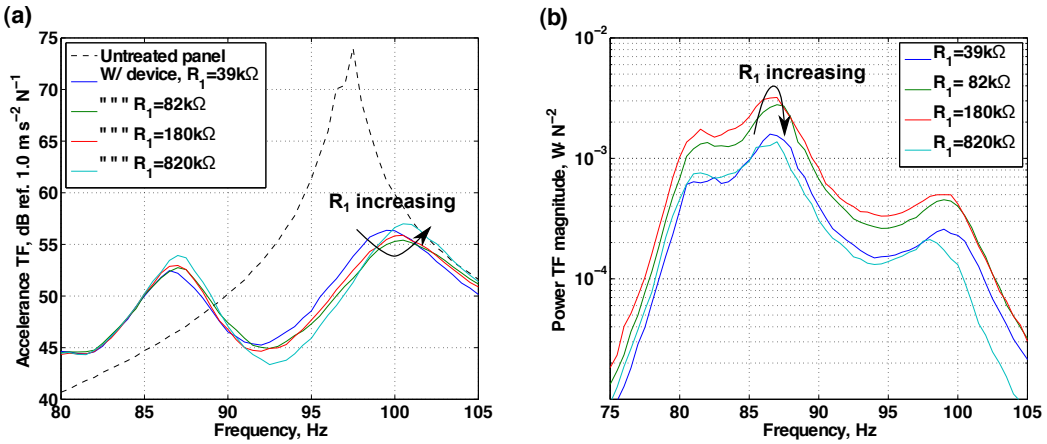

Figure H.27: (a) Panel accelerance TF around (1,1) mode and (b) piezoelectric device power TF for a variety of resistances R_1.

ence the magnitude of the vibration suppression around the (1,1) mode. This suggests that the larger piezoelectric vibration control device, in contrast to the much smaller sample used in FRF testing, exhibits enough electromechanical coupling through the many piezoelectric corrugations to take advantage of shunt damping effects in the energy harvesting circuit.

What is perhaps more interesting, however, is the effect on the panel response measured for the higher of the two split resonances, at 100 Hz. For low R_1, this resonance occurs at 99 Hz. Increasing load resistance dampens this resonance and increases the frequency to 100 Hz. Further increasing R_1 reduces the damping effect and increases the resonance up to 101 Hz. This imitates the piezoelectric shunt damping effects characteristic of other more frequently studied systems like cantilevered piezoelectric beams [40]. This indicates that the attached piezoelectric device itself is dampened and stiffened to varying degrees for the different selections of R_1, yielding new split resonance locations and amplitudes for the host panel which the device is reactively suppressing.

Figure H.27 (b) plots the measured device power TF for the same selections of load resistance. Resistances below or above the optimum range, around $R_1 = 82$ to

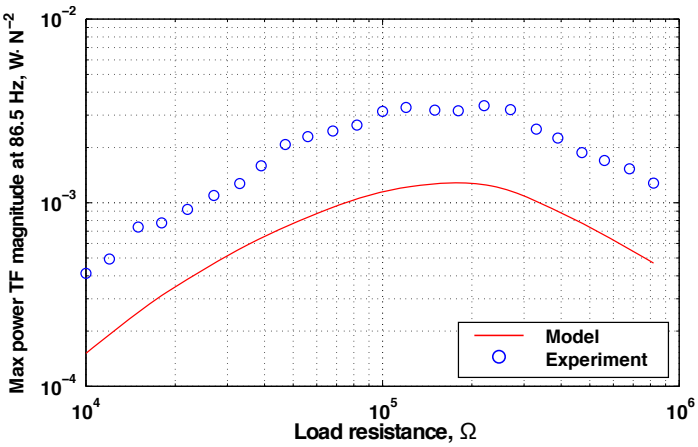

Figure H.28: Comparison of modeled and measured electrical power TF magnitude of the piezoelectric device at 86.5 Hz for various R_1.

180 kΩ, were found to produce the least electrical power. Thus, selection of the load resistance both optimally achieves electrical power as well as achieves best vibration suppression of targeted panel resonances for which the device was originally designed. It is here observed that both objectives are best met by nearly the same choice of R_1: vibration suppression of the panel is best achieved using $R_1 = 82$ kΩ while energy harvesting objectives maximize power for $R_1 \approx 150$ kΩ.

Figure H.28 plots the power TF magnitude at 86.5 Hz for various load resistances. Modeled results are uniformly less than those measured. As observed in Figure H.26, this disparity is explained by the fact that the model predicts the maxima to occur at 100 Hz instead of 86.5 Hz. However, the trend between the two plots is similar and shows a clear optimum range of load resistance for maximizing electrical power output. This range also corresponds roughly to the same region in which vibration suppression of the panel resonance was best achieved.

H.7 Conclusions

This paper presented a model based on the generalized Hamilton's principle to approximate the coupled electro-elastic response of a host structure and attached distributed

piezoelectric vibration control devices. The purpose of the model is to estimate the benefit of such devices in achieving two objectives: *(i)* vibration suppression of the panel via reactive and resistive dynamics and *(ii)* energy harvesting through deformation of the piezoelectric spring layer and coupling to an external circuit.

One such device design was considered in detail. These devices used a distributed spring layer constructed from a circularly corrugated piezoelectric film having electrodes appropriately etched to maximize the voltage output. One sample was attached to a shaker table to measure acceleration and voltage FRFs which were compared against model predictions. The model was found to be in close agreement regarding the location of the SDOF natural frequency of the device and also accurately replicated the effects of electromechanical coupling through the piezoelectric spring layer as the external load resistance was modified.

The model was then employed to evaluate the relative influence of mechanical and electromechanical damping on the two objectives of structural vibration attenuation and the harvesting of the absorbed energy into the added devices. Mechanical damping was found to be uniformly detrimental to energy harvesting objectives. In contrast, due to the high bending and shearing stiffnesses of the circularly corrugated spring layer, greater mechanical damping uniformly improved narrow and broadband vibration attenuation. Electromechanical damping benefits were observed to be maximized simultaneously with maximum power output from the applied device. This agrees with existing results in literature regarding shunt damping induced in power harvesting but extends this result to thereafter dampen the vibrations of the structure to which the harvester is attached, which has yet to be evaluated in literature.

Analysis of modal effects of the top mass layer were considered in light of earlier results in Chapter C showing this dynamic to be of greater benefit in passive vibration attenuation than the top mass oscillating in translation. For lightly electromechanically coupled spring layers, *e.g.* a smart foam sample, placement of the piezoelectric film on the top mass as it vibrated in the modal "pumping" dynamic was found to

yield best results both for vibration suppression and energy harvesting. However, for a device which employed a spring layer of greater coupling, *e.g.* the circularly corrugated piezoelectric spring, placement of the piezoelectric material in the spring layer itself was of significantly greater benefit for both objectives, even if the mass layer were oscillating modally. Thus, though the smart foam sample employed a similar total mass of piezoelectric material as compared to when the film were placed on the top mass, ultimately, maximizing structural vibration attenuation and energy harvesting requires highly electromechanically coupled harvester designs, which is best achieved in this study using the circularly corrugated spring layer.

A larger piezoelectric device using the corrugated piezoelectric spring layer was then manufactured and applied to a lightly-damped structural panel which was excited by random vibration. The added device represented roughly a 1% addition of mass to the host structure and was designed so as to reactively suppress the (1,1) mode of the panel. The addition of the device was seen to significantly suppress this resonance, akin to classical vibration absorbers, and the electromechanical coupling effects due to shunt damping were observed to further suppress the panel vibration by changing the stiffness and damping characteristics of the spring layer as the electrical load resistance was modified. The electrical power TF was maximized when the load resistance was slightly greater than that corresponding to the choice which most suppressed the panel vibration. This indicates both objectives may be nearly achieved simultaneously for the piezoelectric vibration control device considered.

H.8 Components of Eq. H.6

$$\mathbf{K} = \sum_{i=b,s,t} \int_{V_i} \left(\mathbf{L_u}\Psi_\mathbf{m}(\mathbf{x})\right)_i^T \mathbf{c}_i^E \left(\mathbf{L_u}\Psi_\mathbf{m}(\mathbf{x})\right)_i \mathrm{d}V_i \tag{H.13}$$

$$\mathbf{M} = \sum_{i=b,s,t} \rho_i \int_{V_i} \left(\Psi_\mathbf{m}^T(\mathbf{x})\right)_i \left(\Psi_\mathbf{m}(\mathbf{x})\right)_i \mathrm{d}V_i \tag{H.14}$$

$$\mathbf{C} = \alpha\mathbf{M} + \beta\mathbf{K} \tag{H.15}$$

Here, $\alpha = 0$ and $\beta = \eta/\omega$ to employ loss factor damping.

$$\Theta = \int_{V_s} \left(\mathbf{L_u}\Psi\left(\mathbf{x}\right)\right)_s^T \mathbf{e}^T \mathbf{L}_v \Psi_v\left(\mathbf{x}\right) \mathrm{d}V_s \tag{H.16}$$

$$\mathbf{F} = \left[\Psi^t\left(\mathbf{x}_{f_1}\right) \cdots \Psi^T\left(\mathbf{x}_{f_{N_f}}\right)\right] \tag{H.17}$$

$$\mathbf{e} = \begin{bmatrix} 0 & 0 & 0 \\ 0 & 0 & 0 \\ e_{13} & e_{13} & 0 \end{bmatrix} \tag{H.18}$$

with components $e_{13} = \left(d_{31}E_p\right) / \left(1 - \nu_p\right)$

The linear differential operator for the Love–Kirchhoff plates is

$$\left(\mathbf{L_u}\right)_{i=b,t} = \begin{bmatrix} \frac{\partial}{\partial x} & 0 & 0 \\ 0 & \frac{\partial}{\partial y} & 0 \\ \frac{\partial}{\partial y} & \frac{\partial}{\partial x} & 0 \end{bmatrix} \tag{H.19}$$

The linear differential operator for the thick orthotropic plate is

$$\left(\mathbf{L_u}\right)_s = \begin{bmatrix} \frac{\partial}{\partial x} & 0 & 0 \\ 0 & \frac{\partial}{\partial y} & 0 \\ 0 & 0 & \frac{\partial}{\partial z_s} \\ 0 & \frac{\partial}{\partial z_s} & \frac{\partial}{\partial y} \\ \frac{\partial}{\partial z_s} & 0 & \frac{\partial}{\partial x} \\ \frac{\partial}{\partial y} & \frac{\partial}{\partial x} & 0 \end{bmatrix} \tag{H.20}$$

Assuming the piezoelectric material is poled through its thickness and that the electric potential varies linearly through the thickness of the material, the corresponding linear differential operator is

$$\mathbf{L}_v = \begin{bmatrix} 0 \\ 0 \\ -\frac{1}{t_s} \end{bmatrix} \tag{H.21}$$

The stiffness matrices of the Love–Kirchhoff plates are

$$\mathbf{c}^{E}_{i=b,t} = \begin{bmatrix} \frac{E_i}{1-\nu_i^2} & \frac{\nu_i E_i}{1-\nu_i^2} & 0 \\ \frac{\nu_i E_i}{1-\nu_i^2} & \frac{E_i}{1-\nu_i^2} & 0 \\ 0 & 0 & \frac{E_i}{2(1+\nu_i)} \end{bmatrix} \tag{H.22}$$

For the thick orthotropic plate the stiffness matrix is expressed as

$$\mathbf{c}^{E}_{s} = \begin{bmatrix} \frac{1}{E_x} & -\frac{\nu_{yx}}{E_y} & -\frac{\nu_{zx}}{E_z} & 0 & 0 & 0 \\ -\frac{\nu_{xy}}{E_x} & \frac{1}{E_y} & -\frac{\nu_{zy}}{E_z} & 0 & 0 & 0 \\ -\frac{\nu_{xz}}{E_x} & -\frac{\nu_{yz}}{E_y} & \frac{1}{E_z} & 0 & 0 & 0 \\ 0 & 0 & 0 & \frac{1}{G_{yz}} & 0 & 0 \\ 0 & 0 & 0 & 0 & \frac{1}{G_{xz}} & 0 \\ 0 & 0 & 0 & 0 & 0 & \frac{1}{G_{xy}} \end{bmatrix}^{-1} \tag{H.23}$$

The capacitance of the piezoelectric layer, $C_p = \left[A_p \left(\epsilon^{\mathbf{T}}_{33} - d^2_{31} E_p\right)\right] / t_s$, is a function of: A_p, the area of the electrodes; $\epsilon^{\mathbf{T}}_{33}$, the permittivity matrix component evaluated at constant stress; d_{31}, the piezoelectric constant; E_p, the Young's modulus of the piezoelectric material; and t_s, the thickness of the piezoelectric material.

References

[1] J.W. Lane. Our children will not be us, Aug./Sept. 2007. Letter to *APS News*. 16(8).

[2] H. Frahm. Device for damping vibrations of bodies, 1911. U.S. Patent #989,958.

[3] H. Oberst and K. Frankenfeld. On the damping of bending vibrations on thin sheet metal by firmly bonded coatings. *Acustica*, 2(4):181–194, 1952.

[4] P. Liénard. Study of a method for measuring the internal friction of plastic coatings employed in bending. *La Recherche Aéronautique*, 20:11–22, 1951.

[5] L. Cremer, M. Heckl, and B.A.T. Petersson. *Structure-Borne Sound: Structural Vibrations and Sound Radiation at Audio Frequencies*. Springer, Berlin, third edition, 2005.

[6] R. Chandra, S.P. Singh, and K. Gupta. Damping studies in fiber-reinforced composites–a review. *Composite Structures*, 46(1):41–51, 1999.

[7] H. Kishi, M. Kuwata, S. Matsuda, T. Asami, and A. Murakami. Damping properties of thermoplastic-elastomer interleaved carbon fiber-reinforced epoxy composites. *Composites Science and Technology*, 64(16):2517—2523, 2004.

[8] J-M. Berthelot, M. Assarar, Y. Sefrani, and A. El Mahi. Damping analysis of composite materials and structures. *Composite Structures*, 85(3):189–204, 2008.

[9] J.C. Snowdon. Vibration of simply supported rectangular and square plates to which lumped masses and dynamic vibration absorbers are attached. *Journal of the Acoustical Society of America*, 57(3):646–654, 1975.

[10] T. Igusa and K. Xu. Vibration control using multiple tuned mass dampers. *Journal of Sound and Vibration*, 175(4):491–503, 1994.

[11] M.S. Khun, H.P. Lee, and S.P. Lim. Structural intensity in plates with multiple discrete and distributed spring-dashpot systems. *Journal of Sound and Vibration*, 276:627–648, 2004.

[12] C-C. Lin, J-F. Wang, C-H. Lien, H-W. Chiang, and C-S. Lin. Optimum design and experimental study of multiple tuned mass dampers with limited stroke. *Earthquake Engineering and Structural Dynamics*, 39:1631–1651, 2010.

[13] J.A. Zapfe and G.A. Lesieutre. Broadband vibration damping using highly distributed tuned mass absorbers. *AIAA Journal*, 35(4):753–755, 1997.

[14] D.J. Thompson. A continuous damped vibration absorber to reduce broad-band wave propagation in beams. *Journal of Sound and Vibration*, 311:824 – 842, 2008.

[15] J.C. Snowdon. Platelike dynamic vibration absorbers. *Transactions of the American Society of Mechanical Engineers, Journal of Engineering for Industry*, 97:88– 93, 1975.

[16] T. Aida, K. Kawazoe, and S. Toda. Vibration control of plates by plate-type dynamic vibration absorbers. *Journal of Vibration and Acoustics*, 117(3A): 332–338, 1995.

[17] Z. Oniszczuk. Forced transverse vibrations of an elastically connected complex rectangular simply supported double-plate system. *Journal of Sound and Vibration*, 270:997–1011, 2004.

[18] D. Zhou and T. Ji. Free vibration of rectangular plates with continuously distributed spring-mass. *International Journal of Solids and Structures*, 43: 6502–6520, 2006.

[19] C.R. Fuller and P. Cambou. An active-passive distributed vibration absorber

for vibration and sound radiation control. *Journal of the Acoustical Society of America*, 104(3):1851, 1998.

[20] P. Marcotte, C. R. Fuller, and P. Cambou. Control of the noise radiated by a plate using a distributed active vibration absorber (dava). In *Active 99, Proceedings of the International Symposium on Active Control of Sound and Vibration*, pages 447–456, Fort Lauderdale, FL, USA, 1999.

[21] M. Liao and T. Okazaki. A computational study of the I-35W bridge collapse, 2009. University of Minnesota, Report.

[22] D. Benasciutti, L. Moro, S. Zelenika, and E. Brusa. Vibration energy scavenging via piezoelectric bimorphs of optimized shapes. *Microsystem Technologies*, 16: 657–668, 2010.

[23] M. Wischke, M. Masur, M. Kröner, and P. Woias. Vibration harvesting in traffic tunnels to power wireless sensor nodes. *Smart Materials and Structures*, 20:085014, 2011.

[24] M.K. Malinowski. Cargonet: micropower sensate tags for supply-chain management and security. Master's thesis, Massachusetts Institute of Technology, Cambridge, Massachusetts, 2007.

[25] N.G. Elvin, N. Lajnef, and A.A. Elvin. Feasibility of structural monitoring with vibration powered sensors. *Smart Materials and Structures*, 15:977–986, 2006.

[26] N.E. duToit. Modeling and design of a MEMS piezoelectric vibration energy harvester. Master's thesis, Massachusetts Institute of Technology, Cambridge, Massachusetts, 2005.

[27] Y. Liao and H.A. Sodano. Structural effects and energy conversion efficiency of power harvesting. *Journal of Intelligent Material Systems and Structures*, 20: 505–514, 2009.

[28] A. Erturk. *Electromechanical modeling of piezoelectric energy harvesters*. PhD thesis, Virginia Polytechnic Institute and State University, Blacksburg, Virginia, 2009.

[29] M. Kim, M. Hoegen, J. Dugundji, and B.L. Wardle. Modeling and experimental verification of proof mass effects on vibration energy harvester performance. *Smart Materials and Structures*, 19, 2010.

[30] M.A. Karami. *Micro-scale and nonlinear vibrational energy harvesting*. PhD thesis, Virginia Polytechnic Institute and State University, Blacksburg, Virginia, 2011.

[31] C.B. Williams, C. Shearwood, M.A. Harradine, P.H. Mellor, T.S. Birch, and R.B. Yates. Development of an electromagnetic micro-generator. *Circuits, Devices and Systems, IEE Proceedings*, 148(6), 2001.

[32] S.P. Beeby, R.N. Torah, M.J. Tudor, P. Glynne-Jones, T. O'Donnell, and C.R. Saha ad S. Roy. A micro electromagnetic generator for vibration energy harvesting. *Journal of Micromechanics and Microengineering*, 17:1257–1265, 2007.

[33] R.L. Waters, C. Chisum, H. Jazo, and M. Fralick. Development of an electromagnetic transducer for energy harvesting of kinetic energy and its applicability to a mems-scale device. In *Proceedings of the nanoPower Forum 2008*, pages 1–6, 2008.

[34] B.P. Mann and N.D. Sims. Energy harvesting from the nonlinear oscillations of magnetic levitation. *Journal of Sound and Vibration*, 319:515–530, 2009.

[35] G.A. Lesieutre, G.K. Ottman, and H.F. Hofmann. Damping as a result of piezoelectric energy harvesting. *Journal of Sound and Vibration*, 269:991–1001, 2004.

[36] G. Poulin, E. Sarraute, and F. Costa. Generation of electrical energy for portable devices comparative study of an electromagnetic and piezoelectric system. *Sensors and Actuators A*, 116:461–471, 2004.

[37] H.A. Sodano, G. Park, and D.J. Inman. Estimation of electric charge output for piezoelectric energy harvesting. *Strain*, 40(2):49–58, 2004.

[38] S.P. Beeby, M.J. Tudor, and N.M. White. Energy harvesting vibration sources for microsystems applications. *Measurement Science and Technology*, 17:R175–R195, 2006.

[39] N.G. Stephen. On energy harvesting from ambient vibration. *Journal of Sound and Vibration*, 293:409–425, 2006.

[40] M.A. Karami and D.J. Inman. Equivalent damping and frequency change for linear and nonlinear hybrid vibrational energy harvesting systems. *Journal of Sound and Vibration*, 330(23):5583–5597, 2011.

[41] A. Erturk and D.J. Inman. *Piezoelectric Energy Harvesting*. John Wiley & Sons, 2011. ISBN 9780470682548.

[42] A. Erturk. Piezoelectric energy harvesting for civil infrastructure system applications: moving loads and surface strain fluctuations. *Journal of Intelligent Material Systems and Structures*, 2011. doi: 10.1177/1045389X11420593.

[43] N.W. Hagood and A. von Flotow. Damping of structural vibrations with piezoelectric materials and passive electrical networks. *Journal of Sound and Vibration*, 146(2):243–268, 1991.

[44] G.A. Lesieutre. Vibrating damping and control using shunted piezoelectric materials. *The Shock and Vibration Digest*, 30(3):187–195, 1998.

[45] K.M. Jeric. An experimental evaluation of the application of smart damping materials for reducing structural noise and vibrations. Master's thesis, Virginia Polytechnic Institute and State University, Blacksburg, Virginia, 1999.

[46] G. Caruso. A critical analysis of electric shunt circuits employed in piezoelectric passive vibration damping. *Smart Materials and Structures*, 10:1059–1068, 2003.

[47] S.O.R. Moheimani. A survey of recent innovations in vibration damping and control using shunted piezoelectric transducers. *IEEE Transactions of Control Systems Technology*, 11(4):482–494, 2003.

[48] F. Casadei, M. Ruzzene, L. Dozio, and K.A. Cunefare. Broadband vibration control through periodic arrays of resonant shunts: experimental investigation on plates. *Smart Materials and Structures*, 19(1), 2010.

[49] R.L. Forward. Electronic damping of vibrations in optical structures. *Journal of Applied Optics*, 18(5):690–697, 1970.

[50] C.L. Davis and G.A. Lesieutre. A modal strain energy approach to the prediction of resistively shunted piezoceramic damping. *Journal of Sound and Vibration*, 184(1):129–139, 1995.

[51] H. Shen, J. Qiu, and M. Balsi. Vibration damping as a result of piezoelectric energy harvesting. *Sensors and Actuators A: Physical*, 169:178–186, 2011.

[52] C. De Marqui Junior, A. Erturk, and D.J. Inman. Piezoaeroelastic modeling and analysis of a generator wing with continuous and segmented electrodes. *Journal of Intelligent Material Systems and Structures*, 21:983–993, 2010.

[53] H.A. Sodano, J-S. Bae, D.J. Inman, and W.K. Belvin. Improved concept and model of eddy current damper. *Journal of Vibration and Acoustics*, 128(3): 294–302, 2006.

[54] H.A. Sodano. *Development of novel eddy current dampers for the suppression of structural vibrations*. PhD thesis, Virginia Polytechnic Institute and State University, Blacksburg, Virginia, 2005.

[55] M. Schmid and P. Varga. Analysis of vibration-isolating systems for scanning tunneling microscopes. *Ultramicroscopy*, 42–44, Part 2:1610–1615, 1992.

[56] T.L. Smith, K. Rao, and I. Dyer. Attenuation of plate flexural waves by a layer of dynamic absorbers. *Noise Control Engineering Journal*, 26(2):56–60, 1986.

[57] M. Strasberg and D. Feit. Vibration damping of large structures induced by attached small resonant structures. *Journal of the Acoustical Society of America*, 99(1):335–344, 1995.

[58] G. Maidanik and K.J. Becker. Noise control of a master harmonic oscillator coupled to a set of satellite harmonic oscillators. *Journal of the Acoustical Society of America*, 104(5):2628–2637, 1998.

[59] I.M. Koç, A. Carcaterra, Z. Xu, and A. Akay. Energy sinks: vibration absorption by an optimal set of undamped oscillators. *Journal of the Acoustical Society of America*, 118(5):3031–3042, 2005.

[60] J.N. Reddy. *Energy and variational methods in applied mechanics: with an introduction to the finite element method*. Wiley, New York, New York, 1984.

[61] L. Meirovitch. *Elements of vibration analysis*. McGraw-Hill, New York, NY, second edition, 1986.

[62] A.K. Noor and W.S. Burton. Computational models for sandwich panels and shells. *Applied Mechanics Reviews*, 49(3):155–199, 1996.

[63] W.S. Burton and A.K. Noor. Assessment of continuum models for sandwich panel honeycomb cores. *Computer Methods in Applied Mechanics and Engineering*, 145(3–4):341–360, 1997.

[64] H. Hu, S. Belouettar, M. Potier-Ferry, and M> Daya. Review and assessment of various theories for modeling sandwich composites. *Composite Structures*, 84 (3):282–292, 2008.

[65] Y. Frostig and M. Baruch. Bending of sandwich beams with transversely flexible core. *AIAA Journal*, 28(3):523–531, 1990.

[66] Y. Frostig, M. Baruch, O. Vilnay, and I. Sheinman. Bending of nonsymmetric sandwich beams with transversely flexible core. *Journal of Engineering Mechanics*, 117(9):1931–1952, 1991.

[67] O.T. Thomsen. Analysis of local bending effects in sandwich plates with orthotropic face layers subjected to localised loads. *Composite Structures*, 25: 511–520, 1993.

[68] G. Kress. Improving single-constrained-layer damping treatment by sectioning the constraining layer. In *Proceedings of the 11th Biennial Conference on Mechanical Vibration and Noise*, Boston, MA, USA, 1987.

[69] R. Plunkett and C.T. Lee. Length optimization of constrained viscoelastic layer damping. *Journal of the Acoustical Society of America*, 48(1):150–161, 1970.

[70] P.R. Mantena, R.F. Gibson, and S.J. Hwang. Optimal constrained viscoelastic taped lengths for maximizing damping in laminated composites. *AIAA Journal*, 29(10):1678–1685, 1991.

[71] A. Arpaci and M. Savci. Response and damping of a rectangular cantilever plate with vibrating beam dampers. *Journal of Sound and Vibration*, 107(2): 243–252, 1986.

[72] P. Marcotte. *A study of distributed active vibration absorbers (DAVA)*. PhD thesis, Virginia Polytechnic Institute and State University, Blacksburg, Virginia, 2004.

[73] K.A. Cook-Chennault, N. Thambi, and A.M. Sastry. Powering MEMS portable devices–a review of non-regenerative and regenerative power supply systems with special emphasis on piezoelectric energy harvesting systems. *Smart Materials and Structures*, 17(4):043001, 2008.

[74] H. Sodano, G. Park, and D.J. Inman. A review of power harvesting from vibration using piezoelectric materials. *Shock and Vibration Digest*, 36:197–205, 2004.

[75] S. Priya. Advances in energy harvesting using low profile piezoelectric transducers. *Journal of Electroceramics*, 19:167–184, 2007.

[76] C.B. Williams and R.B. Yates. Analysis of a micro-electric generator for microsystems. *Sensors and Actuators A*, 52:8–11, 1996.

[77] C. Guigou and C.R. Fuller. Control of aircraft interior broadband noise with foam–pvdf smart skin. *Journal of Sound and Vibration*, 220(3):541–557, 1999.

[78] P. Leroy, A. Berry, P. Herzog, and N. Atalla. Experimental study of a smart foam sound absorber. *Journal of the Acoustical Society of America*, 129(1): 154–164, 2011.

[79] A. Kundu and A. Berry. Active control of transmission loss with smart foams. *Journal of the Acoustical Society of America*, 129(2):726–740, 2011.

[80] G.C. Tibbetts. Transducer having piezoelectric film arranged with alternating curvatures, 1977. U.S. Patent #4,056,742.

[81] C.A. Gentry-Grace. *A study of smart foam for noise control applications*. Ph.d. thesis, Virginia Polytechnic Institute and State University, Blacksburg, Virginia, 1998.

[82] J.P. Den Hartog. *Mechanical Vibrations*. Dover Publications, New York, NY, fourth edition, 1985.

[83] R.L. Weaver. The effect of an undamped finite degree of freedom "fuzzy" substructure: Numerical solutions and theoretical discussion. *Journal of the Acoustical Society of America*, 100(5):3159–3164, 1996.

[84] R.L. Weaver. Mean and mean-square responses of a prototypical master/fuzzy structure. *Journal of the Acoustical Society of America*, 101(3):1441–1449, 1997.

[85] A. Erturk and D.J. Inman. An experimentally validated bimorph cantilever model for piezoelectric energy harvesting from base excitations. *Smart Materials and Structures*, 18, 2009.

[86] S. Roundy. On the effectiveness of vibration-based energy harvesting. *Journal of Intelligent Material Systems and Structures*, 16:809–823, 2005.

[87] E.K. Reilly, L. Miller, R. Fain, and P.K. Wright. A study of ambient vibrations for piezoelectric energy scavenging. *POWERMEMS: International Workshop on Micro and Nanotechnology for Power Generation and Energy Conversion Applications (Washington, DC)*, pages 312–315, 2009.

[88] N.E. duToit, B.L. Wardle, and S-G. Kim. Design considerations for mems-scale piezoelectric mechanical vibration energy harvesters. *Integrated Ferroelectrics*, 71:121–160, 2005.

[89] J. Granstrom, J. Feenstra, H.A. Sodano, and K. Farinholt. Energy harvesting from a backpack instrumented with piezoelectric shoulder straps. *Smart Materials and Structures*, 16:1810–1820, 2007.

[90] O. Bilgen, Y. Wang, and D.J. Inman. Electromechanical comparison of cantilevered beams with multifunctional piezoceramic devices. *Mechanical Systems and Signal Processing*, 2011. doi: 10.1016/j.ymssp.2011.09.002.

[91] C.D. Richards, M.J. Anderson, D.F. Bahr, and R.F. Richards. Efficiency of

energy conversion for devices containing a piezoelectric component. *Journal of Micromechanics and Microengineering*, 14:717–721, 2004.

[92] Y.C. Shu and I.C. Lien. Efficiency of energy conversion for a piezoelectric power harvesting system. *Journal of Micromechanics and Microengineering*, 16:2429–2438, 2006.

[93] J.J. McCoy. Harvesting mechanical energy via structural vibrations. *Journal of the Acoustical Society of America*, 130(4):1783–1786, 2011.

[94] L. Meirovitch. *Analytical methods in vibrations*. Macmillan, University of Michigan, 1967.

[95] A. Preumont. *Mechatronics: Dynamics of Electromechanical and Piezoelectric Systems*. Springer, 2006.

[96] A.W. Leissa. *Vibration of Plates*. NASA SP-160, 1969.

[97] O. Beslin and J. Nicolas. A hierarchical functions set for predicting very high order plate bending modes with any boundary conditions. *Journal of Sound and Vibration*, 202(5):633–655, 1997.

[98] L. Dozio. On the use of the trigonometric ritz method for general vibration analysis of rectangular kirchhoff plates. *Thin-Walled Structures*, 49:129–144, 2011.

[99] T.D. Dang, R.K. Kapania, and M.J. Patil. Ritz analysis of discontinuous beams using local trigonometric functions. *Computational Mechanics*, 49:1–16, 2010.

[100] Y. Gu, R.L. Clark, C.R. Fuller, and A.C. Zander. Experiments on active control of plate vibration using piezoelectric actuators and polyvinylidene fluoride (pvdf) modal sensors. *Journal of Vibration and Acoustics*, 116:303–308, 1994.

[101] A. Baz and J. Ro. Vibration control of plates with active constrained layer damping. *Smart Materials and Structures*, 5:272–280, 1996.

[102] G. Caruso, S. Galeani, and L. Menini. Active vibration control of an elastic plate using multiple piezoelectric sensors and actuators. *Simulation Modelling Practice and Theory*, 11(5-6):403–419, 2003.

[103] C. Paulitsch, P. Gardonio, and S.J. Elliot. Active vibration control using an inertial actuator with internal damping. *Journal of the Acoustical Society of America*, 119(4):2131–2140, 2006.

[104] P.E. Cambou. A distributed active vibration absorber (DAVA) for active-passive vibration and sound radiation control. Master's thesis, Virginia Polytechnic Institute and State University, Blacksburg, Virginia, 1998.

[105] D.N. Manikanahally and M.J. Crocker. Vibration absorbers for hysterestically damped mass-loaded beams. *Journal of Vibration and Acoustics*, 113:116–122, 1991.

[106] M.N. Hadi and Y. Arfiadi. Optimum design of absorber for mdof structures. *Journal of Structural Engineering*, 124(11):1272–1280, 1998.

[107] M.P. Singh, S. Singh, and L.M. Moreschi. Tuned mass dampers for response control of torsional buildings. *Earthquake Engineering and Structural Dynamics*, 31(4):749–769, 2002.

[108] C.C. Chang and Henry T.Y. Yang. Control of buildings using active tuned mass dampers. *Journal of Engineering Mechanics*, 121(3):355–366, 1995.

[109] R.I. Wright. *A hierarchical noise control system using adaptable tuned vibration absorbers.* PhD thesis, Virginia Polytechnic Institute and State University, Blacksburg, Virginia, 2003.

[110] C. Libove and S.B. Batdorf. A general small-deflection theory for flat sandwich plates. *National Aeronautics and Space Administration Report No. 899*, pages 139–156, 1948.

[111] Q.H. Cheng, H.P. Lee, and C. Lu. A numerical analysis approach for evaluating elastic constants of sandwich structures with various cores. *Composite Structures*, 74:226–236, 2006.

[112] Y. Liu and K.W. Wang. Enhanced active constrained layer damping treatment for broadband vibration suppression. *Journal of Vibration and Control*, 8(6): 777–803, 2002.

[113] S.J. Estéve and M.E. Johnson. Reduction of sound transmission into a circular cylindrical shell using distributed vibration absorbers and helmholtz resonators. *Journal of the Acoustical Society of America*, 112(6):2840–2848, December 2002.

[114] J.N. Reddy. On refined computational models of composite laminates. *International Journal for Numerical Methods in Engineering*, 27(2):361–382, 1989.

[115] O.T. Thomsen. Theoretical and experimental investigation of local bending effects in sandwich plates. *Composite Structures*, 30(1):85–101, 1995.

[116] Y. Frostig. Classical and high-order computational models in the analysis of modern sandwich panels. *Composites: Part B*, 34:83–100, 2003.

[117] K. Idrisi. *Heterogeneous (HG) blankets for improved aircraft interior noise reduction.* PhD thesis, Virginia Polytechnic Institute and State University, Blacksburg, Virginia, 2008.

[118] G.Z. Voyiadjis and P.I. Kattan. *Mechanics of Composite Materials with MATLAB.* Springer–Verlag, 2005.

[119] G.B. Shaw and R.P. Trost. Statistical analysis of hearing loss among navy personnel. Technical Report CRM D0011228.A2/Final, Centers for Naval Analyses, February 2005.

[120] Martin Kurz and Inc. Co. Dynapore product information brochure. Technical data sheet, June 2001.

[121] 3M Industrial Business Electronics Markets Materials Division. 3m viscoelastic damping polymer 110. Technical data sheet, April 2003.

[122] C.R. Fuller, J.P. Maillard, M. Mercadal, and A.H. vonFlotow. Control of aircraft interior noise using globally detuned vibration absorbers. *Journal of Sound and Vibration*, 203(5):745–761, 1997.

[123] S. Roundy and P.K. Wright. A piezoelectric vibration based generator for wireless electronics. *Smart Materials and Structures*, 13:1131–1142, 2004.

[124] H.J. Song, Y.T. Choi, G. Wang, and N.M. Wereley. Energy harvesting utilizing single crystal pmn-pt material and application to a self-powered accelerometer. *Journal of Mechanical Design*, 131, 2009.

[125] A. Erturk, J.M. Renno, and D.J. Inman. Modeling of piezoelectric energy harvesting from an l-shaped beam-mass structure with an application to uavs. *Journal of Intelligent Material Systems and Structures*, 20:529–544, 2009.

[126] P-H. Wang, X-H. Dai, D-M. Fang, and X-L. Zhao. Design, fabrication and performance of a new vibration-based electromagnetic micro power generator. *Microelectronics Journal*, 38:1175–1180, 2007.

[127] S.R. Anton and D.J. Inman. Vibration energy harvesting for unmanned air vehicles. In *Smart Structures and Materials 2008: Active and Passive Smart Structures and Integrated Systems II, Proceedings of SPIE 6928, San Diego*, pages 1–10, 2008.

[128] A. Erturk, W.G.R. Vieira, C. DeMarqui Jr., and D.J. Inman. On the energy harvesting potential of piezoaeroelastic systems. *Applied Physics Letters*, 96, 2010.

[129] J.M. Renno, M.F. Daqaq, and D.J. Inman. On the optimal energy harvesting from a vibration source. *Journal of Sound and Vibration*, 320:386–405, 2009.

[130] D.J. Inman. *Vibration with Control*. Wiley, Hoboken, NJ, first edition, 2006.

[131] E. Lefeuvre, A. Badel, C. Richard, L. Petit, and D. Guyomar. A comparison between several vibration-powered piezoelectric generators for standalone systems. *Sensors and Actuators A*, 126:405–416, 2006.

[132] R.G. Jacquot and J.E. Foster. Optimal cantilever dynamic vibration absorbers. *Journal of Engineering for Industry*, 99:138–141, 1977.

[133] J.R. Liang and W.H. Liao. Piezoelectric energy harvesting and dissipation on structural damping. *Journal of Intelligent Material Systems and Structures*, 20: 515–527, 2009.

[134] C.A. Gentry, C. Guigou, and C.R. Fuller. Smart foam for applications in passive–active noise radiation control. *Journal of the Acoustical Society of America*, 101(4):1771–1778, 1997.

[135] C. De Marqui Junior, A. Erturk, and D.J. Inman. An electromechanical finite element model for piezoelectric energy harvester plates. *Journal of Sound and Vibration*, 327(1):9–25, 2009.

[136] N.S. Bakhvalov and G.P. Panasenko. *Homogenization Averaging Processes in Periodic Media*. Kluwer Academic, 1989.

[137] L. Jaouen, A. Renault, and M. Deverge. Elastic and damping characterizations of acoustical porous materials: available experimental methods and applications to a melamine foam. *Applied Acoustics*, 69:1129–1140, 2008.

[138] COMSOL Inc. *COMSOL Multiphysics User's Guide*. COMSOL AB., Burlington, MA, October 2007.

[139] P. Leroy, N. Atalla, and A. Berry. Three dimensional finite element modeling of smart foam. *Journal of the Acoustical Society of America*, 126(6):2873–2885, 2009.

[140] K.C. Bailo, D.E. Brei, and K. Grosh. Investigation of curved polymeric piezoelectric active diaphragms. *Journal of Vibration and Acoustics*, 125:145–154, 2003.

[141] J-Q. Liu, H-B. Fang, Z-Y. Xu, X-H. Mao, X-C. Shen, D. Chen, H. Liao, and B-C. Cai. A mems-based piezoelectric power generator array for vibration energy harvesting. *Microelectronics Journal*, 39:802–806, 2008.

[142] F. Lu, H.P. Lee, and S.P. Lim. Modeling and analysis of micro piezoelectric power generators for micro-electromechanical-systems applications. *Smart Materials and Structures*, 13(1):57, 2004.

[143] C.A. Gentry-Grace. *A study of smart foam for noise control applications*. Ph.d. thesis, Virginia Polytechnic Institute and State University, Blacksburg, Virginia, 1998.

[144] C. Libove and R.E. Hubka. Elastic constants for corrugated-core sandwich plates. *National Advisory Committee for Aeronautics, Technical Note 2289*, 1951.

[145] A. Erturk, P.A. Tarazaga, J.R. Farmer, and D.J. Inman. Effect of strain nodes and electrode configuration on piezoelectric energy harvesting from cantilevered beams. *Journal of Vibration and Acoustics*, 131(1), 2009.

[146] T.E. Carmichael. The vibration of a rectangular plate with edges elastically

restrained against rotation. *The Quarterly Journal of Mechanics and Applied Mathematics*, 12(1):29–42, 1959.